Synthesis of Low Dimensional Boron Nitride Nanomaterials for Thermal Management Applications

A thesis submitted for the degree of

Doctor of Philosophy



Jesus Antonio I. Acapulco Jr.

St. Catherine's College, University of Oxford

January 2020

Declaration

I confirm that the work presented in this thesis is my own work. No part of this thesis has been accepted or is currently being submitted for any degree, diploma, certificate or other qualification in this University or elsewhere. This thesis is my own work, except where indicated.

Abstract

This thesis investigates the synthesis of boron nitride (BN) nanomaterials using the chemical vapour deposition (CVD) technique, in order to propose an efficient means of generating high-quality BN nanomaterials of different morphologies whose properties can be controlled, so that they can be optimised for real-world applications, particularly for thermal management.

It is found out that the growth of BN nanotubes (BNNTs) followed a tip-growth mechanism and this was confirmed by varying the duration of reaction studied through scanning electron microscopy (SEM). This study shows that the powder precursor of boron and magnesium oxide generated gaseous boron oxide and magnesium that was found to be deposited on the surface of the SiO_2 target substrate in the form of magnesium borate. This observation was investigated by thermal gravimetric analysis (TGA), energy-dispersive x-ray spectroscopy (EDX), and X-ray photoelectron (XPS) depth profiling. The lower melting point of magnesium borate compared to the synthesis temperature enabled the formation of catalyst droplets that was found to be crucial to generating the nanotubular structure. Hindering the formation of catalyst droplets resulted in the synthesis of BN nanosheets. Hybrid one-dimensional nanostructures such as BNNTs coated with CNT were synthesised by adding methane as carbon source in the synthesis.

The properties of BN nanomaterials can be tailored by controlling their morphology that has been observed by the increase of thermal conductivity of BN nanotubes compared to BN nanosheets at the same weight percent in isopropanol that was measured using the transient plane source (TPS) method. These controllable properties make BN nanomaterials a promising material that can be used as fillers in composites and liquid solutions for thermal management and other applications.

Performing Density Functional Theory (DFT) calculations showed insights regarding BN bond formation and it was found out that a small difference of energy barrier was present between the synthesis with and without the catalyst droplet, from which it can be inferred that BN bond formation can still occur in the absence or presence of the catalyst droplet. BN bond formation occurring on the MgO (100)-(111) step-edge surface was shown to have more stable energy than those on the MgO (111) facet surface, which led to the development of zigzag chirality. These theoretical findings are found to be in good agreement with the empirical results. Lastly, it was found out that the activation energy for BNNT growth is 58.88 kcal/mol by correlation of the growth rate and the Arrhenius equation.

Preface

Oral presentations

June 2018	**Chemical Vapour Deposition Synthesis of Boron Nitride Nanotube** Invited talk Carbon Chemistry Institute Zaragoza, Spain
June 2018	**Nucleation and Growth of Boron Nitride Nanotubes** Invited talk Institute of Computational Chemistry and Catalysis, University of Girona Girona, Spain
August 2017	**Functional h-BN coating on CNTs** S Meysami, M Carter, X Liu, K Evers, J A Acapulco Jr., V Babenko, N Grobert NanoteC17, University of Nantes Nantes, France
July 2017	**Micro- and Nano- Materials and Thermal Engineering** Research presentation The University of Tokyo Tokyo, Japan
July 2017	**The Graduate Program for Mechanical Systems Innovation (GMSI) and the Global Leader Program for Social Design and Management (GSDM)** Invited participant Saitama, Japan
February 2017	**Hetherington Prize 2017 Winner, Best Second-year DPhil Research Talk** Research presentation Department of Materials, University of Oxford Oxford, United Kingdom

Poster presentations

November 2018 — ***In Situ* Experimental and Theoretical Studies of the Nucleation and Growth towards Controlling the Morphology of Boron Nitride Nanotubes Using Chemical Vapour Deposition Techniques**
Nominated as Best Poster
J A Acapulco Jr., S Meysami, V Babenko, K Evers, R Jones, M Swart, and N Grobert
2018 MRS Fall Meeting and Exhibit
Boston, Massachusetts, United States of America

March 2018 — **STEM for BRITAIN 2018 CHEMISTRY**
J A Acapulco Jr., S Meysami, V Babenko, K Evers, R Jones, and N Grobert
House of Commons,
Attlee Suite, Portcullis House
London, United Kingdom

February 2018 — **Growth of Boron Nitride Nanotubes Using Chemical Vapour Deposition**
Poster presentation
Department of Materials, University of Oxford
Oxford, United Kingdom

Publications

2020 — **An Experimental and Theoretical Investigation of the Chirality and Growth Activation Energy of Hexagonal Boron Nitride Nanomaterials**
J A Acapulco Jr., M Swart, and N Grobert
Written up

2017 — **Vertically-aligned Silicon Carbide Nanowires as Visible-Light-Driven Photocatalysts**
J Hong, S Meysami, V Babenko, C Huang, S Luanwuthi, J A Acapulco, P Holdway, P Grant, and N Grobert
Applied Catalysis B: Environmental 218, 267- 276 (2017)

Acknowledgements

Completion of this thesis would not be possible without the help of many people. Thus, I would like to thank the following for their guidance and support:

First and foremost, to Prof Nicole Grobert, my supervisor, for letting me be a part of this wonderful team. Thank you for giving me advice that helped me stay on track.

I owe many thanks to Dr Seyyed Shayan Meysami for helping me kick-start my research. He was always available to check my experiments and we had a lot of discussions that aided the advancement of my work.

I would like to thank the members of the Nanomaterials by Design group for making the everyday work as exciting as possible. Shout out to Albert, Pablo, Dominique, Koen, Ruth, Pierre, and Santamon for the amazing times. NbD! NbD! NbD!

I had an amazing opportunity to work and collaborate with the Institut de Química Computacional i Catàlisi, Universitat de Girona. I am thankful to Prof Marcel Swart for the guidance during my visit there and for giving his insights on the theoretical calculations in this thesis. This collaboration would not have been possible without the help from the HPC-Europa3 programme and the Barcelona Supercomputing Centre.

Many thanks to Mr Greg Cook, Mrs Jennifer Holter, Dr Ian Griffiths, Mr Graham Wyatt, and Dr Neil P. Young of the Oxford Materials Electron Microscopy and Microanalysis (EM&M) group for training me on the use of different microscopes and providing wonderful technical support.

I am thankful to Dr Colin Johnston, Dr Phil Holdway, and Nicola Flanagan, the personnel of the Oxford Materials Characterisation Services (OMCS), for the training they provided me and for the data acquisition of my samples.

Special thanks to the Oxford Philippines Society (OPS) for keeping the Filipino spirit. To the Beshiecakes group, JD, and Vinmar, thank you guys!

Huge thanks to Dr Danica Salazar for lending her professional skills in the English language.

I would like to thank June and Rodel for always welcoming me when I visit my brother in Cambridge.

Lastly, I am deeply indebted and will always be grateful to my family, Nanay, Tatay, kuya Ivan and kuya JU for their love and support. Most importantly to Him, who has been the source of my strength and who made all of these possible be the glory, honour, dominion, and power, forever and ever!

Contents

Declaration..... i

Abstract..... ii

Preface..... iii

Acknowledgement..... v

Contents..... vii

List of symbols and abbreviations..... xi

List of figures..... xiii

1 Introduction 1

1.1 Boron nitride (BN) nanomaterials 1

1.2 Thesis overview 3

1.2.1 Background and aims of this thesis 3

1.2.2 Structure of this thesis 7

1.3 Literature review 8

1.3.1 Structures of BN nanomaterials 8

1.3.1.1 hexagonal boron nitride (h-BN) 8

1.3.1.2 BN nanosheets (BNNSs) 10

1.3.1.3 BN nanotubes (BNNTs) 12

1.3.2 Discovery and key developments of boron nitride nanotubes 14

1.3.2.1 Arc-discharge method 15

1.3.2.2 Laser ablation/vaporisation method 17
1.3.2.3 Substituted reaction/template-assisted BNNT synthesis 18
1.3.2.4 Ball-milling method 20
1.3.2.5 Chemical vapour deposition 21
1.3.3 Properties of BNNTs 24
1.3.3.1 Mechanical properties of BNNTs 24
1.3.3.2 Thermal conductivity of BNNTs 25
1.3.3.3 Electronic properties of BNNTs 26
1.3.3.4 Oxidation resistance of BNNTs 27
1.3.4 Potential applications for BN nanomaterials 29
1.3.4.1 BN nanomaterials for thermal management applications 29
1.3.4.2 Other applications for BN nanomaterials 32
1.3.5 DFT studies in the synthesis of BN nanomaterials 33
1.4 Method of analysis 36
1.4.1 Electron microscopy (scanning and transmission) 36
1.4.2 Energy-dispersive X-ray spectroscopy (EDX) 40
1.4.3 Electron energy-loss spectroscopy (EELS) 42
1.4.4 Raman spectroscopy 44
1.4.5 Theoretical approach 46
1.4.5.1 *Ab initio* theory 46
1.4.5.2 Density Functional Theory (DFT) 48
2 **Synthesis and growth mechanism of BNNTs** 51
2.1 Introduction 52
2.2 Materials and methods 55
2.2.1 CVD synthesis of BNNTs 55

2.2.2 Characterisation 56
2.3 Results and discussion 57
2.3.1 Structure and composition analysis 57
2.3.2 Particle on tip investigation 61
2.3.3 Evolution of catalyst droplet 63
2.3.4 Formation mechanism of BNNTs 70
2.4 Conclusion 73
3 Morphology control and hybrid BN nanomaterials 74
3.1 Introduction 75
3.2 Materials and methods 77
3.2.1 Morphology control and hybrid BN nanomaterial synthesis 77
3.2.2 Structure and composition characterisation 79
3.2.3 Band gap and thermal conductivity measurements 80
3.3 Results and discussion 82
3.3.1 BN nanosheets 82
3.3.2 BN nanobamboos 88
3.3.3 Diameter decrease of BNNTs 97
3.3.4 Hybrid BN nanomaterials 103
3.3.5 Electronic and thermal properties 111
3.4 Conclusion 115
4 Correlating the experimental and theoretical results in the synthesis of BNNTs .. 116
4.1 Introduction 117
4.2 Computational details 118
4.2.1 Potential energy surface calculation 120
4.2.2 $B_2O_2 + H_2$ potential energy surface 123

4.2.3 B_2O_2 + NH_3 potential energy surface 130
4.3 Results and discussion 137
4.3.1 Modelling the nucleation and growth of BNNTs 137
4.3.2 BN precursors at atomic level 140
4.3.3 BN precursors at molecular level 146
4.3.4 Activation energy of BNNT growth 157
4.4 Conclusion 160
5 Summary and future research 161
5.1 Summary of findings 161
5.1.1 The BOCVD method yields BNNTs of a high quality 161
5.1.2 The synthesis of BNNTs follows a tip-growth mechanism proved by studying the evolution of the catalyst droplets 162
5.1.3 The properties of BN nanomaterials can be controlled by synthesising different structures 163
5.1.4 Theoretical calculations support the experimental results and proved the synthesis of zigzag BNNT 164
5.2 Future work 166
5.2.1 Aerosol-assisted CVD synthesis of BNNTs 166
5.2.2 BN nanomaterials used in composite science 168
5.2.3 Calculation of properties for tailored applications 170
Bibliography 172
Appendix: Additional information 185

List of symbols and abbreviations

Å	Angstrom
°C	degree Celsius
TPa	terapascal
GPa	gigapascal
$Wm^{-1}K^{-1}$	Watts per meter Kelvin
K	Kelvin
a.u.	arbitrary units
σ*	sigma antibonding orbitals
π*	pi antibonding orbitals
eV	electron volts
hr	hour
µm	micrometre
nm	nanometre
Ω	Ohm
Δ	change
k	growth rate
E_a	activation energy
R	universal gas constant
A	proportionality coefficient
T	temperature
sccm	standard cubic centimetres per minute
1D	one-dimensional
2D	two-dimensional
ADF	Amsterdam Density Functional
ADF-STEM	annular dark field scanning transmission electron microscopy
AFM	atomic force microscopy

BN	boron nitride
BNNTs	boron nitride nanotubes
BOCVD	boron oxide chemical vapour deposition
c-BN	cubic-boron nitride
CNTs	carbon nanotubes
CPU	central processing unit
CVD	chemical vapour deposition
DFT	Density Functional Theory
DFTB	Density Functional Based Tight Binding
FC	frozen-core
EDX	energy-dispersive X-ray spectroscopy
EELS	electron energy-loss spectroscopy
FETs	field-effect transistor setup
FFT	fast Fourier transform
H-BN	hexagonal-boron nitride
HRTEM	high-resolution transmission electron microscopy
LT	Linear transit
MW-BNNT	Multi-walled boron nitride nanotube
NASA	National Aeronautics and Space Agency
P	product
P(complex)	product complex
QUILD	Quantum-regions Interconnected by Local Descriptions
R	reactant
R(complex)	reactant complex
SEM	scanning electron microscopy
SW	single-walled
TEM	transmission electron microscopy
TPS	transient plane source
TGA	thermal gravimetric analysis
TS	transition state
VLS	vapour-liquid-solid
VEELS	valence electron energy loss spectroscopy
XPS	X-ray photoelectron spectroscopy
ZLP	zero loss peak

List of figures

Figure 1.1 Number of published articles on BN nanotubes (black column), BN nanosheets (red column), and hexagonal BN (blue column) from 1992 to 2018 acquired from Google Scholar. 2
Figure 1.2 (A) Published articles collected in Google Scholar from 1991 to 2018 comparing boron nitride nanomaterials (BNNTs and BN nanosheets) and carbon nanomaterials (CNTs and graphene), black and red, respectively. Note that the x-axis changes magnitude at 2500 articles. (B) Statistics on published papers on BNNTs acquired from the report of Zhi [5]..... 3
Figure 1.3 Proposed growth mechanisms by (A) Lourie et al.[6] following root-growth. Left: nanotube-cap nucleation. Right: at a later stage of growth; note the flag-like initial cap, the conventional nanotube middle section, and the root at the nanotube-catalyst junction consisting of incomplete BN layers. (B) Ma et al.[9], similar to the nanotube 'tip growth' in the metal catalyst CVD method. (C) Growth model of BNNTs presented by Su et al.[10]..... 4
Figure 1.4 Theoretical calculations by molecular dynamics showing the (A) nucleation of BNNT from $B_2O_2 + NH_3$ by McLean et al. [17] and (B) growth of BNNT from the surface of a boron droplet initiated by a cap structure by Santra et al. [18]. 5
Figure 1.5 (A) Structures of h-BN and graphite as presented by Souche et al. [20]. (B) Optical image of hexagonal boron nitride (h-BN) single crystal from Watanabe et al. [21]..... 8
Figure 1.6 Basic structure of 2D BN nanostructures where BNNR stands for BN nanoribbon [26]..... 10
Figure 1.7 (A) Schematic representation of rolling h-BN to form BNNT. (B)Vectors (n,m) for a single-walled BNNT on a h-BN sheet [30]. (C) Armchair and (D) Zigzag chirality of BNNTs..... 12
Figure 1.8 Different morphologies of BNNTs (A) single-walled [31], (B) double-walled [32], (C) multi-walled [11], (D) capped end [33], (E) capped inner nanotube [34], and (F) cap stacked structure or 'nanobamboo' [35]. 13
Figure 1.9 Timeline of BNNTs from discovery and key developments. 14
Figure 1.10 (A) Schematic representation of arc-discharge nanotube growth equipment with a horizontal orientation [43]. (B) TEM image of a BN soot sample collected

after arc discharge where dark arrows identify one long BN multi-walled nanotube while a light arrow indicates another tube and (C) High resolution TEM image focussing on a single BN nanotube from Chopra et al. [44]..... 15
Figure 1.11 Synthesised BNNTs by Golberg et al.[51] utilising the laser ablation method. HRTEM images of representative nanotubes at nitrogen pressures of (a) 8.4 and (b) 5.4 GPa..... 17
Figure 1.12 HRTEM images of the synthesised BNNTs by laser vaporisation technique reported by Arenal et al. [55] showing (a) bundles of BNNTs with nanoparticles, (b) double-walled BNNTs, (c) single-walled BNNTs, and (d) BN onion-like structures.. 18
Figure 1.13 (A) Schematic illustrations from Han et al. [56] of carbon nanotubes as a template to produce new one-dimensional nanoscale materials by (a) filling, (b) coating, (c) carbon nanotubes confined reaction to produce carbide and nitride nanorods, and (d) carbon nanotubes substituted reaction to produce boron nitride nanotubes. HRTEM images of (B) the sacrificial carbon nanotubes and (C) the result after BN substitution..... 18
Figure 1.14 Anodic aluminium oxide template-assisted synthesis of BNNTs by Moskovits et al. (a) SEM image of template-grown boron nitride nanotubes and (b) TEM image of BN nanotubules [61]. 19
Figure 1.15 (A) Schematic of a ball-milling setup. (B) SEM and (C) TEM images of synthesised BNNTs using the ball-milling method as reported by Chen et al. [62]... 20
Figure 1.16 SEM and TEM images of BNNTs synthesised using the chemical vapour deposition method. (A and B) Precursor of in situ generated borazine by Lourie et al. [6]. (C and D) Precursor of in situ generated B_2O_2 and Mg by Tang et al. [11]. (E and F) Addition of iron oxide in the powder precursor by Zhi et al. [12]. 21
Figure 1.17 Experimental setup of the production of B_2O_2 species as intermediate for the synthesis of BNNTs by Tang et al. [11]..... 22
Figure 1.18 Thermal gravimetric analysis comparing CNTs and BNNTs in air. 28
Figure 1.19 Thermal diffusivity values of epoxy/BN nanocomposite films at different BNN loadings (square) compared with those for PVA/BNNs films (circle). Inset: Photograph of a piece of film with 50% BNN loading..... 29
Figure 1.20 Thermal conductivities of nanofluids using (A) CNT [101], (B) silver nanowires [102], (C) copper oxide nanomaterials [103], and (D) aluminium oxide nanoparticles [104] at different concentrations. 30
Figure 1.21 Plot of specific modulus vs specific strength of different materials at (A) room temperature and (B) 700 °C; (Blue) Baseline materials, (green) near-term, and (red) exploratory [110]..... 32
Figure 1.22 Potential energy surface of BN bond formation showing reaction barriers at the (a) terrace) and (b) step-edge on an iron surface as reported by Riikonen et al[118]..... 34
Figure 1.23 Potential energy surface showing (a) barrier for B diffusion, (b) B2 association/dissociation reaction, and BN association/dissociation reaction on Mg(100) surface reported by Riikonen et al.[119] 35

Figure 1.24 Schematic illustration comparing an (A) optical microscope and a (B) transmission electron microscope. (C) Photograph image of the JEOL JEM-3000F used in this study. *37*
Figure 1.25(A) SEM image showing the filaments structures, (B) TEM image showing hollow morphology, and (C) HRTEM image showing the layers of sheets that comprise the walls of the nanotube acquired for this thesis. *38*
Figure 1.26 Examples of the h-BN structures after an exposure to a TEM beam with different acceleration voltages: (a) 80 kV, (b) 120 kV, and (c) 200 kV from the report of Kotakoski et al. [123]. *39*
Figure 1.27 TEM image of BNNT (A) before and after the exposure to three different beam sizes: (B) size 1 of 90 nm, (C) size 2 of 50 nm at left side and size 3 of 5 nm at right side reported by Celik-Aktas et al. [128]. *40*
Figure 1.28 EDX analysis for this thesis. (A) Region of interest for EDX analysis indicated by the white dashed square. Elemental mapping of (B) boron, (C) nitrogen, and (D) carbon. (E) Corresponding EDX spectra. *40*
Figure 1.29 EELS characterisation for this work. (A) Region of interest for EELS analysis indicated by the white dashed square. (B) High loss EELS spectrum image. Elemental mapping of (C) boron, (D) nitrogen, (E) carbon, and (F) oxygen. (G) Corresponding EELS spectrum. *42*
Figure 1.30 Raman spectrum of h-BN presented by Stenger et al. [134]. This spectrum shows the low frequency peak at -52.5 cm^{-1} (anti-Stoke), 52.5 cm^{-1} (Stokes), and the high frequency peak at 1366 cm^{-1} (Stokes). *44*
Figure 1.31(A) Raman spectra of BNNTs reported by Lee et al. [140] and (B) Raman spectra of BNNTs synthesised for this study. *45*

Figure 2.1 Schematic illustration of the fundamental concept of the chemical vapour deposition (CVD) method. *52*
Figure 2.2 Schematic illustration of the experimental setup utilising a one end closed quartz tube by Lee et al. [13]. *53*
Figure 2.3 (A) Schematic flow of the CVD setup: (1) Ammonia and (2) argon gas cylinders, (3) Flow regulator, (4) Flashback arrester (in case of flammable gases), (5) Mass flow controller, (6) Manual (safety) flow control switch, (7) Stainless steel flange with O-ring, (8) Alumina tube, (9) Tube furnace heating element and thermocouple, (10) Bubbler filled with water, and (11) Gas outlet. (B) Detailed experimental setup showing the B + MgO powder precursor and substrate inside the furnace for the synthesis of BNNTs. *54*
Figure 2.4 Digital photographs of the SiO_2 wafer (A) before and (B) after synthesis. (C) SEM image and (D) Raman spectra of the white deposit on the substrate. (E) TEM image of the synthesised product and (F) HRTEM image of the edge showing lattice spacing of 0.32 nm. (G) EDX spectrum of a single BNNT in which boron, nitrogen, and copper are detected. EDX elemental mapping of a single as-synthesised nanotube showing (H) STEM image of region of interest (ROI), (I) boron, and (J) nitrogen. EDX acquisition with the help of Pablo Quijano Velasco. *57*

Figure 2.5 (A) ADF-STEM image of BNNT, dashed square indicates the ROI for EELS. (B) EELS spectra acquired from red, blue, and green spots indicated in panel A. (C) High-loss EELS image and elemental mapping of (D) boron, (E) nitrogen, and (F) carbon. EELS acquisition with the help of Dr Ian Griffiths. *59*
Figure 2.6 (A) SEM image of synthesised BNNT showing the spherical tips of the nanotubes. (B) TEM image of a single BNNT with the spherical structure. Inset shows HRTEM image of the tip particle. EDX analysis of the particle on the tip of the nanotube. (C) STEM image emphasizing the region of interest. Elemental mapping under the selected region of interest showing (D) magnesium, (E) oxygen, (F) boron, and (G) nitrogen. *61*
Figure 2.7 EDX spectra of (A) particle on the tip of the nanotube and (B) background showing the corresponding elements being detected. *62*
Figure 2.8 TGA plot of the powder precursor (A) from 50 to 1,200 °C, and (B) temperature hold for 10 mins. (C) Cross-section SEM images of deposited material on the surface of the SiO2 target substrate. Inset is the top view. TGA data acquisition with the help of Sabin Sulzer. *63*
Figure 2.9 (A) Cross-section EDX elemental mapping of the deposited thin film with detected elements of (B) boron, (C) magnesium, (D) oxygen, and (E) silicon. *64*
Figure 2.10 XPS depth profiling of (A) B1s, (B) Mg1s, (C) O1s, and (D) C1s showing the behaviour during ion beam etching of 10 secs. (black spectra), 30 secs. (grey spectra), and 60 secs. (light grey spectra). XPS depth profiling acquisition with the help of Dr Phil Holdway. *65*
Figure 2.11 (A) Experimental design to prove conversion of thin film to spherical structures on the target substrate by thermal dewetting. SEM images of the thin film (B) before and (C) after thermal dewetting. (D) and (E) cross-section images, respectively. *67*
Figure 2.12 Schematic illustration of (A) the embryonic stage of the growth. SEM images at (B) 10 mins and (C) 60 mins reaction. *68*
Figure 2.13 (A) Schematic illustration of the evolution of the catalyst droplet in the synthesis of BNNTs. (B) Diameter distribution of the evolution of the catalyst droplet. (C) TEM image of the synthesised BNNT with respect to the catalyst tip particle. (D) HRTEM image with (E) schematic representation. *70*

Figure 3.1 Schematic illustration of the synthesis of BN nanomaterials using different approaches to introducing the catalyst droplet (A1) is the typical BOCVD method. (A2) Substrate with the solid layer of catalyst. (B) Thermal dewetting of the catalyst with the exposure of BN precursors. (C) Formation of nanotubes through the catalyst medium. (D) Nanosheet generation through the absence of catalyst droplets. *75*
Figure 3.2 Schematic illustration of fabricating the thin film as a source of catalyst droplets. *78*
Figure 3.3 Schematic illustration of the experimental design for the synthesis of BNNTs by using a thin film and B_2O_3 as B precursor. *79*
Figure 3.4 (A) SEM image of synthesised BN nanomaterial using boron + iron oxide as powder precursor indicating nanosheet structures grown perpendicular to the target

substrate. (B) HRTEM image of the nanosheets with lattice spacing measured to be 0.34 nm in the inset from the region of interest indicated by the white dashed square. (B) 3 hr period synthesis. (D) Corresponding Raman spectra of the synthesised nanosheets suggesting h-BN network based on the strong E_{2g} peak at 1370 cm^{-1}. (E) ADF-STEM image for the EELS analysis showing the vacuum and sample region, red and blue spot, respectively. (F) Acquired EELS spectra from the vacuum (red line) and BN nanosheet (blue line)..... 82

Figure 3.5 EDX elemental mapping of the surface of the SiO_2 target substrate after the powder precursor, boron and iron oxide, was heated at synthesis temperature. (A) SEM image of a cross-section of the target substrate showing the region of interest indicated by the white dashed square corresponding to the elemental mapping of (B) iron, (C) oxygen, (D) boron, and (E) silicon. 84

Figure 3.6 SEM images of the product obtained by using (A) nickel oxide, (B) iron oxide, and (C) magnesium oxide as metal oxide in the powder precursor B + metal oxide. (D) Raman spectra of corresponding products of different metal oxides. 85

Figure 3.7 Synthesis of BN nanomaterials using tungsten as a target substrate and boron + iron oxide as a powder precursor. (A) Photograph image after the synthesis showing a white deposit on the surface of the tungsten sheet. (B) SEM image of the white deposit. 86

Figure 3.8 Synthesis of BN nanomaterials using iron-rich stainless steel as a target substrate and boron + iron oxide as powder precursor. (A) SEM image of the synthesised product showing abundant presence of 1D nanostructure. (B) TEM image of a single 1D synthesised product showing a bamboo-like structure. (C) Raman spectra showing a strong peak at 1364 cm^{-1}, suggesting that the synthesised product is composed of the h-BN network. Composition analysis of the synthesised BN nanotube using stainless steel as target substrate showing (D) EEL spectrum and (E) High-loss EELS image of the region of interest for EELS analysis. The spatially resolved elemental maps of (F) boron, (G) nitrogen, and (H) carbon..... 88

Figure 3.9 Composition analysis of the tip of the synthesised BN nanotube. (A) STEM image showing the region of interest indicated by the white square corresponding to the elemental mapping of (B) boron, (C) nitrogen, (D) iron, and (E) oxygen, (F) carbon, and (G) chromium. 90

Figure 3.10 Composition analysis by EDX of the surface of the stainless steel used as a target substrate. (A) Cross-section SEM image showing the region of interest indicated by the white dashed square corresponding to the elemental mapping of (B) iron, (C) chromium, (D) oxygen, and (E) carbon. 91

Figure 3.11 Growth analysis of the BN nanotubes synthesised using a stainless-steel target substrate. (A) TEM image of a single BN nanotube showing the tip and the bamboo structure. (B) HRTEM image of the interface between the catalyst particle and the BN nanotube corresponding to the red dashed square in panel A. (C) HRTEM image of the junction of segments of the bamboo structure of the BN nanotube corresponding to the yellow dashed square in panel A. Panels on the right hand side depict the schematic illustration of the HRTEM images indicating the segments..... 92

Figure 3.12 (A) ADF-STEM image of the BN nanobamboo showing two segments. (B) EEL spectra obtained from different spots on the BN nanobamboo segment. (C) B- and (D) N-K edges showing the behaviour of π and σ* peaks at different spots..... 93*
Figure 3.13 Schematic illustration of the tip-growth model of BN nanotubes. (A) Showing the droplet formation, indicated in yellow, which can come from the partial melting of the solid target substrate, indicated in green, or by achieving eutectic point between boron and iron. (B) Precipitation of BN sheets on the surface of the catalyst droplet. (C) Lift-off of the catalyst droplet from the precipitated BN nanobamboo segment exposing a clean surface for precipitation of (D) the new BN nanobamboo segment. (E) Periodic growth of the BN nanobamboo segments. 95
Figure 3.14 Thin film fabrication and thickness control showing photographs of the surface of the target substrate (A) before and (B) after experimental run. (C) Top-view SEM image of the deposited thin film. SEM images of the cross-section of thin-film thickness as a function of time (D) 1, (E) 3, (F) 5, and (G) 10 mins. (H) Summary plot of thickness as a function of time. 97
Figure 3.15 Catalyst droplet evolutions at different temperatures. (A) Temperature profile of the working furnace. SEM images of (B) thin film of magnesium borate under heat treatment at (C) 880 °C, (D) 1,050 °C, and (E) 1,200 °C..... 99
Figure 3.16 SEM images of synthesised BNNTs at (A) low-, and (B) high-temperature conditions. TEM images of synthesised BNNTs at (D) low-, and (E) high-temperature conditions. (C) Raman spectra of corresponding as-synthesised products. (F) EELS spectra of the BNNTs synthesised at high temperature..... 100
Figure 3.17 Proposed mechanism for the synthesis of BNNTs using a thin film 102
Figure 3.18 (A) SEM image of synthesised hybrid BN nanomaterials with methane flow indicating 1D nanostructure. (B) TEM image of a representative 1D structure showing a nanotube morphology. (C) HRTEM image showing the lattice spacing of the walls measured to be 0.33 nm. (D) Corresponding Raman spectra of the synthesised product showing major peaks at 1,344.6 cm^{-1} and 1,573.38 cm^{-1} suggesting a carbon hexagonal network. (E) EELS spectrum of the synthesised nanotube showing fine K edges of B, C, and N. Inset ADF image acquiring the EELS spectrum..... 103
Figure 3.19 (A) HAADF-STEM image of the synthesised hybrid BN nanotubes. (B) Elemental line profiles measured across the nanotube indicated by the yellow line in panel A. (C) EEL spectra acquired from panel A corresponding to (i) vacuum, (ii) edge of the wall, (iii) mid-section of the wall, and (iv) hollow middle demonstrating the near-edge fine structure of B, C, and N. TEM images indicating carbon and BN wall of the nanotube by (D) discontinuous wall and (F) apparent change of lattice spacing. (E) and (G) Schematic illustrations of panels D and F, respectively. (H) High-loss EELS image of the region of interest for EELS elemental mapping of (I) boron, (J) nitrogen, and (K) carbon..... 104
Figure 3.20 (A) SEM image of synthesised hybrid nanomaterials with methane and boron oxide without ammonia flow showing the presence of filament structures. (B) HRTEM image of a representative 1D nanostructure showing nanotube morphology with measured lattice spacing of 0.33 nm. (C) Corresponding Raman spectra of the

synthesised product showing major peaks at 1,324 cm^{-1} and 1,550 cm^{-1} suggesting a carbon network. (D) Corresponding EELS spectra showing K edges of B and C. Background removal was applied to B and N-K edges indicated by the dashed red line. (E) High-loss EELS image for the EELS analysis for acquiring spatially resolved elemental maps of (F) boron, (G) carbon, and (H) nitrogen..... 108

Figure 3.21 (A) Low-loss EEL spectra of BN nanotube (black), carbon-coated BN nanotube (red), and boron-doped carbon nanotube (blue). Dashed spectra are the zero-point energy loss of corresponding materials. (B) Zoomed-in range for the optical gap measurements of different synthesised materials. 111

Figure 3.22 Photograph images of BN nanotubes dispersed in (i) acetone, (ii) ethanol, (iii) water, (iv) isopropanol, and (v) hexane at (A) 0 mins, (B) 40 mins, (C) 80 mins, and (D) 120 mins. (E) Thermal conductivity measurement of BN nanotubes (red) and BN nanosheets (blue) in isopropanol at different weight percentages. 113

Figure 4.1 Comparison of the computational features between (A) traditional DFT using the ADF programme and (B) DFT using QUILD as a wrapper around the ADF programme, showing that similar results are obtained in geometry optimisation of ammonia but for less computational time. (C) Shows the level of basis set with corresponding energy error and CPU time ratio relative to SZ. Trigonal planar geometry is obtained for geometry optimisation of ammonia using DZ while DZP results in a trigonal pyramidal shape..... 119

Figure 4.2 Schematic illustration of a typical double-well energy surface where R is the reactant, R(complex) is the reactant-complex, $TS^{\ddagger}$ is the transition state, P(complex) is the product-complex, and P is the product. 121

Figure 4.3 Computed total bond energy of different conformation of B_2O_2; (A) trans, (B) cis, and (C) linear showing that linear conformation of B_2O_2 is the most stable due to its lowest total bond energy value. Colour coding: red is oxygen atom while yellow is boron atom..... 122

Figure 4.4 Determining the (A) reactant complex and (B) product of different configurations for the binding of the hydrogen molecule to B_2O_2. Colour coding: white is hydrogen atom, red is oxygen, and yellow is boron..... 123

Figure 4.5 Linear transit calculation showing the plot of (A) energy as a function of distance change of the hydrogen molecule binding to B_2O_2. Line plots corresponding to the energy of changing atomic coordinates (red), hydrogen-hydrogen bond (blue), hydrogen-boron bond, and hydrogen-oxygen bond (yellow). Optimised geometry of (B) reactant and (C) product (green). Representative geometries having higher energy compared to the reactant and product at (D) -760 kcal/mol and (E) -710 kcal/mol. These geometries are good guesses for the transition state for the bonding of hydrogen in B_2O_2..... 125

Figure 4.6 Transition state calculation of the (A) 1^{st} and (B) 2^{nd} transition state geometry guess. Calculation indicates that the 1^{st} geometry does not achieve geometry convergence compared to the 2^{nd} geometry. Furthermore, the 2^{nd} geometry showed only 1 negative Hessian value after convergence with a lesser geometry change from the initial geometry input..... 126

Figure 4.7 Frequency calculation obtained from the converged TS calculation showing the (A) IR spectra and (B) vibration at -1,584 cm^{-1} portrayed by arrows indicating a true TS structure due to one and only one imaginary frequency. 128
Figure 4.8 Potential energy diagram of hydrogen breaking the B-B bond of the B_2O_2 boron precursor molecule. 129
Figure 4.9 Potential energy diagram of ammonia breaking the B-B bond of the B_2O_2 boron precursor molecule..... 130
Figure 4.10 Potential energy diagram of the reaction OBH + NH_3. 133
Figure 4.11 Saturation of B-N bonding of B_2O_2 boron precursor molecule by ammonia showing the potential energy diagram of the (A) 2^{nd}, (B) 3^{rd}, and (C) 4^{th} ammonia introduction. It can be seen that further ammonia reaction with boron oxide increased the energy barrier, which may be due to the water abstraction and weak interaction of incoming ammonia with the hydroxyl group. 133
Figure 4.12 Comparison of energy barrier of (A) hydrogen and (B) ammonia on breaking the B-B bond of the saturated B-N bond of B_2O_2 boron precursor molecule, suggesting that the ammonia molecule is more likely to break the B-B bond than the H_2 molecule..... 135
Figure 4.13 TEM data to model the calculation for the growth of the BNNT. (A) TEM image of the tip of the BN nanotube supported by carbon lacey showing the catalyst and the BN wall of the BNNT. The white dashed square labelled B and C corresponds to the HRTEM image of (B) the interface between the BN wall and the catalyst showing their lattice spacing and (C) the end part of the catalyst with layers of BN, respectively. Right panels depict graphical representations of the HRTEM images. 137
Figure 4.14 Model representation for the nucleation and growth of a BNNT. (A) BN species form building blocks for the formation of BN sheets on the surface of the catalyst. (B) The precipitated BN sheets continue to grow, forming the nanotubular structure. (C) Continued growth of the generated BNNT. (D) Exposure of the surface of the catalyst promotes BN sheet precipitation. (E) Initial structure of the inner nanotube. (F) The inner nanotube continues to grow and proceeds to step D for further growth. 138
Figure 4.15 Geometry optimisation with corresponding energies of different facets (A) (100), (B) (110), (C) (111) and step-edges (D) (100)-(110), (E) (100)-(111), (F) (100)-(110)-(111) of the MgO catalyst. The darker coloured atoms indicate the lower layers. 139
Figure 4.16 Adsorption energy of (A) boron and (B) nitrogen in the catalyst of different facets..... 140
Figure 4.17 Different formation pathways to generate B-N bonding where (A) boron moves towards nitrogen while (B) nitrogen moves towards boron to form BN with corresponding energy profiles. 142
Figure 4.18 (A) Mechanism and (B) potential energy diagram of boron atom toward the formation of the B-N bond on the adsorbed NB molecule on the MgO (100)-(111) step-edge. Atomic configuration of (C) NB molecule, (D) BNB molecule, and (E) BN

sheet at the MgO (100)-(111) step-edge. The darker-coloured atoms indicate the lower layers..... 143
Figure 4.19 Linear transit calculation of energy as a function of distance in a two-atomic (A) boron-boron, (B) nitrogen-nitrogen, and (C) boron-nitrogen system..... 144
Figure 4.20 Adsorption of boron oxide on different surfaces of magnesium oxide facets (A) (100), (B) (110), (C) (111), step-edges (D) (100)-(110), (E) (100)-(111), and (F) (100)-(110)-(111). Top panels show the cross-section view while bottom panels show top views. Colour coding: red is oxygen, yellow is boron, and grey is magnesium. The darker-coloured atoms indicate the lower layers. 146
Figure 4.21 Adsorption of ammonia on different surfaces of magnesium oxide facets A) (100), (B) (110), (C) (111), step-edges (D) (100)-(110), (E) (100)-(111), and (F) (100)-(110)-(111). Top panels show the cross-section while bottom panels show top views. Colour coding: white is hydrogen, red is oxygen, and grey is magnesium. The darker-coloured atoms indicate the lower layers. 147
Figure 4.22 Bond energy analysis of B-N bond formation on (A) facet (100) and (B) step-edge (100)-(111). 148
Figure 4.23 Saturation of B-N bonding of B_2O_2 boron precursor molecule by periodic addition of ammonia to the site-edge (100)-(111) surface. 150
Figure 4.24 Addition of B_2O_2 boron precursor molecule to the saturated B-N complex. The final structure shows the first formation of the hexagonal B-N network. 152
Figure 4.25 (A) HRTEM of the interface between the BNNT and the catalyst. (B) Reverse FFT from panel A indicated by the red square showing the hexagonal network and chirality with respect to the long axis of the BNNT. (C) Measured distance of two BN bonds from panel B. (D) Calculated optimised geometry of a hexagonal BN structure. The blue arrows indicate the growth direction of the BNNT..... 153
Figure 4.26 Potential energy diagram comparing the energy barriers of the formation of B-N bonds from the boron and nitrogen precursor molecules in the (A) absence and (B) presence of magnesium oxide. 155
Figure 4.27 Adsorption energy as a function of number of BN sheets on the surface of MgO (111) facet. (A) Pristine MgO (111) surface, (B) single BN sheet, (C) two BN sheets, (D) single BN sheet on (111) surface, (E) two BN sheets on (111) surface, and (F) four BN sheets on (111) surface. Top panels correspond to a cross-section view while bottom panels show top views. 156
Figure 4.28 SEM images of growth of BNNTs at constant time, 10 mins, at different temperatures (A) 1,200 °C, (B) 1,150 °C, and (C) 1,100 °C. (D) Determination of activation energy (E_a) from the Arrhenius plot of the growth rate of BNNTs..... 157

Figure 5.1 Experimental setup for aerosol-assisted CVD synthesis of BNNTs. 166
Figure 5.2 Results utilising methyl borate in aerosol-assisted CVD synthesis. SEM images at (A) low and (B) high magnification. EDX analysis of the (C) region of interest showing detected elemental mapping of (D) boron, (E) nitrogen, (F) carbon, (G) oxygen, and (H) silicon. (I) Corresponding EDX spectrum and (J) Raman spectra of the synthesised material. 167

Figure 5.3 Photograph images of (A) boric acid and melamine solution in water and (B) water bath process. A change of transparency of the solution is clearly seen. (C) The white felt-like product obtained after the freeze-drying step. (D) Photograph image after pyrolysis. TEM images at (E) low and (F) high magnification with (G) corresponding Raman spectra of the BN fibre produced by Ruth Jones. 168
Figure 5.4 Photograph images of composite fabrication with (A) blank epoxy, and (B) epoxy with 20 wt. % of commercially-made h-BN produced by Pierre Romain. 169
Figure 5.5 Molecular structures for the calculation of band gap for (A) BNNT, (B) CNT, and (C) BNNT coated with CNT. 170

Figure A.1 Diameter distribution of the as-synthesised BNNTs. 185
Figure A.2 EELS spectra from Figure 2 focussed on the K edge of (A) boron and (B) nitrogen clearly showing the weight change ratio of the π and σ*. 185*
Figure A.3 Raw XPS ion beam etching data (A) Pristine thin film, (B) 10, (C) 30, and (D) 60 seconds of etching time. 186
Figure A.4 Phase diagram of B_2O_3-MgO system[253] 186
Figure A.5 Phase diagram of tungsten – boron[186] 187
Figure A.6 Phase diagram of iron – boron[254]. 188
Figure A.7 Phase diagram of (A) FeO –B_2O_3 [255] and (B) Fe_2O_3 – B_2O_3 [256] system. 188

Chapter 1

Introduction

1.1 Boron nitride (BN) nanomaterials

Boron nitride (BN) nanomaterials are chemical compounds constructed from an equal number of boron and nitrogen atoms that are similar in structure and properties to recently discovered carbon nanomaterials such as fullerenes [1], graphenes [2, 3], and carbon nanotubes [4]. Like their carbon counterparts, BN nanomaterials possess excellent mechanical properties (Young's modulus ~0.9 TPa and fracture strength ~35 GPa, section 1.3.3.1) and high thermal conductivity (section 1.3.3.2). In addition, BN nanomaterials have resistance against oxidation reaching up to ca. 900 °C in air, which gives them a promising application as a protective layer in high-temperature conditions (section 1.3.3.4). Moreover, BN nanomaterials are considered to be insulators with a band gap in the range of ca. 3-6 eV. BN nanosheets are known as the thinnest electrically insulating material, which makes them a good complementary material as dielectric substrates for improving the electron mobility of graphene in device fabrication.

Although the unique properties of BN nanomaterials have attracted considerable research interest due to their potential applications (Figure 1.1), researchers have been facing the challenge of upscaling production, given that for any application to work, one must have a significant amount of the material. For instance, the high thermal conductivity and high electrical resistivity of BN nanomaterials make them ideal fillers for thermal

interface materials, if a sufficient quantity can be produced. Thus, BN nanomaterial synthesis must be investigated for us to have the fundamental understanding that will enable us to design reactors that can improve the yield, and give us greater control of the morphology and composition of this material so that it can be tailored to a wide variety of thermal management and other applications.

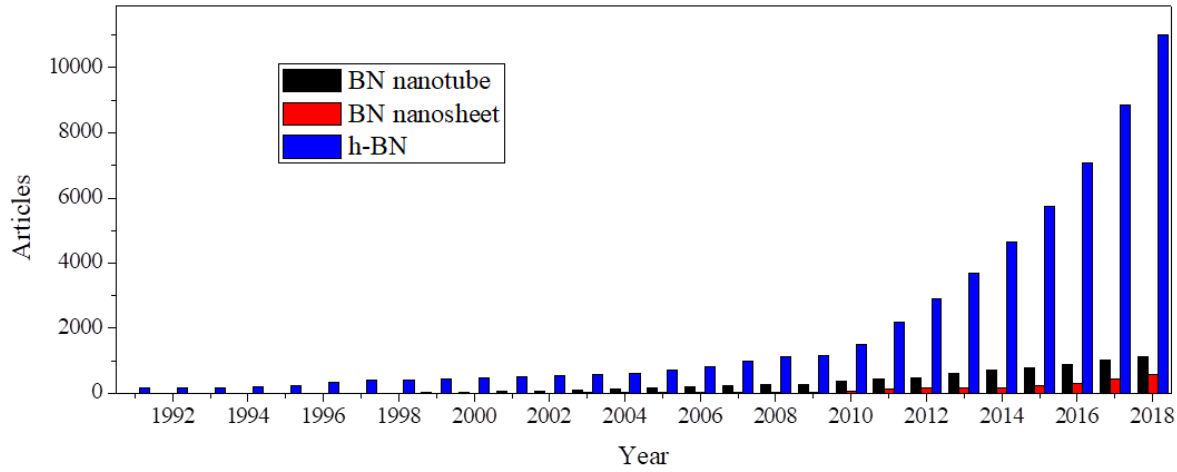


Figure 1.1 *Number of published articles on BN nanotubes (black column), BN nanosheets (red column), and hexagonal BN (blue column) from 1992 to 2018 acquired from Google Scholar.*

In this work, the CVD synthesis of BN nanomaterials was investigated to elucidate the nucleation and growth of these nanomaterials. Different techniques such as electron microscopy, energy-dispersive x-ray spectroscopy (EDX), Raman spectroscopy, thermal gravimetric analysis (TGA), and electron energy-loss spectroscopy (EELS) were utilised to characterise the synthesised nanomaterials. Both experimental and theoretical methods were used to answer questions on the processes of nucleation and growth of boron nitride nanotubes (BNNTs); the precursors required for this growth; the ways in which the structure of BN nanomaterials affect their properties; why a certain chirality is synthesised; and how BN nanomaterials can be used in thermal management and wider applications.

1.2 Thesis overview

1.2.1 Background and aims of this thesis

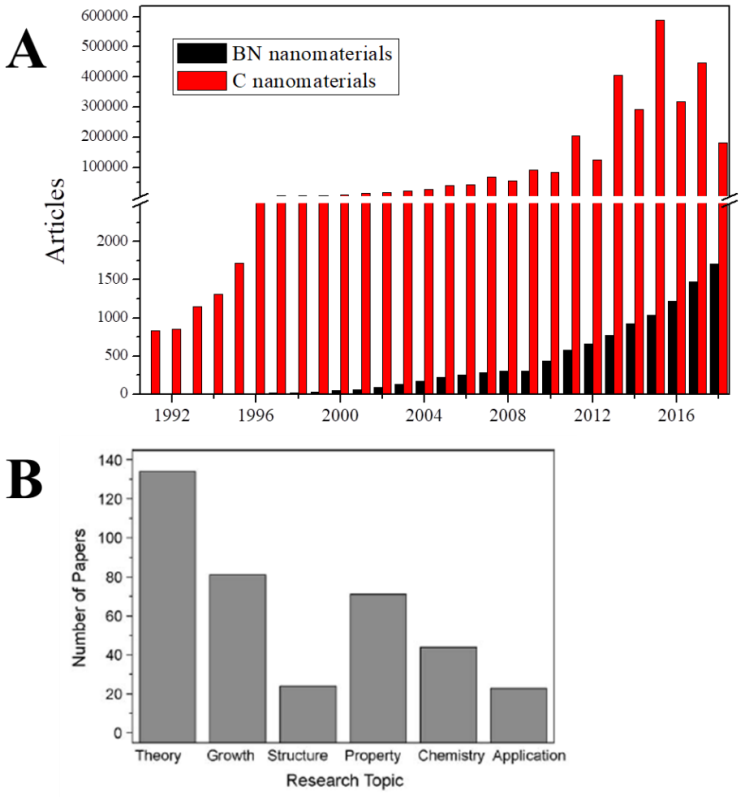


Figure 1.2 (A) *Published articles collected in Google Scholar from 1991 to 2018 comparing boron nitride nanomaterials (BNNTs and BN nanosheets) and carbon nanomaterials (CNTs and graphene), black and red, respectively. Note that the x-axis changes magnitude at 2500 articles. (B) Statistics on published papers on BNNTs acquired from the report of Zhi [5].*

As presented in Figure 1.2A, although there has been an increase in research interest over the years, published research articles on BN nanomaterials are still outnumbered by research articles on carbon nanomaterials by a factor of 1/100. This difference can be attributed to the lack of fundamental understanding of the growth mechanism shown in Figure 1.2B. Lourie *et al.* [6] reported a root-growth mechanism in which nanotubes nucleated on a nickel boride particle with often irregular initiation caps and grew subsequently by incorporation of additional BN, and proposed the model shown

in Figure 1.3A. On the other hand, a tip-growth model was suggested by other groups [7, 8]. An example of a tip-growth model is the reaction between melamine and boric acid in the synthesis of BNNTs [9] that showed bulbous tips that were found to be BN cages with amorphous B-N-O clusters and served as the initiating particle for nanotube growth, as shown in Figure 1.3B. This growth mechanism was also adapted by Su *et al.* [10] according to the observed EELS elemental mapping showing that the metal catalyst acted as a 'container' in helping the breakdown and reaction of boron with atmospheric nitrogen to form BN layers on the catalyst surface (Figure 1.3C).

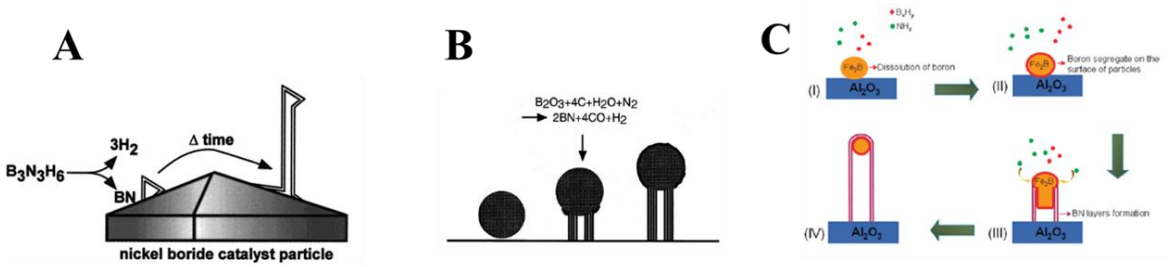


Figure 1.3 *Proposed growth mechanisms by (A) Lourie* et al.*[6] following root-growth. Left: nanotube-cap nucleation. Right: at a later stage of growth; note the flag-like initial cap, the conventional nanotube middle section, and the root at the nanotube-catalyst junction consisting of incomplete BN layers. (B) Ma* et al.*[9], similar to the nanotube 'tip growth' in the metal catalyst CVD method. (C) Growth model of BNNTs presented by Su* et al.*[10].*

The growth model followed the steps of (i) formation of the boron-containing catalyst attributed to the solid solution of boron in iron; (ii) segregation of boron on the surface of the catalyst; (iii) reaction of boron on the catalyst surface with nitrogen source species producing a BN layer; (iv) incorporation of nitrogen atoms on the surface of the boron-containing catalyst that leads to the growth of the tube structure. Nevertheless, BNNTs synthesised in different experimental setups are assumed to follow the vapour liquid solid (VLS) mechanism that leads to growth by tip-growth, base-growth or mix-growth model [8, 11-15]. According to Wagner and Ellis [15], the VLS mechanism

involves the heating of a precursor to a suitable temperature at which a nanosize catalyst begins to form either in a liquid or partially melted form condensed on the substrate surface. This mechanism usually arises when their partial vapour pressure reaches a certain value that enables this nanosize catalyst to be stable. It is then assumed that the formed BN species diffuse into the condense catalyst, which then becomes supersaturated and leads to the precipitation of BNNTs [16].

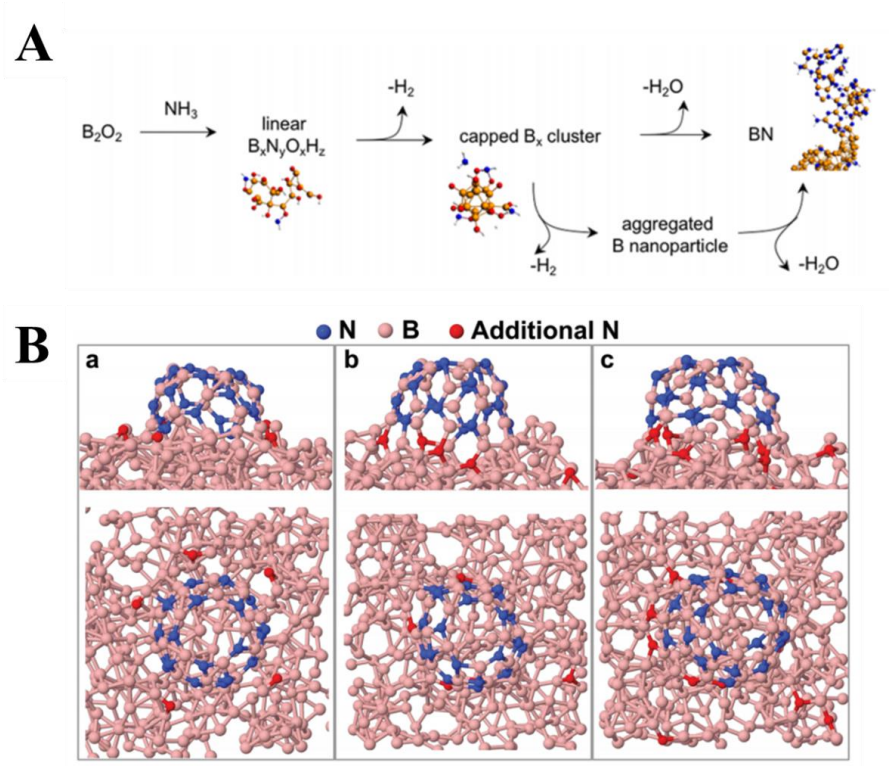


Figure 1.4 *Theoretical calculations by molecular dynamics showing the (A) nucleation of BNNT from B_2O_2 + NH_3 by McLean et al. [17] and (B) growth of BNNT from the surface of a boron droplet initiated by a cap structure by Santra et al. [18].*

As for theoretical studies, McLean *et al.* [17] reported non-equilibrium molecular dynamics simulations showing how BN nanomaterials nucleate under the conditions of the boron oxide chemical vapour deposition (BOCVD) system. They showed that the boron and nitrogen precursors form boron nanoparticles that aid the formation of BN rings with the generation of H_2O and H_2, as presented in Figure 1.4A. In addition, Santra *et al.* [18] reported a mechanism of the growth of BNNTs from the surface of a liquid boron droplet

by *ab initio* molecular dynamics simulations and showed that nitrogen atoms prefer to reside on the droplet surface that starts to form boron nitride islands below 2400 K. These BN islands become the cap structures of the BNNTs through further growth (Figure 1.4B). However, these theoretical investigations deal with molecular dynamics, meaning there is a lack of insight on BN chemistry in the formation of BNNTs, such as the electronic structures of complex molecules being generated, the energy barriers of the BN bonding, and how the hexagonal structure of the BN network forms. The reason for the lack of BN chemistry is because molecular dynamics rely on classical mechanics. To address this problem, quantum mechanics must be applied such as first-principle calculations that are usually carried out using density functional theory (DFT).

As noted by reports dealing with the synthesis of BNNTs [11, 19], the growth mechanism is still not fully understood, and there is little experimental evidence showing the stages involved and correlating them to theoretical calculations in the growth mechanism. This thesis will provide experimental evidence of the growth mechanism by investigating the evolution of the growth of the nanotube with respect to time using post-electron microscopy. The evolution of the catalyst droplet that was found to be responsible for the nanotubular structure was studied by transmission electron microscopy (TEM), EDX, and TGA. Control of different morphologies such as two-dimensional (2D) BN nanosheets and one-dimensional (1D) BN nanobamboos was investigated by hindering the formation of the catalyst droplet and using an iron-based catalyst droplet, respectively. High-resolution TEM (HRTEM) studies of the interface between the catalyst droplet and the BNNTs provided the model for conducting DFT studies leading to the correlation of the experimental and theoretical calculations, particularly the preferred adsorption of boron species on the catalyst facets that resulted in the zigzag chirality of the BNNTs.

1.2.2 Structure of this thesis

Following a brief survey of existing literature on BN nanomaterials in this chapter, Chapter 2 will address the research gap concerning the nucleation and growth of BN nanomaterials through the experimental discovery of the embryonic stages of the synthesis of BNNTs achieved by utilising a simplified and direct method of BOCVD. It will show that magnesium-rich catalyst droplets are responsible for the formation of the nanotubular structure that is generated through heating the mixture of amorphous boron and magnesium oxide. I conducted all the synthesis experiments in this thesis together with characterization of SEM, TEM, Raman spectroscopy, and TGA. EELS data were acquired using JEOL ARM-200F that was operated by Dr. Ian Griffin. XPS depth profiling results were obtained using Thermo Scientific K Alpha spectrometer operated by Dr Phil Holdway.

With the mechanism established, in Chapter 3 tailored morphology is demonstrated through the control of the catalyst droplets by changing the metal oxide in the powder precursor, using different target substrates, and fabricating a thin film as a source of the catalyst droplet for nanotubular growth. This makes it possible to tune the properties of BN nanomaterials so that they can be optimised for specific uses, most promisingly as fillers for thermal management applications. The results to be presented in Chapter 3 will show an improvement of the thermal conductivity of isopropanol solution containing 10 wt. % of BN nanomaterials.

The correlation between the experimental and theoretical calculation by DFT of the synthesis of BN nanomaterials is presented in Chapter 4, showing the electronic structures of the intermediate species, energy barriers of BN bond formation, and the formation of the hexagonal BN network. I conducted the calculations myself where I was taught by

Prof. Marcel Swart. Guidance and discussions on carrying out the plans of my calculations were provided also by Prof. Marcel Swart.

Chapter 5 concludes the thesis by summarising the results and presenting the exciting potential for future experiments that has led to the development of new projects in the Nanomaterials by Design research group based in the University of Oxford.

1.3 Literature review

This section is a review of existing theoretical and experimental research on BN nanomaterials, particularly the derivatives of the hexagonal BN structure: BN nanosheets and nanotubes, which will be compared to the corresponding carbon system: graphite, graphene, and carbon nanotubes.

1.3.1 Structures of BN nanomaterials

The best-known structure of boron nitride is hexagonal boron nitride (h-BN), followed by cubic boron nitride (c-BN). These allotropes follow the same molecular structure as the typical carbon allotropes graphite (hexagonal carbon) and diamond (cubic carbon). As a result, these C and BN materials share almost the same properties.

1.3.1.1 hexagonal boron nitride (h-BN)

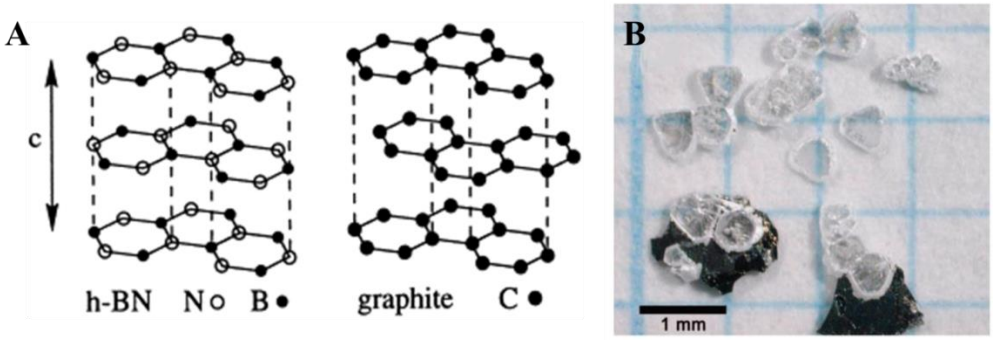


Figure 1.5 *(A) Structures of h-BN and graphite as presented by Souche* et al. *[20]. (B) Optical image of hexagonal boron nitride (h-BN) single crystal from Watanabe* et al. *[21].*

Hexagonal boron nitride (h-BN) has the same crystal structure as graphite (Figure 1.5A) where alternating boron and nitrogen atoms are arranged in a honeycomb lattice with an interlayer spacing of 3.33 Å. BN bonds are 1.44 Å with bond angles of 120° [20, 22]. In-plane boron and nitrogen atoms are strongly bonded by sp^2 hybridised covalent bond while the interlayers are bonded by van der Waals forces. h-BN and graphite have been shown to differ in layer stacking: while h-BN has AA stacking (boron and nitrogen atoms form two neighbouring layers on top of each other), graphite has AB stacking (also known as Bernal stacking, where the carbons of one layer are located at the centre of the hexagon of the neighbouring layer). The h-BN appears transparent (Figure 1.5B), which is unlike its carbon counterpart graphite. In addition to this difference in optical property, h-BN differs to graphite in electrical properties. This is due to a difference in electronic structure that is attributed to three reasons:

(1) The P_z orbital of the boron atoms is vacant while the neighbouring P_z orbital of nitrogen atoms is occupied. Thus, free electrons do not overlap or undergo conduction, resulting in the insulating property of BN;

(2) due to the difference in electronegativity in the BN system, π-electrons are localized on the nitrogen atoms, giving h-BN a partially negative charge that results in the partially ionic nature of h-BN; and

(3) the stabilisation of the AA stacking of h-BN from the inter-layer electrostatic interaction, where boron atoms having a partial positive charge in one layer resides on the negatively charged nitrogen atoms on the other layer.

1.3.1.2 BN nanosheets (BNNSs)

Boron nitride nanosheets (BNNSs) are 2D nanomaterials that typically consist of single, double, or multiple layers of h-BN. Two general approaches to acquiring BNNSs are:

(1) Top-down method from h-BN crystals by mechanical cleavage [23] and chemical exfoliation [24]

(2) Bottom-up method from boron and nitrogen precursor by chemical vapour deposition technique [25].

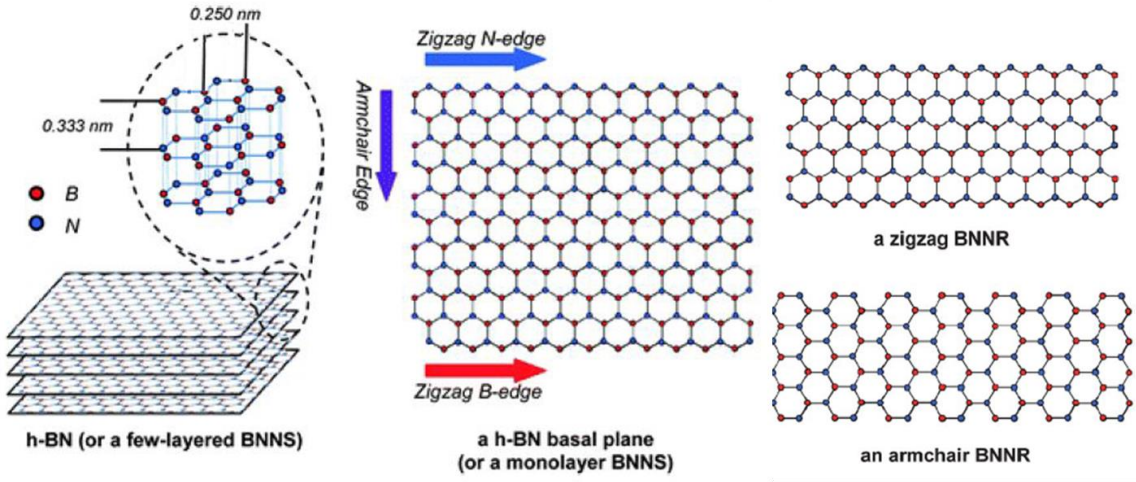


Figure 1.6 *Basic structure of 2D BN nanostructures where BNNR stands for BN nanoribbon [26].*

As illustrated in Figure 1.6, the edge of BNNSs can have either a zigzag or armchair orientation. The crystallographic parameters of h-BN and graphite are almost identical to each other as summarized in Table 1.1.

Table 1.1 Crystallographic information of h-BN and graphite [27, 28].

Materials	Crystal structure	Bond length (Å)	Lattice parameters (Å)	Interlayer spacing (Å)
h-BN	hexagonal	1.44	*a*:2.5 *c*:6.66	3.33
Graphite	hexagonal	1.42	*a*:2.46 *c*:6.7	3.35

BNNSs have been making their way into the field of nanodevices in the form of a heterogeneous layered structure composed of graphene, a conducting material, and BN nanosheets, a non-conducting material. In addition, based on the report of Pakdel *et al.* [29], perpendicularly grown BNNSs on the target substrate have been found to have a superhydrophobic property that gives them a great potential application as a protective layer.

1.3.1.3 BN nanotubes (BNNTs)

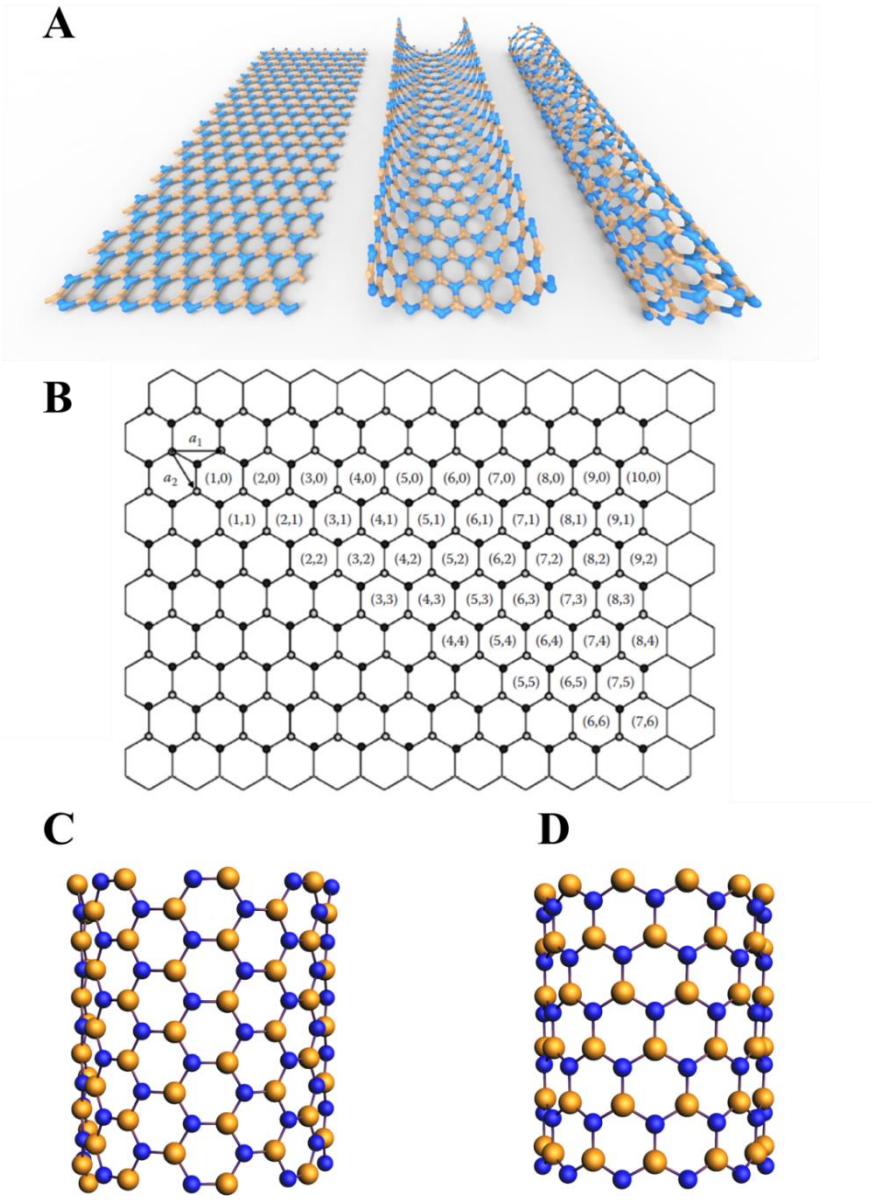


Figure 1.7 *(A) Schematic representation of rolling h-BN to form BNNT. (B)Vectors (n,m) for a single-walled BNNT on a h-BN sheet [30]. (C) Armchair and (D) Zigzag chirality of BNNTs.*

BNNTs can be derived by rolling and folding BN nanosheets into cylindrical forms as shown in Figure 1.7A. BNNTs can be classified by vectors (n,m) according to the rolling/chiral angles as presented in Figure 1.7B. Nanotubes rolled in the (n,n) configuration are known as armchair nanotubes while (n,0) configuration represents the zigzag nanotube structure, as illustrated in Figure 1.7C and D, respectively.

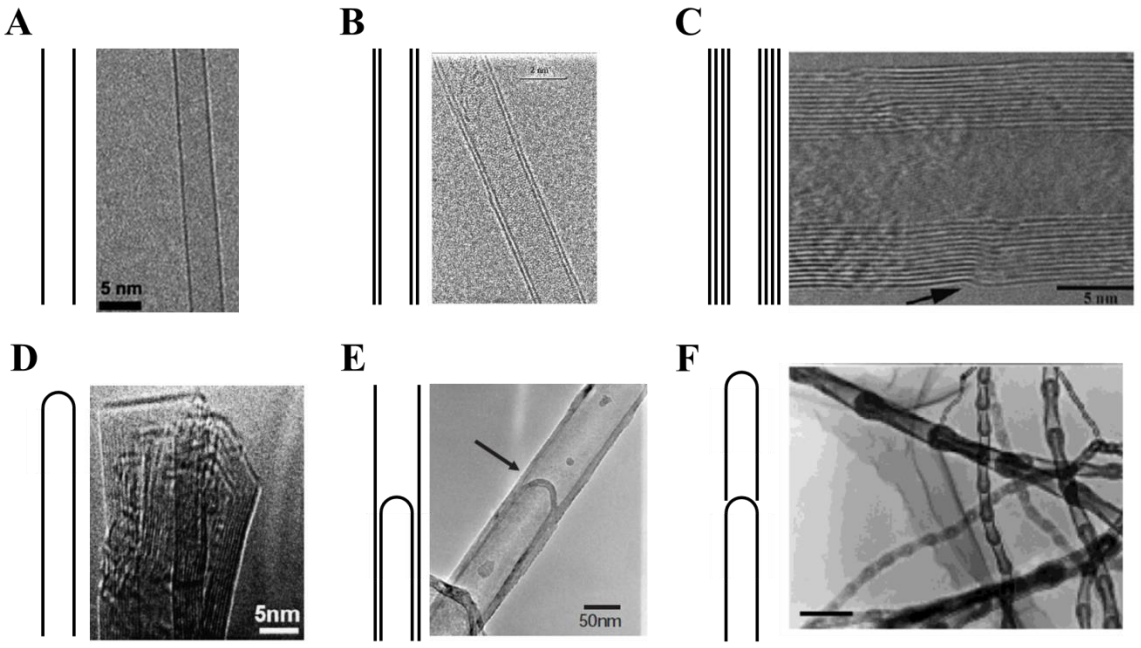


Figure 1.8 *Different morphologies of BNNTs (A) single-walled [31], (B) double-walled [32], (C) multi-walled [11], (D) capped end [33], (E) capped inner nanotube [34], and (F) cap stacked structure or 'nanobamboo' [35].*

Depending on the number of layers of h-BN sheets involved, BNNTs can be single-walled (Figure 1.8A), in which a single layer of h-BN sheet is rolled into a tube, or double-walled (Figure 1.8B), or multi-walled (Figure 1.8C), in which several stacked h-BN sheets are rolled into a single tube. BNNTs can possess capped ends as shown in Figure 1.8D. According to Terrones *et al.* [36], these caps are formed by non-hexagonal BN networks such as squares, pentagons, and octagons that introduce the curvature of the BN wall, leading to a capped or closed-end structure. This cap structure can be found inside the BNNTs or can be stacked up to form what are known as 'nanobamboo' structures, as shown in Figure 1.8E and F, respectively. Identifying these cap structures with respect to the catalyst particles will contribute to the determination of the growth mechanism of BNNTs.

BNNTs have been speculated to enhance fuel efficiency in the field of transportation due to their good mechanical properties (i.e. Young's modulus ~0.9 TPa and

fracture strength ~35 GPa) and low density ~2.1 g/cm^3. In fact, researchers working on space applications, particularly the United States' National Aeronautics and Space Agency (NASA), have been investigating the use of BNNTs as building blocks for spacecraft. Aside from the mechanical properties and density of BNNTs, their extraordinary thermal stability that reaches 900 °C and exceeds that of its carbon counterpart make them the ideal material to be used in space. This is especially true given that the boron content of BNNTs enables them to capture harmful neutrons due to boron's large neutron capture cross-section, giving them the ability to protect astronauts and valuable materials from radiation, as reported by Harrison *et al.* [37] and Thibeault *et al.* [38].

1.3.2 Discovery and key developments of boron nitride nanotubes

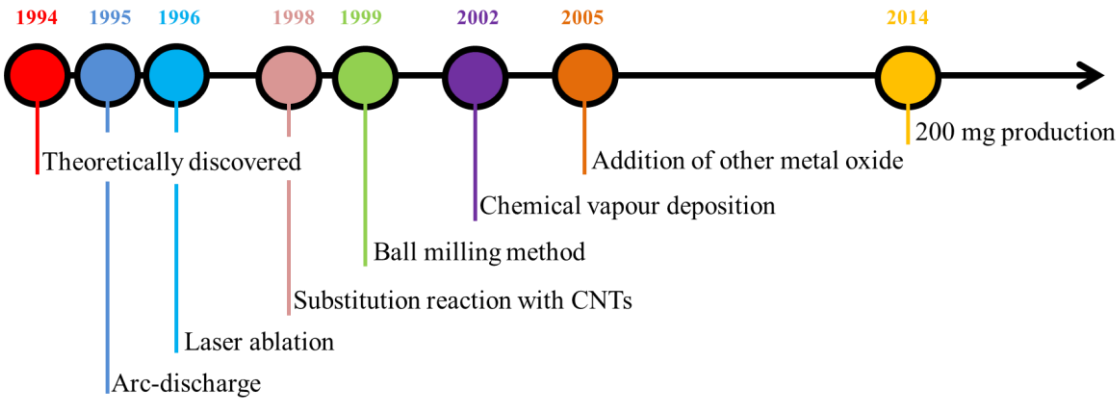


Figure 1.9 *Timeline of BNNTs from discovery and key developments.*

By 1994, researchers on CNTs had already begun investigating potential applications of CNTs, such as electrical resistance measurement [39] and filling with uranium oxide [40]. Using computer simulation, Blase *et al.* [41] utilised the structure of carbon nanotubes and replaced it with the neighbouring atoms of carbon: boron and nitrogen. When their calculations showed BNNTs to be stable, they conducted further investigations of the material's electronic properties. Their report presents the dependence of the electronic properties of BNNTs as a function of tube diameter and chirality, and

infers that tubes having radii greater than 6 Å were found to have wide band gap semiconductors and be less dependent on the chirality. This work laid the foundation for exploring different types of nanotubes aside from CNTs. In the same year, Blase *et al.* were able to conclude that in contrast to CNTs, neither the number of walls, nor the radius or chirality of BNNTs affect the band gap [42].

1.3.2.1 Arc-discharge method

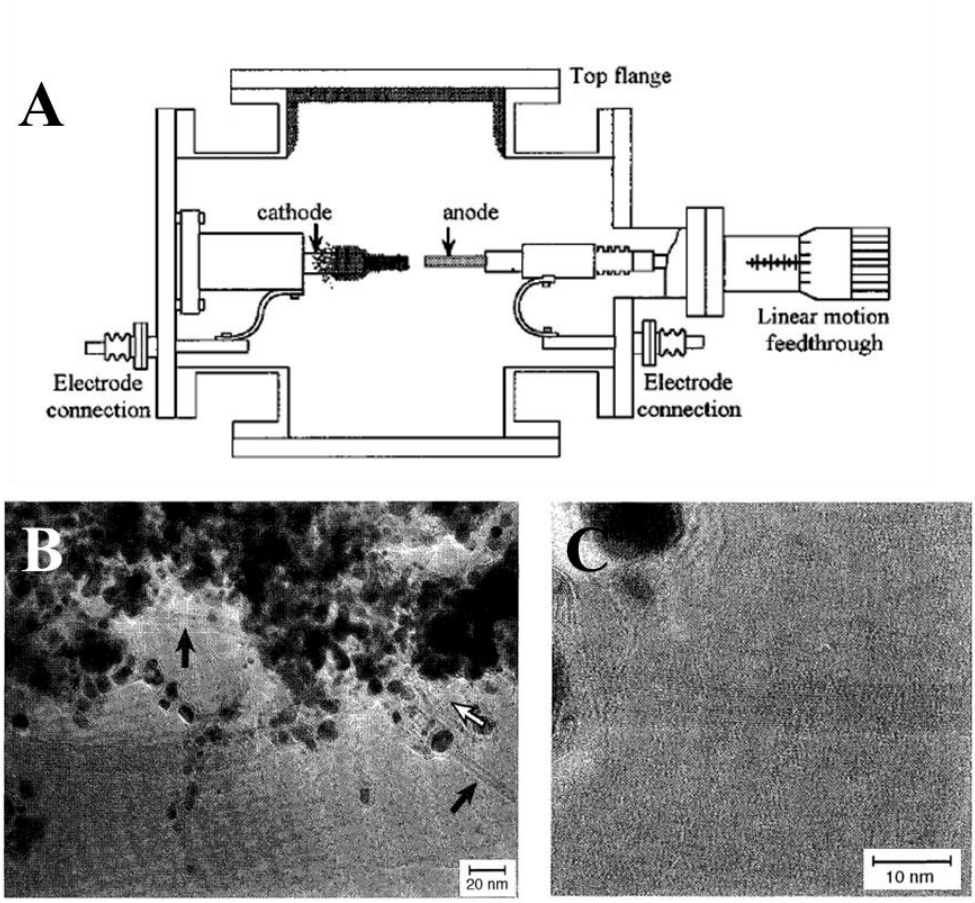


Figure 1.10 *(A) Schematic representation of arc-discharge nanotube growth equipment with a horizontal orientation [43]. (B) TEM image of a BN soot sample collected after arc discharge where dark arrows identify one long BN multi-walled nanotube while a light arrow indicates another tube and (C) High resolution TEM image focussing on a single BN nanotube from Chopra* et al*. [44].*

A year later, the group of Blase in collaboration with Zettl's lab synthesised BNNTs by using an arc-discharge method [44]. The arc-discharge technique generally

involves the use of two high-purity graphite electrodes as the anode and the cathode to introduce an arc (the schematic experimental setup is shown in Figure 1.10). A pressed rod composed of h-BN was placed inside a drilled hole in the tungsten anode that served as a precursor. The group was able to confirm the nanotubular structure using TEM (Figure 1.10B and C) and investigate the composition by EELS. The reaction temperature reached ca. 3,700 K, indicated by the melted portion of tungsten. Nanotubes were identified to be multi-walled, having inner diameters of 1 to 3 nm and outer diameters of 6 to 8 nm (see Figure 1.10C). A good match of interlayer distance was observed between the synthesised nanotube and inter-planar distance of bulk h-BN. This approach was found to be repeatable using different precursors such as HfB_2 as electrodes [45-47] and conductive boron compounds (ZrB_2 and YB_6) for the arcing to happen [48-50]. N_2 was introduced in the reactor chamber and served as nitrogen source. Although the high-temperature reaction of 3,000 K in the arc-discharge method induced the formation of good crystallinity of BNNTs, this high-temperature synthesis also led to the production of non-nanotube structures such as nanocones and nanobundles, and to a significant presence of metallic nanoparticles as seen in Figure 1.10B, thus affecting the overall uniformity of the synthesis. Moreover, the synthesis yield was too low, hindering the study of the material's properties, and more importantly, of its synthesis mechanism.

1.3.2.2 Laser ablation/vaporisation method

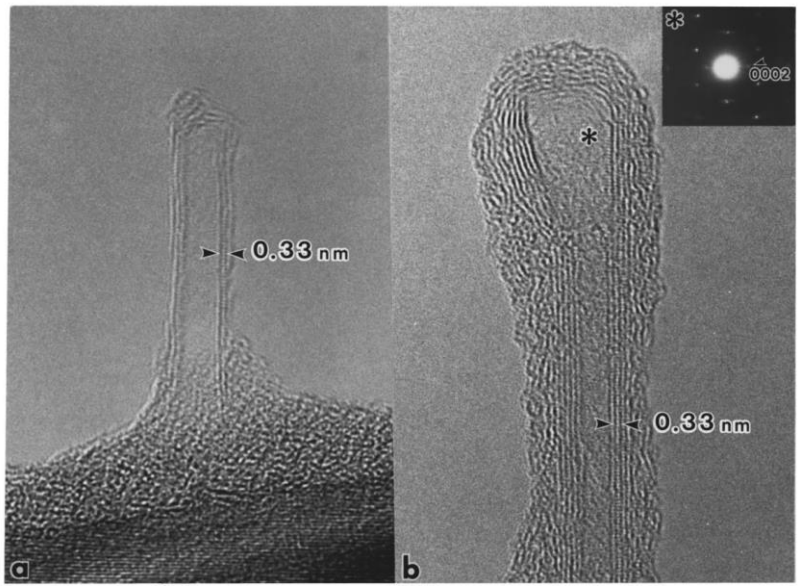


Figure 1.11 *Synthesised BNNTs by Golberg* et al.*[51] utilising the laser ablation method. HRTEM images of representative nanotubes at nitrogen pressures of (a) 8.4 and (b) 5.4 GPa.*

The laser ablation method for growing BNNTs was introduced by Golberg *et al.* [51] in 1996. The group obtained multi-walled boron nitride nanotubes (MW-BNNTs) by heating c-BN micro-crystals via a CO_2 laser with temperatures reaching up to 5,000 K. The BNNTs were found to be short (ca. 30 nm in length), and protruding from an amorphous melted BN residue as seen in Figure 1.11. The technique was further developed by Laude *et al.* [52] and Chen *et al.* [53], who produced BNNTs that are longer (micron scale) and have fewer layers (1-3 walls). What is promising about this method is that it has demonstrated the production of single-walled carbon nanotubes (SW-CNTs) in high yields at a rate of ca. 0.6 g/hr, which researchers hope to replicate in the production of single-walled BNNTs (SW-BNNTs) [54, 55]. However, the drawback to the laser ablation method is the high amount of side products such as BN cones, onions, and amorphous boron flakes that are easily found on the sample, as seen from the report of Arenal *et al.* presented in Figure 1.12. The synthesised BNNTs were shown to have amorphous boron inside (Figure 1.12A), as well as onion-like BN structures (Figure 1.12D).

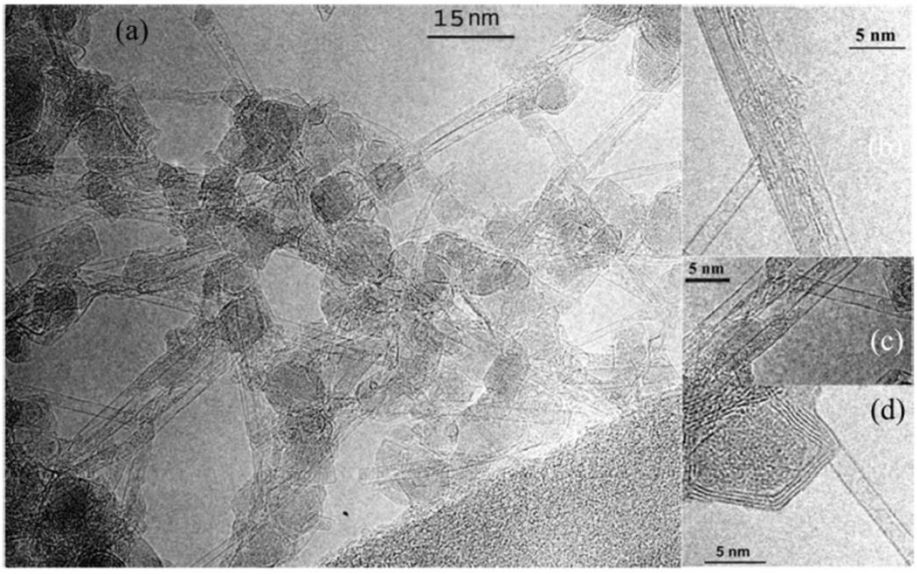


Figure 1.12 *HRTEM images of the synthesised BNNTs by laser vaporisation technique reported by Arenal* et al. *[55] showing (a) bundles of BNNTs with nanoparticles, (b) double-walled BNNTs, (c) single-walled BNNTs, and (d) BN onion-like structures.*

1.3.2.3 Substituted reaction/template-assisted BNNT synthesis

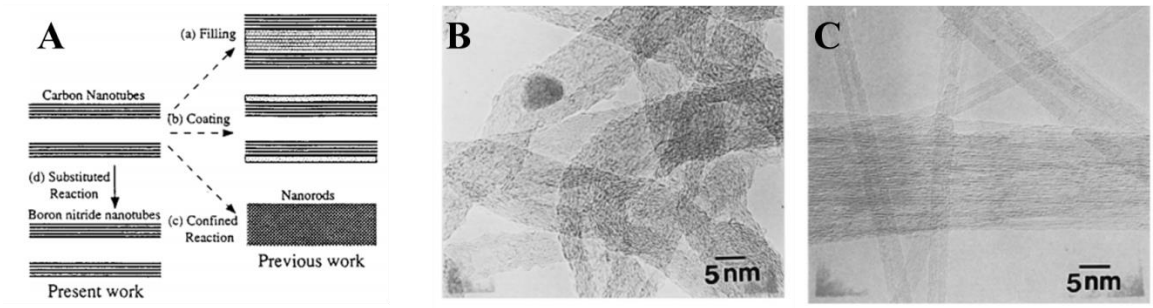


Figure 1.13 *(A) Schematic illustrations from Han* et al. *[56] of carbon nanotubes as a template to produce new one-dimensional nanoscale materials by (a) filling, (b) coating, (c) carbon nanotubes confined reaction to produce carbide and nitride nanorods, and (d) carbon nanotubes substituted reaction to produce boron nitride nanotubes. HRTEM images of (B) the sacrificial carbon nanotubes and (C) the result after BN substitution.*

Because of the significant improvement of the production yield of CNTs reaching milligram level, a method was developed to use CNTs as a sacrificial template to synthesise and improve the yield of BNNTs. Pioneered by Han *et al.* [56] in 1998, substituted reaction follows the schematic illustration in Figure 1.13A. The sacrificial

template of CNTs was reacted to boron oxide gas by heating the reactor chamber up to 1,700K under nitrogen atmosphere for half an hour. The synthesis was confirmed through TEM images presented in Figure 1.13C, which show the BNNTs produced from the CNT sacrificial templates (Figure 1.13B). However, the authors do note that certain aspects of the growth mechanism in this method are not fully understood, such as the observed significant change of nanotube diameter from 10 nm as CNT to 4 nm as BNNT. Moreover, the authors indicated that this method only resulted in an efficiency of 60% conversion from CNT to BNNT, and mostly produced $B_xC_yN_z$ nanotubes, whose purification could not reach 100% conversion to pure BNNT [57]. Other reports [58-60] further confirmed that the use of CNTs as template to produce BNNTs generates mostly $B_xC_yN_z$. The conversion from CNT to $B_xC_yN_z$ requires subsequent oxidation in order to acquire pure BNNT. However, removal of carbon in the tube lattice is not easily achievable and success of removal causes structural damage to the final product.

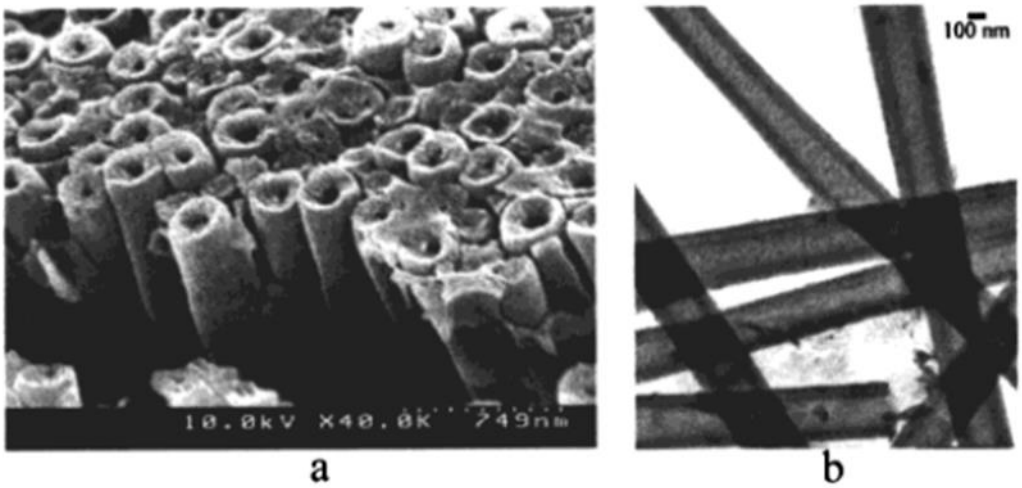


Figure 1.14 *Anodic aluminium oxide template-assisted synthesis of BNNTs by Moskovits* et al*. (a) SEM image of template-grown boron nitride nanotubes and (b) TEM image of BN nanotubules [61].*

Another method of template-assisted synthesis of BNNTs was demonstrated by the group of Moskovits [61] using the pores of an anodic aluminum oxide. The deposition

involved the use of trichloroborazine as precursor and reaction temperature of 750 °C. The product showed a close-packed array of well-aligned tubular structures having a diameter of ca. 280 nm with a wall thickness of ca. 100 nm (Figure 1.14). The method also showed a promising synthetic strategy by which the authors were able to fabricate layered nanostructures that are metal/insulator/metal (C/BN/C) coaxial nanotubes. However, detailed investigations revealed that the obtained BNNTs exhibited polycrystalline structure which degrades the properties of the BNNTs such as the mechanical and thermal conductivity properties.

1.3.2.4 Ball-milling method

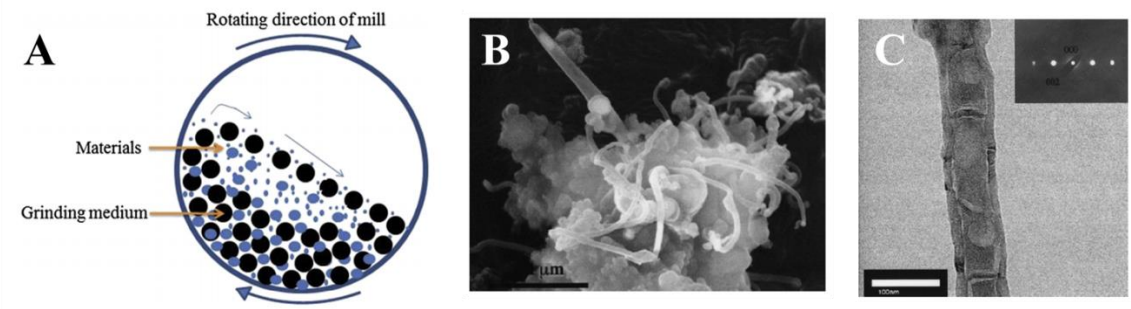


Figure 1.15 *(A) Schematic of a ball-milling setup. (B) SEM and (C) TEM images of synthesised BNNTs using the ball-milling method as reported by Chen* et al. *[62].*

The group of Chen [62, 63] introduced the method of ball milling for producing BNNTs, schematically represented in Figure 1.15A. The group proposed a mechanism for the formation of BNNTs that involved the milling of the boron powder precursor to 100 nm-sized boron particles that served as nucleation site as these nm-scale boron particles are annealed at temperatures of 1000 °C under nitrogen atmosphere. The advantages of the ball-milling method are its low cost and ease of control, while the disadvantage is the lack of homogeneity of the BNNTs produced. As seen from the SEM image in the report by Chen *et al.* (Figure 1.15B), the nanotubes suffered non-uniform diameters, were less abundant, and appeared to be connected to micron-sized particles. This would need further

processing to isolate the nanotubes. The nanotubes were also found to have bamboo-like nanostructures (Figure 1.15C) by TEM. Other studies also have shown that the ball-milling method produces BNNTs with poor homogeneity [53, 64, 65].

1.3.2.5 Chemical vapour deposition

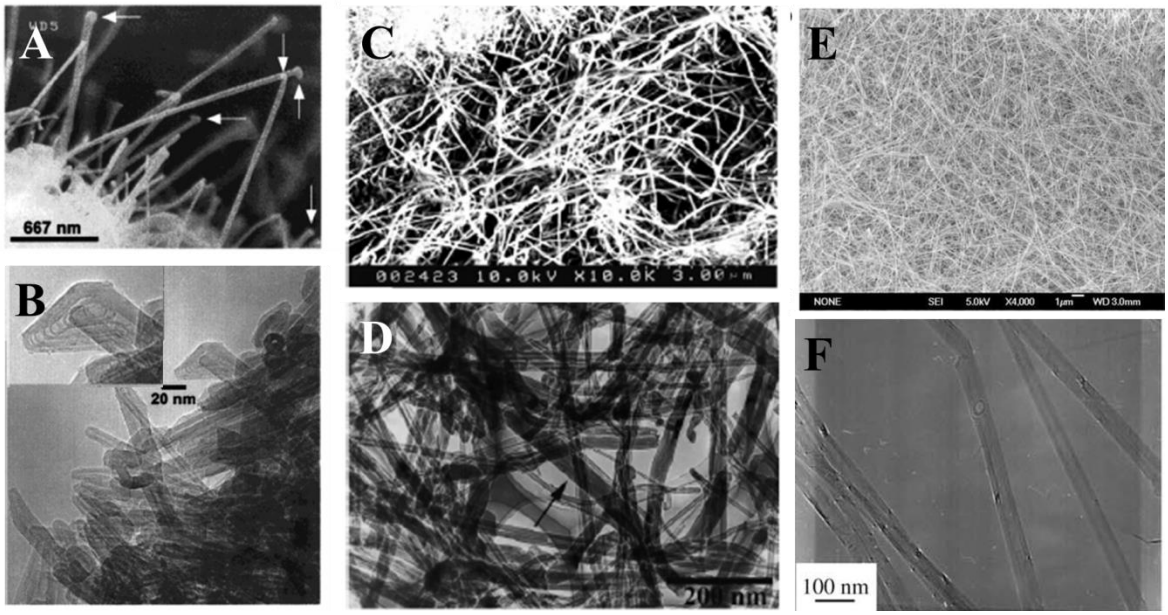


Figure 1.16 *SEM and TEM images of BNNTs synthesised using the chemical vapour deposition method. (A and B) Precursor of* in situ *generated borazine by Lourie* et al. *[6]. (C and D) Precursor of* in situ *generated B_2O_2 and Mg by Tang* et al. *[11]. (E and F) Addition of iron oxide in the powder precursor by Zhi* et al. *[12].*

The chemical vapour deposition (CVD) method of synthesising BNNT was realised as early as 2000 by Lourie *et at.* [6] utilising *in situ* generation of borazine in the reaction system. The group proposed a root-growth mechanism based on their SEM and TEM images (Figure 1.16A and B) showing one end of the nanotube as fractured or ragged and the other end often with irregular caps. The success of the method gained much attention since it offered greater control of synthesis conditions such as temperature, pressure, and rate flow of gaseous precursors. However, *in situ* generation of borazine was not ideal because of the potential risk coming from the high level of H_2 production.

This led to a search for a safer approach, and to the discovery of a key development in the synthesis of BNNTs by CVD: the boron oxide chemical vapour deposition (BOCVD) method first reported by Tang *et al.* [11]. The BOCVD method involves the use of B_2O_2 intermediate species to produce BNNTs generated *in situ* when MgO and B are allowed to react at 1,300 °C. Searcy and Myers [66] have proved that B_2O_2 will form under these conditions. This B_2O_2 vapour is then transported to another chamber by argon where ammonia is being introduced to produce $BN_{(s)}$, as schematically shown in Figure 1.17.

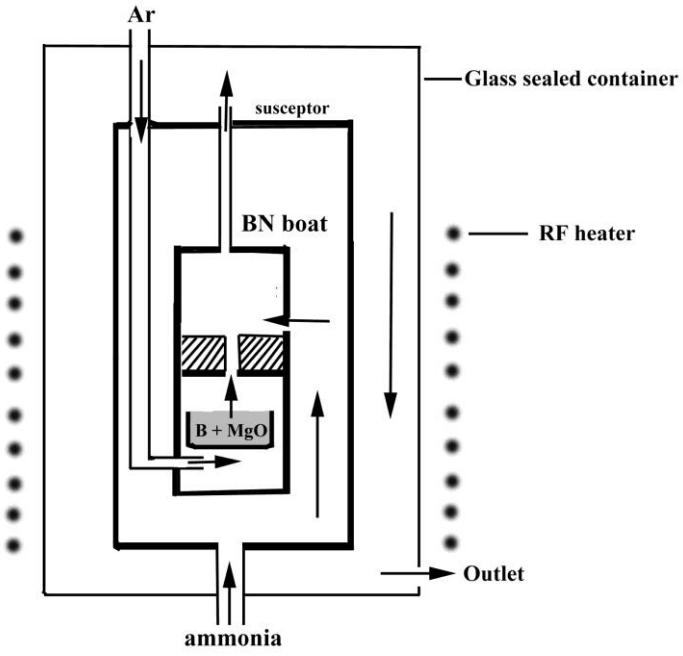


Figure 1.17 *Experimental setup of the production of B_2O_2 species as intermediate for the synthesis of BNNTs by Tang* et al. *[11].*

They suggested that the chemical reaction is:

$$2B_{(s)} + 2MgO_{(s)} \rightarrow B_2O_{2(g)} + Mg_{(g)} \quad (1)$$

$$B_2O_{2(g)} + 2NH_{3(g)} \rightarrow 2BN_{(s)} + 2H_2O_{(g)} + H_{2(g)} \quad (2)$$

The group claimed to have 40% conversion rate in terms of the boron to boron nitride ratio. The SEM image of the acquired product showed that abundant levels of BNNTs and nanotube structures were confirmed by TEM (Figure 1.16C and D, respectively). It was suspected that the growth of nanotubes was based on the vapour-liquid-solid (VLS) mechanism. However, the group failed to find strong evidence to support their proposed mechanism such as traces of catalyst or metal nanoparticles. The BOCVD method was then extended by adding other metal oxides in the powder precursor to improve the yield, as reported by Zhi *et al.* [12] (see Figure 1.16E and F). The group claimed that adding FeO served as an effective catalyst while MgO served as boron precursor generator. However, these claims were not justified by systematically showing how these different metal oxides affected the synthesis of BNNTs. For example, the report was not able to present the FeO catalyst on the synthesised BNNTs. Moreover, these authors indicated that the details of the mechanism were still unclear.

Compared to other methods, CVD has been preferred by researchers due to the ease and modifiability of the experimental setup, which goes from simple annealing of FeB particles under nitrogen gas protection [7] to association of floating catalysts [67]. Given the benefits of the CVD method as discussed in this section, this thesis utilised the CVD method to synthesise BN nanomaterials, while quantifying what parameters were needed to grow these materials.

1.3.3 Properties of BNNTs

The increasing interest in BNNT research is largely due to the properties they have to offer. In this section, a detailed review of the properties of BNNT is presented by comparing these to the corresponding carbon system, CNT.

1.3.3.1 Mechanical properties of BNNTs

Table 1.2 Young's modulus summary comparison of CNTs and BNNTs.

Materials	Young's modulus (TPa)		Reference
CNTs	1.09 – 1.25	(experimental)	[68]
	0.84~0.99	(theoretical)	[69]
	0.27~0.95	(experimental)	[70]
BNNTs	0.784–0.912	(theoretical)	[71]
	0.71– 0.83	(theoretical)	[72]
	0.5 – 0.7	(experimental)	[73, 74]
	1.22 ± 0.24	(experimental)	[75]

Theoretical investigations have reported that BNNTs have high Young's modulus that is only slightly lower than that of CNTs [71, 73, 75-77], as shown in Table 1.2. In terms of yield strength, that of BNNTs is also slightly lower than that of CNTs. The elastic properties of a single MW-BNNT synthesised using the arc-discharge method have been investigated by Chopra and Zettl [75]. The measurement was achieved by observing the thermal vibration amplitude of a cantilevered MW-BNNT in TEM. The value of the axial Young's modulus was found to be 1.22 ± 0.24 TPa, a value higher than the theoretical calculations; this was attributed to the highly crystalline characteristics of the synthesised MW-BNNT, which had very few defects. In another report, Suryavanshi *et al.* [74] measured the effective elastic modulus by using the electric-field-induced resonance method in the TEM. The group recorded an average effective elastic modulus of 722 GPa. This value is lower than the value reported by Chopra and Zettl [75], which may be due to

the intrinsic quality of the BNNTs synthesised using different methods, since the BNNTs used by Suryavanshi *et al.* [74] were synthesised through CVD.

Theoretical work by Dumitrica *et al.* [78] investigated the dislocations that can be formed in BNNTs under high tension by using *ab initio* calculations based on DFT approximation and molecular dynamics. Their findings indicate that BNNTs have a thermodynamic yield limit higher than the value recognized for CNTs both for the critical strain and the critical tension. Although this theoretical result confirms previous work done by Bettinger [79], this has not been fully recognized by experimental findings.

1.3.3.2 Thermal conductivity of BNNTs

Table 1.3 Comparison of the thermal conductivity of CNTs and BNNTs.

Materials	Thermal conductivity ($Wm^{-1}K^{-1}$) at room temperature		Reference
CNTs	~6,000	(theoretical, SWCNT)	[80]
	>3,000	(experimental, MW-CNT, D~14 nm)	[72]
	~1,000	(experimental, MW-CNT, D~10 nm)	[72]
	~300	(experimental, MW-CNT, D~35 nm)	[72]
BNNTs	>CNTs'	(theoretical)	[81]
	~180–300	(theoretical, SW-BNNT)	[82]
	~180–300	(experimental, MW-BNNT, D~35 nm)	[72]

Among the most attractive properties of BNNTs is very high thermal conductivity (See Table 1.3), combined with high electrical resistivity (see section 1.3.3.3) [83]. Usually, materials that conduct heat also conduct electricity, but not BNNTs. It has been demonstrated that the thermal conductivity of CNTs is due to electrons and phonons [72, 84, 85] while the thermal conductivity of BNNTs is exclusively due to phonons [86]. It is not yet clear if the thermal conductivity of BNNTs is higher than that of CNTs (i.e. 6,000 $Wm^{-1}K^{-1}$), as has been predicted by some theoretical works [72, 80, 81]. It has also been calculated that the specific heat of BNNTs is higher than its parent structure, h-BN [87].

The group of Xiao *et al.* [88] claimed that there is a direct relationship between temperature and specific heat of BNNTs, whereas the temperature decreases, the specific heat of BNNTs also decreases. In addition, these authors showed that the thermal conductance of SW-BNNTs had a universal quantisation at low temperature, which was independent from the diameter and chirality of the nanotube.

Chang *et al.* [86] presented improved thermal conductivity when isotropically pure boron (11B) was incorporated in MW-BNNTs measuring from 160 $Wm^{-1}K^{-1}$ to 300 $Wm^{-1}K^{-1}$ at 275 K. There are 3 reasons behind this ca. 50% enhancement of thermal conductivity: the significant isotopic disorder (19.9%), the 1D structure that promotes phonon localization due to isotope scattering, and the isotope that can affect the phonon scattering time [89]. This 50% enhancement of thermal conductivity was also observed by Mingo *et al.* [82] after performing theoretical calculations using (8,0) SW-BNNTs instead of the MW-BNNTs used by Chang *et al.* [72].

1.3.3.3 Electronic properties of BNNTs

In contrast to the dependence of the electronic property of CNTs on their diameter and chirality, BNNTs have a constant wide band gap at 5.0 – 6.0eV, which makes it an insulating material that is not dictated by its structure. According to Lan *et al.* [90], the dielectric constant of BNNTs is 5.90, which is universal for all BNNTs regardless of their radius and chirality. Various methods have been suggested to modify the band structure of BNNTs, although only doping and applying electric field [87, 91] have been realised experimentally. In addition, the synthesis method employed in generating BNNTs was found to affect their electronic properties. According to Radosavljevic *et al.* [92], BNNTs grown by laser ablation are intrinsically p-doped, as confirmed using a prototype BNNT field-effect transistor setup (FETs). Fluorine and carbon doping was found to be an

effective method for improving the transport property of BNNTs [93, 94]. Resistivity of BNNTs was observed to decrease from ca. 300 Ωcm to 0.2 Ωcm by fluorine doping [93]. Golberg *et al.* [95] investigated the electrical property of an individual BNNT doped with carbon and found it to exhibit well-defined semiconducting characteristics observed from the measured resistance of ca. 1GΩ (pure BN nanofiber is at ca. 5 GΩ while pure CNT is at ca. 7 kΩ).

Bai *et al.* [96] observed a current passing through the BNNT after bending which was also found to be a reversible process. The transport property was determined to be bias-sign sensitive, as a result of the hysteresis showed by the I-V curves taken on deformed BNNTs. Nakhmanson [97] attempted to explain the relationship of the deformation-driven electrical transport of BNNTs by using *ab initio* calculations, and suggested that the carrier transport is smooth when the directions of an applied field and polarisation field are coincident while transport is obstructed when these directions become opposite.

1.3.3.4 Oxidation resistance of BNNTs

Several papers have reported that BNNTs possess ultimately high resistance to oxidation [98, 99]. MW-BNNTs showed that they are stable in air at at least 700 °C and improves at higher temperatures up to 900 °C for BNNTs with diameters lower than 20 nm and exhibiting high crystallinity with low defects [99].

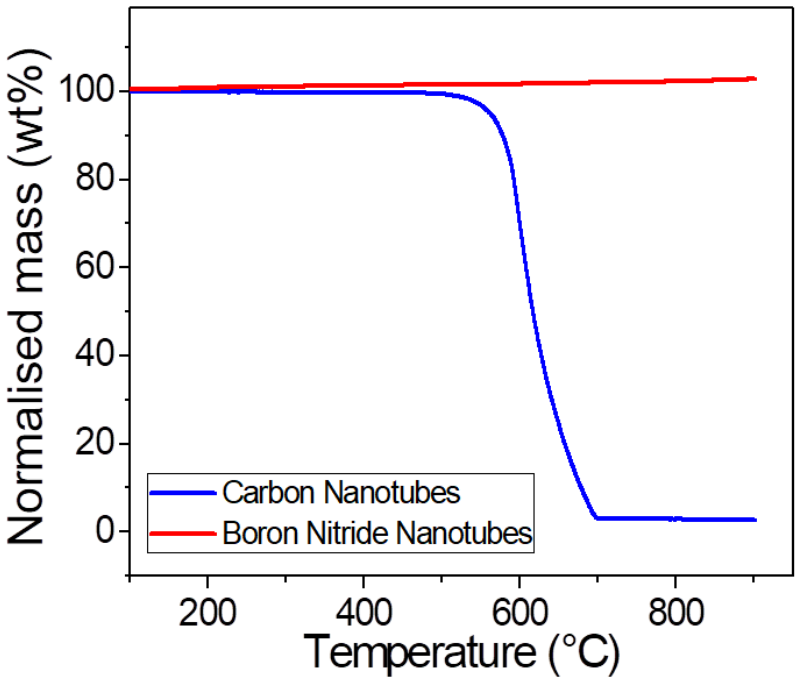


Figure 1.18 *Thermal gravimetric analysis comparing CNTs and BNNTs in air.*

Figure 1.18 shows oxidation resistance comparing CNTs and BNNTs in air. CNTs showed a sharp decrease in weight at temperature around 600 °C, losing about 70% of its original weight. However, BNNTs had a change of anti-oxidation profile at around 900 °C and oxidation took place above this temperature. The oxidation property of nanotubes is strongly linked to the quality of the tube structure: i.e., whether they are free of defects, have perfect cylindrical structure, and have continuous crystalline walls [95, 99].

1.3.4 Potential applications for BN nanomaterials

1.3.4.1 BN nanomaterials for thermal management applications

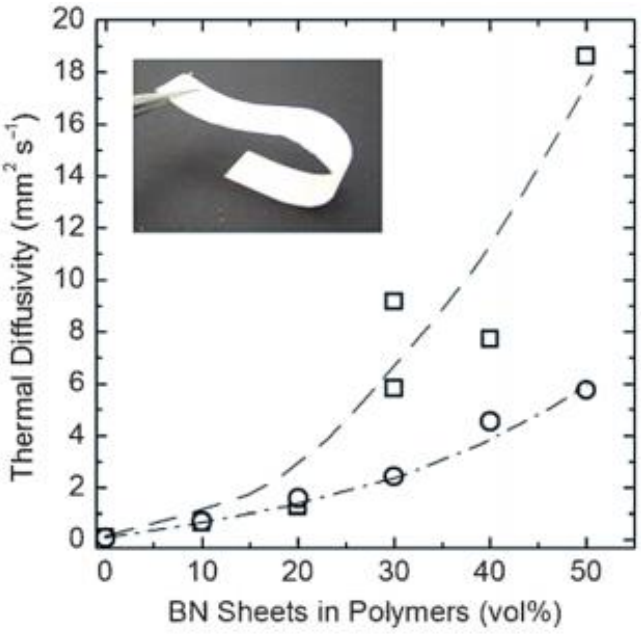


Figure 1.19 *Thermal diffusivity values of epoxy/BN nanocomposite films at different BNN loadings (square) compared with those for PVA/BNNs films (circle). Inset: Photograph of a piece of film with 50% BNN loading.*

The unique properties of BN nanomaterials that have just been described in section 1.3.3 make them ideal for thermal management applications. Both nanosheet and nanotube structures of BN nanomaterials have drawn much attention for heat transfer and other uses. For instance, Song *et al.* [100] reported that BN nanosheets used as fillers in epoxy composite at a loading of 50 vol. % exhibited exceptional thermal transport performance, with a measured in-plane thermal diffusivity reaching up to 19 mm^2s^{-1}, which is equivalent to a thermal conductivity of 30 $Wm^{-1}K^{-1}$ that is close to 15 % of the thermal conductivity of aluminium metal, as shown in Figure 1.19.

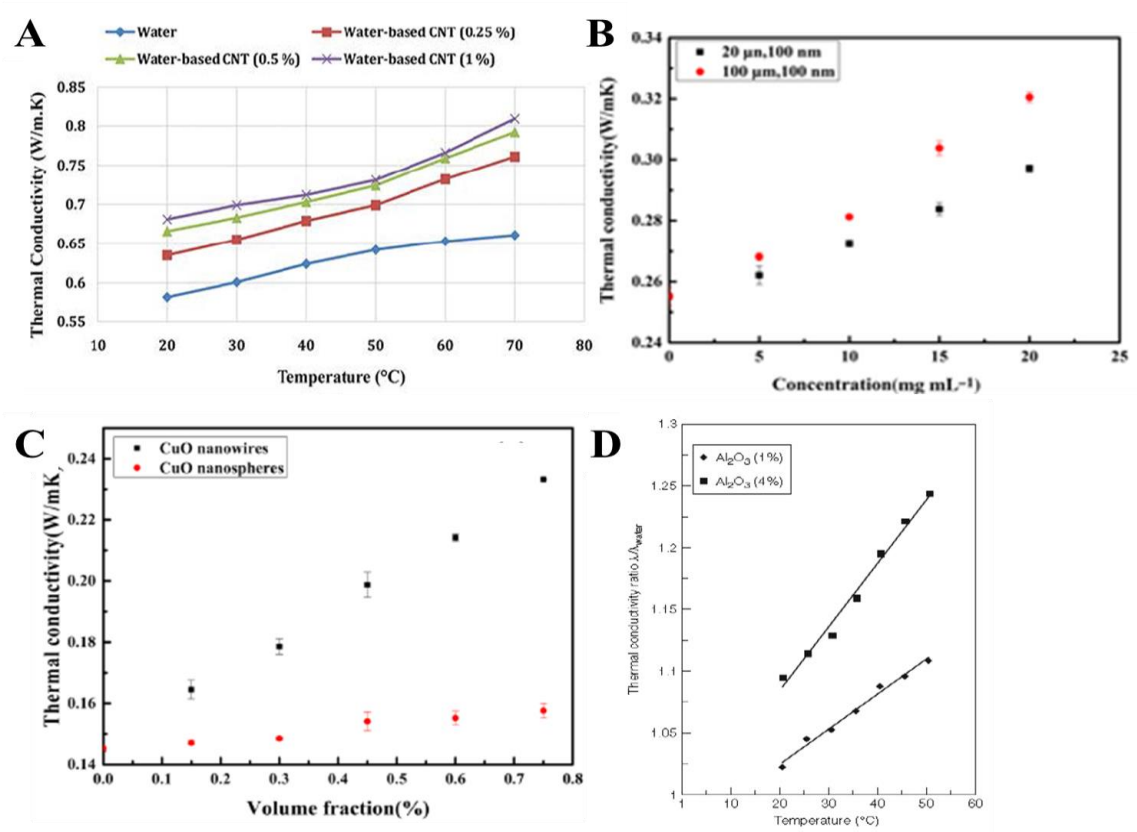


Figure 1.20 Thermal conductivities of nanofluids using (A) CNT [101], (B) silver nanowires [102], (C) copper oxide nanomaterials [103], and (D) aluminium oxide nanoparticles [104] at different concentrations.

Over the past decade, there has been an increasing interest in the usage of nanomaterials in liquids, particularly in thermal management applications particularly, such as developing energy-efficient heat transfer fluids for ultra-high-performance cooling known as nanofluid technology [105]. Figure 1.20 shows different nanomaterials reported in different liquids to improve the thermal conductivity. Presented in Figure 1.20A, Amiri *et al.* [101] reported that the thermal conductivity of CNT-COOH-based water showed an improvement from their base fluids to increasing weight concentrations of 0.25 %, 0.5 % and 0.1 % with an enhancement values of 10.34 %, 13.79 %, and 17.24 % at 20 °C, respectively. Figure 1.20B is taken from the report of Zhu *et al.* [102] showing a linear increase of thermal conductivity was observed as the concentration of silver nanowire was increased in ethylene glycol. Thermal conductivity enhancement of 16.42 % was observed

for 20 µm lengths of silver nanowires while 25.59 % enhancement was obtained when 100 µm lengths of silver nanowires were used. The shape of the nanomaterial showed to have a contribution to the enhancement of the thermal conductivity of the nanofluid. As reported by Zhu *et al.* [103] shown in Figure 1.20C, a 0.75 % volume fraction of copper oxide nanospheres in dimethicone resulted to a 6.98 % thermal conductivity enhancement while at the same volume fraction of copper oxide nanowires gave a thermal conductivity enhancement of 60.78 %. Thermal conductivity of nanofluids revealed to be dependent also on the temperature where a direct relationship is observed as reported by Das *et al.* [104] in using aluminium oxide nanoparticles as presented in Figure 1.20D.

The use of BN nanomaterials for thermal management applications holds its promise from its additional unique properties in comparison to those of their carbon and other 1D nanostructure counterparts. For example, the insulating property of BN nanomaterials, as presented in section 1.3.3.3, is a good complementary property to its high thermal conductivity, particularly in thermal management for electronic devices. The miniaturisation of electronic devices requires effective thermal management, as heat is known to be a leading cause of the degradation of the performance and reliability of these devices [106, 107].

The unique properties mentioned above also make BN nanomaterials a viable solution in the field of energy storage, where temperature is known to have a serious impact on the performance, safety, and cycle lifetime of batteries [108]. BN nanomaterials are also expected to be used as protective layer for devices working in extreme conditions due to the material's high oxidation resistance (see section 1.3.3.4) and high chemical stability [109]. Their remarkable properties make low-dimensional BN nanomaterials one of the most promising materials that can meet current needs and drive future advancements in technology.

1.3.4.2 Other applications for BN nanomaterials

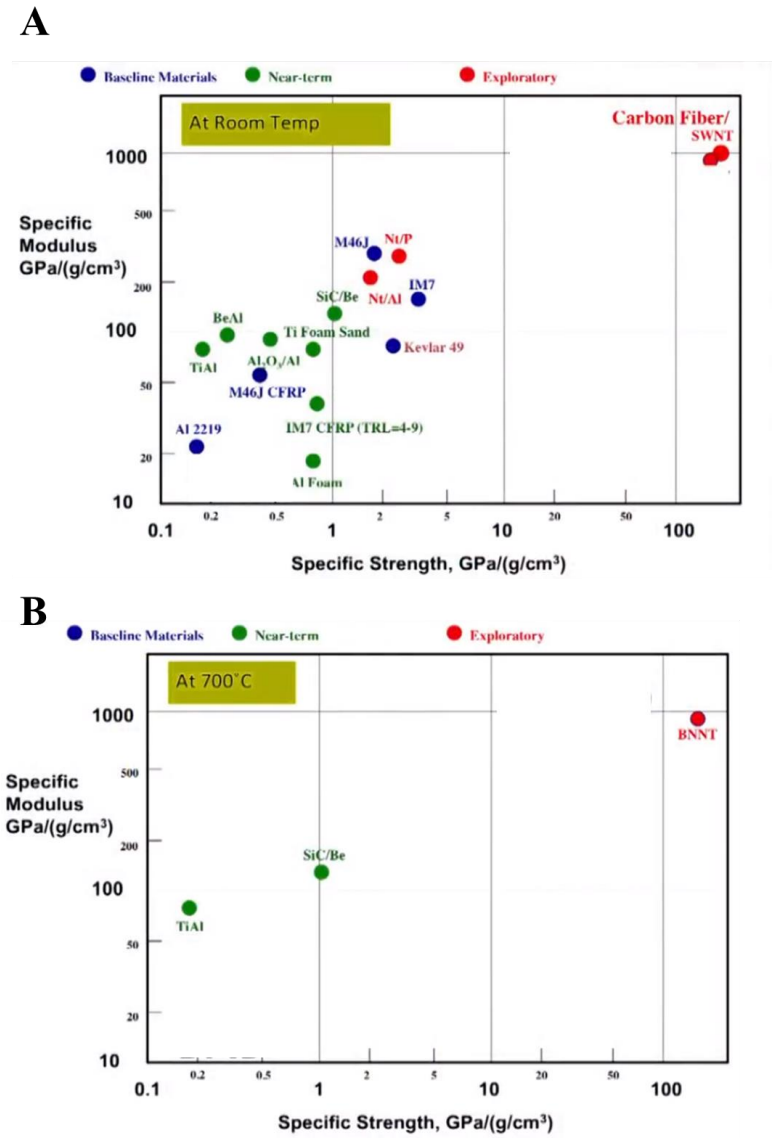


Figure 1.21 *Plot of specific modulus vs specific strength of different materials at (A) room temperature and (B) 700 °C; (Blue) Baseline materials, (green) near-term, and (red) exploratory [110].*

Another example of a potential application of BNNTs is in improving the fuel efficiency of modes of transportation, such as cars and airplanes. As seen in Figure 1.21 acquired from Harris *et al.* [110], different materials possess different mechanical properties (specific modulus vs specific strength) where blue plots correspond to commercially available materials, green plots are materials that are in the final stages of

research, and red plots correspond to new materials. Materials that are located in the upper right part of the plot are ideal for transport applications. However, as the temperature changes from room temperature to 700 °C (Figure 1.21A to B), most of the materials do not maintain their structural integrity. The excellent mechanical properties combined with the high oxidation resistance of BNNTs make them the best-suited material for such transport applications.

1.3.5 DFT studies in the synthesis of BN nanomaterials

The studies involving the DFT calculations of BN nanomaterials particularly the synthesis mechanism is not as much abundant compared to its carbon counter-part [111-114]. In fact, the first report of *ab initio* study on BNNT synthesis can be found in the year 1999 [115] reporting that open-ended growth of single-walled armchair BNNTs occurs in a non-catalytic system. The lack of DFT studies in the synthesis of BN nanomaterials is due to the challenge of modelling catalytic process. *Ab initio* studies that involves catalytic process concentrate in investigating situations where the catalyst is reactive enough to dissociate a precursor but not too reactive to block the synthesis [116]. An example of this is the synthesis of ammonia and its rate limiting step, the N_2 dissociation [117]. In the synthesis of BN nanomaterials, the use of DFT can provide adsorption energies, reaction energies, and reaction barriers of bond formation of molecules on a catalyst.

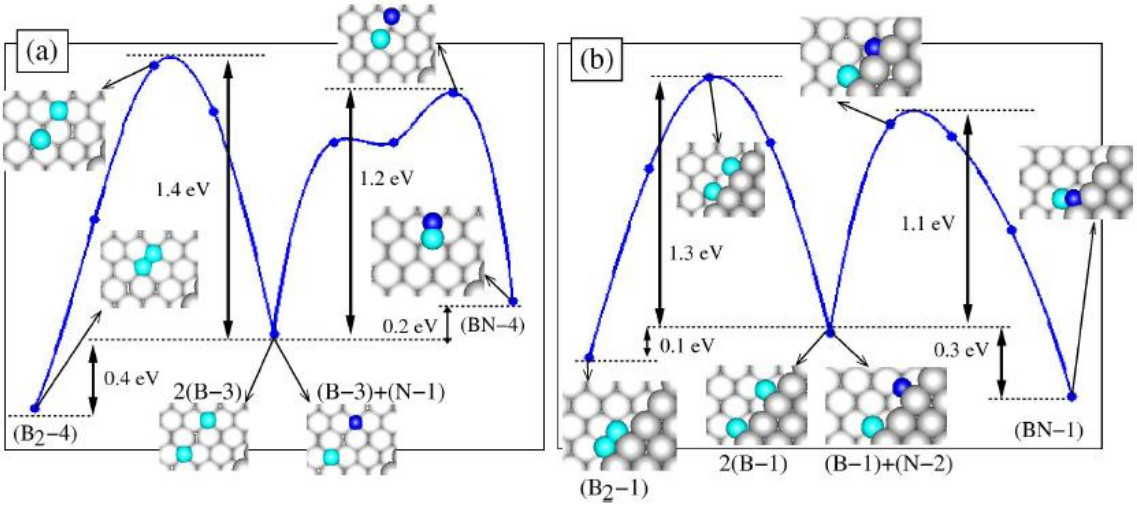


Figure 1.22 Potential energy surface of BN bond formation showing reaction barriers at the (a) terrace) and (b) step-edge on an iron surface as reported by Riikonen et al[118].

Shown in Figure 1.22 is the report of Riikonen *et al*. investigating the interaction of boron and nitrogen atoms in iron[118]. The authors modelled the catalyst nanoparticle by slabs in supercell geometry that consist of 3-6 atomic layers. The calculations were performed with programmes in the framework of DFT as implemented in two different codes namely: SIESTA and VASP. All calculations were done using Perdew-Burke-Ernzerhof (PBE) general gradient approximation exchange-correlation (XC) functional. They presented that the iron nanoparticle in their system stabilised the BN molecule on the step-edge due to the different coordination behaviour the step-edge offers. BN is likely to form due to the exothermic reaction with an energy value of -0.3 eV compared to -0.1 eV in B_2 formation.

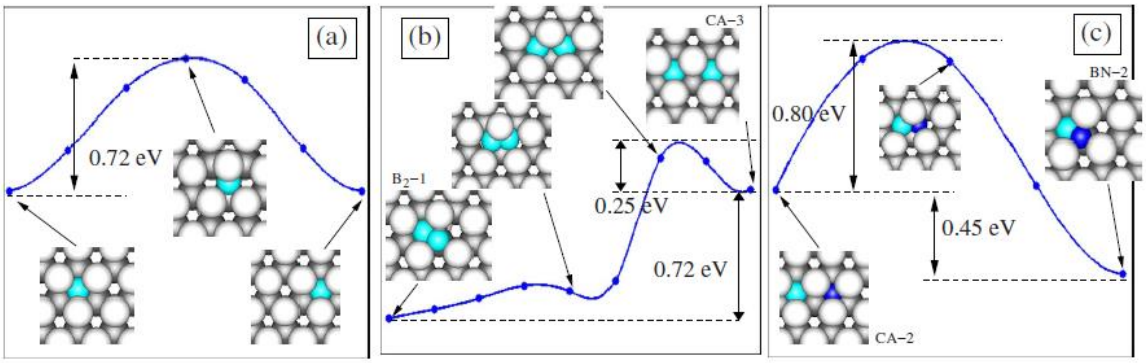


Figure 1.23 Potential energy surface showing (a) barrier for B diffusion, (b) B2 association/dissociation reaction, and BN association/dissociation reaction on Mg(100) surface reported by Riikonen et al.[119]

Motivated by experimental results on magnesium [11, 12, 120], Riikonen *et al.* later also investigated this element as a catalyst for the generation of BNNTs[119] as shown in Figure 1.23. Their results revealed that magnesium promotes BN molecule formation on the surface of the (100) facet of magnesium. However, the authors further stated that their results still needed to be correlated with experimental findings. Furthermore, their study dealt only with boron and nitrogen atoms for iron and magnesium catalysts. It is therefore safe to conclude that there is a lack of studies involving the molecular state of boron and nitrogen precursors, and a need to perform first-principle theoretical calculations by DFT addressing the nucleation and growth of BNNTs on the basis of direct empirical results. It is this gap in the literature that this thesis will fill by merging the empirical and theoretical perspectives on BNNT synthesis explored throughout the thesis.

1.4 Method of analysis

1.4.1 Electron microscopy (scanning and transmission)

The morphology and structure of BNNTs depend on the synthesis technique employed. Electron microscopy is a characterisation technique for imaging BNNTs which allows for the measurement of nanotube size as well as of the quality and presence of defects or side products. Scanning electron microscopy (SEM) is a microscopic analysis technique commonly used to study the surface and structure of a material. An electron beam is sent to the surface of the sample from an electron gun. The electron beam interacts with the sample, resulting in the occurrence of multiple events such as generation of secondary electrons and backscattered electrons. A detector receives these electron interactions, which are then processed into an image. It is important to take note that there must be a conducting path for the electrons to flow from the sample to the ground (typically the sample holder) to avoid sample charging. Sample charging causes problems in imaging such as drift, blur, and low contrast. Insulating materials such as BN materials are coated with a thin layer of platinum to avoid charging. This prevents the accumulation of static electric charge on the specimen during image acquisition and helps to improve the quality of the images being obtained. SEM is used to measure lengths of BNNTs and assess the degree of alignment.

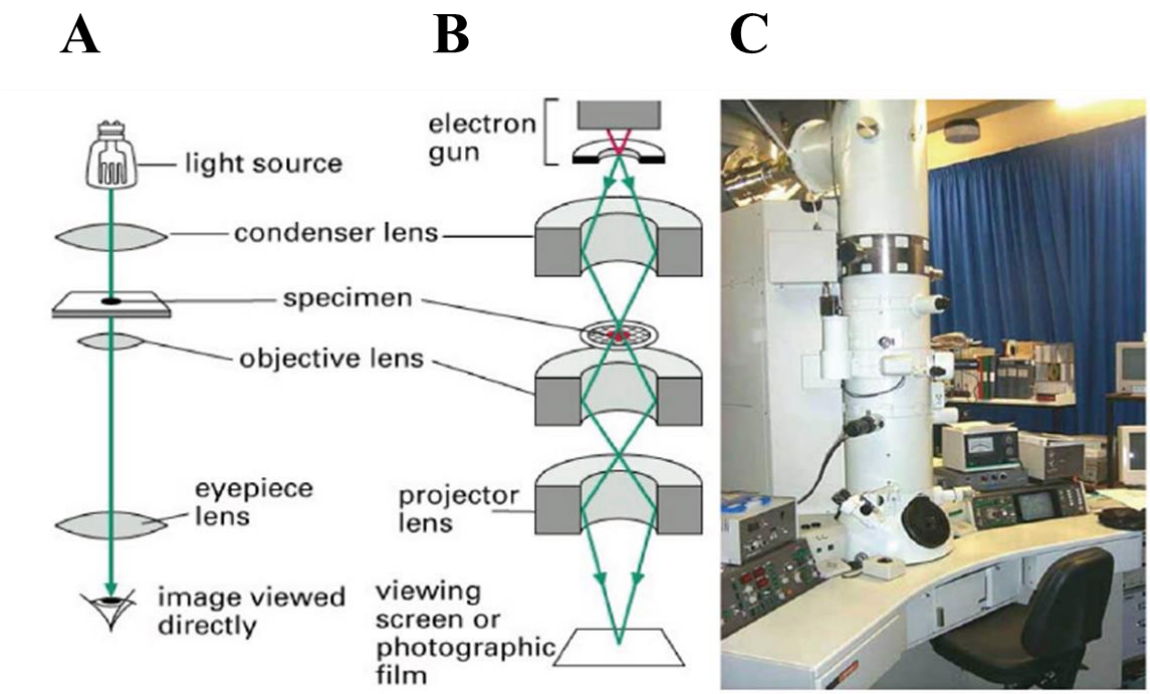


Figure 1.24 Schematic illustration comparing an (A) optical microscope and a (B) transmission electron microscope. (C) Photograph image of the JEOL JEM-3000F used in this study.

Transmission electron microscope (TEM) works the same basic principle as an optical microscope, as seen in Figure 1.24, but uses electrons instead of light. TEMs generate images by utilizing high voltage electron beam. This electron beam is produced by an electron gun at the top of a TEM and travels through the microscope's vacuum tube. In contrast of having glass lens to focus the light in the case of light microscopes, the TEM employs electromagnetic lens which focuses the electrons into a very fine beam. This beam then passes through the specimen (50 to 100 nm thickness) and the electrons either scatter or hit a fluorescent screen at the bottom of the microscope. An image of the specimen with its assorted parts will be displayed on the screen in different shades according to its density. This image can be studied directly within the TEM or captured to be subjected to other image analysis programmes. Figure 1.24C shows a photograph image of the JEOL JEM-3000F 300 kV field emission gun (FEG) that was used in this study, compared to SEM, allows for higher level of morphology characterisation, thanks to its

point resolution of below 0.17 nm and an information limit of below 0.10 nm [121, 122] which makes it possible to measure nanotube diameters, count the number of concentric walls, and view the tube morphology, as presented in section 1.3.1.3. Figure 1.25 shows electron microscopy images acquired for this work that will be further presented and discussed in Chapters 2 and 3. High-resolution transmission electron microscopy (HRTEM) is vital to modelling the theoretical calculations on the B-N bond formation that is presented in Chapter 4.

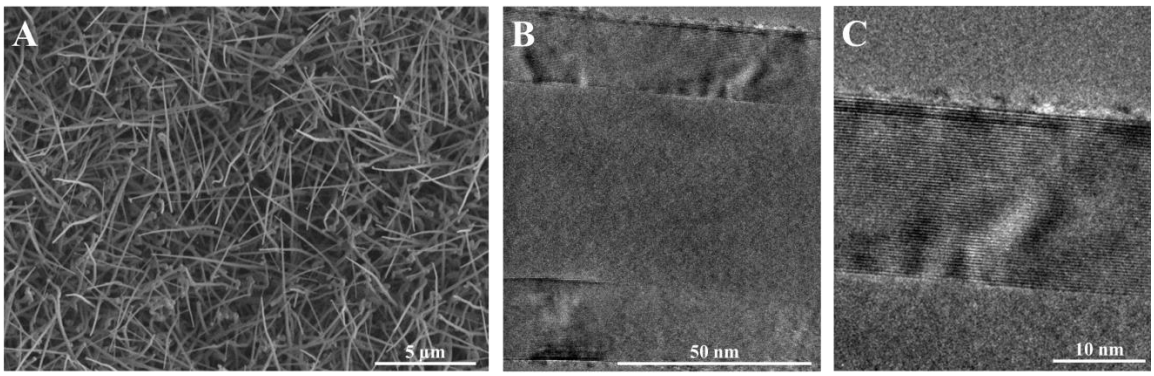


Figure 1.25*(A) SEM image showing the filaments structures, (B) TEM image showing hollow morphology, and (C) HRTEM image showing the layers of sheets that comprise the walls of the nanotube acquired for this thesis.*

In electron microscopy analysis, it is important to consider possibility of sample damage that can take in the form of ballistic knock-on process such as Frenkel defect consisting of a vacancy and an interstitial defect that occurs when an electron in an accelerating electron beam irradiates on a material. In this process, the energy transferred in an elastic collision between the electron and the nucleus exceeds the displacement energy, that varies from ~ 0.1 eV for Van der Waals bonding to tens eV for ionics. This process requires a minimum electron beam energy that is called threshold energy before it can occur. The value varies with the atomic number of the sample. In a paper reported by Kotakoski *et al.* [123] typical defect structures were observed on a monolayer of h-BN

after exposure of different acceleration voltage of a TEM beam as shown in Figure 1.26. The authors indicate that undercoordinated atoms of one species are knocked out more frequently under the electron beam. Addition of h-BN layer increases its stability making it less prone to electron beam damage [124-126]. As reported by Gilbert *et al.* [124] the electron beam of a JEOL 2010 TEM operated at 80 kV was condensed to a diameter of 10-20 nm at a current density of 37 A/cm^2 to introduce nanopores in a multilayer h-BN. In nanotube structures particularly multi-wall BNNTs, a much higher acceleration voltage and a much smaller beam size is needed to damage the structure suggesting that nanotubes hold greater stability than nanosheets [127]. As reported by Celik-Aktas *et al.* [128] a high energy electron irradiation TEM operated at 200 keV with the diameter of the electron beam smaller than the diameter of the nanotube was used to cut a multi-wall BNNT. Shown in Figure 1.27 is their report of multi-wall BNNT exposed at different sizes of electron beam. The authors reported that electron beam cutting was achieved with the 5 nm beam with a dosage of 1.45x10^5 A/cm^2. Partial structure collapse was observed under beam sizes 1 and 2. The electron beam size was varied by changing the convergence angle of the TEM and the smallest beam can be achieved using 120 µm condense aperture. In this work, the beam size was not varied to introduce partial structure collapse of the BNNT. However, it is noteworthy to consider that the samples in this work may have been damage under TEM analysis due to the high acceleration voltage being used.

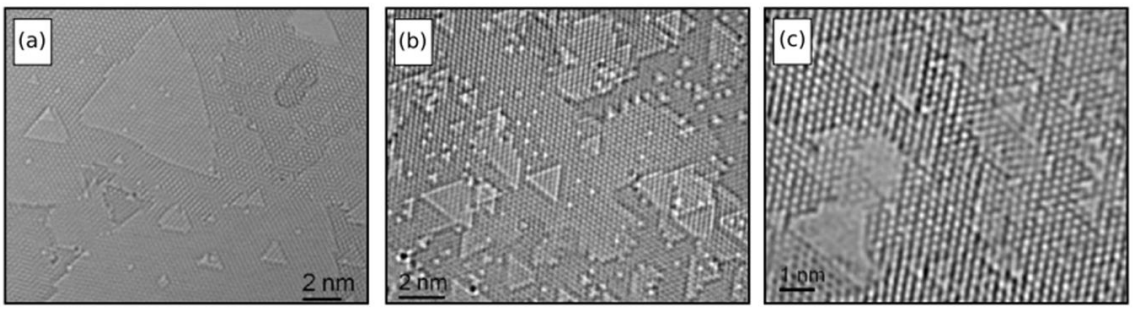


Figure 1.26 Examples of the h-BN structures after an exposure to a TEM beam with different acceleration voltages: (a) 80 kV, (b) 120 kV, and (c) 200 kV from the report of Kotakoski et al. [123].

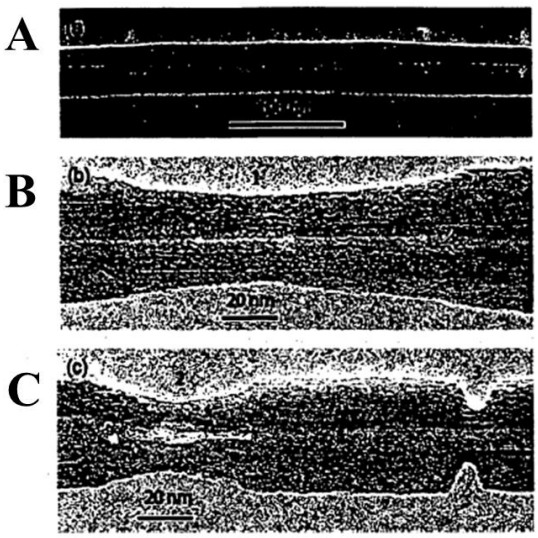


Figure 1.27 *TEM image of BNNT (A) before and after the exposure to three different beam sizes: (B) size 1 of 90 nm, (C) size 2 of 50 nm at left side and size 3 of 5 nm at right side reported by Celik-Aktas et al. [128].*

1.4.2 Energy-dispersive X-ray spectroscopy (EDX)

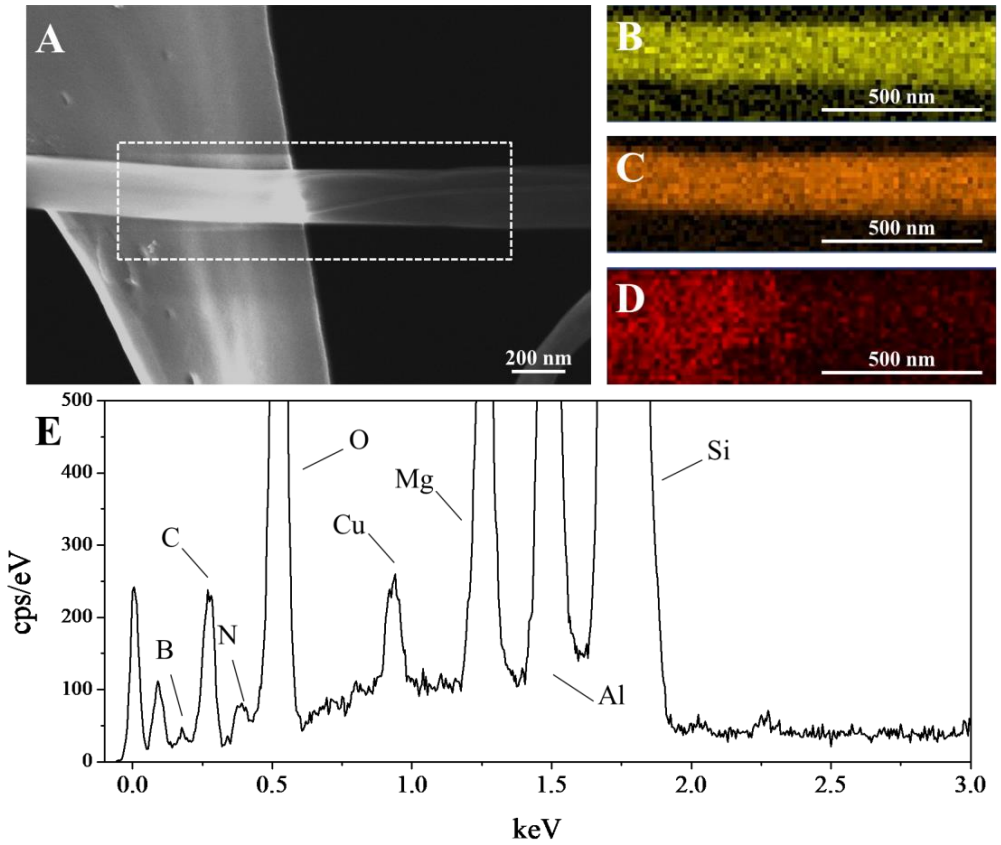


Figure 1.28 *EDX analysis for this thesis. (A) Region of interest for EDX analysis indicated by the white dashed square. Elemental mapping of (B) boron, (C) nitrogen, and (D) carbon. (E) Corresponding EDX spectra.*

Energy dispersive x-ray spectroscopy (EDX) is a characterisation technique that can be used in both SEM and TEM to measure the elemental composition of regions in a sample. High-energy beam electrons may eject inner shell electrons from atoms in the sample, causing outer shell electrons to drop in to fill these holes. As these electrons drop from higher energy to lower energy states, an x-ray can be emitted with energy equal to the difference in energy between the two orbits, and this energy is characteristic for specific elements. These x-rays are collected, with x-rays of characteristic energies indicating the presence of particular elements. EDX has been demonstrated to be effective in determining element composition, particularly catalysts and contaminants in BNNTs [8, 129]. It must be noted that EDX analysis for the quantification of light elements such as Be, B, C, N, O and F does not have a good reliability due to their low photon energies that leads to complications such as (1) high absorption in the specimen and in the detector, (2) the low energy peaks is positioned close to the electronic noise of the detection system that is seen at about 0 keV, and (3) light elements gives low yield of X-rays. With this disadvantage of the EDX, a complementary technique that is the electron energy-loss spectroscopy (EELS) is used. However, EDX provides insights in qualitative analysis of elements present in the sample.

Presented in Figure 1.28 is an example of EDX characterisation for this thesis. EDX elemental mapping can provide insight regarding the qualitative distribution of elements in the material as seen from Figure 1.28B to D corresponding to boron, nitrogen, and carbon. The EDX spectrum is also acquired in this analysis as presented in Figure 1.28E. It must be noted that this spectrum needs to be subtracted from the background. Further findings obtained from this characterisation technique are presented in Chapters 2 and 3 of this study.

1.4.3 Electron energy-loss spectroscopy (EELS)

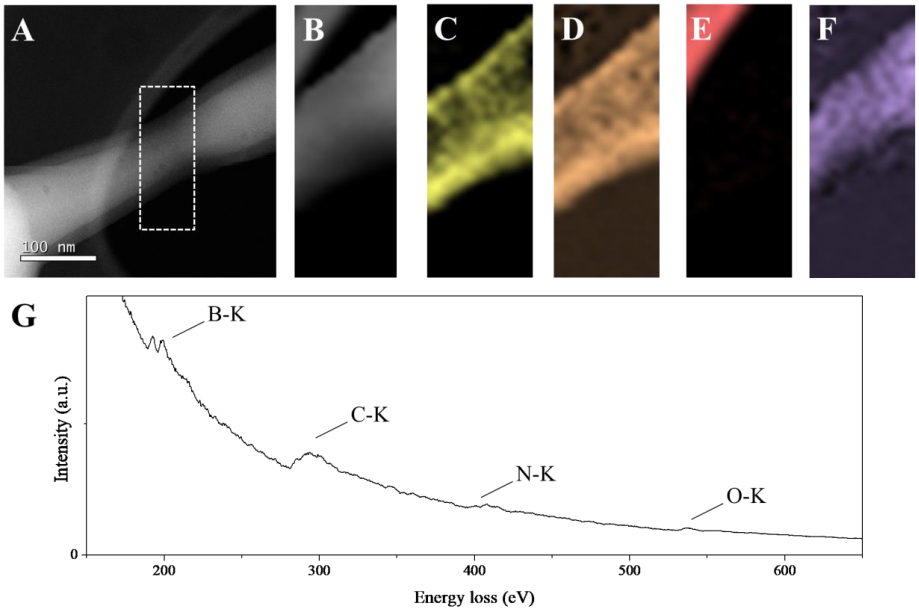


Figure 1.29 *EELS characterisation for this work. (A) Region of interest for EELS analysis indicated by the white dashed square. (B) High loss EELS spectrum image. Elemental mapping of (C) boron, (D) nitrogen, (E) carbon, and (F) oxygen. (G) Corresponding EELS spectrum.*

Complementary to EDX, electron energy-loss spectroscopy (EELS) is another spectroscopy technique that excels in measuring atomic composition, chemical bonding, valence and conduction band electronic properties, and surface properties [130]. In EELS, a beam of electrons with known energy is interacted with the sample material. The interaction makes some of the electrons lose energy and causes a minor shift of pathway (inelastic scattering). The amount of energy loss is measured by an electron spectrometer that interprets the terms of the factor caused by the energy loss such as phonon interaction, inter- and intra-band transitions, plasmon excitations, inner shell ionisation, and Cherenkov radiation. Compared to EDX, EELS works best at relatively low atomic numbers up to the 3d transition metals due to the sharp excitation edges of these low atomic numbers. Thus, EELS is ideal for the present work, as it can provide a good determination of the stoichiometry of BN nanomaterials. This technique makes it possible

to determine the B:N ratio of BNNTs with a value of 1.14 that is consistent with the stoichiometry of BN material [9, 10, 16]. Furthermore, this technique enhances our understanding of the growth mechanism of BNNTs. Su *et al.* [10] suggested that the BNNTs followed a tip-growth mechanism as observed through EELS elemental mapping. This is in good agreement with the earlier growth mechanism proposed by Oku [7], concluding that boron in liquid-phase Fe_2B starts to precipitate on the catalyst surface and reacts with nitrogen from NH_z radicals to yield BN layers. However, it should be noted that different mechanisms are presented due to different approaches of synthesising BNNTs.

A detailed discussion of the growth mechanism will be presented in Chapter 2. Figure 1.29 presents a sample EELS characterisation for this thesis. EELS characterisation is used in this study to confirm the purity composition of the synthesised BN nanomaterials, particularly the bonding nature of the atoms presented in Chapters 2 and 3. The calculation of B/N ratios are acquired by using EELSMODEL [131, 132] programme where the programme models the spectra by making use of a power-law background, hydrogenic cross-section for each edge, and an equalization function for each edge to simulate the fine structure. The equalization function can be shown to approximate the relative density of unoccupied states for the given excitation edge. Developers of the EELSMODEL programme reports a 2 % accuracy error attributed to the approximations introduced in the model [133]. This accuracy error is added on top of the calculated B/N ratio error in this work. Finally, EELS was used to determine the band gaps of the synthesized nanostructures of this work that is shown in Chapter 3.

1.4.4 Raman spectroscopy

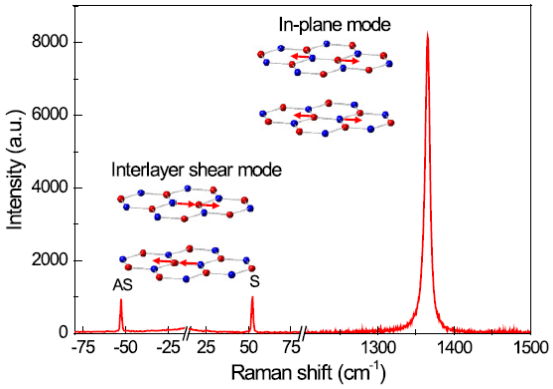


Figure 1.30 *Raman spectrum of h-BN presented by Stenger* et al. *[134]. This spectrum shows the low frequency peak at -52.5 cm^{-1} (anti-Stoke), 52.5 cm^{-1} (Stokes), and the high frequency peak at 1366 cm^{-1} (Stokes).*

Raman spectroscopy is based on the inelastic scattering of photons that is known as Raman scattering. When light interacts with a material, the energy of the light can change (inelastic scattering) or stay the same (elastic scattering or Rayleigh scattering). The change of energy may be either up-shifted or down-shifted due to the interaction of the incident photon to the phonons (quantized lattice vibration) of the material. h-BN have unique Raman spectroscopic signatures that relate to their molecular vibration modes. The Raman spectrum of an h-BN (Figure 1.30) has the E_{2g} mode at low frequency with anti-Stokes (AS) and Stokes (S) peaks, and at high frequency with Stokes peak or the so-called G band mode [134]. The E_{2g} mode at low frequency has been less observed because it is close to the high Rayleigh background and may also be due to the limit of Raman detectors such as frequency cut-off of the notch filter. On the other hand, the high frequency E_{2g} mode has the high intensity and experimental peak position at ca. 1366 ± 1 cm^{-1} also observed in bulk h-BN.

Raman spectroscopy has proved to be an efficient and non-destructive technique for characterising CNTs. This has provided information not only on the geometric, electron, and phonon structure, but also on the physical effects [135, 136]. Arenal *et al.*

[137] investigated the Raman behaviour of a SW-BNNT synthesised by laser vaporisation of h-BN under nitrogen protection. The study involved the use of UV (229 and 244 nm) and visible (514 nm) Raman spectroscopy. They found that the high-energy mode E_{2g} of SW-BNNTs is blue-shifted compared to bulk h-BN E_{2g} and suggested that the shift was due to the interaction of the neighbouring sheets in h-BN.

Zettl *et al.* [138] investigated the Raman scattering of MW-BNNTs and $B_xC_yN_z$ nanotubes. The group claimed that multi-walled $B_xC_yN_z$ nanotubes are structured radially phase-separated BN and carbon shells. In another investigation [139], sp^3 bonding of BN vibration was noted by studying the temperature-dependent Raman spectra of bamboo-like BNNTs. The contamination level of synthesised BNNTs was also quantified by Raman analysis. In Arenal *et al.*'s [137] study, under visible range of Raman scattering, a large fraction of boric acid which was not detectable by TEM was revealed. Figure 1.31 shows good agreement between the Raman characterisation reported by Lee *et al.* [140] and the Raman characterisation for this thesis.

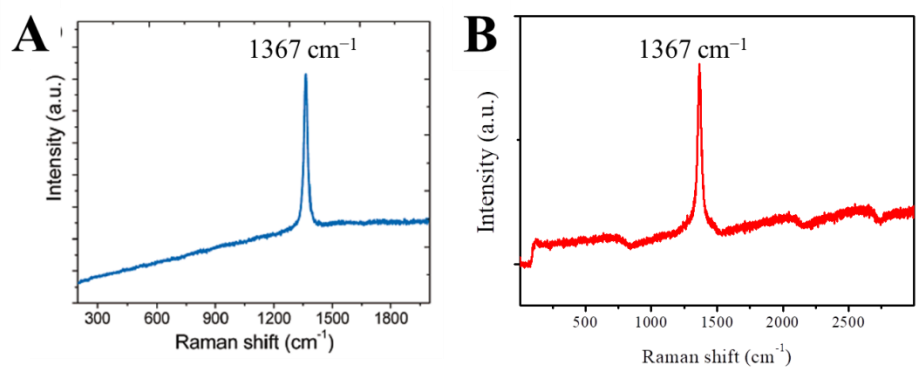


Figure 1.31*(A) Raman spectra of BNNTs reported by Lee* et al. *[140] and (B) Raman spectra of BNNTs synthesised for this study.*

1.4.5 Theoretical approach

1.4.5.1 *Ab initio* theory

In theoretical chemistry, the properties and behaviour of atoms and molecules are typically investigated using *ab initio* quantum chemistry, the theory that serves as the foundation of quantum mechanics [141-143]. *Ab initio* theory is based on a postulate of quantum mechanics that holds that wavefunction Ψ fully describes the state of a system (atoms or molecules) dependent on time, following the Schrödinger equation

$$i\hbar \frac{\partial \Psi}{\partial t} = H\Psi \qquad \text{(equation 1.1)}$$

introduced by Erwin Schrödinger [144], where H is the Hamiltonian operator that corresponds to the total energy of the system. The equation can be separated into time-dependent and time-independent, which is then rewritten as:

$$H\Psi = E\Psi \qquad \text{(equation 1.2)}$$

However, this equation is only limited to simple systems and cannot be solved analytically for larger systems. Thus, the Born-Oppenheimer approximation [145, 146] was proposed, which states that electronic and nuclear motions can be separated due to the difference in mass between the electrons and the nuclei that leads to the calculation of the electronic energy for the fixed nuclear positions.

According to Wolfgang Pauli [147], the wavefunction describing the electrons must be antisymmetric with respect to the interchange of any pair of electrons. This means that the wavefunction must change sign when two electrons are exchanged. In order to

satisfy this condition, a linear combination of Slater determinants Ψ_{SD} is applied to approximate the wavefunction Ψ

$$\Psi_{SD} = \frac{1}{\sqrt{n!}} \begin{vmatrix} \psi_1(1) & \psi_2(1) & \cdots & \psi_n(1) \\ \psi_1(2) & \psi_2(2) & \cdots & \psi_n(2) \\ \vdots & \vdots & \ddots & \vdots \\ \psi_1(n) & \psi_2(n) & \cdots & \psi_n(n) \end{vmatrix}$$

(equation 1.3)

where ψ_i are orbitals (single-electron wavefunctions), and n is the total number of electrons. Although the exact electronic wavefunction is given by an infinite sum of Ψ_{SD}, a further approximation is made in which only one determinant is used: the Hartree-Fock method, in which instead of explicit electron-electron repulsion, an average effect is taken into account. Utilising the variational principle, the set of orbitals ψ_i that give the most accurate total wavefunction Ψ_{SD} can be determined, corresponding to the Ψ_{SD} associated with the lowest energy. This improves the basis set, or the set of functions used to describe the orbitals in the Hartree-Fock method. It also leads to an energy value that is higher than the exact energy value, a difference that is compensated by a limiting value called the Hartree-Fock limit. In practice, the orbitals ψ_i are approximated by a linear combination of basis functions φ_j:

$$\psi_i = \sum_j C_{ji}\varphi_j$$

(equation 1.4)

Overall, solving the Schrödinger equation using the Hartree-Fock approximation involves finding a set of coefficients c_{ji} that minimises the energy of the electronic system. The basis functions φ_j must be selected such that the wavefunction approaches the Hartree-

Fock limit as closely as it can. A part of the energy being higher than the exact energy of the system is due to the approximation by a single determinant wavefunction $\Psi_{SD,}$ which does not take into consideration the Coulomb correlation that is the interaction of electrons in the electronic structure of a quantum system. Thus, to improve the calculation of the energies and molecular geometry, the Coulomb correction is subsequently applied.

Generally, the smaller the system being investigated, the greater the accuracy of *ab initio* calculations. Using this method to investigate large systems therefore requires very high computational resources, such as enormous amounts of computer CPU time and memory and disk space. To put this in perspective, the Hartree-Fock method formally scales as N^4, where N is the number of the basis function. Hence, a calculation ten times as big takes ten thousand times longer to complete with correlated calculations generally taking even more time.

1.4.5.2 Density Functional Theory (DFT)

In answer to the limitations and high demand for computing resources of the *ab initio* method, a more efficient alternative is offered by the density functional theory (DFT) [148]. The DFT method is founded on the premise that the energy of a molecule can be determined from the electron density instead of a wavefunction as presented by Hohenberg and Kohn [149]. Thus, the energy is a functional of the electron density following the equation

$$E = E[\rho] \qquad \text{(equation 1.5)}$$

This was further developed by Kohn and Sham with the postulate that a reference of N non-interacting electrons move with an effective local external potential, $\upsilon S(r)$, such that its density, $\rho S(r)$, is equal to the exact density, $\rho(r)$, of the interacting electron system [150]. By construction, the density of this non-interacting system equals the real, interacting system expressed by the equation

$$E[\rho(r)] = T_s[\rho(r)] + E_n[\rho(r)] + E_c[\rho(r)] + E_{XC}[\rho(r)] \qquad \text{(equation 1.6)}$$

where $T_S[\rho(r)]$ represents the kinetic energy of the electrons of the non-interacting reference system, $E_n[\rho(r)]$ is the electrostatic attraction between the electrons and the nuclei, and $E_C[\rho(r)]$ is the classical Coulomb repulsion of the electronic cloud with itself. $E_{XC}[\rho(r)]$ is the so-called exchange-correlation energy, which not only accounts for the self-interaction correction exchange and Coulomb correlation between electrons, but also includes a correction for the fact that $TS[\rho(r)]$ differs from the exact kinetic energy $T[\rho(r)]$. The exact electron density is then expressed as a linear combination of the Kohn-Sham orbital densities

$$\rho(r) = \sum_i |\phi_i|^2 \qquad \text{(equation 1.7)}$$

The orbitals ϕ_i are obtained from the one-electron Kohn-Sham equation

$$h_{eff}\phi_i = \varepsilon_i\phi_i = [\tfrac{1}{2}\nabla^2 + \upsilon_S(r)]\,\phi_i \qquad \text{(equation 1.8)}$$

The Kohn-Sham potential $\upsilon s(r)$, which the reference electron experiences, comprises the attractive potential, $\upsilon_{ne}(r)$, of the nuclei, and the classical Coulomb

repulsion, $\upsilon_C[\rho(r)]$, with the electron density, $\rho(r)$, as well as the self-interaction correction and all exchange correlation effects contained in the so-called exchange-correlation potential, $\upsilon_{XC}[\rho(r)]$. The exchange-correlation potential is not known exactly and is dealt with as the functional derivative f $E_{xc}[\rho]$ with respect to ρ. The terms υ_C and υ_{XC} are dependent on the density of the system being calculated, and is resolved by using the self-consistent field (SCF) procedure, where a 'guess' is made for the density to obtain the potential υ and solve the Kohn-Sham equations. This results in a set of orbitals ϕ_i from which a better density can be constructed using equation 1.7 that is then used as the new 'guess' density. This process repeats until the density 'converges' or equals the previous iterations, and this results in the Kohn-Sham orbitals for which the energy reaches its lowest value following equation 1.7 and 1.8.

For the exchange-correlation potential, $\upsilon_{XC}[\rho(r)]$, its exact form is not known and is dealt with by developing approximations. Currently in DFT, the main types of functionals that approximate the exchange-correlation potential are local density approximation (LDA), generalized gradient approximation (GGA), meta-GGA, and hybrid DFT methods. In this thesis, most DFT calculations were carried out using the Becke [151] functional for exchange and the Perdew [152] functional for correlation.

Chapter 2

Synthesis and growth mechanism of BNNTs

This chapter contributes to our fundamental understanding of the growth mechanism of boron nitride nanotubes (BNNTs) by investigating the evolution of the catalyst droplets during BNNT synthesis, which is found to follow a tip-growth mechanism in chemical vapour deposition (CVD). Energy-dispersive X-ray spectroscopy (EDX) and X-ray photoelectron (XPS) depth profiling show that the gaseous species generated from the powder precursor, boron and magnesium oxide, deposit a thin film of magnesium borate on the surface of the target substrate. Thermal dewetting enables the transformation of the thin film into droplets that serve as a catalyst for the formation of BNNTs.

2.1 Introduction

The concept of chemical vapour deposition (CVD) is schematically illustrated in Figure 2.1. Here, the reactants are transported by convection and diffusion to the reaction zone, where the energy supply drives the occurrence of gas-phase reactions. The reactants are then transported to the surface of the target substrate. Adsorption happens chemically and/or physically. On the surface of the target substrate, further reactions occur that lead to material formation together with the desorption of volatile by-products. Finally, the by-products are carried away from the reaction zone by convective and diffusive transportation.

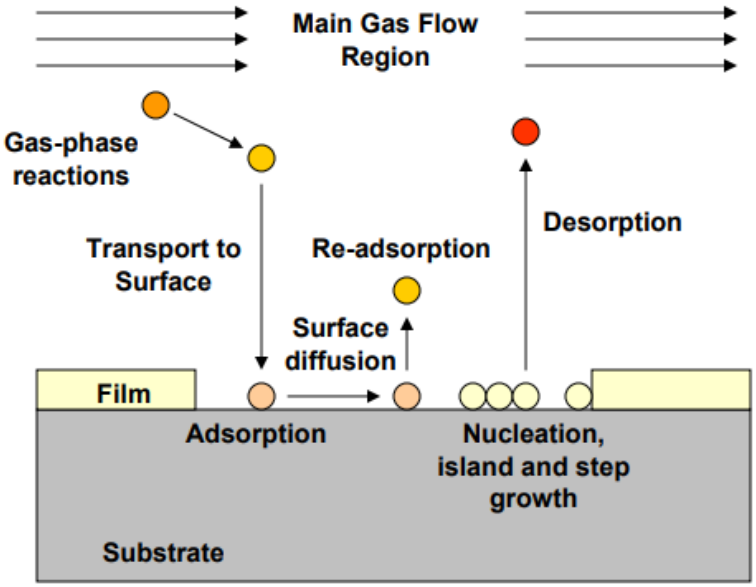


Figure 2.1 *Schematic illustration of the fundamental concept of the chemical vapour deposition (CVD) method.*

Different experimental CVD setups have been developed and used for the synthesis of BNNTs. However, early experimental setups involved complex procedures [10], hazardous chemicals [6], or very high temperatures [9] which led other researchers to look for better alternatives. The subsequent development of the boron oxide chemical vapour deposition (BOCVD) technique [11, 12] resulted in significant progress and allowed other

researchers to reproduce the experimental setup. However, the difficulty of controlling the temperature particularly in the growth area was found to be the drawback, since the pioneering experimental setup involved the use of induction heating. Efforts were therefore made to design an experimental setup that would enable the precise control of growth conditions [13, 16, 140].

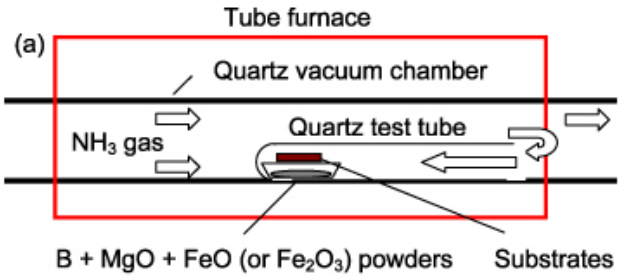


Figure 2.2 *Schematic illustration of the experimental setup utilising a one end closed quartz tube by Lee* et al. *[13].*

In a study by Lee *et al.* [13], growth conditions were controlled by using a conventional horizontal tube furnace with a quartz tube vacuum chamber, inside which was placed a quartz tube closed at one end. The precursors were placed in the closed-end tube located in the middle of the working furnace (setup presented in Figure 2.2). The authors claimed that the tube with one end closed was vital to the synthesis of BNNTs, and that no BNNTs were achieved by using an open-end tube since the trapping of the gaseous precursor was necessary for synthesis to occur. However, this claim is not in agreement with the results reported by Lourie [6] and Pakdel [16], which show that the synthesis of BNNTs is achievable even without using an closed-end tube. The contradicting ideas on whether or not to use a closed-end tube in the experimental setup are an indication of the many questions that are still left unanswered with regard to the synthesis of BNNTs. Thus, to understand the growth mechanism of BNNTs, a simplified method of BOCVD was utilised by using amorphous boron and magnesium oxide powder precursor. Ammonia was

used as nitrogen source. The structure and composition of the synthesised product were investigated using scanning electron microscopy (SEM), transmission electron microscopy (TEM), energy-dispersive x-ray spectroscopy (EDX), and energy electron loss spectroscopy (EELS). The growth of the BNNTs was studied by varying the reaction time, and was characterised by SEM and EDX, which made it possible to confirm the formation of the catalyst droplets responsible for the nanotubular structure. The evolution of the catalyst droplet was examined using Thermal gravimetric analysis (TGA) and X-ray photoelectron spectroscopy (XPS).

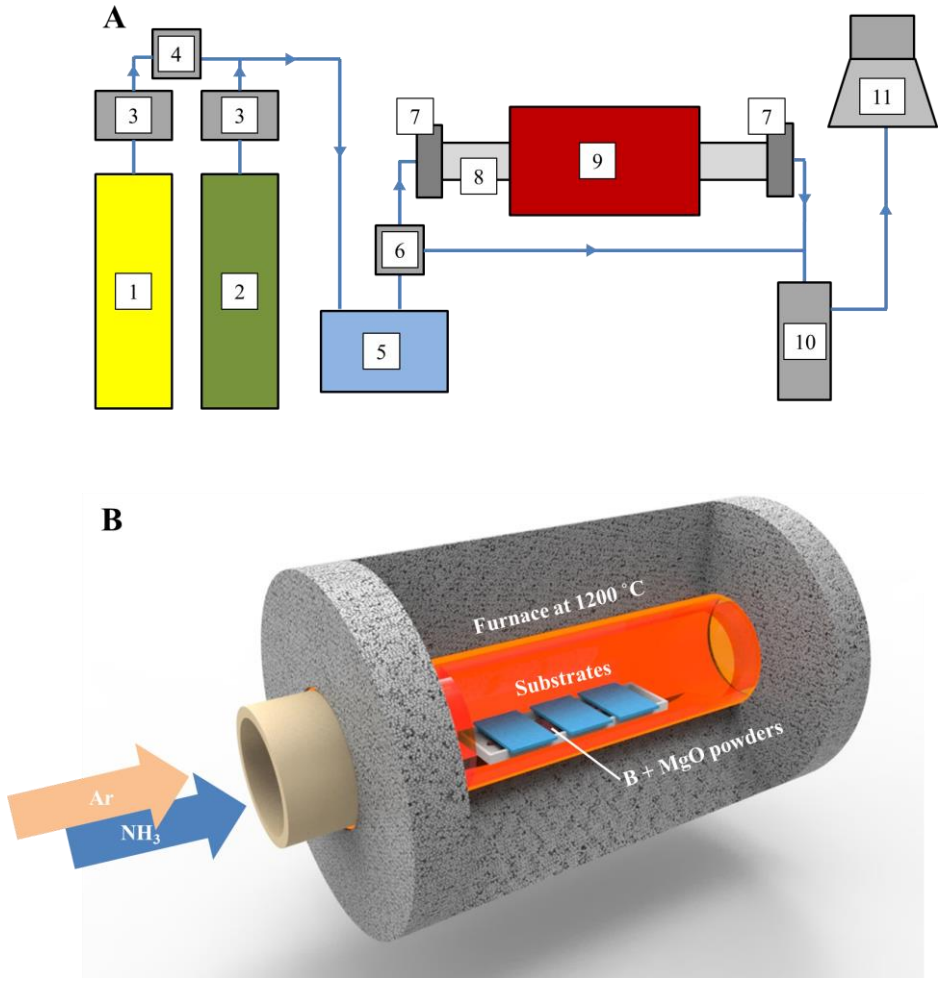


Figure 2.3 *(A) Schematic flow of the CVD setup: (1) Ammonia and (2) argon gas cylinders, (3) Flow regulator, (4) Flashback arrester (in case of flammable gases), (5) Mass flow controller, (6) Manual (safety) flow control switch, (7) Stainless steel flange with O-ring, (8) Alumina tube, (9) Tube furnace heating element and thermocouple, (10) Bubbler filled with water, and (11) Gas outlet. (B) Detailed experimental setup showing the B + MgO powder precursor and substrate inside the furnace for the synthesis of BNNTs.*

2.2 Materials and methods

2.2.1 CVD synthesis of BNNTs

The CVD setup in this work is schematically presented in Figure 2.3A. The setup used a tube furnace (TSG15, Elite) with an alumina tube (ALM 5848, outer diameter 60mm x inner diameter 50 mm x 1200 mm, Almath) connected to the gas inlets controlled by a mass flow controller (Mass-Flo®, MKS instruments UK ltd). The other end of the alumina tube was connected to a bubbler filled with water to prevent back flow, filter outgoing gases, and provide visual checking to ensure the absence of leaks in the setup. Inside the alumina tube shown in Figure 2.3B, a 0.5-g mixture of amorphous boron (≥95% boron, Sigma-Aldrich 15580) and magnesium oxide (≥99.99%, Sigma-Aldrich 529699) powder precursor with molar ratio of 1:1 was contained in an alumina boat and SiO_2 substrates were placed on top. Prior to the heating of the furnace, 1 slm of argon (99.998% argon, BOC) for 10 mins was used to flush the system. The rector furnace was heated up to 1,200 ˚C with 300 sccm argon flow. Upon reaching 1,200 ˚C, 66.67% of ammonia in Ar was then introduced to the system with a total flow rate of 300 sccm in 1 hr. Ammonia was diluted with argon to avoid generating a high level of H_2 gas and keep the reaction safe. Reaction time was varied from 10 mins to 1 hr and temperatures from 1,100 to 1,250 °C in order to investigate the growth mechanism of BNNTs. After reaction, the furnace was cooled under Ar flow and the setup was carefully removed for characterisation.

2.2.2 Characterisation

A JEOL-840F SEM was used to investigate the morphology of the as-synthesised product. Prior to SEM studies, the synthesised products were coated with a 4-nm layer of platinum using a 208HR High Resolution Sputter Coater. For the study of the individual nanotubes and their internal structures, a JEOL-3000F TEM operated at 300 kV was used, and the sample was prepared by drop cast using acetone on copper TEM grids. Zeiss Merlin Energy-dispersive X-ray spectroscopy was used to perform EDX while a JEOL ARM-200F operated by Dr Ian Griffin was used to conduct EELS using the samples prepared from TEM studies. Prior to EELS characterisation, the samples were baked at 70 °C for at least 4 hrs. Raman spectra were obtained using a LabRam Aramis confocal Raman microscope equipped with a 532-nm green laser. No prior treatments were done on the product samples for Raman spectroscopy studies. TGA data were acquired using an STA 449 F1 Jupiter NETSCH under air and argon atmospheres. X-ray photoelectron spectroscopy experiments were carried out using a Thermo Scientific K Alpha spectrometer equipped with monochromated X-rays and ion profiling with a spatial resolution of 0.30 microns.

2.3 Results and discussion

2.3.1 Structure and composition analysis

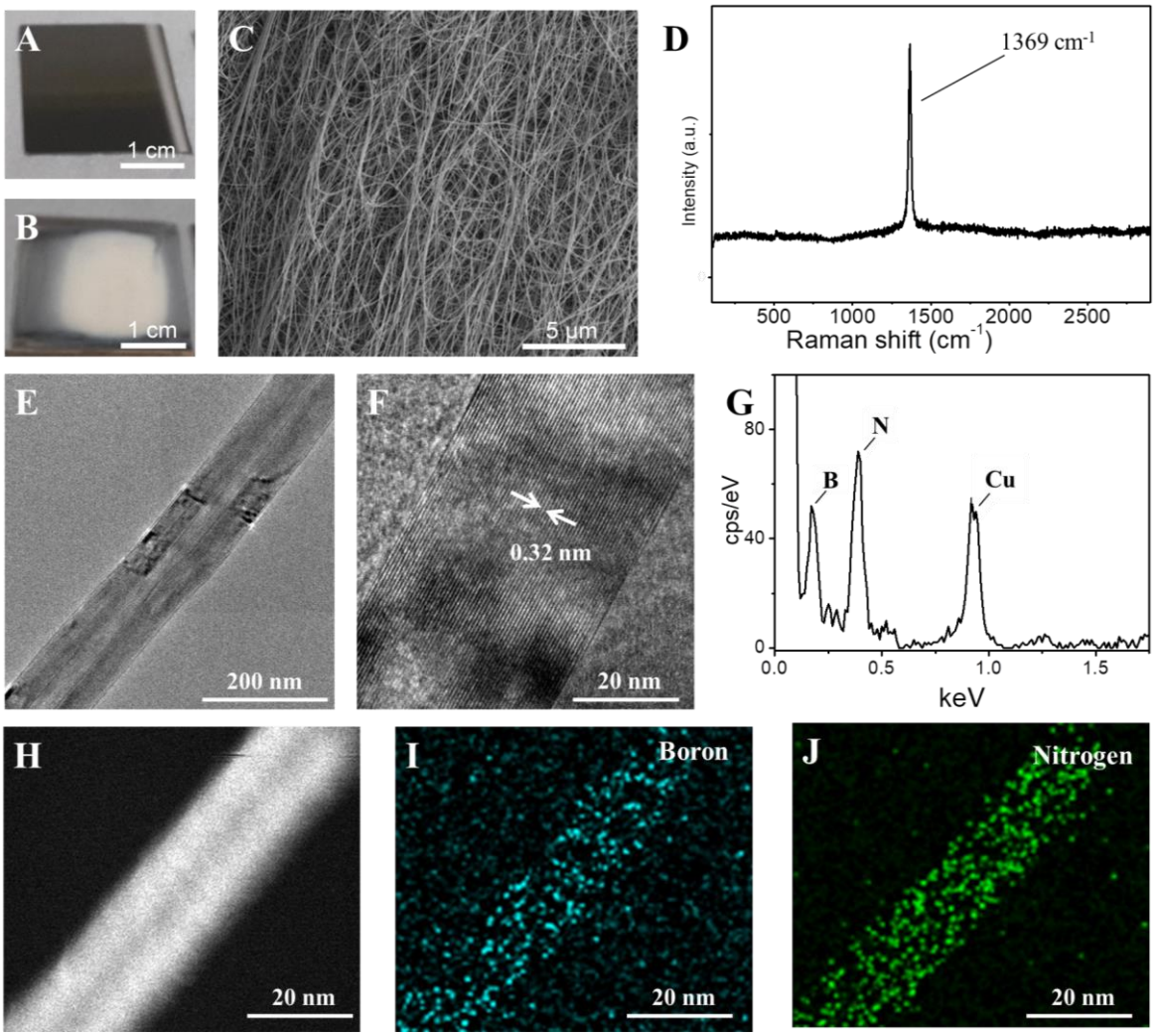


Figure 2.4 *Digital photographs of the SiO_2 wafer (A) before and (B) after synthesis. (C) SEM image and (D) Raman spectra of the white deposit on the substrate. (E) TEM image of the synthesised product and (F) HRTEM image of the edge showing lattice spacing of 0.32 nm. (G) EDX spectrum of a single BNNT in which boron, nitrogen, and copper are detected. EDX elemental mapping of a single as-synthesised nanotube showing (H) STEM image of region of interest (ROI), (I) boron, and (J) nitrogen. EDX acquisition with the help of Pablo Quijano Velasco.*

After the synthesis reaction, white deposits were observed on the surface of the target substrate as seen from the photograph image of the SiO_2 wafer before and after the reaction (Figure 2.4A and B, respectively). SEM analysis revealed these white deposits to have the fibre-like morphologies shown in Figure 2.4C. There were no visible side

products such as nanocones, and the diameter of these fibres measured ca. 130 nm (See Figure A.1 in the Appendix). The Raman spectra (Figure 2.4D) of the synthesised white deposit fibres showed a dominant peak located at 1369 cm^{-1}, which is attributed to the E_{2g} mode and is known to be the in-plane BN vibrational mode within the BN plane. In comparison with the Raman peak of bulk h-BN located at 1366 cm^{-1}, the peak of this as-synthesised product was slightly blue-shifted due to the multi-walled characteristic of the BNNT [137, 153].

Figure 2.4E shows the TEM image of the synthesised fibre on which can be seen cylindrical nanotube structures having clean surfaces and an average inner diameter of about 30 nm. Shown in Figure 2.4F is the high-resolution transmission electron microscopy (HRTEM) image of a representative wall part of a nanotube exhibiting well-defined lattice fringes that show the perfect crystalline structure of the nanotube. The interlayer spacing was measured to be 0.32 nm, which corresponds to the (002) plane of h-BN crystal. The interlayer spacing has a 8.5% error realized from the magnification error of the TEM and standard deviation, 5.8% and 6.2%, respectively. The magnification error of the TEM falls in good agreement to the expected error range that is 5 % to 10 % [154] that was acquired by obtaining the d-spacing of the carbon lacey using the DIFPACK plug-in in the programme DigitalMicrograph® and compared to the amorphous carbon d-spacing [155, 156] with values of 0.36 and 0.34 nm, respectively. The EDX spectrum (Figure 2.4G) showed peaks assigned to boron, nitrogen, and copper located at 0.183, 0.392, and 0.930 eV, respectively. No carbon was present, as indicated by the absence of a carbon peak located at 0.277 eV, implying that the synthesised nanotube was purely BN. The copper signal acquired from the analysis came from the TEM copper grid. Figure 2.4H depicts the EDX elemental mapping analysis showing that boron and nitrogen are uniformly distributed along and across the nanotube (Figure 2.4I and J, respectively).

These results demonstrate that the use of amorphous boron and magnesium oxide as powder precursor without adding a closed-end tube in the experimental setup produces BNNTs of a high abundance level covering the 3x3 cm target substrate SiO_2 surface.

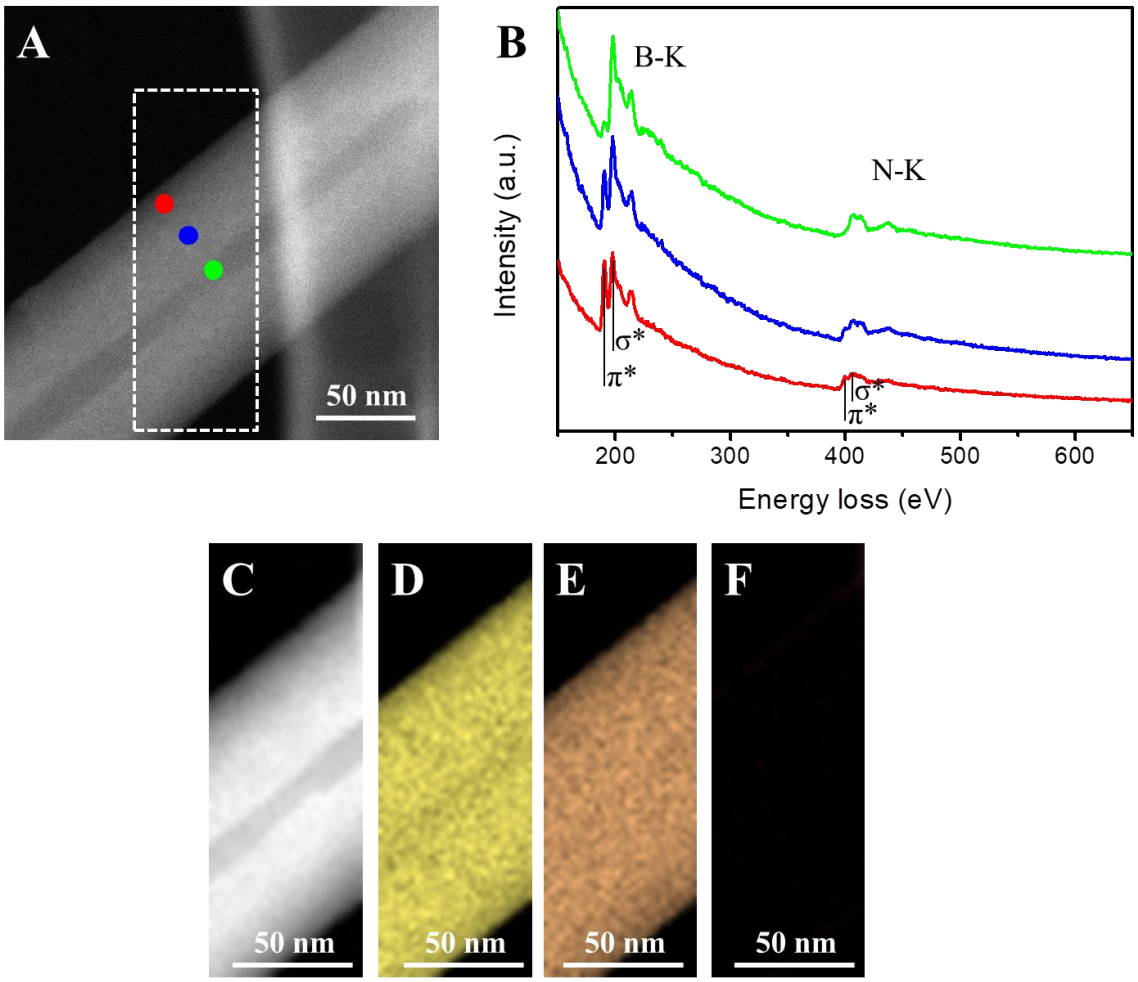


Figure 2.5 *(A) ADF-STEM image of BNNT, dashed square indicates the ROI for EELS. (B) EELS spectra acquired from red, blue, and green spots indicated in panel A. (C) High-loss EELS image and elemental mapping of (D) boron, (E) nitrogen, and (F) carbon. EELS acquisition with the help of Dr Ian Griffiths.*

A detailed investigation of the composition of the synthesised BNNTs was carried out by EELS. Figure 2.5A shows the annular dark field scanning transmission electron microscopy (ADF-STEM) image of the selected BNNT where EELS spectra were taken from the red, blue, and green spots presented in Figure 2.5B, while the white dashed

square indicates the region for EELS elemental mapping analysis. All of the spectra taken from different spots of the nanotube showed K-edges of boron and nitrogen at 188 and 401 eV, respectively [44, 157]. No C-K edge at 288 eV was observed in this spectrum, indicating that there was no carbon incorporated in the synthesised product. The clear peaks of π^* and σ^* on the K-edge of B and N revealed the hybridised sp^2-bonded B and N atoms in the h-BN layer. The evolution of the weight ratio between the π^* and σ^* peaks as the probe scans from the edge to the centre of the nanotube, as depicted clearly in Figure A.2 in Appendix, is characteristic of a cylindrical structure as reported by Stephan *et al.* [158], where the orientation of the electron beam with respect to the h-BN layers varies continuously from parallel to perpendicular. The calculated B/N ratios acquired by using EELSMODEL [131, 133] and values are as follows: red spot = 1.011± 0.02, blue spot = 1.013 ± 0.02, and green spot = 1.013 ± 0.02. The high-loss EELS image spectrum is presented in Figure 2.5C. The results of the adsorption mapping with respect to the K-edge values of boron (Figure 2.5D), nitrogen (Figure 2.5E), and carbon (Figure 2.5F) clearly show the intensity signals of boron and nitrogen and the absence of a carbon signal. The EELS results confirm that there was successful synthesis of high-quality BNNTs, judging from their pure BN composition and the clear distinction of the π^* and σ^* peaks of boron and nitrogen coming from the sp^2 hybridisation BN bond.

2.3.2 Particle on tip investigation

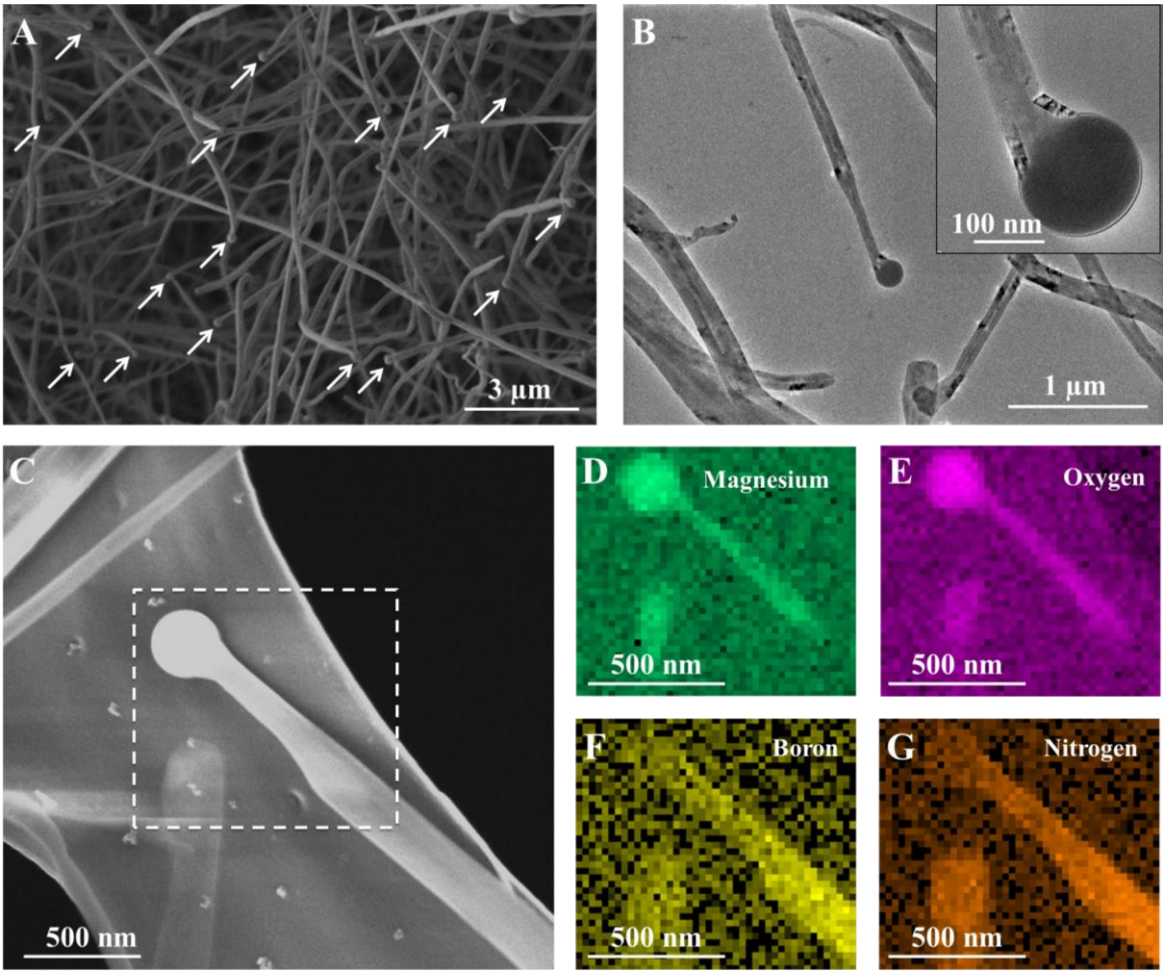


Figure 2.6 (*A) SEM image of synthesised BNNT showing the spherical tips of the nanotubes. (B) TEM image of a single BNNT with the spherical structure. Inset shows HRTEM image of the tip particle. EDX analysis of the particle on the tip of the nanotube. (C) STEM image emphasizing the region of interest. Elemental mapping under the selected region of interest showing (D) magnesium, (E) oxygen, (F) boron, and (G) nitrogen.*

As indicated by the white arrows in Figure 2.6A, the synthesised BNNTs possessed spherical tip structures. The TEM image in Figure 2.6B shows that these nanospheres were not empty, as can clearly be seen in the inset, in contrast to the tips observed by Lourie *et al.* [6]. As is obvious from the inset, the spherical tip contained a particle. The TEM analysis further verifies that the diameter of the nanotube is not dependent on the size of this particle. Furthermore, this particle seems to be responsible for the formation of the BNNTs, and can therefore determine the nucleation and growth of the material. The EDX

elemental mapping shown in Figure 2.6C indicates that the particle on the tip was mainly composed of magnesium (Figure 2.6D) and oxygen (Figure 2.6E). Comparable composition intensities of boron and nitrogen were observed, as seen in Figure 2.6F and G, respectively. The top surface of the nanoparticle had less boron and nitrogen content, which demonstrates that the spherical nanoparticle was open for new precursor reactions. These results strongly prove the occurrence of a tip-growth mechanism of BNNT synthesis using the BOCVD method, which is in good agreement with the growth mechanisms speculated in the literature [7, 11, 13, 16].

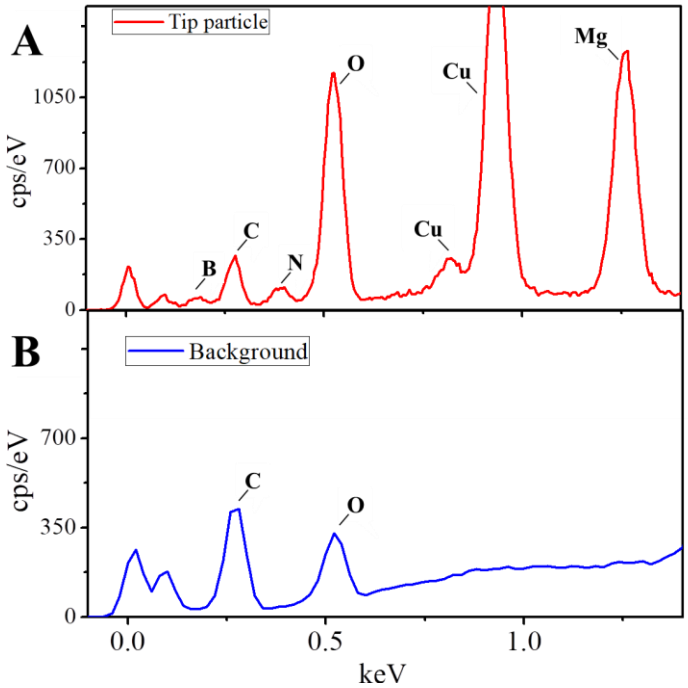


Figure 2.7 *EDX spectra of (A) particle on the tip of the nanotube and (B) background showing the corresponding elements being detected.*

Figure 2.7 shows that the EDX spectra acquired from the tip particle had a B:N ratio of 0.93 ± 0.55 based on the atomic percent, confirming the presence of a thin BN coating on the surface of the spherical nanoparticle. The calculated atomic percentage of Mg:O ratio is 1.34 ± 0.35 that may suggest the presence of MgO; it should be noted, however, that MgO has a much higher melting point than the synthesis temperature. It is

obvious therefore, that the spherical structure could not have been formed directly from MgO. Thus, the tip particle that is responsible for the formation of the nanotubular structure must have transformed from a different state beforehand, such as from a liquid to a solid state.

2.3.3 Evolution of catalyst droplet

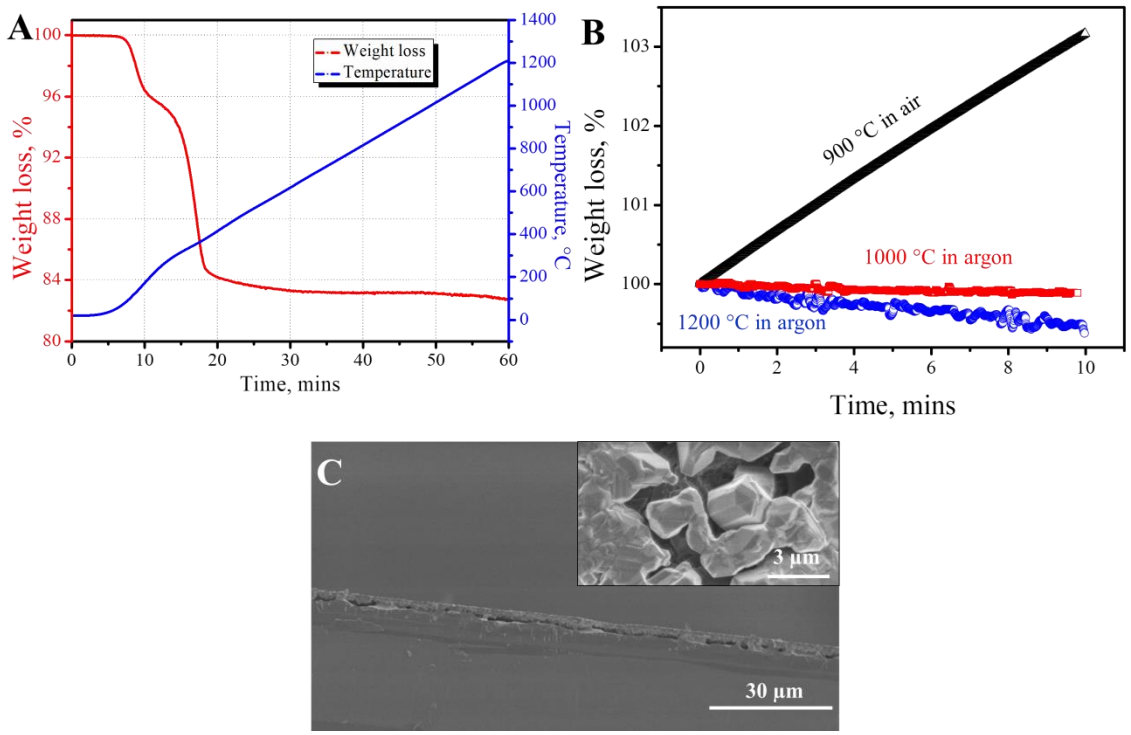


Figure 2.8 *TGA plot of the powder precursor (A) from 50 to 1,200 °C, and (B) temperature hold for 10 mins. (C) Cross-section SEM images of deposited material on the surface of the SiO2 target substrate. Inset is the top view. TGA data acquisition with the help of Sabin Sulzer.*

According to Searcy *et al.* [66], the mixture of B with MgO produces B_2O_2 and Mg gases. To verify this, TGA was carried out in order to study the transformation of the powder precursor from solid to gas, as shown in Figure 2.8A. A massive drop in weight was observed within 20 mins at a temperature of 400 °C, which can be accounted for by the evaporation of moisture in the powder precursor. The delay of moisture evaporation was due to the adjustments being made by the TGA in the first 15 mins such as the

stabilisation of heating rate from 30 to 20 °C/min. The weight stabilised at the temperature range of 600 to 1,000 °C and started to decrease at 1,000 °C. The loss of weight may have been due to the production of gaseous species, in this case, B_2O_2 and Mg. Figure 2.8B shows the powder precursor holding the temperature at 900 °C in air (black plot), 1,000 °C in argon (red plot), and 1,200°C in argon (blue plot). Under air atmosphere, a significant increase in the weight was observed, verifying oxidation. This oxidation is not ideal in the synthesis of BNNTs since it passivates the surface of the powder precursor. This hinders the generation of the gaseous intermediate species, i.e. B_2O_2 and Mg gases, and eventually blocks the synthesis of BNNTs. Under inert atmosphere, production of the gaseous intermediate species increased as the temperature increased, resulting in a 0.7 wt. % loss in 10 mins at 1,200 °C. Cross-section SEM analysis confirmed that a material had been deposited uniformly along the surface of the SiO_2 wafer target substrate, as can be seen in Figure 2.8C, where the inset shows the top view of the deposited material. It can be inferred from this observation that the catalyst may have initially had a thin film structure, but later became a spherical droplet to satisfy the tip particle in the formation of BNNTs.

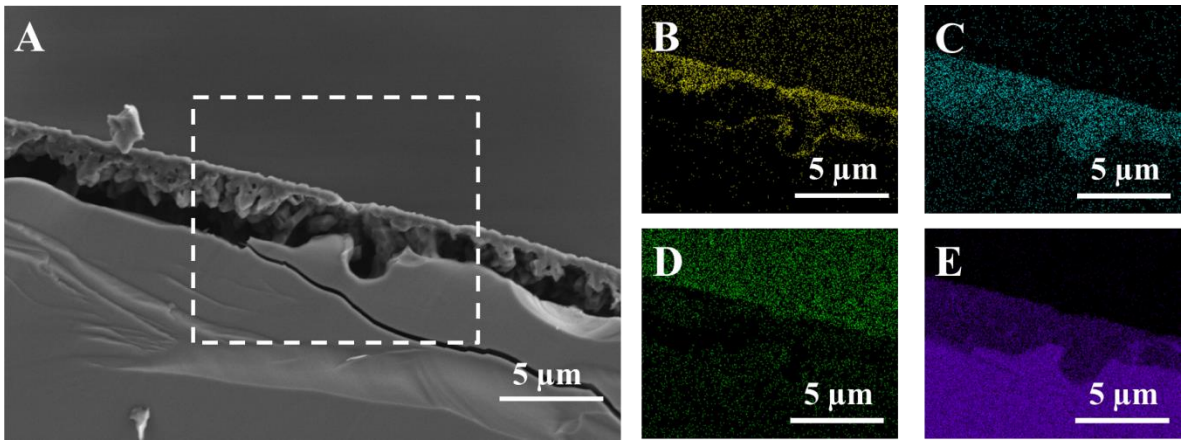


Figure 2.9 *(A) Cross-section EDX elemental mapping of the deposited thin film with detected elements of (B) boron, (C) magnesium, (D) oxygen, and (E) silicon.*

Figure 2.9A shows the cross-section EDX analysis of the deposited thin film. EDX elemental mapping detected elements of boron (Figure 2.9B), magnesium (Figure 2.9C), oxygen (Figure 2.9D), and silicon (Figure 2.9E). A clear distinction can be observed in the intensities of magnesium, boron, and silicon, where magnesium and boron were in the area of the fabricated thin film while silicon was on the SiO_2 substrate. Oxygen is shown to be scattered on the acquired mapping, although a higher intensity was observed in the vacuum region, which may have come from the sample holder.

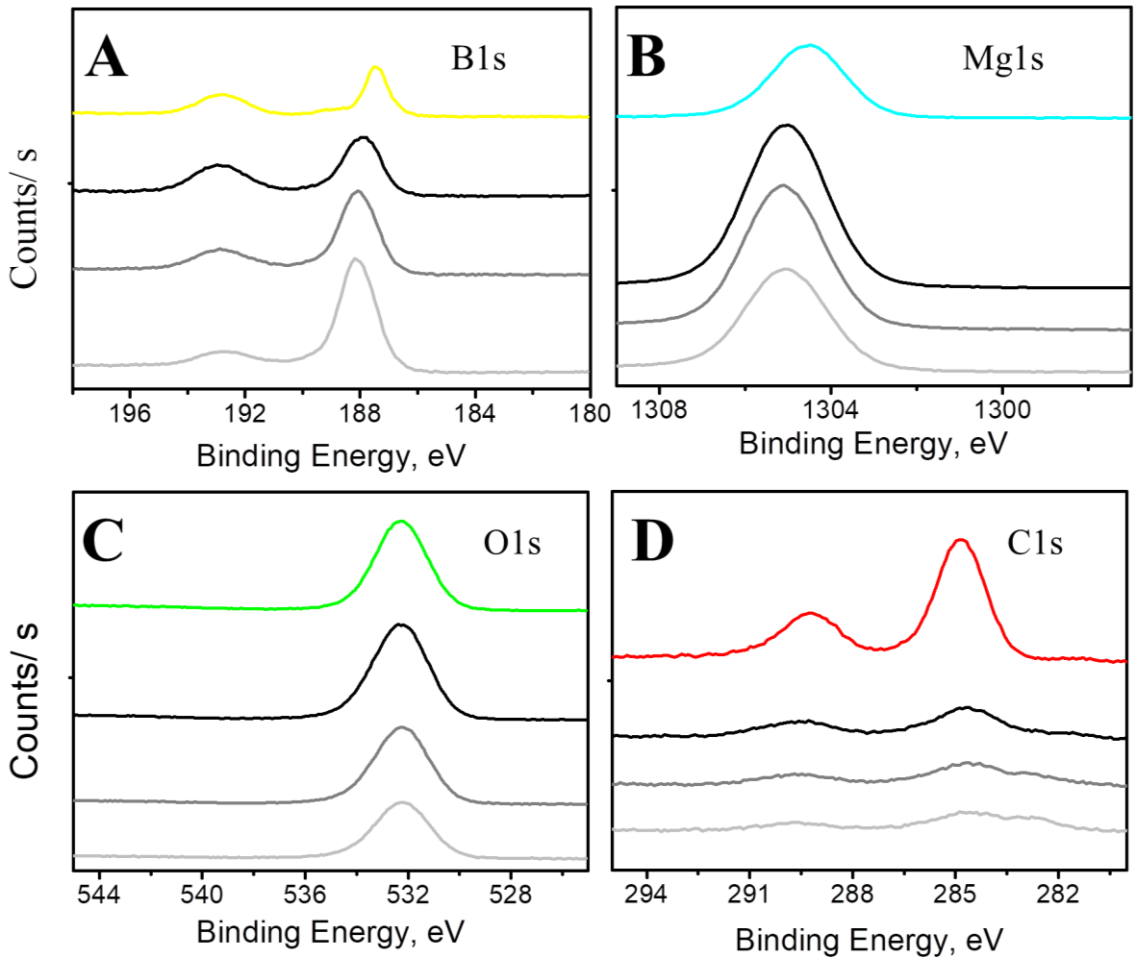


Figure 2.10 *XPS depth profiling of (A) B1s, (B) Mg1s, (C) O1s, and (D) C1s showing the behaviour during ion beam etching of 10 secs. (black spectra), 30 secs. (grey spectra), and 60 secs. (light grey spectra). XPS depth profiling acquisition with the help of Dr Phil Holdway.*

XPS depth profiling provided more detailed insight on the deposited material together with its inner core. The peak behaviour of B1s (Figure 2.10A), Mg1s (Figure 2.10B), O1s (Figure 2.10C), and C1s (Figure 2.10D) was monitored under XPS depth profiling corresponding to 10 secs (black spectra), 30 secs (grey), and 60 secs (light grey). Raw XPS data are presented in Figure A.3 in the Appendix.

The B1s characteristic showed two peaks, one at a lower energy of 187.43 eV and another at a higher energy of 193 eV, which are attributed to elemental boron and boron trioxide (B_2O_3) [159, 160], respectively. After 60 seconds of ion beam etching, an increase in intensity was observed for the elemental boron peak while a decrease in intensity was seen for the B_2O_3 peak. The Mg1s characteristic showed a peak shift from 1304.29 eV to 1305.11 eV after 10 secs of exposure to the ion beam with an apparent increase in intensity. The position and intensity of the Mg1s peak remained stable after 60 secs of XPS depth profiling. O1s showed a decreasing trend. Two peaks were observed for the C1s feature located at 285.04 eV assigned to metal carbide, and 289 eV assigned to metal carbonate, suggesting the presence of carbon in the deposited material. However, these peaks showed a significant loss of feature after 60 secs of ion beam etching, indicating that the carbon was only on the surface of the deposited material, which may have come from the exposure of the thin film at ambient conditions.

The melting point of magnesium oxide is 2,852 °C, which is not the temperature during the fabrication of the thin film. Thus, evaporation of magnesium oxide from the mixture of the powder precursor (boron and magnesium oxide) did not happen. This is the same case as boron since boron has a melting point of 2,076 °C. Thus the powder precursor underwent phase transformation from solid to gas and deposited on the surface of the SiO_2 substrate located on top of the powder precursor.

With these accumulated results, this work has been able to determine that the deposited material was in the form of magnesium borate, which came from the condensation of the two gases generated *in situ* from the powder precursor. It is therefore important to produce a catalyst droplet that has a lower melting point than the synthesis temperature of 1,200 °C to satisfy the hydrophobic conditions that result in the synthesis of BNNTs.

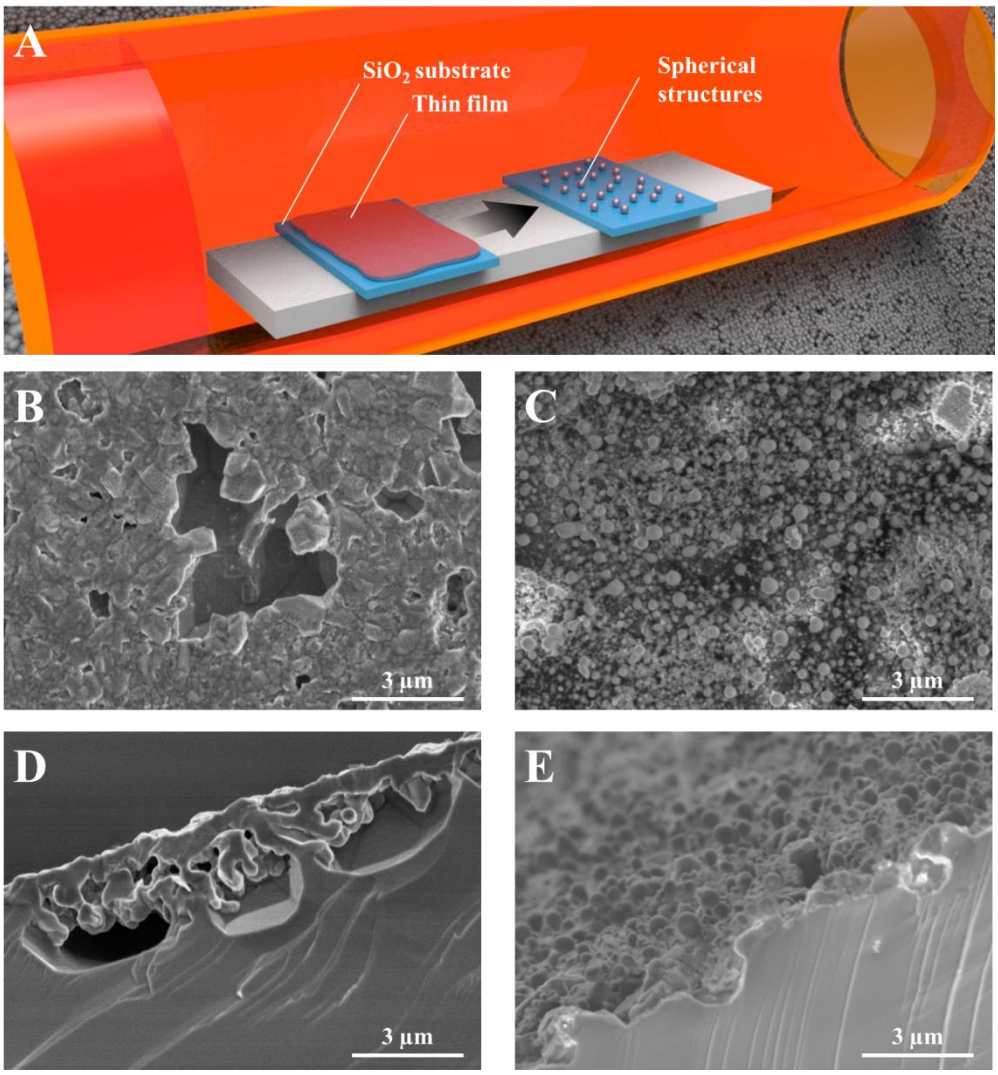


Figure 2.11 *(A) Experimental design to prove conversion of thin film to spherical structures on the target substrate by thermal dewetting. SEM images of the thin film (B) before and (C) after thermal dewetting. (D) and (E) cross-section images, respectively.*

As schematically depicted in Figure 2.11A, the formation of the droplet was studied by subjecting the thin film to high temperature of 1,200 °C. SEM images before and after the thermal dewetting process are shown in Figure 2.11B and C, respectively, indicating the generation of the spherical nanostructure. It can be conjectured that when heated, the magnesium borate molecules in the thin film formed droplets because of the stronger attraction between magnesium borate molecules than between magnesium borate molecules and silicon dioxide molecules in the substrate, meaning that the deposited material on the surface of the substrate was weakly adsorbed. This result is similar to what happens in a hydrophobic condition in a liquid-solid system, in which liquid molecules are more strongly attracted to other liquid molecules than to solid molecules.

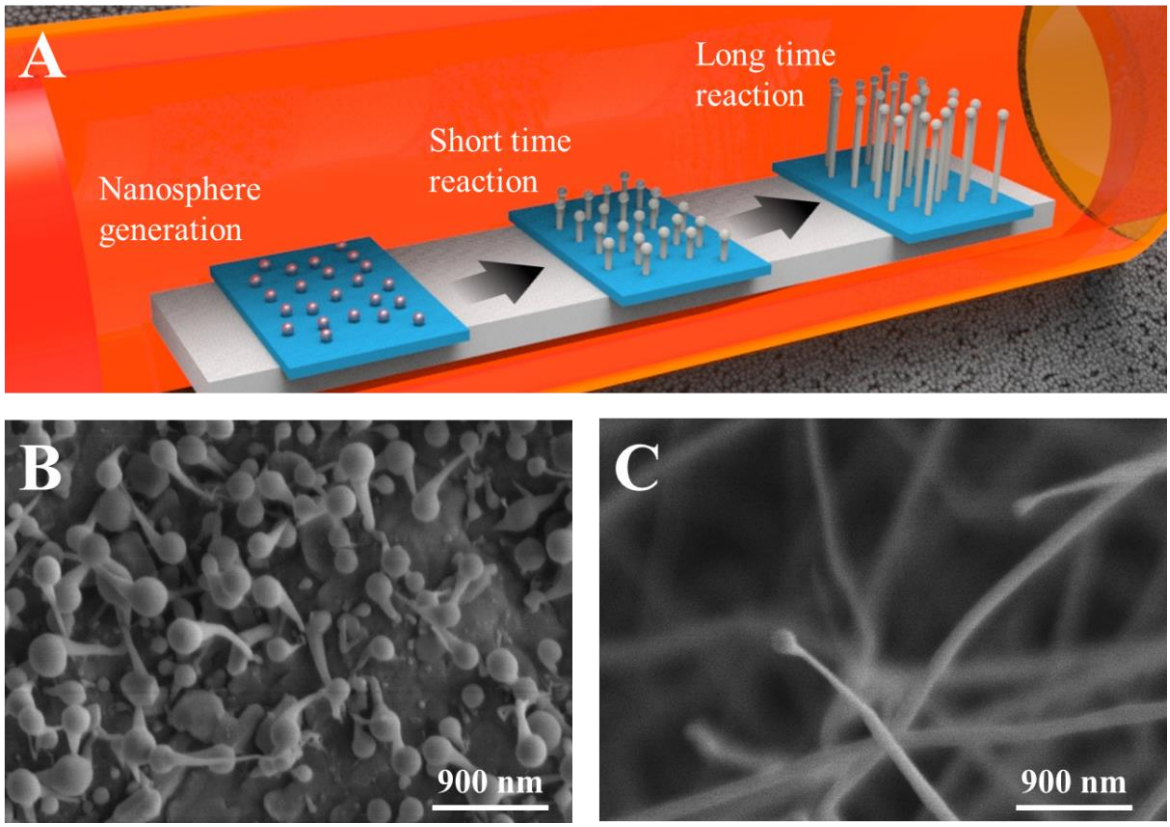


Figure 2.12 *Schematic illustration of (A) the embryonic stage of the growth. SEM images at (B) 10 mins and (C) 60 mins reaction.*

Time variation studies revealed the early stages of growth of BNNTs presented in Figure 2.12. These studies were conducted at 10 mins of ammonia exposure at 1200 °C. SEM images revealed that nanospheres having tail-like structures with average lengths of ca. 538 nm were generated, as shown in Figure 2.12B. Indeed, the interface between the catalyst and the SiO_2 target substrate exhibited weak interaction due to the whole catalyst being lifted off as the BNNTs formed. This confirms that the BNNTs synthesised followed a tip-growth mechanism. A vapour-liquid-solid (VLS) mechanism [15] has been generally accepted as one of the mechanisms of the synthesis of 1D nanomaterials and, so far, this work has proven experimentally the initial growth of BNNTs in a CVD system.

2.3.4 Formation mechanism of BNNTs

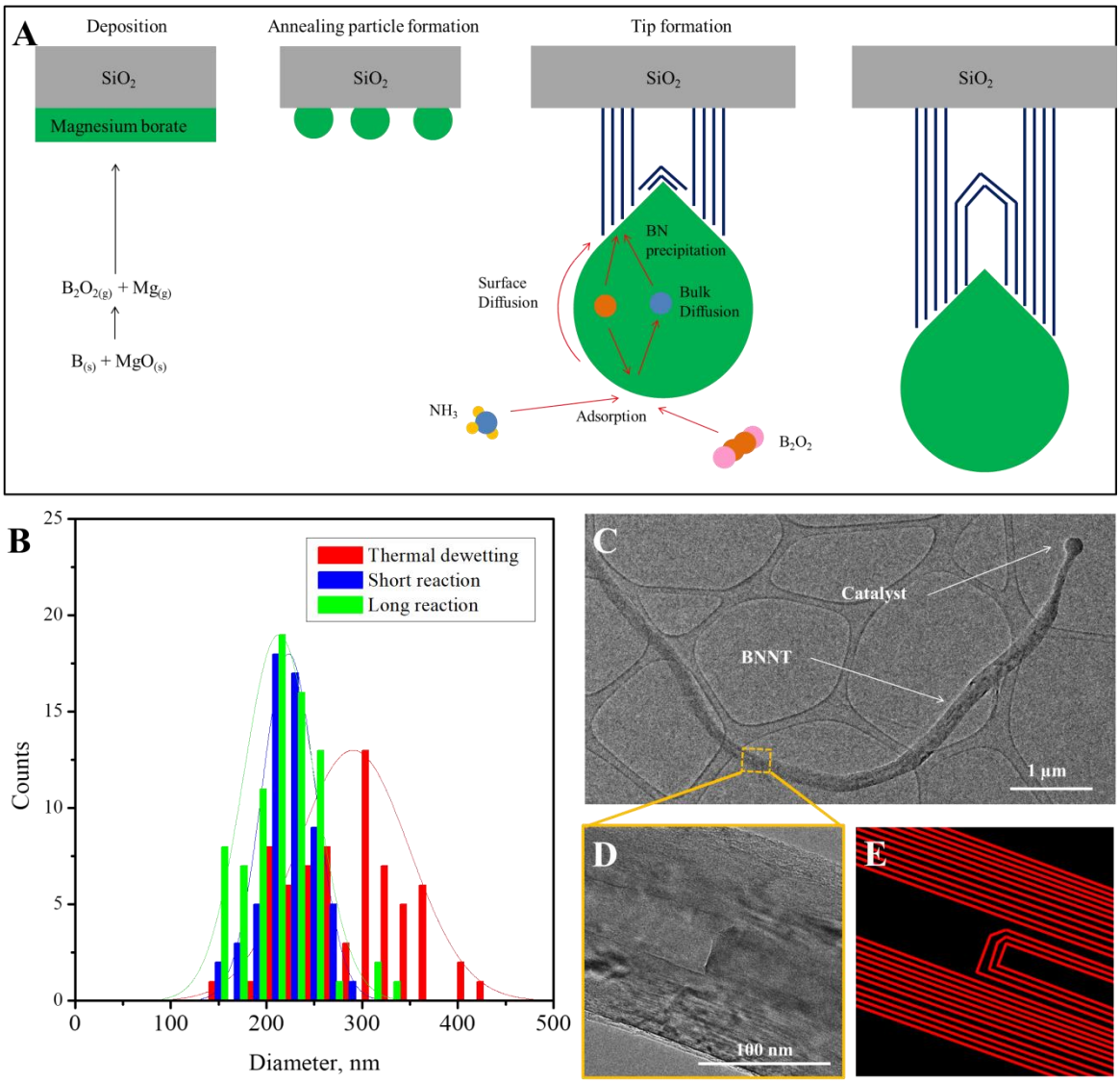


Figure 2.13 *(A) Schematic illustration of the evolution of the catalyst droplet in the synthesis of BNNTs. (B) Diameter distribution of the evolution of the catalyst droplet. (C) TEM image of the synthesised BNNT with respect to the catalyst tip particle. (D) HRTEM image with (E) schematic representation.*

This work confirms the evolution of the catalyst droplets and the mechanism of the synthesis of BNNTs that is schematically illustrated in Figure 2.13A. The mixture of boron and MgO produces gases of B_2O_2 and Mg at 1,200 ˚C. These generated gases are trapped and start to accumulate on the surface of the SiO_2 wafer target substrate, which leads to the deposition of magnesium borate. This thin film of magnesium borate then undergoes

restructuring through thermal dewetting, as indicated by the formation of spherical structures. This result shows that the generated magnesium borate has a lower melting point than the temperature of the reactor chamber. According to the binary phase diagram [161] of MgO-B_2O_3 (Figure A.4 in Appendix), the generated magnesium borate may have taken the form MgB_4O_7. Orthorhombic crystal $Mg_3B_2O_6$ cannot be assigned to the deposited thin film due to its melting point of 1,410 °C [162], which is higher than the synthesis temperature and therefore does not satisfy the thermal dewetting conditions. The same is true for mono- and tri-clinic $Mg_2B_2O_5$, which have melting points of 1,353.18 and 1,360.43 °C respectively [163]. The spherical structure of the catalyst droplet indicates a weak interaction between the thin film and the substrate that closely resembles the interaction that occurs in hydrophobic conditions.

The precipitation of BN takes place once ammonia is introduced in the reaction. During 10 mins of ammonia exposure, the nanospherical structures are revealed to have developed tail-like morphologies. Indeed, the interface between the catalyst and the SiO_2 target substrate exhibits a weak interaction due to the whole catalyst being lifted off from the substrate, thus accommodating the growth of BNNTs.

A decrease in size of the nanospherical particle is observed once the growth of the BNNT is initiated, with a measured value from 290 (±58.97) to 223.25 (±28.23) nm (Figure 2.13B). This shrinkage may have been caused by the diffusion of the boron atoms from the magnesium borate catalyst droplets to the precipitation of BNNTs. The driving force of the diffusion of the boron is from the change of charge on the surface of the magnesium borate once ammonia is adsorbed. This mechanism is in good agreement with the results reported by Li *et al.* [164] showing that a strong electric field is generated upon the adsorption of ammonia on the surface of $Mg_3B_2O_6$. The exposed surface allows further diffusion of the BN species via surface or bulk diffusion, leading to the continuous growth

of the BNNTs, as indicated by the presence of the spherical particle on the tip. A slight decrease in diameter of the tip to 10.84 nm occurs as the growth continues, suggesting a complete diffusion of boron atoms in the bulk magnesium borate resulting in the transformation to magnesium oxide as shown by the tip particle characterisation of the fully grown BNNTs.

The structure of the synthesised nanotubes was investigated with respect to the tip catalyst particle presented in Figure 2.13C. Interestingly, an inner nanotube can be observed in Figure 2.13D. As schematically presented in Figure 2.13E, the inner nanotube shows a cap structure. This cap structure indicates that during the synthesis, the boron and nitrogen precursor diffused in the catalyst droplets which have formed on the bottom surface of the tip particle. BNNT growth is terminated when the supply of ammonia is cut off. It is assumed that the surface of the catalyst is not deactivated, since continuous growth of BNNTs is still observed within three hours of reaction. This work demonstrates that the synthesis of BNNTs is mainly driven by a reduction-oxidation reaction starting from the generation of *in-situ* gases in the B and MgO precursor, and followed by the formation of BNNT from ammonia, B_2O_2, and the catalyst. The synthesis is confirmed to follow a tip-growth mechanism. This work has also been able to capture experimentally the various processes within the VLS mechanism, particularly the evolution of the catalyst droplets formed using the BOCVD method, which leads to the growth of BNNTs.

2.4 Conclusion

This chapter has confirmed the different stages in the nucleation and growth of BNNTs in CVD synthesis by investigating the evolution of the catalyst droplets. At high temperature conditions (1,000-1,200 °C), the mixture of boron and MgO generated B_2O_2 and Mg gases that led to the formation of magnesium borate (MgB_4O_7) on the surface of the target substrate. The 995 °C melting point of the thin film of magnesium borate enabled its transformation into droplets through thermal dewetting. The droplets formed served as a catalyst for the formation of BNNTs. The introduction of ammonia in the reaction induced the boron to diffuse from the droplets of magnesium borate, driven by the strong electric field generated from the adsorption of ammonia on the surface of the substrate [164], which resulted in the conversion of magnesium oxide.

A mechanism for the nucleation and growth of BNNTs is demonstrated by separating the different stages of development of the synthesis: accumulation of the catalyst on the substrate, formation of catalyst droplets, and growth of BNNTs. This work can serve as a fundamental basis for upscaling production of BNNTs and achieving greater control of their morphology. This will enable us to utilise the extraordinary properties of BNNTs, particularly their high thermal conductivity, for technological applications such as their use as fillers in solutions that can serve as coolant in various devices.

Chapter 3

Morphology control and hybrid BN nanomaterials

This chapter discusses the synthesis of BN nanosheets, which is achieved by hindering the formation of catalyst droplets by utilising a metal such as iron or nickel, which, when reduced from their oxide form in a powder precursor, has a higher boiling point than the synthesis temperature of 1,200 °C. Tungsten as a target substrate results in the synthesis of BN nanosheets, while iron-rich stainless steel as a target substrate leads to the synthesis of BN nanobamboos. The diameter of the BNNT is decreased up to 10 nm by controlling the thickness of the thin film of magnesium borate that serves as the source of the catalyst droplets. Synthesis at 1,050 °C forms separate BNNTs, while synthesis at 1,200 °C produces clustered BNNTs. Hybrid nanostructures such as BNNTs coated with CNT are synthesised by incorporating methane as a carbon source in the synthesis. Lastly, measurements of the optical band gap and thermal conductivity of the synthesised BN nanomaterials are presented.

3.1 Introduction

Despite the proven effectiveness of the chemical vapour deposition (CVD) method in BN nanomaterial synthesis, it has not yet been possible to produce highly uniform BN nanomaterials with predefined properties using this method, or to have full control over the parameters of BN nanomaterial growth. This is because there are fundamental aspects of CVD synthesis that still need to be fully understood, such as the effects of different catalysts used in synthesis. For example, at the same molar ratio of B:MgO:FeO at 2:1:1, Lee *et al.* [13] reported to have synthesised BN nanotubes, while Pakdel *et al.* [29] claimed to have generated BN nanosheets. There have also been reports of experiments using mixtures of different metal oxides, such as magnesium oxide [11] and iron oxide [12]. However, there remains a gap in the literature for a systematic investigation of the particular effects of each metal oxide in the synthesis of BN nanomaterials.

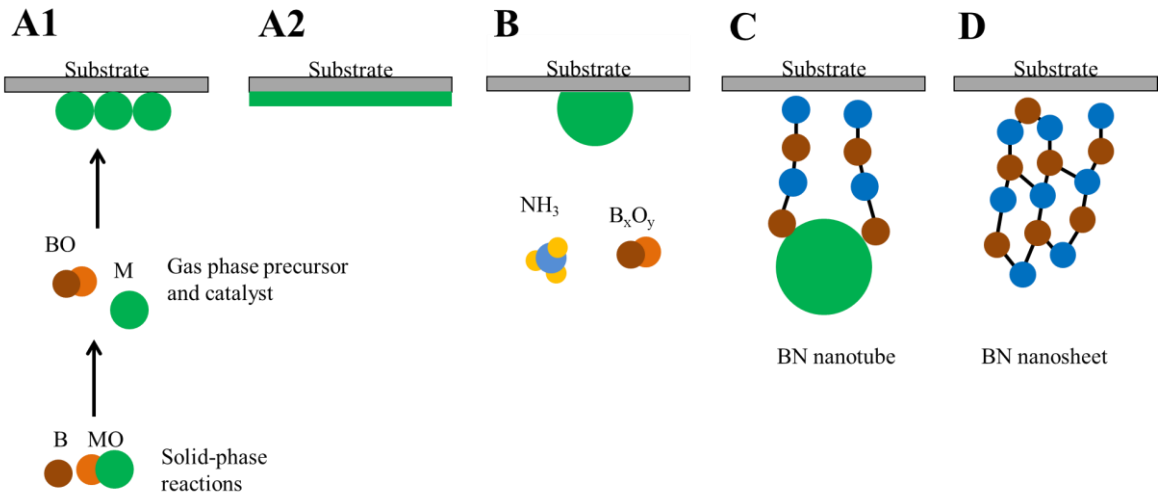


Figure 3.1 *Schematic illustration of the synthesis of BN nanomaterials using different approaches to introducing the catalyst droplet (A1) is the typical BOCVD method. (A2) Substrate with the solid layer of catalyst. (B) Thermal dewetting of the catalyst with the exposure of BN precursors. (C) Formation of nanotubes through the catalyst medium. (D) Nanosheet generation through the absence of catalyst droplets.*

This chapter investigates the formation of catalyst droplets leading to the final structure of synthesised BN nanomaterials achieved by:

- changing the metal oxide in the powder precursor such as magnesium oxide, iron oxide, and nickel oxide;
- using different target substrates such as iron-rich stainless steel, and tungsten sheet;
- controlling the formation of catalyst droplets on the thin film of magnesium borate through the variation of the synthesis temperature and the thickness of the thin film during synthesis.

As shown in Figure 3.1, changing the metal oxide in the powder precursor involves the boron oxide chemical vapour deposition (BOCVD) method, where the boron precursor (BO) and the metal catalyst (M) are generated together by solid-phase reaction (Figure 3.1A1). Different BN nanostructures can be synthesised depending on the properties of the metal reduced from the metal oxide added in the powder precursor. For example, the metal reduced from magnesium oxide when it is used as the metal oxide in the powder precursor is magnesium, with a boiling point of 1,091 °C (1,363 K). This boiling point, which is lower than the synthesis temperature of 1,200 °C, leads to the effective generation of catalyst droplets that facilitate the formation of BN nanotubes, as illustrated in Figure 3.1A1 to B to C. On the other hand, insufficient production of the metal catalyst results in the synthesis of nanosheets, as shown in Figure 3.1D. This work will also demonstrate that the use of iron (II,III) oxide produces BN nanosheets, given that the iron reduced from iron oxide is in the solid phase due to its significantly high boiling point of 2,862 °C (3,134 K), which is far above the synthesis temperature of 1,200 °C, leading to the generation of boron precursor (BO) with hindered formation of the gas-phase metal catalyst (M). With this absence of catalyst droplets, it is expected that BN nanosheets will be synthesised.

Figure 3.1A2 illustrates a target substrate where the catalyst is generated (1) directly from the surface of the target substrate or (2) from a prefabricated thin film that will proceed to form the catalyst droplets as depicted in Figure 3.1A2 to B to C. Different modifications of the target substrate can affect the synthesis of BN nanomaterials, such as varying the composition and thickness of the prefabricated thin film used. This investigation will determine the relationship between growth parameters and the morphology and properties of nanotubes, and thereby provide clearer insight into the reasons behind the formation of different BN nanostructures.

3.2 Materials and methods

3.2.1 Morphology control and hybrid BN nanomaterial synthesis

A CVD setup similar to the one presented in the previous chapter (section 2.2.1) was also used for the experiments described in this chapter. The powder precursor of B (≥95% boron, Sigma-Aldrich 15580) + metal oxide was contained in an alumina boat (ALM 5848, outer diameter 60mm x inner diameter 50 mm x 1200 mm, Almath). The metal oxide of the powder precursor was varied by using magnesium oxide (≥99.99%, Sigma-Aldrich 529699), iron oxide (99.7% trace metals basis, Sigma-Aldrich 400866), and nickel oxide (99.995% trace metals basis, Sigma-Aldrich 481793), following a molar ratio of 1:1 boron:metal. The effect of the target substrate was studied using a SiO_2/Si wafer (MTI Corporation), a stainless steel sheet (Sigma-Aldrich, GF32240135) and a tungsten sheet (Sigma-Aldrich, GF58867970).

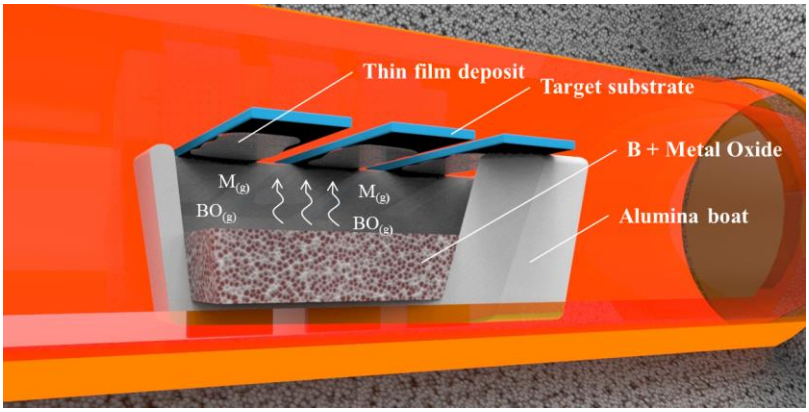


Figure 3.2 *Schematic illustration of fabricating the thin film as a source of catalyst droplets.*

The synthesis in which a thin film was used as a source for catalyst droplets was done by first fabricating the thin film through the heating of boron and magnesium oxide at 1,300 °C under Ar atmosphere, as illustrated in Figure 3.2. The thickness of the thin film was controlled by holding the temperature. The thermal evolution from the deposited thin film to the formation of catalyst droplets was investigated by subjecting the thin film to different temperatures for 1 min. Prior to this, the temperature profile of the reactor was obtained by using a K-type (Chromel/Alumel) thermocouple under an argon flow rate of 1.000 L/min. The synthesis of carbon-coated BN nanotubes was achieved by introducing a methane flow of 30 sccm using a boron + iron oxide precursor. Boron-doped carbon nanotubes were synthesised by removing ammonia from the synthesis.

In the thermal CVD synthesis of carbon nanotubes following a heterogeneous catalyst process, catalysts in the form of nanodots should be generated that serve as the nucleation site for the growth of carbon nanotubes. The catalyst can be introduced to the system either in the form of gas, using the floating catalyst method [165-167] or as a pre-deposited solid catalyst nanoparticle or film on the surface of the substrate. This thesis will demonstrate that the use of a thin film enables the separation of the three main factors in the synthesis of BN nanomaterials: the boron precursor, the nitrogen precursor, and the catalyst.

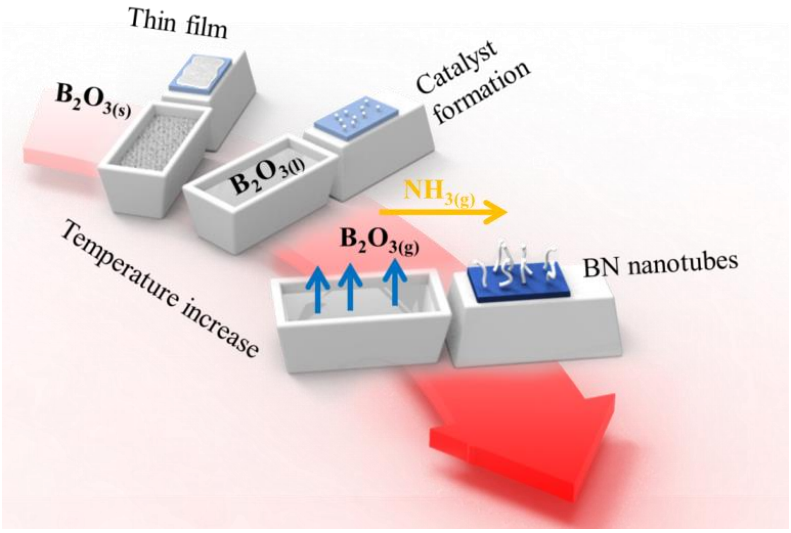


Figure 3.3 *Schematic illustration of the experimental design for the synthesis of BNNTs by using a thin film and B_2O_3 as B precursor.*

The fabrication of the thin film allows a higher level of control of the catalyst density and size, thus leading to better control of the properties of the synthesised BN nanomaterial. Furthermore, the present results demonstrate that the boron-containing compounds that form BNNTs can be generated after the production of the catalyst through the vaporisation of B_2O_3 alone to B_2O_3(g) [168-170]. Figure 3.3 shows the schematic experimental setup where a thin film of magnesium borate is utilised as a source of catalyst droplets and B_2O_3 as boron precursor. This method follows two steps: (1) a thin film of magnesium borate is fabricated by heating the boron and magnesium oxide at 1,300 °C, (2) the fabricated thin film of magnesium borate is placed after the B_2O_3 at varying temperatures of 1,050 and 1,200 °C with ammonia as a nitrogen source in the synthesis of BN nanomaterials.

3.2.2 Structure and composition characterisation

A JEOL-840F scanning electron microscope was used to investigate the morphology of the as-synthesised product through scanning electron microscopy (SEM)

images. Internal structures, crystallinity, and lattice spacing were studied by obtaining transmission electron microscopy (TEM) and high-resolution transmission electron microscopy (HRTEM) images under a JEOL-3000F transmission electron microscope. Composition analysis was conducted through energy-dispersive X-ray spectroscopy (EDX) analysis using a Zeiss Merlin EDX. Raman spectra were obtained using LabRam Aramis confocal Raman microscope equipped with a 532-nm green laser. A JEOL ARM-200F was used to conduct electron energy loss spectroscopy (EELS) obtaining annular dark field scanning transmission micrograph (ADF-STEM) images.

3.2.3 Band gap and thermal conductivity measurements

Instead of the UV-VIS spectroscopy that is often used to study the optical band gap of the bulk form of nanomaterials, the present study uses valence electron energy loss spectroscopy (VEELS) in STEM, which makes it possible to investigate particular optical band gap values for individual nanomaterials [171, 172]. The zero loss peak (ZLP) occurs at 0 eV in the spectrum and contains electrons that have zero or negligible energy loss, that is, elastically scattered electrons. The ZLP has the highest intensity in the spectrum. The region from 0 to 50 eV of the spectrum is the low-loss region. This region represents the energy that is lost by the electrons through the excitation of valence electrons within the sample. The low-loss region also exhibits a broad peak, which is a representation of resonant oscillations of valence electrons, also known as plasmons. The plasmon peak is located at an energy, E_P, which usually lies between 3 to 30 eV for most solids. The valence electron densities that can be studied at the low-loss region are directly linked to the dielectric function of the material, thus correlating to the optical adsorption [173]. The wide band gap of BN nanomaterials suggests that either a multiphoton process or UV light is required to excite an electron from valence to the conduction band. Arenal *et al.* [174,

175] reported the optical gap of a single-walled BN nanotube through VEELS in STEM, which was measured at 5.8 ± 0.2 eV.

Thermal conductivity measurements involved the use of the transient plane source (TPS) method using a Hot Disk model number 3500. This method is commonly used in the determination of bulk thermal parameters. In this approach, a thin disk consisting of a nickel double spiral embedded in Kapton [176, 177] insulation was used, which acted as both heat source and temperature sensor. To measure thermal conductivity, the heater/sensor was placed in contact with the material of interest, and a step power input function was applied. The temperature transient was recorded by measuring the change of resistive load of the heater/sensor, which is a function of the heat conductance of the system with which the heater/sensor is in contact. The thermal properties of the surrounding material with any potential boundary effects can influence the shape of the temperature transient. Although each bulk thermal characteristic had apparent effects on heat transport, a sufficient amount of information was collected from the transient to simultaneously extract thermal conductivity and diffusivity without the specific heat capacity [178, 179]. An important issue in investigating the thermal enhancement of nanomaterials suspended in fluids is sedimentation. Various practical and theoretical experiments are done in order to consider sedimentation. For example, visual observation method is used in order to survey the direct sedimentation of nanoparticles [180-182]. Light scattering method has been used to measure the diameter of nanoparticles in order to analyze their sedimentation [183]. The sedimentation of nanoparticles causes a decrease in the thermal conductivity of solutions. In this study, visual observation has been conducted to study the sedimentation achieved by dispersing 8 mg of synthesized BNNTs in 2 mL of acetone, ethanol, water, isopropanol, and hexane. These solutions were then sonicated using a sonic bath and left to stand for 40, 80, and 120 mins to observe sedimentation.

3.3 Results and discussion

3.3.1 BN nanosheets

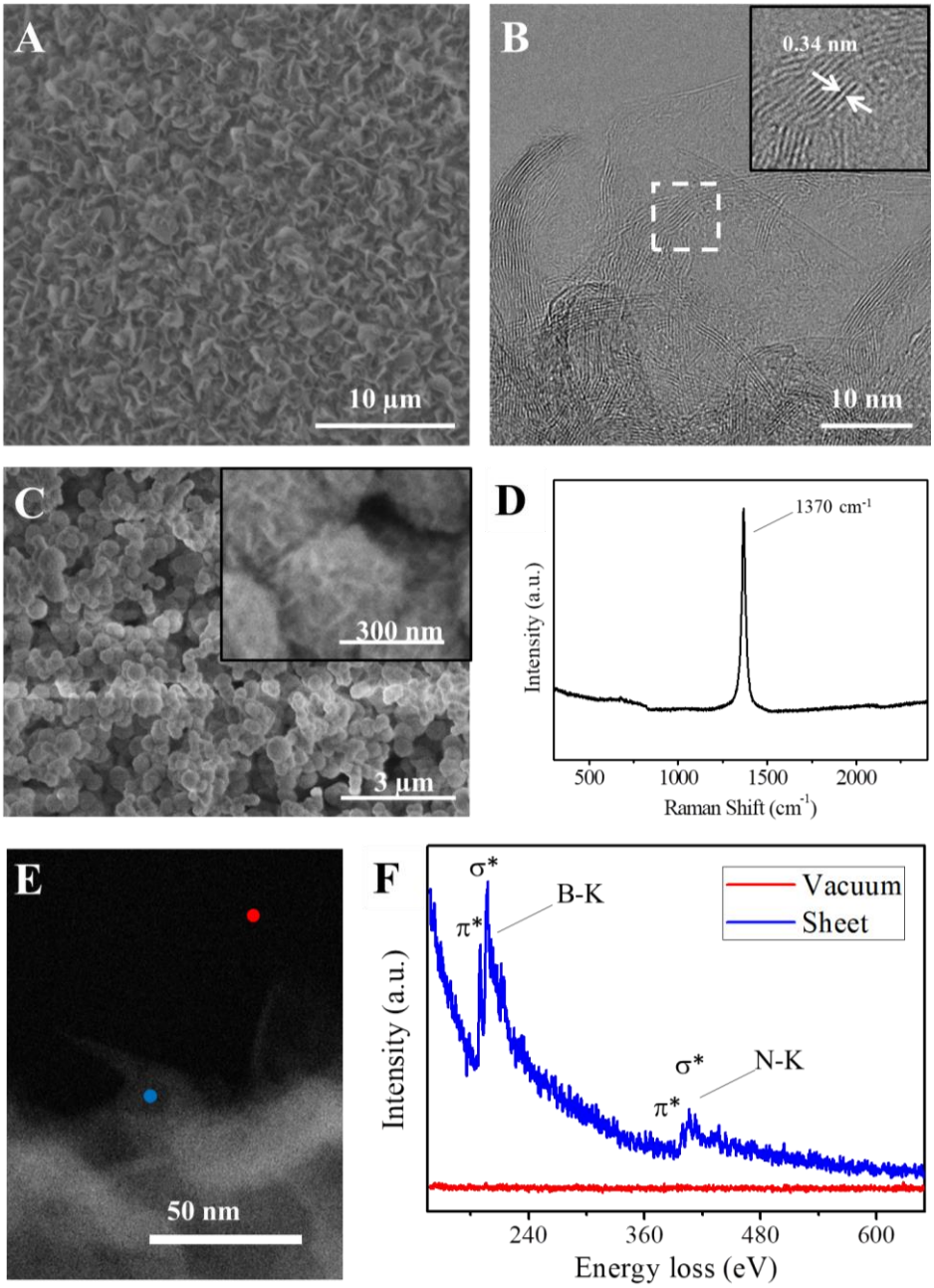


Figure 3.4 *(A) SEM image of synthesised BN nanomaterial using boron + iron oxide as powder precursor indicating nanosheet structures grown perpendicular to the target substrate. (B) HRTEM image of the nanosheets with lattice spacing measured to be 0.34 nm in the inset from the region of interest indicated by the white dashed square. (B) 3 hr period synthesis. (D) Corresponding Raman spectra of the synthesised nanosheets suggesting h-BN network based on the strong E_{2g} peak at 1370 cm^{-1}. (E) ADF-STEM image for the EELS analysis showing the vacuum and sample region, red and blue spot, respectively. (F) Acquired EELS spectra from the vacuum (red line) and BN nanosheet (blue line).*

Figure 3.4 shows the characterisation of the synthesised product using iron oxide as a metal oxide in the powder precursor (boron + metal oxide). Figure 3.4A shows that the substrate was homogeneously coated by nanosheets appearing to be perpendicularly grown with respect to the surface of the target substrate. The HRTEM image, shown in Figure 3.4B, revealed that the nanosheets had a structure analogous to graphite. The inset of the HRTEM image shows the highly ordered lattice fringes with spacing of 0.34 nm that corresponds to the (002) crystallographic plane of the hexagonal configuration of the BN sheets. The measured spacing gave a 9.6% error following the procedure described at section 2.3.1. The increase in growth time to 3 hrs showed a change of microstructure seen from the SEM image in Figure 3.4C. The inset shows that the surface of these spherical structures was composed of BN nanosheets.

Figure 3.4D shows a strong peak at a Raman shift of 1370 cm^{-1} that is attributed to the B-N high-frequency vibrational mode (E_{2g}) within the h-BN sheets. The Raman spectra showed that there was no carbon contamination or doping on the synthesised BN nanosheets due to the absence of the carbon G band peak which is commonly found at ca. 1600 cm^{-1}, thus indicating at this early stage that BN nanosheets synthesised in this method offer a high level of purity.

The chemical composition and stoichiometry of the synthesised BN nanosheets were further verified by EELS, presented in Figure 3.4E and F. Figure 3.4E shows the ADF-STEM image during the acquisition of the EELS spectra. A region of the vacuum and the sample was selected to calibrate the acquired spectra from the sample for any contamination or additional features being acquired as indicated by the red and blue spot, respectively. Figure 3.4F shows the EELS spectra of the vacuum (red line) and the BN nanosheets (blue line) from the region of interest shown in Figure 3.4E. Clear K-edges were seen at 188 and 401eV, which is attributed to the B and N K-shell ionization edges

that existed on the synthesised BN nanosheets with a calculated B/N ratio is 1.010 ± 0.02. It has been reported [184, 185] that the sharp peaks on the left part of the B-K and N-K edges denote 1s-π* antibonding orbits, while the peaks on the right part of the adsorption edges denote 1s-σ* antibonding orbits. This EELS signature is common for an sp^2-hybridised layered BN network. No carbon presence was observed in the synthesised BN nanosheets due to the absence of a C-K adsorption edge that is found at ca. 300 eV, a result which is in good agreement with the Raman analysis. It can therefore be inferred that hindering the generation of the droplet catalyst results in the synthesis of high-purity BN nanosheets.

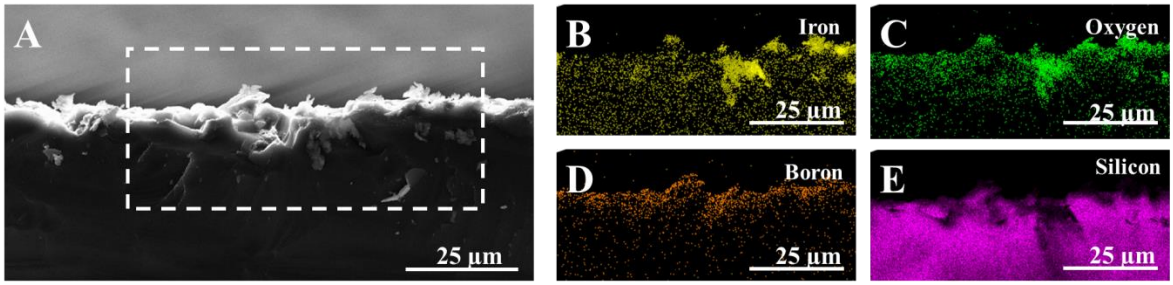


Figure 3.5 *EDX elemental mapping of the surface of the SiO_2 target substrate after the powder precursor, boron and iron oxide, was heated at synthesis temperature. (A) SEM image of a cross-section of the target substrate showing the region of interest indicated by the white dashed square corresponding to the elemental mapping of (B) iron, (C) oxygen, (D) boron, and (E) silicon.*

In the previous chapter, EDX analysis of the cross-section of the SiO_2 target substrate showed that magnesium was transported to the surface of the target substrate and led to the formation of catalyst droplets responsible for the generation of nanotubular structures. Here, it is expected that the conditions for the formation of the droplet structure will not be satisfied, since the high boiling point of iron will hinder the phase transformation to the gaseous state that makes it possible for iron to be transported to the surface of the substrate.

EDX spectroscopy was used to investigate the elemental distribution of any deposited material on the surface of the SiO_2, as shown in Figure 3.5. Note that in Figure 3.5B, less iron was observed on the surface of the substrate; in addition, the image shows iron to be clustered rather than finely distributed on the surface unlike magnesium in section 2.3.2. Oxygen, in Figure 3.5C, showed a high similarity of distribution with iron, indicating that iron was in an oxidized state. Elemental mapping seen in Figure 3.5D revealed that unlike iron, boron was uniformly scattered on the surface of the substrate and was not concentrated in any region. The EDX elemental mapping also showed that a significant amount of boron was generated, which must have come from the boron oxide during the heat treatment. Silicon was then observed underneath the boron layer that corresponded to the SiO_2 wafer substrate.

From the EDX analysis presented, it can be inferred that the generation of the metal responsible for nanotube formation was inefficient, thus leading to the synthesis of nanosheets. A uniform distribution along the surface of the substrate is therefore one of the parameter in order to generate catalyst droplets for the formation of the nanotubular structure.

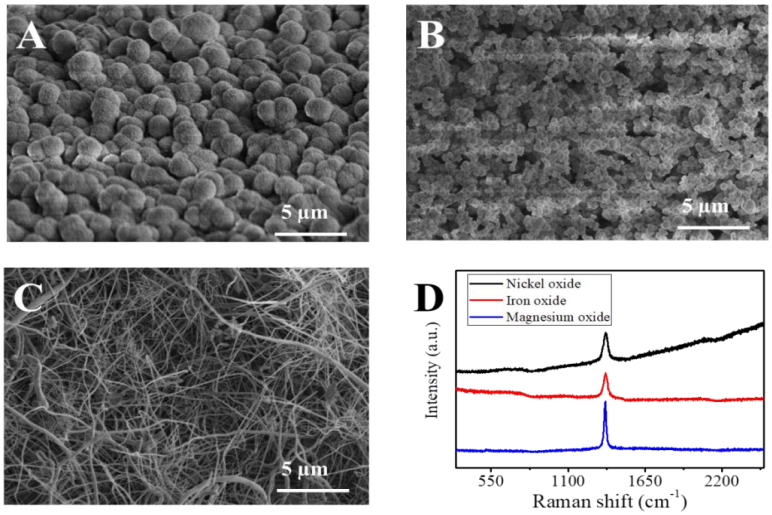


Figure 3.6 *SEM images of the product obtained by using (A) nickel oxide, (B) iron oxide, and (C) magnesium oxide as metal oxide in the powder precursor B + metal oxide. (D) Raman spectra of corresponding products of different metal oxides.*

Controlling the metal phase through its boiling point was further investigated by using nickel oxide with a boiling point of 2,913 °C (3,186.15 K) at its reduced state. Figure 3.6 presents the summary of the synthesised BN nanomaterials generated using different metal oxides with their corresponding Raman spectra. The SEM image shows that nickel (Figure 3.6A) and iron oxide (Figure 3.6B) both produced BN nanosheets. Magnesium oxide, however, yielded BN nanotubes (Figure 3.6C). Raman spectroscopy showed that all synthesised BN materials, regardless of the catalyst material used, had a distinct E_{2g} peak.

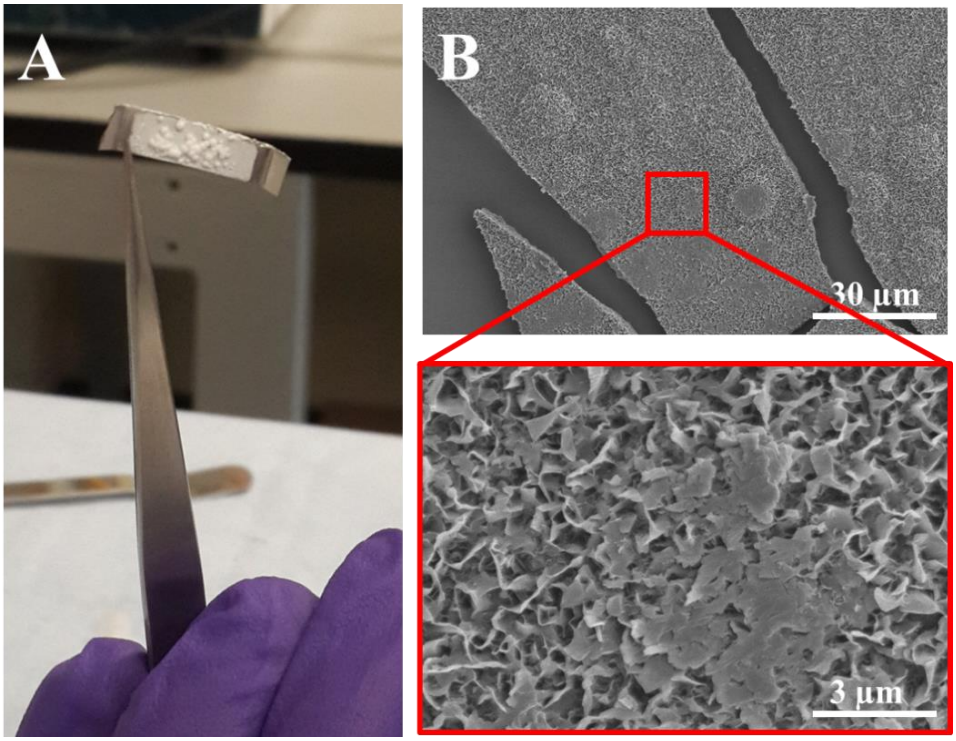


Figure 3.7 *Synthesis of BN nanomaterials using tungsten as a target substrate and boron + iron oxide as a powder precursor. (A) Photograph image after the synthesis showing a white deposit on the surface of the tungsten sheet. (B) SEM image of the white deposit.*

BN nanosheets were synthesised using a tungsten target substrate from a boron + iron oxide powder precursor. As can be seen in Figure 3.7A, the surface of the tungsten sheet had white deposits. The SEM image in Figure 3.7B shows that BN nanosheets grew perpendicular to the surface of the tungsten substrate. Tungsten has a melting point of

3,422 °C, which is higher than the synthesis temperature of 1,200 °C, from which it can be inferred that no catalyst droplets were generated during the synthesis, thus hindering the conditions for the production of nanotubes. Furthermore, the eutectic point of the boron-tungsten binary system (see Figure A.5 in the Appendix) is at 95% boron content with a melting temperature of 1,970 °C, which is still higher than the synthesis temperature, thereby indicating that no droplet catalyst could be generated [186].

It can be concluded that BN nanomaterials with certain morphologies can be synthesised by controlling the catalyst that is responsible for the formation of the nanotubular structure. In particular, suppressing the gaseous metal generated from the powder precursor can lead to the synthesis of BN nanosheets.

3.3.2 BN nanobamboos

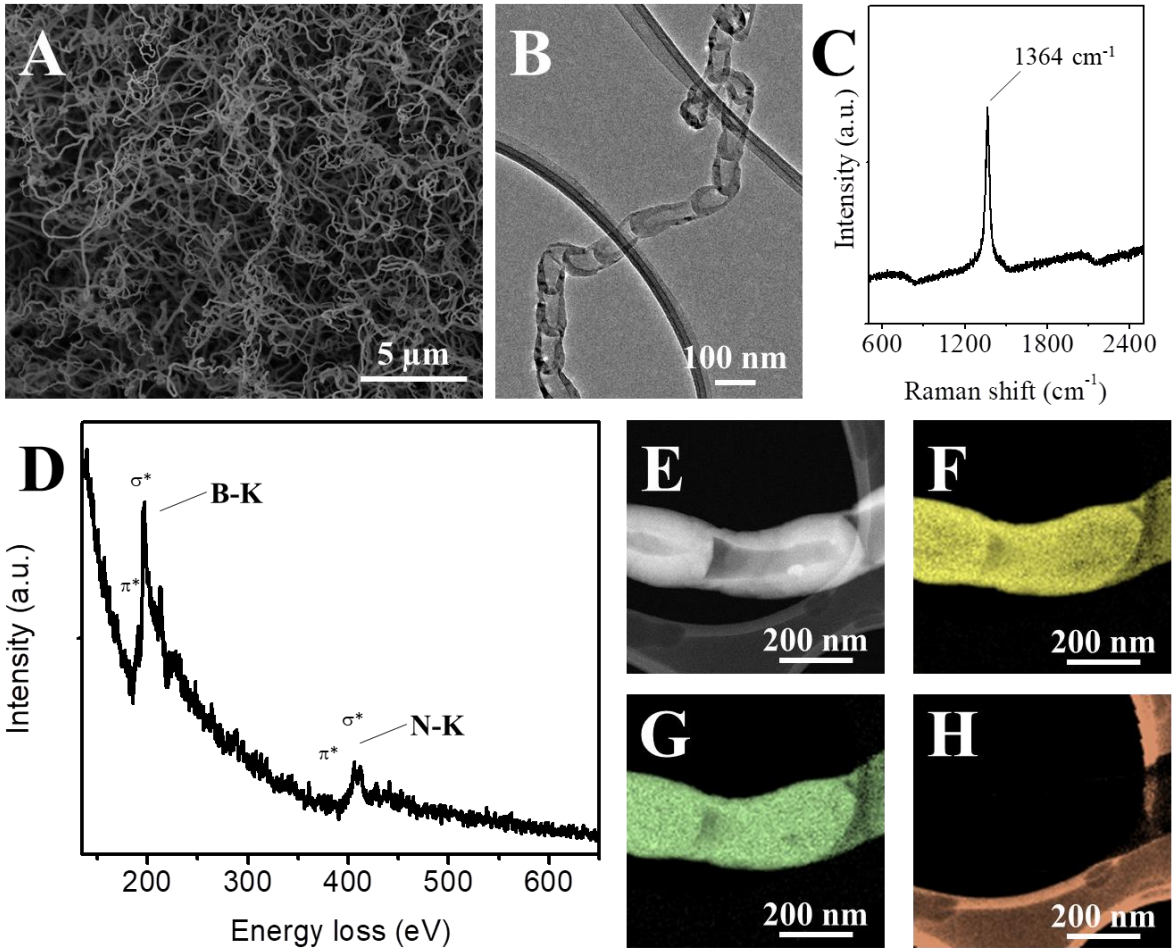


Figure 3.8 *Synthesis of BN nanomaterials using iron-rich stainless steel as a target substrate and boron + iron oxide as powder precursor. (A) SEM image of the synthesised product showing abundant presence of 1D nanostructure. (B) TEM image of a single 1D synthesised product showing a bamboo-like structure. (C) Raman spectra showing a strong peak at 1364 cm^{-1}, suggesting that the synthesised product is composed of the h-BN network. Composition analysis of the synthesised BN nanotube using stainless steel as target substrate showing (D) EEL spectrum and (E) High-loss EELS image of the region of interest for EELS analysis. The spatially resolved elemental maps of (F) boron, (G) nitrogen, and (H) carbon.*

Iron-rich stainless steel as target substrate produced a 1D structure with diameters ranging from tens to hundreds of nanometers as shown in Figure 3.8A. Figure 3.8B presents a representative TEM image of the synthesised fibres and shows the inner morphology indicating a hollow structure. The generated structure resembled bamboo. The observed BN nanobamboos synthesised using an iron-rich target substrate are composed of successively jointed segments, which were short variable-diameter compartments with one

end sealed and the other open. Figure 3.8C shows the Raman signature of the synthesised BN nanomaterial. A strong E_{2g} peak was observed, indicating that the structure was composed of h-BN.

The EELS analysis shown in Figure 3.8D revealed that the BN nanobamboo was composed of boron and nitrogen, as demonstrated by the evident B and N adsorption K-edges at ca. 188 and ca. 401 eV, respectively. The structure showed segments of caps, which were created by the non-hexagonal bonding of boron and nitrogen. Terrones *et al.* [187] have reported that the caps in the BN nanostructure can be made with the help of a metal catalyst. The elemental maps acquired from EELS (Figure 3.8C to E) displayed a significant amount of boron and nitrogen with no carbon found along the nanotube except on the carbon lacey support of the TEM grid. In addition, the boron and nitrogen atomic species were uniformly distributed along the entire nanotube. Based on the EEL spectra, the claim of having no carbon contamination along the nanotube was further confirmed by the compositional profile of carbon shown in Figure 3.8H. No observation of strong N K-edge associated to the N_2 gas was observed suggesting that there is no N_2 gas inside the nanotubes. However, it is noteworthy that the hollow structure inside the nanotube is likely to be filled with gaseous species. In this case, it is speculated that it may be filled with Ar gas since Ar was used as the inert atmosphere during the synthesis although major edges of argon was difficult to observe in EELS possibly due to the high signal detection of boron from the nanostructure itself.

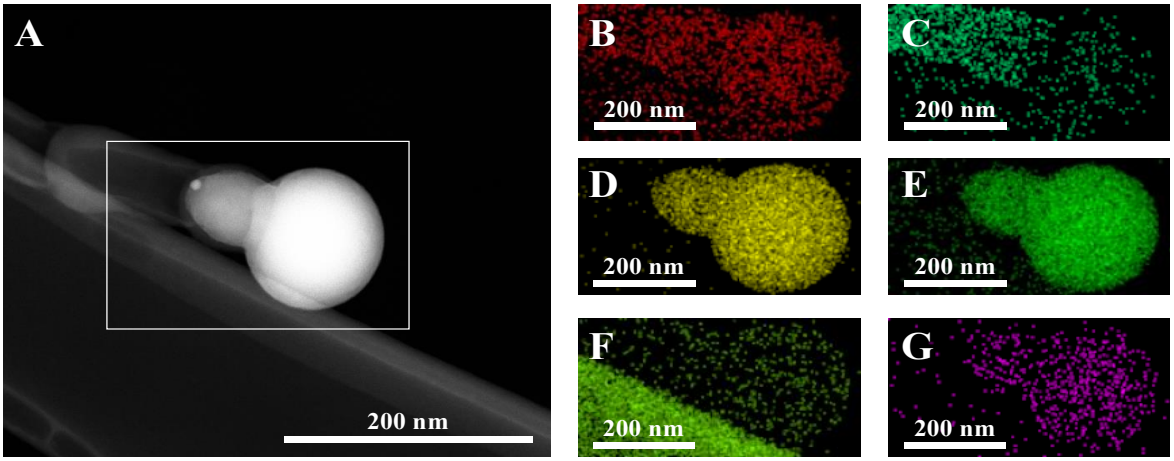


Figure 3.9 *Composition analysis of the tip of the synthesised BN nanotube. (A) STEM image showing the region of interest indicated by the white square corresponding to the elemental mapping of (B) boron, (C) nitrogen, (D) iron, and (E) oxygen, (F) carbon, and (G) chromium.*

The tip of the BN nanotube was characterised using EDX to study the composition shown in Figure 3.9. Similar to the investigation of the tip particle in the previous chapter (section 2.3.2), a clear similarity was observed here showing the presence of a catalyst indicated by the high contrast of the STEM image in Figure 3.9A. This region was subjected to EDX analysis, which revealed the presence of boron, nitrogen, iron, oxygen, carbon, and chromium corresponding to Figure 3.9B to G, respectively. The elemental maps of boron and nitrogen showed that they were well-distributed along the structure of the nanotube. In addition, boron was found to extend along the catalyst tip, indicating that boron interacted first with the tip of the catalyst and then started to precipitate once ammonia was introduced in to the system. Interestingly, high concentrations of iron were on the tip particle together with oxygen. As expected, a significant amount of carbon background from the carbon lacey support from the TEM grid was observed. However, there was a clear carbon presence on the tip particle. Chromium was also detected on the particle tip. Following a tip-growth mechanism, this indicates that droplet catalysts were generated prior to the BN nanotube formation.

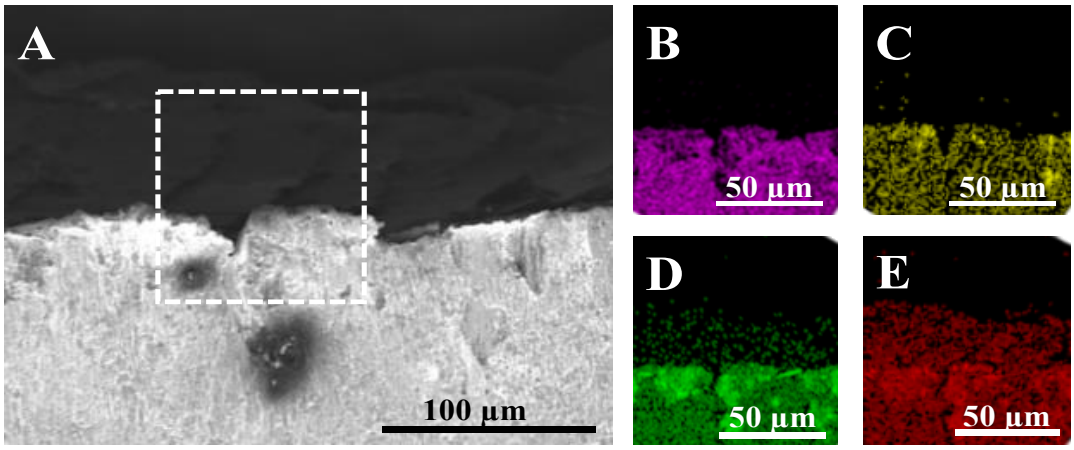


Figure 3.10 *Composition analysis by EDX of the surface of the stainless steel used as a target substrate. (A) Cross-section SEM image showing the region of interest indicated by the white dashed square corresponding to the elemental mapping of (B) iron, (C) chromium, (D) oxygen, and (E) carbon.*

A cross-sectional EDX map of the stainless-steel substrate is shown in Figure 3.10. Significant amounts of iron, chromium, oxygen, and carbon were detected, as seen in Figure 3.10B to E, respectively. The elements found on the tip of the BN nanotube are a good match to the elements present in the stainless-steel substrate. Although carbon was present on the target substrate, the carbon did not migrate to the nanotube, thereby preventing the formation of a BCN nanostructure or carbon nanotube.

Reports of stainless steel as a target substrate in the literature [19, 188] offer less correlation between the target substrate and the growth morphology of the BN nanomaterial being synthesised. The catalyst investigated here formed directly on the target substrate, demonstrating that catalyst formation does not necessarily have to occur via a vapour-liquid-solid (VLS) mechanism. This is because the surface of the stainless-steel target substrate partially melted at synthesis temperature due to the eutectic point between boron and iron with a melting point of 1174 °C. The generation of the boron intermediate species interacted with the iron-rich surface of the target substrate, leading to the formation of a boron-iron alloy complex with a melting point that satisfied the conditions required for the formation of droplets that eventually served as a catalyst for the production of nanotubes.

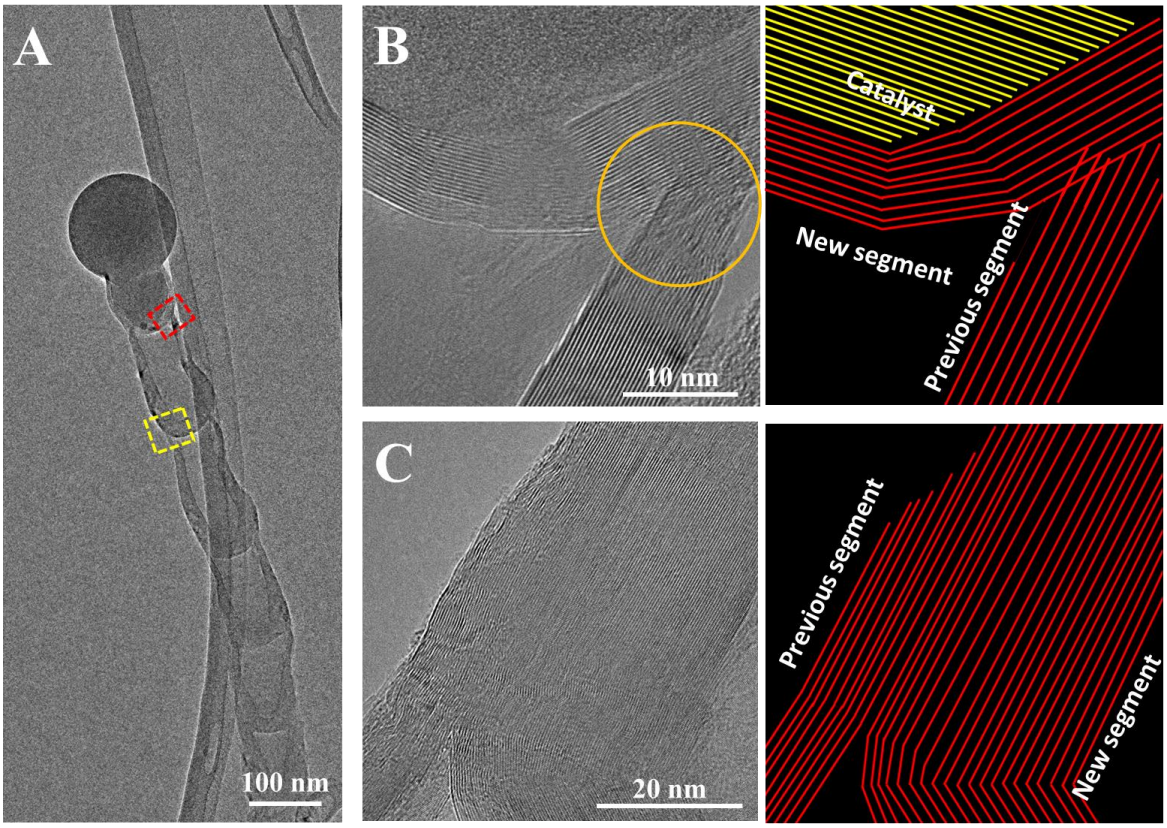


Figure 3.11 *Growth analysis of the BN nanotubes synthesised using a stainless-steel target substrate. (A) TEM image of a single BN nanotube showing the tip and the bamboo structure. (B) HRTEM image of the interface between the catalyst particle and the BN nanotube corresponding to the red dashed square in panel A. (C) HRTEM image of the junction of segments of the bamboo structure of the BN nanotube corresponding to the yellow dashed square in panel A. Panels on the right hand side depict the schematic illustration of the HRTEM images indicating the segments.*

The growth mechanism of the nanobamboo was studied using TEM, focussing particularly on the interface sections. Figure 3.11A is a typical TEM image of the BN nanotube showing the dense tip and the grown BN nanostructure. As stated before, the structure of the nanotube seemed to have a grouping of caps. The HRTEM image of the interface between the catalyst and the nanotube, in the red dashed square shown in Figure 3.11B, shows that the catalyst was covered with BN sheets. These BN sheets are conjectured to be the newly grown segments that further increase the length of the BN nanotube. On the lower right side of Figure 3.11B indicated by an orange circle, the wall of the previously grown cap segment can be seen, showing that the sheets of this segment were adsorbed on the surface of the newly grown segment. The alignment of the sheets on

different segments indicates a mismatch, and the sheets from the newly precipitated segment clearly show contact on the surface of the catalyst. A clear schematic representation is depicted on the right of Figure 3.11B. It was expected that this newly precipitated BN segment would detach from the surface of the catalyst due to the increased amount of BN-sheet interaction, which made the BN segment less attracted to the surface of the catalyst. The interface between the segments of the caps showed no preferred adsorption. As seen in Figure 3.11C, corresponding to the yellow-dashed square in Figure 3.11A, the previously precipitated BN segment adhered onto the bottom part of the other BN segment. The topmost layers of caps were terminated, as seen by the discontinued BN layers found on the right panel of Figure 3.11C. It was observed that the wall thickness of the segment decreased gradually from the sealed end to the open end. The measured average layer spacing of the BN sheets was 0.343 nm, which is consistent with the interplanar distance of three-dimensional graphite-like BN structures.

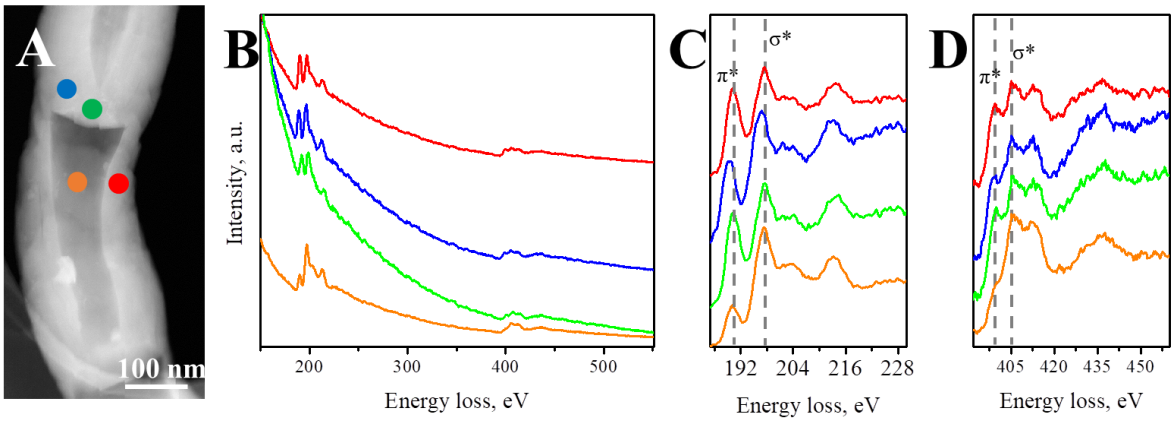


Figure 3.12 *(A) ADF-STEM image of the BN nanobamboo showing two segments. (B) EEL spectra obtained from different spots on the BN nanobamboo segment. (C) B- and (D) N-K edges showing the behaviour of π* and σ* peaks at different spots.*

Figure 3.12A shows different spots of EELS analysis that correspond to the open end edge (red), the curve to the sealed end (blue), the sealed end (green), and the hollow middle (orange). Calculated B/N ratios were 1.079 ± 0.02 for the red spot, 1.117 ± 0.02 for

the blue spot, 1.051 ± 0.02 for green spot, and 1.047 ± 0.02 for the orange spot, indicating that the variable-diameter growth did not originate from the change of the supply of B and N sources.

The fine structures of the B- and N- K edges shown in Figure 3.12C and D, respectively, confirmed that the h-BN network had a sp^2-type configuration. Moreover, the evolution of the weight ratio between the π* and σ* peaks as the probe scanned from the edge to the hollow or wall centre is characteristic of a cylindrical structure [158], where the orientation of the electron beam with respect to the h-BN layers varies continuously from parallel to perpendicular. Interestingly, a shift of 1.0 eV in both π* and σ* peaks was observed as the probe moved towards the curve spot of the BN wall segment, regardless of the starting point of the probe, for example, when the probe moved from the open edge wall (red spot) to the closed curve wall (blue spot). A shift of these peaks indicated that the chemical surrounding of an atom of interest in a compound changed the charge distribution of its valence band. The resulting effective potential on that atom was related in varying degrees to all the electronic levels of that atom and therefore gave rise to an energy shift in a spectrum.

The B-K edge at the curve spot suggested that there was a change of the bonding environment of boron. The cap morphology seen in the HRTEM image implied that the non-hexagonal BN network had occurred. The π* and σ* peaks for the N-K edge shown in Figure 3.12D remained at the same position but only the weight ratio changed. This observation indicated that the chemical environment of the nitrogen stayed the same, as it continued to have boron as neighbouring atoms. Thus, to comply with the closed curvature gap, a pentagonal bonding structure had be attained, and the results corresponding to the B-K edge suggested that B-B bond took place on the curve sites of the caps in good agreement with the observed increase of boron based on the calculated B/N ratios. This

shift of B-K edge was also observed by Gai *et al.* [189], who showed that the π* and σ* peaks of boron at B-B bond had less energy loss compared to B-C and B-O bonding.

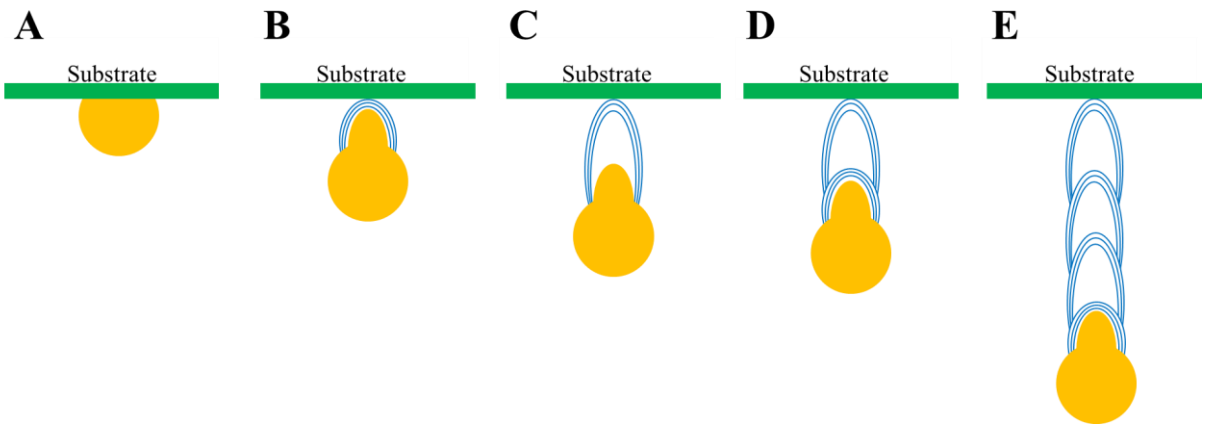


Figure 3.13 *Schematic illustration of the tip-growth model of BN nanotubes. (A) Showing the droplet formation, indicated in yellow, which can come from the partial melting of the solid target substrate, indicated in green, or by achieving eutectic point between boron and iron. (B) Precipitation of BN sheets on the surface of the catalyst droplet. (C) Lift-off of the catalyst droplet from the precipitated BN nanobamboo segment exposing a clean surface for precipitation of (D) the new BN nanobamboo segment. (E) Periodic growth of the BN nanobamboo segments.*

Figure 3.13 is a schematic illustration of the growth of BN nanobamboos. In the growth process, the iron-rich target substrate generates liquid droplets at the synthesis temperature (Figure 3.13A). These droplets can be generated by obtaining the composition at the eutectic point of iron and boron (see Figure A.6 in Appendix) that is 17% boron with a melting point of 1,174 °C, which is below the synthesis temperature of 1,200 °C. In an oxide system such as FeO – B_2O_3 and Fe_2O_3 – B_2O_3, catalyst droplets at the synthesis temperature are still expected to be generated as indicated by the phase diagram shown in Figure A.7 in Appendix.

According to Li *et al.* [153], in a high-temperature environment, the surface of a stainless-steel target substrate forms liquid droplets caused by partial melting. The boron oxide and ammonia vapours present around the liquid droplets are dissolved and further react to produce BN species. BN crystals begin to precipitate when the concentration of the

BN species is greater than the saturation threshold. The liquid droplets also serve as a frame to form the segment of the nanobamboo structure, as shown in Figure 3.13B. The continuous supply of boron and nitrogen species produces the final structure of the BN cap segment. The increase in number of BN sheets in the BN cap segment tends to decrease the adsorption on the catalyst, causing the lift-off of the catalyst from the precipitated BN nanobamboo segment as illustrated in Figure 3.13C. The surface of the catalyst droplet becomes available for the formation of new BN cap segments for the continued growth of the BN nanobamboo (Figure 3.13D).

Although it is possible for species such as iron, chromium, oxygen, and carbon, which are native to the stainless-steel substrate, to be incorporated into the growing BN crystal [16], it must be noted that these species have higher affinity to each other rather than to the boron and nitrogen atoms because of their electronegativity. The periodic growth of BN cap segments will continue as long as there is a supply of boron and nitrogen intermediate species (Figure 3.13E). It has been proven by Trentler *et al.* [190] that BN nanotubes grow from the liquid-solid interface in order to give the lowest liquid–solid interfacial energy. Thus, after the precipitation of the first BN sheet on the surface of the catalyst, the next BN sheet will precipitate in between the precipitated BN sheet and the catalyst.

3.3.3 Diameter decrease of BNNTs

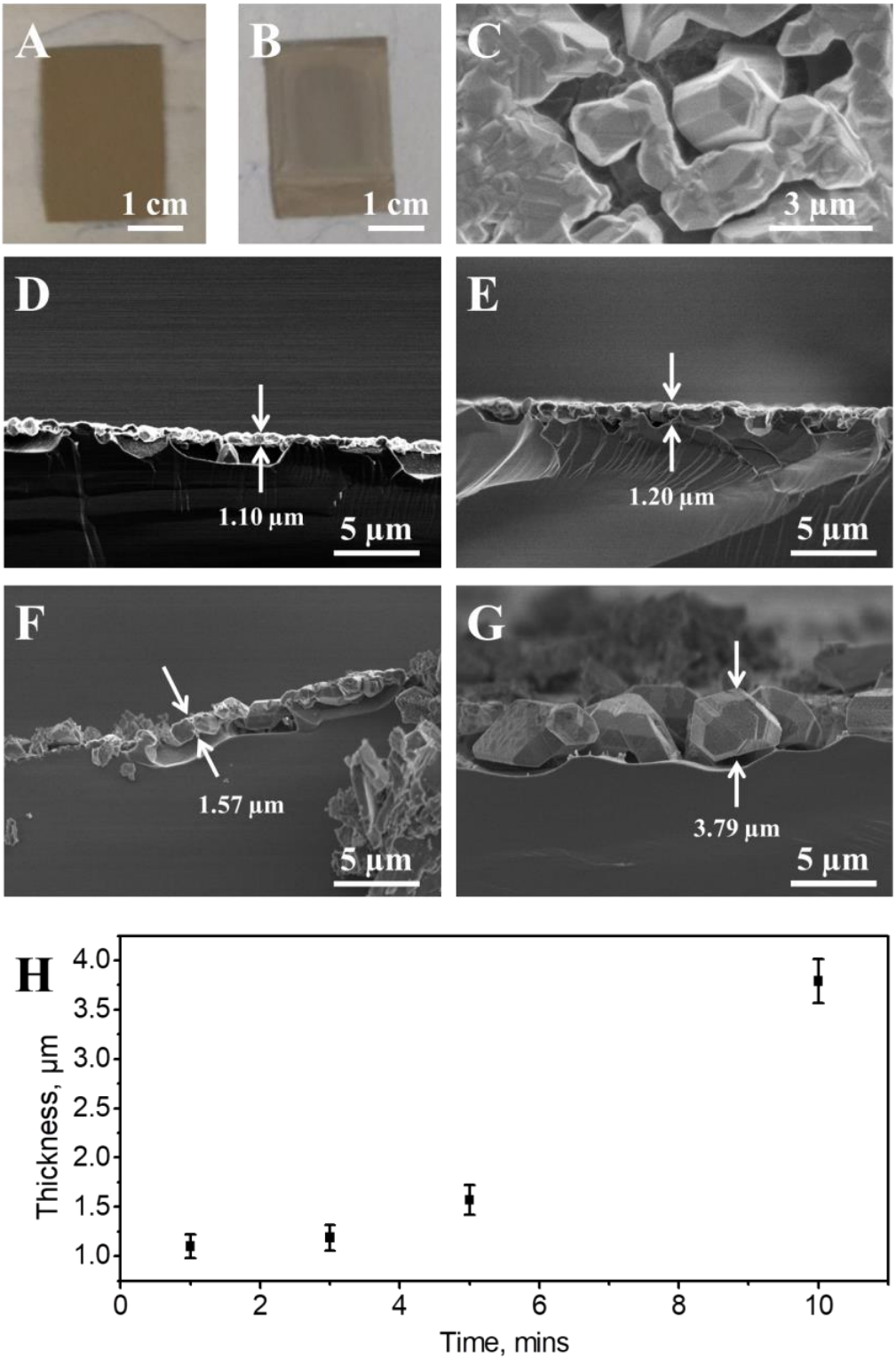


Figure 3.14 *Thin film fabrication and thickness control showing photographs of the surface of the target substrate (A) before and (B) after experimental run. (C) Top-view SEM image of the deposited thin film. SEM images of the cross-section of thin-film thickness as a function of time (D) 1, (E) 3, (F) 5, and (G) 10 mins. (H) Summary plot of thickness as a function of time.*

Figure 3.14 shows the fabrication of the thin film of magnesium borate to serve as catalyst for the synthesis of BNNTs with controllable thickness. Photograph images of SiO_2 wafers before and after the fabrication of thin film showed a change of colour (Figure 3.14A and B, respectively). As discussed previously, the mixture of B and MgO produces gases of B_2O_2 and Mg at elevated temperatures. Initial physical assessment indicated that the deposited material was not magnesium oxide due to its colour. The SEM image in Figure 3.14C shows that a material had been deposited on top of the SiO_2 wafer.

The thickness of the thin film of magnesium borate can be controlled by changing the duration of heating at constant temperature. Figure 3.14D to G show the cross-section SEM images of the thin films of magnesium borate fabricated at 1, 3, 5, and 10 mins, respectively. A summary plot of the thickness as a function of time is shown in Figure 3.14H. As expected, the thickness of the thin film increased as deposition time increased. Interestingly, the SEM image of the cross-section of the thin film shows a gap between the fabricated thin film and the substrate, indicating that the interface between the deposited material and the SiO_2 target substrate did not have a strong adsorption.

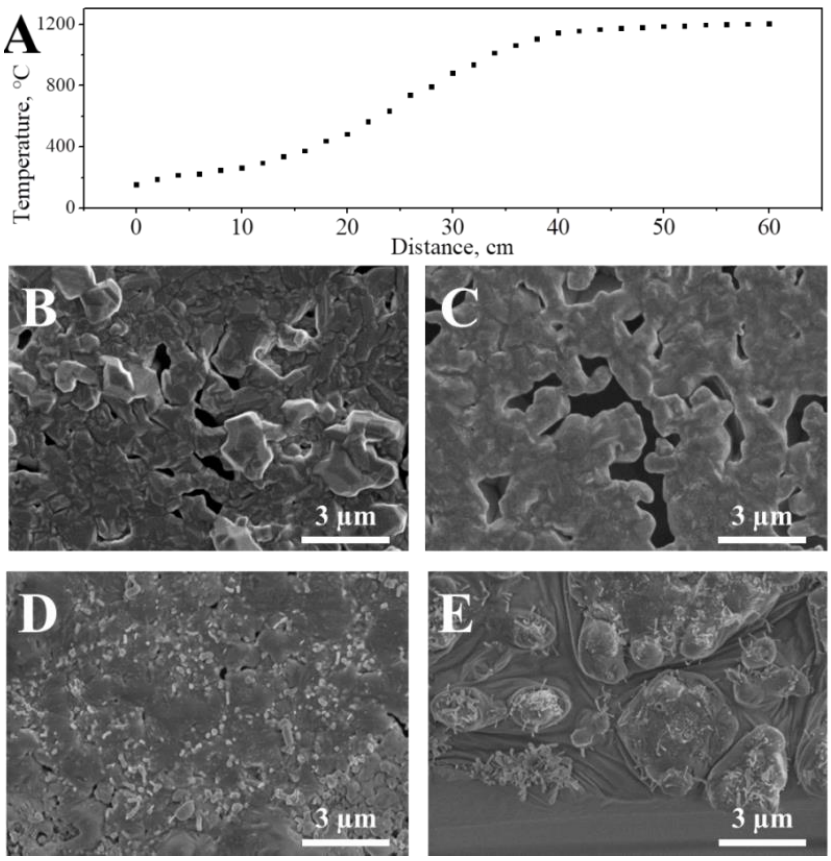


Figure 3.15 *Catalyst droplet evolutions at different temperatures. (A) Temperature profile of the working furnace. SEM images of (B) thin film of magnesium borate under heat treatment at (C) 880 °C, (D) 1,050 °C, and (E) 1,200 °C*

To investigate the temperature dependence of the catalyst droplet in its pristine thin-film form, the thin film was subjected to different temperatures presented in Figure 3.15. The temperature profile of the horizontal furnace was acquired first, as seen in Figure 3.15A. The fabricated thin films with similar thickness could then be heated at different temperatures by placing them at different positions inside the working furnace. The SEM analysis revealed changes in the morphology of the thin film depending on the temperature treatment. The rough surface of the pristine thin film became smooth when heated at 880 ℃ as seen from the SEM image in Figure 3.15B and C, respectively. At 1,050 ℃, catalyst particles across the surface started to be visible while at 1,200 ℃, these catalyst particles tended to be in clusters. These observations prove that the synthesis of BNNTs can be achieved even at temperatures lower than the BOCVD temperature of 1,300 ℃.

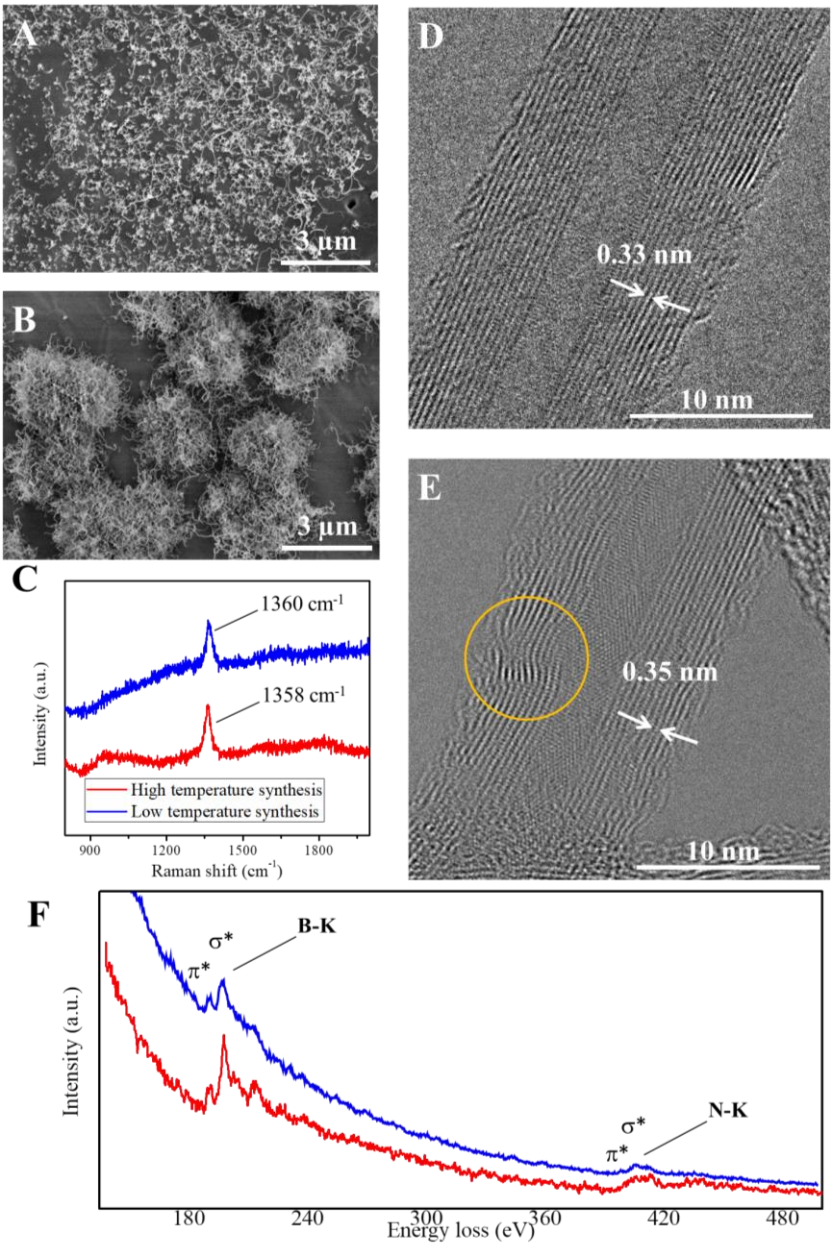


Figure 3.16 *SEM images of synthesised BNNTs at (A) low-, and (B) high-temperature conditions. TEM images of synthesised BNNTs at (D) low-, and (E) high-temperature conditions. (C) Raman spectra of corresponding as-synthesised products. (F) EELS spectra of the BNNTs synthesised at high temperature.*

This study has so far been able to determine that the synthesis of BNNTs is dependent on the catalyst formation and not on the generation of boron-containing $B_2O_{2(g)}$ intermediate species. In order to confirm that a different boron precursor can be used to synthesise BNNTS, the use of B_2O_3 as an alternative precursor was also investigated.

A film with a thickness of 1.5 µm was used to synthesise BNNTs at different temperatures. The SEM images shown in Figure 3.16A and B represent the synthesis of BNNTs at 1050 and 1200 °C, respectively. BNNTs grown at a low temperature were separated while BNNTs grown at a high temperature had a clustered morphology. The Raman spectroscopy analysis in Figure 3.16C showed a prominent peak located at 1,360 and 1,358 cm^{-1} for the BNNTs synthesised at 1,050 and 1,200 °C, respectively.

HRTEM images of BNNTs obtained from low- and high-temperature synthesis conditions are shown in Figure 3.16D and E with 10.3% and 10.5% error, respectively. The BNNTs synthesised at low temperature had good crystallinity, as indicated by the highly ordered BN walls seen in the TEM image. All nanotubes were long, straight, and of good crystal quality, exhibiting a uniform wall thickness of around 5 nm, and an inner diameter in the range of 2-3 nm. BNNTs synthesised at a high temperature showed a similar wall thickness and inner diameter, however, they also exhibited a bent morphology as observed in the SEM analysis. This bent structure observed in micron scale may have been caused by the nanoscale bending of the wall as seen in the region circled in orange in Figure 3.16E. A difference in lattice spacing was detected when comparing low- with high- temperature synthesis, which was likely due to the observed bending of the BNNTs.

The BNNTs generated using this method was also shown to have the thinnest diameter of all the materials synthesised in this work. The representative EELS analysis shown in Figure 3.16F suggested that the synthesised BNNTs were pure BN, as indicated by the definitive edge of B-K and N-K exhibiting peaks of π^* and σ^* with calculated B/N ratios of 1.031 ± 0.02 and 1.011 ± 0.02 for low-, and high-temperature synthesis conditions of BNNTs, respectively. The absence of C-K edge located at 284 eV indicated no carbon contamination. This was expected since there was no carbon source involved in the synthesis method.

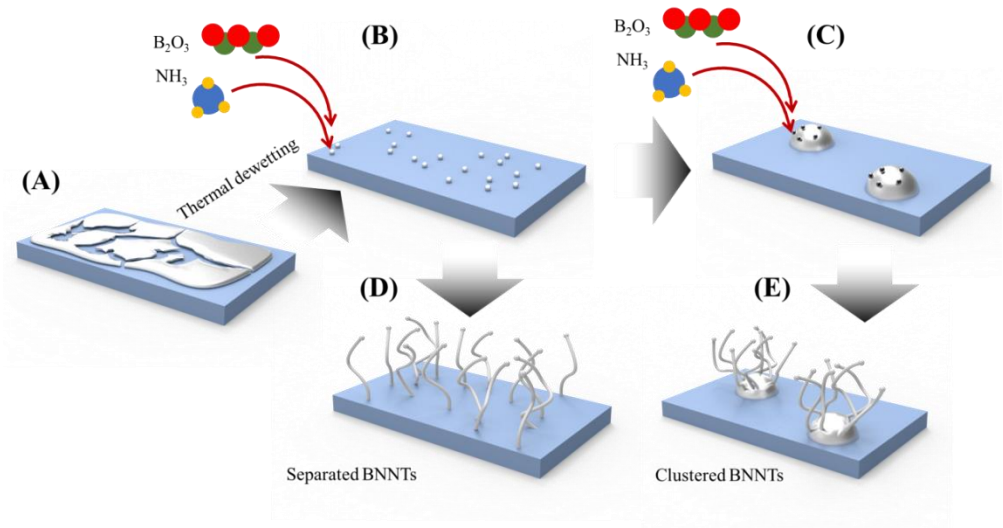


Figure 3.17 *Proposed mechanism for the synthesis of BNNTs using a thin film*

The complete separation of the three main components that govern the synthesis of BNNTs enables a higher level of control of growth parameters, unlike the commonly used BOCVD method where the catalyst is generated together with the boron species. In this study, the catalyst could be generated separately through the fabrication of the thin film of magnesium borate, which was then subjected to a heat treatment for thermal dewetting. This work has proven that B_2O_3 can be used as a sole boron precursor without the occurrence of the reduction-oxidation between boron and metal oxide in the powder precursor reported by other groups [11]. This experimental design also offers continuous growth of BNNTs, unlike the classical BOCVD method where the precursors are passivated by the formation of side products on top of the powder precursor [191, 192].

The structure of the BNNTs depends on the conditions of the dewetting of the thin film. As illustrated in Figure 3.17, at low-temperature synthesis, catalyst particles were generated on the surface of the thin film. Ammonia and boron oxide then supersaturate in the generated droplet melt, which led to the growth of well-separated BNNTs. On the other hand, the synthesis of BNNTs at a high temperature formed agglomerates of the melts that generated droplets of a larger size, resulting in clusters of BNNTs.

3.3.4 Hybrid BN nanomaterials

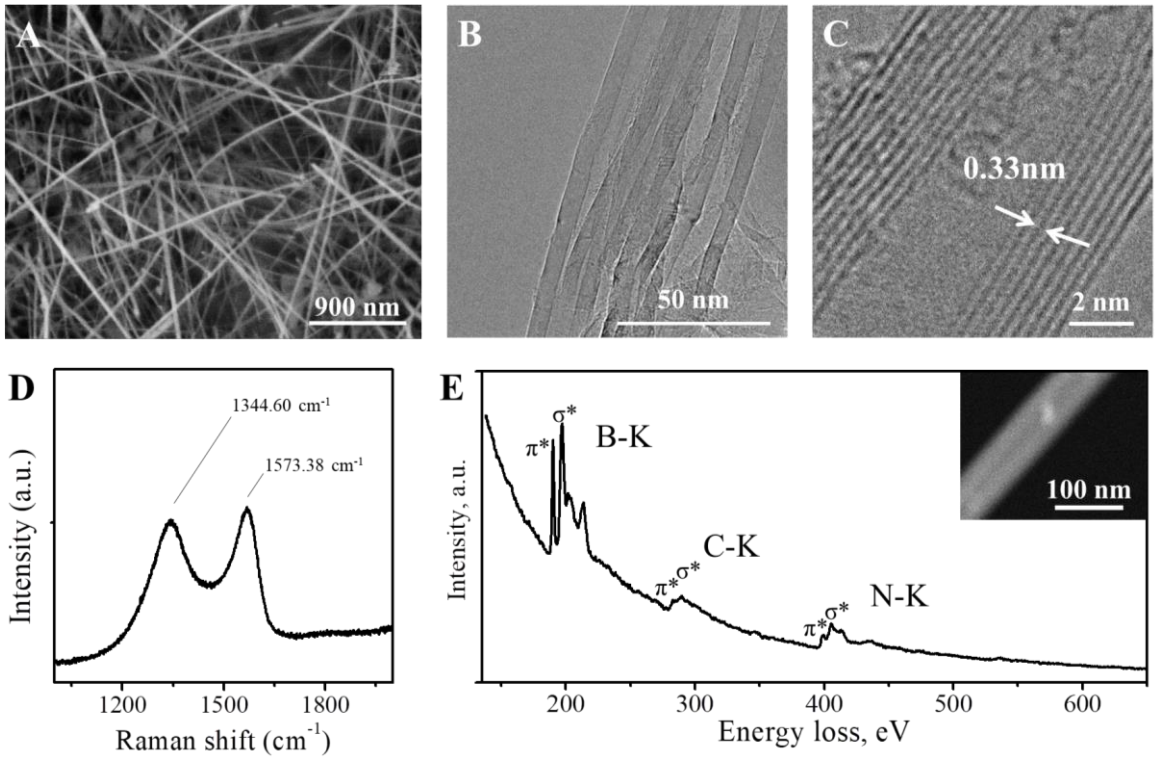


Figure 3.18 *(A) SEM image of synthesised hybrid BN nanomaterials with methane flow indicating 1D nanostructure. (B) TEM image of a representative 1D structure showing a nanotube morphology. (C) HRTEM image showing the lattice spacing of the walls measured to be 0.33 nm. (D) Corresponding Raman spectra of the synthesised product showing major peaks at 1,344.6 cm^{-1} and 1,573.38 cm^{-1} suggesting a carbon hexagonal network. (E) EELS spectrum of the synthesised nanotube showing fine K edges of B, C, and N. Inset ADF image acquiring the EELS spectrum.*

The separation of the precursors in gaseous form and the catalyst in its melt form can introduce new types of nanomaterials. Figure 3.18 shows the coating of BNNTs with carbon by introducing methane in the reaction system. The SEM image in Figure 3.18A of the synthesised product shows uniform 1D nanostructures. The TEM image in Figure 3.18B shows that the synthesised 1D nanostructure followed a nanotube structure due to the presence of hollowness in the inner section. Furthermore, the HRTEM image presented in Figure 3.18C shows that the synthesised nanotube had good crystallinity with an average lattice spacing of 0.33 ± 9.3 % nm. By Raman spectroscopy, two peaks were observed that can be attributed to the D and G peak of carbon nanotubes as seen in Figure

3.18D. A representative EELS spectrum was obtained from the synthesised nanotube shown in Figure 3.18E, where the inset is the nanotube of interest. K edges assigned to boron, carbon, and nitrogen at ca. 188 eV, 284 eV, and 401 eV, respectively, were clearly observed. These edges also exhibited well-defined π* and σ* peaks. However, these results must be carefully evaluated since they may give the impression that the synthesised material was in the form of a doped or coated nanotube.

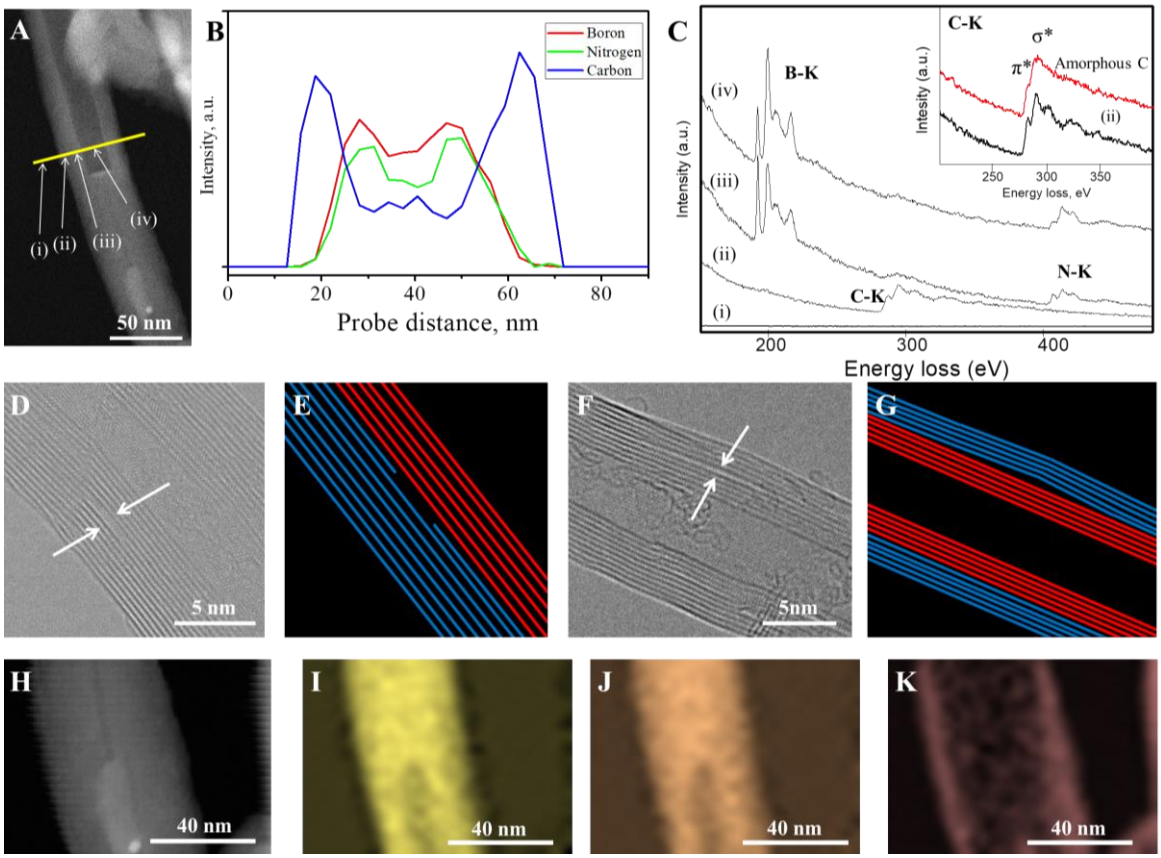


Figure 3.19 *(A) HAADF-STEM image of the synthesised hybrid BN nanotubes. (B) Elemental line profiles measured across the nanotube indicated by the yellow line in panel A. (C) EEL spectra acquired from panel A corresponding to (i) vacuum, (ii) edge of the wall, (iii) mid-section of the wall, and (iv) hollow middle demonstrating the near-edge fine structure of B, C, and N. TEM images indicating carbon and BN wall of the nanotube by (D) discontinuous wall and (F) apparent change of lattice spacing. (E) and (G) Schematic illustrations of panels D and F, respectively. (H) High-loss EELS image of the region of interest for EELS elemental mapping of (I) boron, (J) nitrogen, and (K) carbon.*

A detailed investigation of the distribution of carbon, boron, and nitrogen in the synthesised hybrid nanotube is presented in Figure 3.19. Figure 3.19B shows the line-scan

EELS analysis corresponding to the yellow line shown in Figure 3.19A. It can be seen that the carbon-rich phase was located on the outer tube surface while the BN-rich phase was inside. Four representative EELS spectra, obtained by moving the electron probe from the vacuum, passing the edge and inner edge of the wall to the inner hollow section of the nanotube corresponding to (i), (ii), (iii), and (iv), are compared in Figure 3.19C. A distinguishable K edge was observed on the edge of the nanotube at ca. 284 eV that was assigned to the C-K edge, and no other K edge was seen, particularly the B- and N-K edges typically at 188 eV and 401 eV, respectively. The C k-edge follows the signature of a graphite spectra indicated by the strong peak of π* and σ* as shown in the inset. Panel C shows pronounced signal of B and N k-edges making the C k-edge less visible. The inset shows a clear signal of the crystalline carbon unlike π* and σ* of amorphous carbon that exhibits a broad peak, black and red line, respectively. This suggested that only carbon in an sp^2 configuration was present on the edge of the nanotube. As the probe went closer to the inner hollow section of the nanotube, two K edges started to appear, which correspond to the B-K and N-K edges. Although defined π* and σ* peaks were observed from the K edges of B, C, and N, it should be noted that the K edges appeared at different probe samplings, specifically the C-K compared to the B and N-K edges. This suggested that the sp^2 configuration is not coming from a BCN network (C-doped BN or BN-doped C nanotube) but rather from an individual sp^2 of pure C and BN network. It is again observed that the weight ratio between the π* and σ* peaks changed due to the change in orientation of the electron beam with respect to the nanotube from the C nanotube or BN nanotube.

The HRTEM analysis on the synthesised nanotubes provided evidence of separation of the carbon coating and the BN wall, even though the lattice spacing of CNT and BNNT were closely related. Figure 3.19D shows a discontinuous wall of carbon nanosheet, emphasized by the white arrows and schematically represented in Figure 3.19E.

This discontinuous sheet indicated that the carbon layers were generated on the surface of the BN nanotube. The formation of a carbon layer on top of the BN nanotube is in good agreement with the previously observed phenomenon where carbon was more likely to precipitate together with the BN species on the catalyst. Another observation during the HRTEM analysis was the noticeable change in lattice spacing shown in Figure 3.19F and schematically presented in Figure 3.19G.

The EELS mapping of the high-loss image in Figure 3.19H with respect to the K-edge values of boron, nitrogen, and carbon was investigated and is illustrated in Figure 3.19I, J, and K, respectively. Strong intensity signals were seen from boron and nitrogen in the inner region of the nanotube while a clear presence of carbon is found on the surface of the nanotube, from which it can be inferred that carbon was indeed coated on the BN nanotube. In addition, HRTEM analysis clearly showed that both carbon and BN were highly crystalline.

Several researchers have reported the synthesis of coated nanotubes, particularly the coating of CNT with BNNT. Chen *et al.* [193] reported the coating of BN on carbon nanotubes that they proved by HRTEM and EELS investigations. Their synthesis involved the infiltration of boric acid in the CNTs, followed by nitridation. However, because CNTs were used as seeds for the BN coating, the resulting coating was highly affected by the surface of the CNT seeds. For instance, the walls of the CNTs were capable of slipping out of alignment (turbostratic surface), leading to uneven nucleation of the BN crystals that formed a polycrystalline BN coating.

In this work, polycrystalline carbon coating was not observed, a result that can be attributed to the high crystallinity of the BNNTs being synthesised. Suenaga *et al.* [50] presented a hybrid C-BN-C sandwich nanotube with well-defined walls and good crystallinity in both the carbon and boron nitride nanotubes. However, the arc-discharge

method used in the synthesis of these nanotubes resulted in products with poor homogeneity. A report involving carbon coating on BN nanotubes was presented by Nakanishi *et al*. [194], who reported that by using a single-walled carbon nanotube as a template, BN nanotubes from ammonia borane complexes could be synthesised inside the carbon-nanotube template through annealing. However, the premise of Nakanishi's work was the same as Chen's work: since CNTs were used as seeds, instead of coating CNTs with BN, the encapsulation of the ammonia borane complex induced the generation of BNNTs inside the CNT. The present work has shown that carbon-coated BN nanotubes can be synthesised directly without going through a CNT seeding process.

Methane being introduced in the synthesis of BN nanomaterial raises an interesting point regarding the growth mechanism, particularly considering the preference of carbon coating on the BN nanotubes and not the incorporation of carbon as doped in BN nanotube. These results lead to two hypotheses: (1) carbon sheets are generated directly on the surface of the synthesised BN nanotube and (2) since boron and nitrogen prefer to bond to each other, the carbon species dissolved in the catalyst does not bond with B or N, but instead proceed to form C-C bonding. To determine which phenomenon took place, an experiment was devised in which the ammonia was not introduced in the synthesis, with the aim of suppressing the nitrogen source. With only boron and carbon sources, it was expected that instead of BNNTs, boron-carbon nanotubes will be synthesised. The presence of a carbon coating on the resulting product would indicate that the carbon sheet did prefer to generate on the surface of the nanotube. On the other hand, the absence of a carbon coating would prove that carbon formed a bond with boron that led to the synthesis of doped nanotubes.

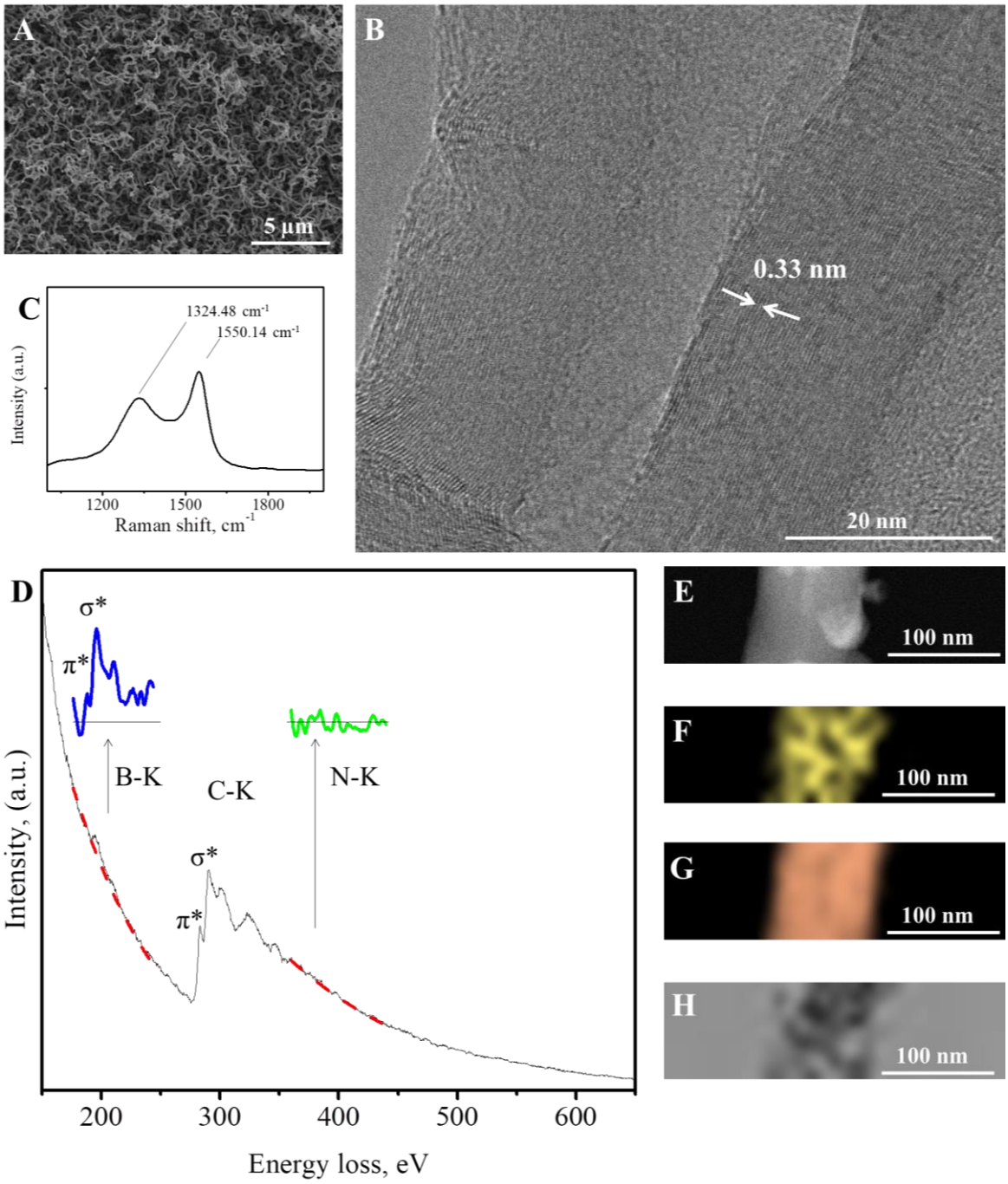


Figure 3.20 *(A) SEM image of synthesised hybrid nanomaterials with methane and boron oxide without ammonia flow showing the presence of filament structures. (B) HRTEM image of a representative 1D nanostructure showing nanotube morphology with measured lattice spacing of 0.33 nm. (C) Corresponding Raman spectra of the synthesised product showing major peaks at 1,324 cm^{-1} and 1,550 cm^{-1} suggesting a carbon network. (D) Corresponding EELS spectra showing K edges of B and C. Background removal was applied to B and N-K edges indicated by the dashed red line. (E) High-loss EELS image for the EELS analysis for acquiring spatially resolved elemental maps of (F) boron, (G) carbon, and (H) nitrogen.*

Figure 3.20 shows the synthesised product in the absence of the nitrogen precursor ammonia. Figure 3.20A is the SEM image showing an abundant presence of uniform 1D nanostructures with curly morphology. The HRTEM image shown in Figure 3.20B suggests that the synthesised material had a nanotube structure with lattice spacing of 0.33 ± 11.7% nm. Raman spectroscopy in Figure 3.20C showed two distinct peaks indicative of the D and G peak features of carbon nanotubes.

EELS analysis enabled the examination of the local atomic-scale elemental compositions of the as-synthesised nanomaterial, which was carried out on the different batches of nanotubes shown in Figure 3.20A. These nanotubes showed characteristic edges in EELS corresponding to K-shell ionization of boron and carbon. A typical EEL spectrum is shown in Figure 3.20D. The fine-edged structure of C-K energy loss in the spectrum testified to a high crystallinity of the synthesised nanotubes, which was also observed to have low radiation damage effect [195]. The C-K edge showed the characteristic $1s \rightarrow \pi^*$ and $1s \rightarrow \sigma^*$ peaks located at 282 eV and 289 eV, respectively. To better investigate the B-K and N-K signals, a subtraction of the high background below both edges was applied corresponding to the blue and green spectra, respectively. The B-K signal intensity was then clearly observed to exhibit the $1s \rightarrow \pi^*$ and $1s \rightarrow \sigma^*$ found at 188 eV and 195 eV, respectively. The shape and the position of the K-edges of boron and carbon indicated the sp^2 bonded environment where boron was incorporated at the trigonal sites in the sp^2 carbon network. In particular, the position of the main π^* resonance at 195 eV is typically observed in an h-BN and multi-walled BN nanotube system [184]. No N-K edge was observed in the synthesised nanomaterial, indicating that there is no presence of an h-BN network.

From the aforementioned observations, it can be concluded that the majority of the boron in the as-produced BC nanotubes had been incorporated into the sp^2 CNTs network

in the form of the sp^2-bonded B-C hybridisation. It should be noted that nearly identical EELS spectra were observed for many EELS runs at different probe positions for the same sample, indicating that the as-synthesised BC nanotubes had uniform boron doping distribution.

Adsorption mapping was conducted to show the distribution of the elements on the synthesised nanotube with the representative ADF-STEM image depicted in Figure 3.20E. The K-edge values of boron, carbon, and nitrogen were mapped, corresponding to Figure 3.20F to H, respectively. Boron and carbon were indeed distributed uniformly along the nanotube structure, indicating that neither single-component boron, or carbon nanotube, or heterogeneous coatings were synthesised. Strong intensity signals were seen from boron and nitrogen along the nanotube while no signal of nitrogen is observed. This showed that the absence of nitrogen precursor enabled carbon to form a bond with boron, leading to the synthesis of boron-doped CNT. The absence of a carbon coating suggested that carbon-sheet formation did not occur on the surface of the nanotube. This further confirmed that carbon from methane was dissolved in the catalyst and allowed to precipitate, resulting in the formation of carbon sheets with boron doping in the final structure.

3.3.5 Electronic and thermal properties

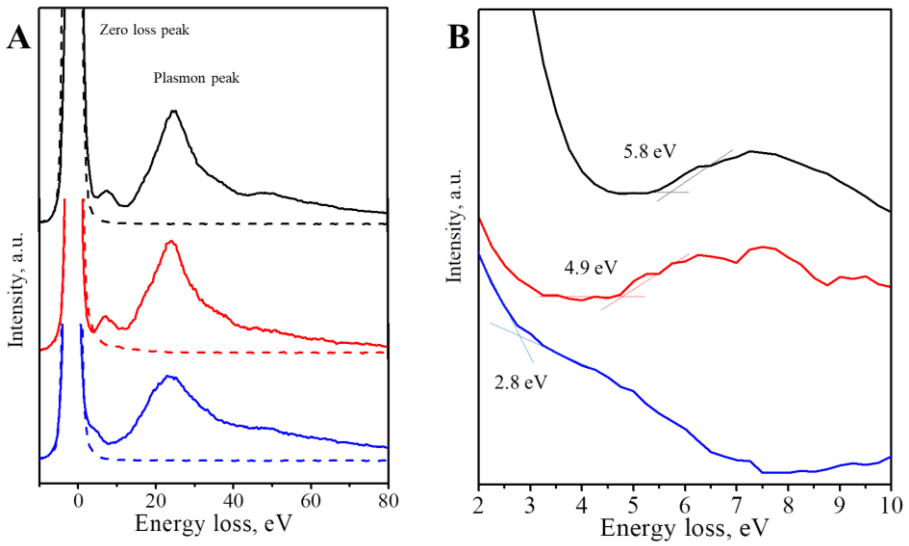


Figure 3.21 *(A) Low-loss EEL spectra of BN nanotube (black), carbon-coated BN nanotube (red), and boron-doped carbon nanotube (blue). Dashed spectra are the zero-point energy loss of corresponding materials. (B) Zoomed-in range for the optical gap measurements of different synthesised materials.*

Figure 3.21A displays the low-loss region of EELS spectrum of BN nanotube (black), carbon-coated BN nanotube (red), and boron-doped carbon nanotube (blue), showing the ZPE and two plasmon peaks from the synthesised materials. The ZLP was then followed with low- and high-intensity peaks that were assigned to the π and π + σ plasmon. The optical band gap in individual nanotubes was measured at the intersection between the flat background and the line fitting the slope of the π peak of the low energy EELS as shown in Figure 3.21B. The removal of the zero loss peak for band gap was done by subtraction of a zero-loss spectrum acquired on vacuum under the same conditions similar to the report by Arenal *et al.* [174]. The measurements were done on 4 different samples of each nanostructure.

The optical band gap of the BNNTs synthesised in this work was found to be 5.80 ± 0.2 eV and is in good agreement with the optical band gap of single-walled BNNTs investigated by Arenal *et al.* with a value of 5.80 eV [196]. This also confirms that the

properties of BN nanotubes, particularly the optical band gap, do not depend on the number of their walls, their diameter, or their chirality, as reported in both theoretical and experimental studies of BNNTs [41, 197, 198].

Interestingly, aside from doping BN nanotubes to modify the optical band gap [93, 94], this work has found that the optical band gap can be shifted by coating BN nanotubes with carbon with a measured value of 4.9 ± 0.3 eV. The boron-doped carbon nanotubes showed an optical band gap of 2.8 ± 0.3 eV. This observation is in accordance with the report by Bangert *et al*. [199], which showed that the substitution of boron in carbon layers of carbon nanotubes exhibits plasmon at ca. 2.5 eV. The development of π plasmon indicates optical band gap tunability since pristine CNTs have no plasmons at energies below 6 eV. In comparison to its carbon counter-part, the band gap of carbon nanotube strongly depends on the number of walls, diameter, and the chirality of the nanotube. As reported by Ouyang et al. zigzag tubes were found to have energy gaps that depend inversely on the square of the tube radius with obtained values of 0.080 eV for (9,0), 0.042 eV for (12,0), and 0.029 for (15,0) nanotubes while armchair tubes showed to have no energy gaps [200]. Thus, the nanotubes synthesized in this study show a more controllable tuning of band gap with a wider range from insulator to semi-conducting properties.

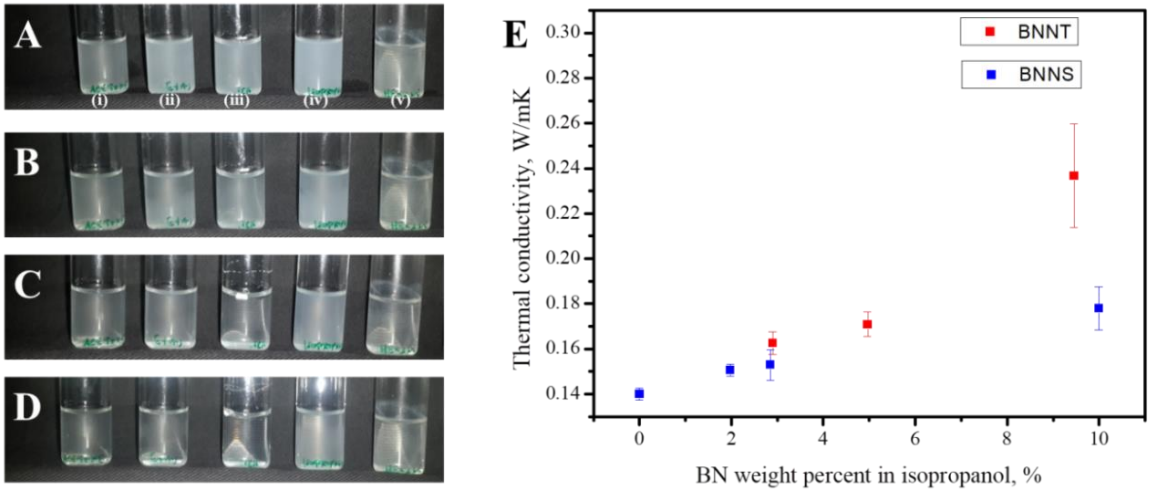


Figure 3.22 *Photograph images of BN nanotubes dispersed in (i) acetone, (ii) ethanol, (iii) water, (iv) isopropanol, and (v) hexane at (A) 0 mins, (B) 40 mins, (C) 80 mins, and (D) 120 mins. (E) Thermal conductivity measurement of BN nanotubes (red) and BN nanosheets (blue) in isopropanol at different weight percentages.*

Prior to thermal conductivity measurements, the dispersion of the BN nanomaterials at different solvents was investigated. Figure 3.22A shows the dispersion of BNNTs in (i) acetone, (ii) ethanol, (iii) water, (iv) isopropanol, and (v) hexane that were left to stand for 40, 80, and 120 mins, where isopropanol showed good stability of dispersion as a function of time. Therefore, isopropanol was used for measuring the thermal conductivity of the synthesised BN nanomaterials. Figure 3.22B shows the thermal conductivity of BNNTs (red) and BN nanosheets (blue) at different weight percentages. Pure isopropanol was shown to have a thermal conductivity of 0.14 ± 0.003 $Wm^{-1}K^{-1}$. At 3 wt. % addition of BN nanotubes or nanosheets, an increase in thermal conductivity was observed. However, BNNTs were observed to have a higher increase in thermal conductivity, an improvement that was clearly seen at 10 wt. %. The greater thermal conductivity enhancement of BNNTs compared to BN nanosheets can be explained by the thermal transport path of the two morphologies. In particular, the nanotube exhibits a high aspect ratio owing to its 1D structure, which offers a more efficient thermal transport path and greater contact. As presented in the literature review in

section 1.3.4.1, comparing the obtained thermal conductivity enhancement results to other nanomaterials of similar structural features, water-based CNT of 1 wt. % was reported to have thermal conductivity enhancement of 17.24 % [101] showing that BNNT had a lower thermal conductivity enhancement even at 3 wt. % for isopropanol-based with a value of 16.14 %. A 25.59 % thermal conductivity enhancement was reported from a 1.79 wt. % of 100 µm silver nanowire in ethylene glycol was reported by Zhu *et al.* [102] which is 1.48 times higher than the 3 wt. % of BNNT in isopropanol. For the copper oxide nanowire, a 0.6 vol. % in dimethicone gave a 31.25 % thermal conductivity enhancement [103] while 0.63 wt. % of BNNT in isopropanol corresponds to a 21.43 % thermal conductivity enhancement. Graphene which is analogous to BNNS was reported to have a thermal conductivity enhancement of 38.09 % in water at 2 wt. % [201] which is higher than the thermal conductivity enhancement of BNNS in this study with a value of 7.57 %. However, it is important to note that the reported thermal conductivity enhancement by Verma et al. [201] was measured at temperature of 321 K.

These results prove that BN nanomaterials can be used as fillers to improve the thermal conductivity of liquid solutions, which can serve as liquid coolants for thermal management in electronic devices and engines. Although the BN nanomaterials showed to have lower thermal conductivity enhancement compared to its carbon, silver, and copper oxide counter-parts, the additional unique properties of BN nanomaterials such as its electrical resistivity and thermal stability compensate to be as a promising material for thermal management applications. In addition, this study's experiments on the dispersion of BN nanomaterials can serve as a good starting point to investigate how the dispersion of BN nanomaterials affects the thermal conductivity of BN-based composites for thermal interface materials.

3.4 Conclusion

This chapter has demonstrated the synthesis of various BN nanomaterials, specifically BN nanosheets, BN nanobamboos, and hybrid BNNTs. BN nanosheets were synthesised by suppressing the generation of the catalyst droplets achieved through the use of iron oxide and nickel oxide as the metal oxide in the powder precursor mixture. The higher boiling point of the metal reduced from iron oxide and nickel oxide compared to the synthesis temperature of 1,200 °C was found to be responsible for the inefficient formation of the catalyst droplets. BN nanobamboos were synthesised using an iron-rich stainless-steel target substrate. The catalyst droplets were generated through partial melting at the eutectic point of boron and iron that was lower than the synthesis temperature. It was proven that the diameter of the BNNT could reach up to 10 nm by controlling the thickness of the thin film of magnesium borate that served as a source of the catalyst droplets.

The addition of gaseous precursors such as methane for carbon species introduced a hybrid 1D nanostructure resulting in carbon-coated BNNTs. This offers a new route to synthesising new layered 1D nanomaterials such as insulating coated conducting (BN-coated CNT) nanotubes or semi-conducting coated insulating (WS_2-coated BNNT) nanotubes. Furthermore, complex nanostructures such as perpendicularly grown 2D BN nanosheets on 1D BNNTs can be synthesised by utilising BNNTs as substrates in the synthesis of BN nanosheets. This is expected to further enhance thermal dissipation due to the additional thermal transport path, and can lead to significantly improved low-dimensional BN nanomaterials that can be used as fillers for thermal management applications.

Chapter 4

Correlating the experimental and theoretical results in the synthesis of BNNTs

---

This chapter aims to bring together theoretical and experimental perspectives on BNNT synthesis by correlating empirical results to results derived from computational approaches. In particular, it uses density functional theory (DFT) to map the potential energy surface (PES) involved in BNNT nucleation and growth, to obtain information such as the energy barriers for BN bond formation. The first section of this chapter will discuss the calculations performed in order to obtain the PES. It is then followed by an investigation of the mechanisms of breaking the B-B bond of the boron precursor B_2O_2 utilising H_2 and NH_3. The atomic and molecular states of the boron and nitrogen precursors are studied with respect to the nucleation of BN nanomaterials. Lastly, the growth-rate-limiting factor that is determined experimentally will be compared with the calculated energy barriers.

The work described in this chapter was carried out in collaboration with Prof Marcel Swart at the Catalan Institution for Research and Advanced Studies (ICREA) and the Institute of Computational Chemistry and Catalysis (IQCC) of the University of Girona in Catalonia, Spain, using the computing equipment of the Barcelona Supercomputing Centre, and funding from the HPC-Europa3 programme.

4.1 Introduction

The extremely high temperature conditions in the synthesis of BNNTs constitute a major roadblock in the direct investigation of the nucleation and growth of this material. Although *in situ* TEM imaging of CNT growth has been reported [202, 203], these studies have been performed under temperature conditions below 900 K, which is much lower than the synthesis temperature of BNNTs at 1,473 K. The laser-based techniques that have recently emerged have been applied in high-temperature conditions [204-206] and can be used in *in situ* investigations, but are yet to be employed in the study of BNNT synthesis.

Researchers have studied the BNNT synthesis mechanism by means of theoretical calculations. As mentioned in section 1.2.1, McLean *et al*. [17] and Santra *et al*. [18] have attempted to explain the nucleation and growth of BNNTs through these theoretical calculations. However, their calculations were carried out based on molecular dynamics, which relies heavily on classical mechanics, and thereby offers a good visual representation of how the precursor atoms generate the final product, but fails to provide significant information such as electronic energies, energy barriers for BN bonding, and the generation of the hexagonal structure of the BN sheet. In order to achieve better representation of the nature and chemistry of atoms and molecules, first-principle calculations based on quantum mechanics must be applied. These calculations are usually conducted using the density functional theory (DFT) or the theory of density functional tight binding (DFTB).

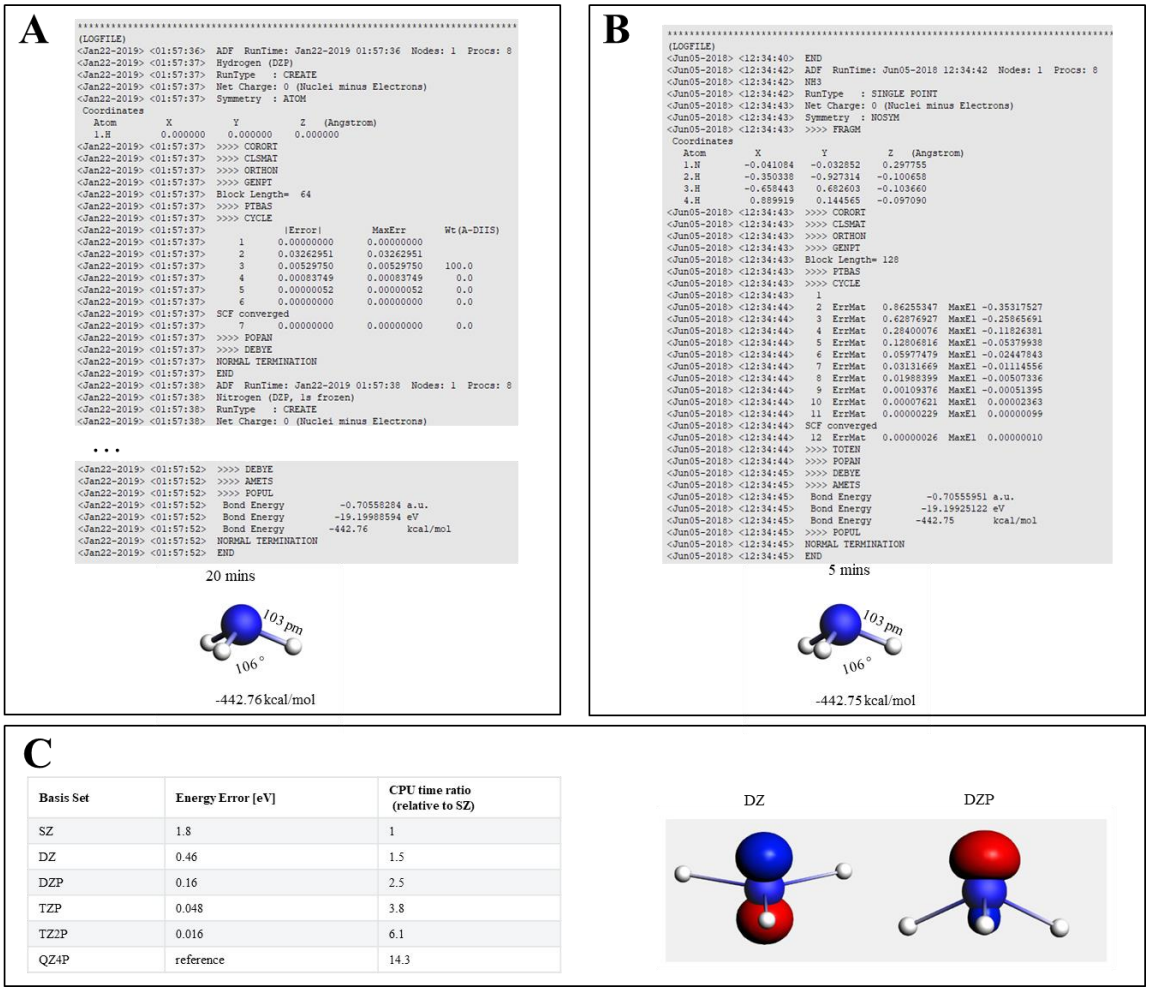
In section 1.3.5, Riikonen *et al.* utilized DFT to investigate BN reactions on the surface of iron[118] and magnesium[119]. However, their results lack a direct correlation with empirical data and the focus of their studies investigate individual boron and nitrogen atoms. In addition to the atomic boron and nitrogen atoms, this chapter provides DFT calculations of the formation of hexagonal BN from molecular boron and nitrogen

precursors, which are B_2O_2 and NH_3, respectively. Calculated energy barriers in the formation of BN bonds in the presence and absence of catalyst are found to be in good agreement with the empirical results. The preference of the zigzag chirality of BNNT is also addressed in this chapter through the stability of BN bond formation at different surface of the catalyst. Finally, the activation energy for the growth of BNNT was obtained by correlation of the growth rate and the Arrhenius equation.

4.2 Computational details

All DFT and DFTB calculations were performed with the Amsterdam Density Functional (ADF) suite programme [207, 208]. Geometries were optimised with the QUILD programme [209] using adapted delocalized coordinates [210] until the maximum gradient component was less than 10^{-4} a.u. The core electrons (e.g. 1s for the second period, 1s2s2p for the third period) were treated with the frozen core (FC) approximation [208]. Energies and gradients were calculated using the BP86-D3/DZP level of theory and were further compared with S12g/TZ2P level of theory [211, 212].

Quantum-regions Interconnected by Local Descriptions [209], known as QUILD, is a subprogramme of ADF developed by Marcel Swart and Matthias Bickelhaupt that allows calculations through multi-level approaches, acquired by applying different computational treatments to different regions of the system under study. QUILD constructs automatically a set of internal coordinates, using the delocalized coordinates to perform geometry optimization that determines the equilibrium and transition state structures. The QUILD programme constructs all input files for ADF, runs ADF, and collects all data; ADF is used only for the generation of the energy and gradients.



Basis Set	Energy Error [eV]	CPU time ratio (relative to SZ)
SZ	1.8	1
DZ	0.46	1.5
DZP	0.16	2.5
TZP	0.048	3.8
TZ2P	0.016	6.1
QZ4P	reference	14.3

Figure 4.1 *Comparison of the computational features between (A) traditional DFT using the ADF programme and (B) DFT using QUILD as a wrapper around the ADF programme, showing that similar results are obtained in geometry optimisation of ammonia but for less computational time. (C) Shows the level of basis set with corresponding energy error and CPU time ratio relative to SZ. Trigonal planar geometry is obtained for geometry optimisation of ammonia using DZ while DZP results in a trigonal pyramidal shape.*

Figure 4.1 shows the computational features comparing traditional DFT calculations using the ADF programme alone, and the same calculations with QUILD serving as a wrapper around the ADF programme, Figure 4.1A and B, respectively. The calculations for locating the minimum energy (geometry optimisation) for ammonia showed similar results, i.e. N-H bond distance of 103 pm, H-N-H bond angle of 106° and bond energies of -442.76 kcal/mol. However, QUILD performed the calculation in ca. 5 mins while the former took 20 mins. This significant difference in computational

capability is a great advantage when performing calculations for a larger system, such as obtaining the energies of different catalyst surfaces, and investigating reactions on these surfaces. It is also important to note that the use of different basis sets affects the accuracy of the calculation. As seen in Figure 4.1C, using different basis sets results in different energy errors, showing that a higher level of accuracy yields fewer energy errors. However, utilising a basis set with a higher level of precision requires higher CPU time consumption. When the geometry optimisation of ammonia was calculated for this study at DZ and DZP basis sets, the former obtained a trigonal planar geometry while the latter resulted in a trigonal pyramidal shape, indicating that the use of the DZP basis set can more correctly represent the structures of molecules in a chemical reaction. DZ stands for Double-zeta that is a basis sets without polarization functions and provides a rather poor expansion basis for the true (numerically computed) atomic orbital. On the other hand, DZP stands for Double zeta polarized basis sets. The basis sets in DZP are derived from DZ, extended with a polarization function. Adding functions such as polarization functions allow to expand the basis set and to obtain more accurate results.

4.2.1 Potential energy surface calculation

A reaction usually has a double-well energy surface where the reactant complex and the product complex are separated by a central barrier, which is the transition state (TS‡) schematically presented in Figure 4.2.

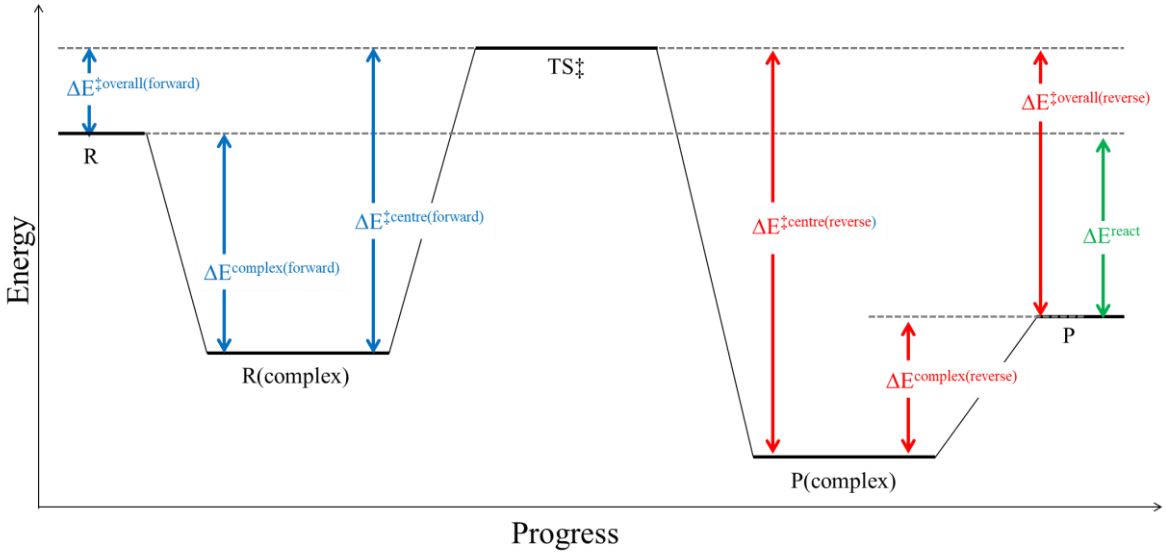


Figure 4.2 *Schematic illustration of a typical double-well energy surface where R is the reactant, R(complex) is the reactant-complex, TS‡ is the transition state, P(complex) is the product-complex, and P is the product.*

$\Delta E^{\ddagger,overall,(forward)}$ is the energy difference between the transition state and the reactant, $\Delta E^{complex,(forward)}$ is the energy difference between the reactant-complex and the reactant, and $\Delta E^{\ddagger,centre,(forward)}$ is the energy difference between the transition state and the reactant-complex. The same assignment with the reverse notation is true for the product. The energy barrier is determined by obtaining the value of $\Delta E^{\ddagger,centre,(forward)}$ and $\Delta E^{\ddagger,complex,(forward)}$. ΔE^{react} is the energy difference between the product and the reactant, which is the change of the total energy of the reaction that predicts the nature of the chemical reaction. In this particular illustration, the chemical reaction is exothermic due to the decrease in energy from the reactant to the product.

The reaction energies (ΔE^{react}) presented in this chapter are energy differences for specific systems. They do not include zero-point or vibrational finite temperature corrections [213]. Vibrational frequencies were calculated for select systems so that the change of Gibbs free energy (ΔG) could be obtained for select reactions at 1 atm and 298 K, where all of the species corresponding to local minima were verified.

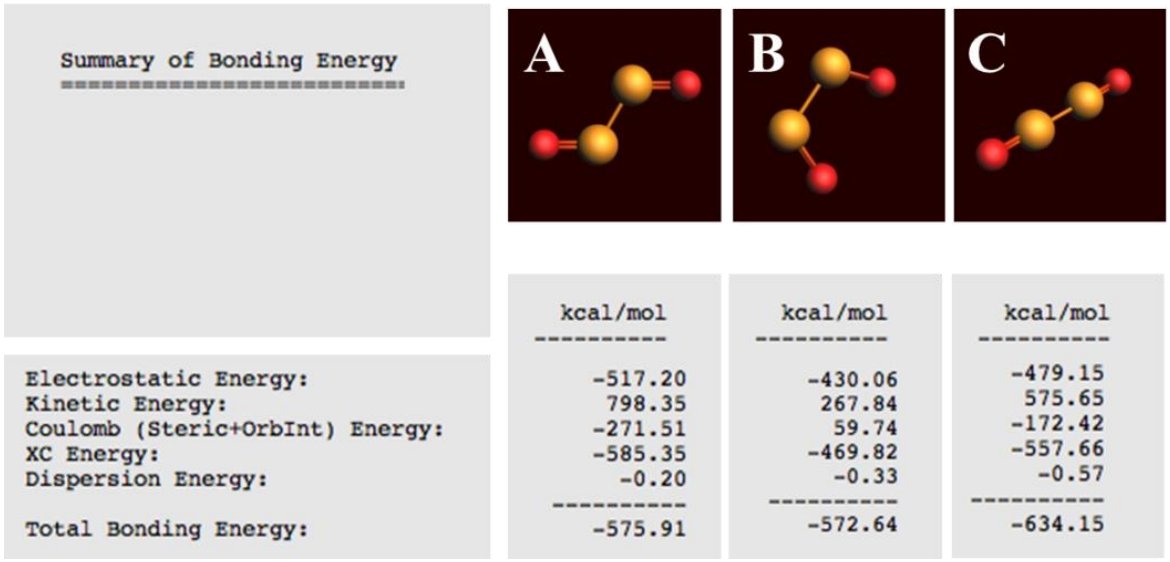


Figure 4.3 *Computed total bond energy of different conformation of B_2O_2; (A) trans, (B) cis, and (C) linear showing that linear conformation of B_2O_2 is the most stable due to its lowest total bond energy value. Colour coding: red is oxygen atom while yellow is boron atom.*

To obtain the conformation of the reactants, particularly the B_2O_2 molecule, bond energy calculation was performed at different conformations as shown in Figure 4.3. Total bonding energy is the sum of the five components namely; (1) Electrostatic interaction energy that is the energy between the fragments of the molecule, (2) Kinetic Energy or Pauli Repulsion refers to the repulsive interactions between the fragments, (3) Coulomb Energy that is accounted to the Steric and Orbital Interaction, 4) XC energy is the energy of the charge density, and (5) dispersion energy which is a correction term coming from dispersion-corrected functional S12g that includes Grimme's D3 dispersion energy [214]. The calculations showed that linear B_2O_2 was the most stable conformation, which is in good agreement with the calculations and experiments reported in the literature [215, 216], and was thus used for investigating the reaction with respect to the nucleation and growth of BNNTs.

4.2.2 $B_2O_2 + H_2$ potential energy surface

In this thesis, following Wang and Huang's method [217] of determining the reactivity of a chemical reaction by mapping the PES, theoretical calculations were also performed to map the PES for the $B_2O_2 + H_2$ reaction, whose results were also later applied to other reactions.

To determine the geometry of the reactant complex, different configurations of the reactant were relaxed while ensuring that the reactants did not form bonds, thus keeping them in the reactant condition. Since the B_2O_2 molecule prefers to have the B-B bond, it was expected that the B-B bond would be broken either by transformation to its monomer BO or insertion of H_2 or NH_3 to form the alternating B-N bond of the hexagonal BN network. In this section, the potential energy surface of the reaction $B_2O_2 + H_2$ will be investigated, particularly the breaking of the B-B bond to form the monomer building block for the hexagonal BN network.

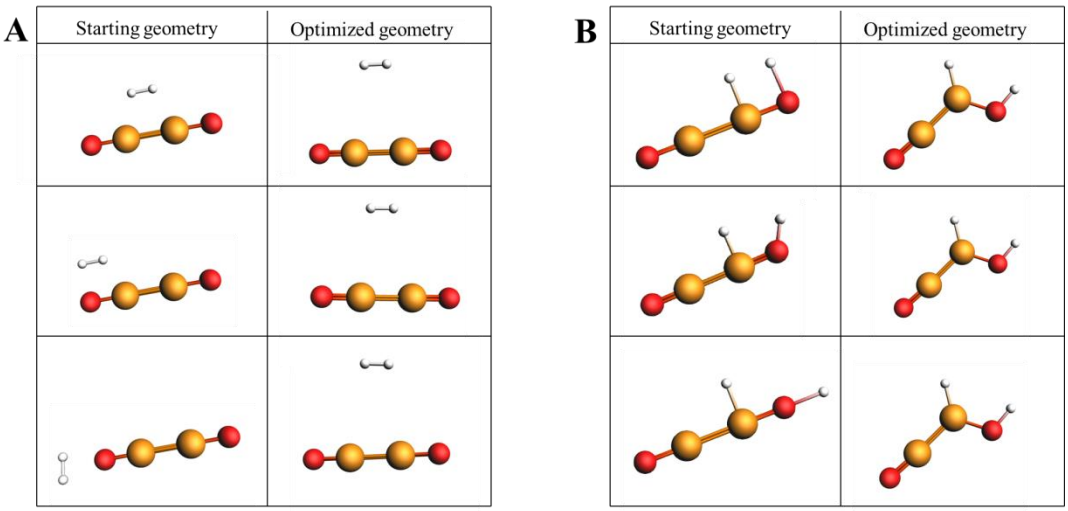


Figure 4.4 *Determining the (A) reactant complex and (B) product of different configurations for the binding of the hydrogen molecule to B_2O_2. Colour coding: white is hydrogen atom, red is oxygen, and yellow is boron.*

The optimised geometries of H_2 and B_2O_2 were brought closer to each other to obtain the reactant complex. As shown in Figure 4.4, three different starting geometries were optimised: first, where H_2 was on top of the B-B bond of B_2O_2 with an H-B distance of 160 pm, second, where H_2 was on top of the BO bond with an H-B (or H-O) distance of 134 pm, and third, where H_2 was located on the oxygen of B_2O_2 both with an H-O distance of 157 pm. All the three starting geometries were shown to have converged in a similar geometry, where H_2 was found at the top of the B-B bond with an H-B distance of 295 pm and an energy value of -784.97 kcal/mol. No change of bond distances of the individual molecule was observed.

For the product geometry shown in Figure 4.4B, the hydrogen atoms were bonded on boron and oxygen with a corresponding bond distance of 100 pm. The hydrogen bonded to boron, i.e. B-B-H, was kept at a 90° angle, while the angle of hydrogen bonded to oxygen, i.e. B-O-H, was varied from 90° to 180°. The three different structures converged into one similar structure where the bond angle of the B-B-O changed from an angle of 180° to 117°, accommodating the hydrogen bonded to boron with a bond distance of 120 pm. Meanwhile, the hydrogen bonded to oxygen was shown to have a smaller bond distance of 98 pm and a bond angle of the B-O-H of 113°. The energy calculated for the converged structure was -798.79 kcal/mol. These structures were later used as the initial and final structures to obtain the transition state via linear transit calculation.

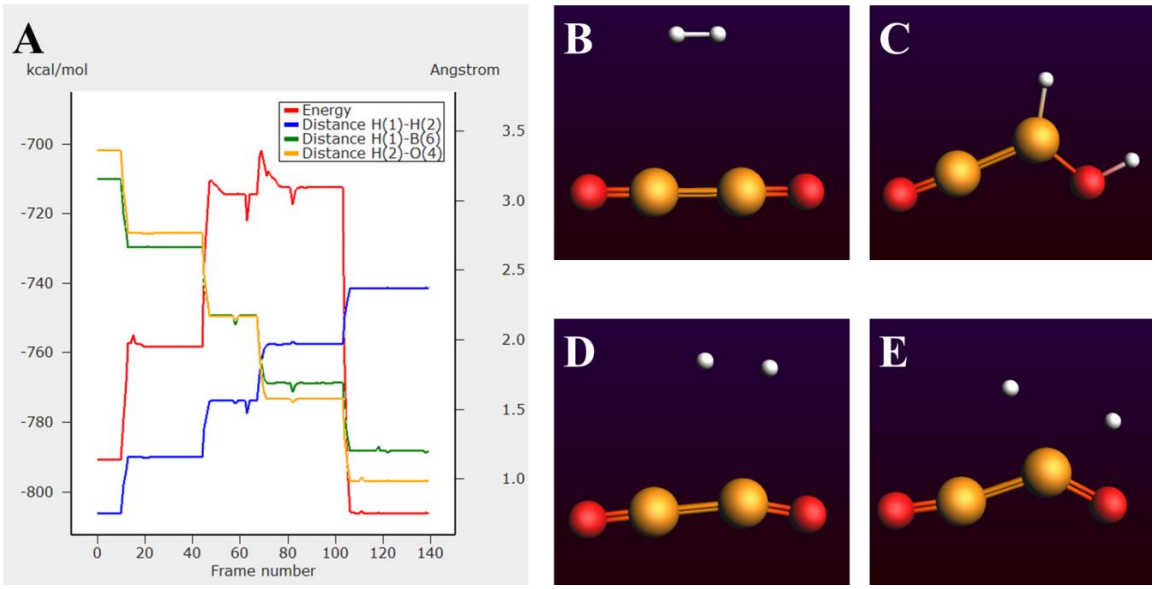


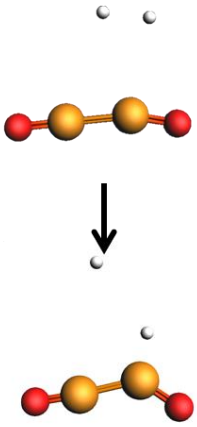
Figure 4.5 *Linear transit calculation showing the plot of (A) energy as a function of distance change of the hydrogen molecule binding to B_2O_2. Line plots corresponding to the energy of changing atomic coordinates (red), hydrogen-hydrogen bond (blue), hydrogen-boron bond, and hydrogen-oxygen bond (yellow). Optimised geometry of (B) reactant and (C) product (green). Representative geometries having higher energy compared to the reactant and product at (D) -760 kcal/mol and (E) -710 kcal/mol. These geometries are good guesses for the transition state for the bonding of hydrogen in B_2O_2.*

Linear transit (LT) calculation is defined as the simultaneous linear change of atomic coordinates from the initial to the final structure of a reaction. Therefore, an LT calculation is essentially a sequence of constrained geometry optimisation that can be used to sketch an approximate path over transition states between the reactants and the products. From this calculation, a reasonable guess for the transition state can be acquired that may serve as a starting point for a search for the true transition state. As shown in Figure 4.5, an LT run was conducted using the optimised reactant H_2 and B_2O_2 complex going to the optimised product of cis-OBB(H)OH. Figure 4.5A shows a plot of the change of reaction coordinates of H-H, H-B, and H-O with the corresponding energy value, blue, green, yellow, and red, respectively. Figure 4.5B and C show the geometry structures of the initial and final products, which are closely similar to the optimised structures mentioned in the previous figure. In between the initial and final structures are two generally high-

energy profiles located at ca. -760 kcal/mol and -710 kcal/mol. Representative structures located in the high-energy profiles were subjected to the transition state calculation shown in Figure 4.5D and E.

A

Stp#	Energy (kcal/mol)	Gmax,adf (a.u.)	Grms,adf (a.u.)	Gmax,deloc. (a.u.)	Grms,deloc. (a.u.)	SymGeo	SymOrb	#negH
1	-752.3750	0.089193	0.026181	0.078072	0.021289	-	NOSYM	1
2	-753.7666	0.089135	0.026128	0.077743	0.021217	-	NOSYM	1
3	-749.0283	0.089347	0.026184	0.077937	0.021300	-	NOSYM	0
4	-746.9855	0.089194	0.026096	0.077378	0.021119	-	NOSYM	1
5	-746.7997	0.088756	0.026070	0.077004	0.021020	-	NOSYM	1
...								
42	-686.8344	0.018753	0.007324	0.023172	0.006057	-	NOSYM	1
43	-688.0939	0.019880	0.007581	0.023384	0.006206	-	NOSYM	1
44	-686.7345	0.018596	0.007105	0.022162	0.005885	-	NOSYM	1
45	-685.4982	0.017399	0.006739	0.021030	0.005560	-	NOSYM	1
46	-684.3767	0.016436	0.006359	0.019918	0.005273	-	NOSYM	1
47	-683.3719	0.015505	0.006034	0.018937	0.005006	-	NOSYM	1
48	-682.4560	0.014722	0.005699	0.018026	0.004762	-	NOSYM	1
49	-681.6278	0.013977	0.005418	0.017230	0.004534	-	NOSYM	1
50	-680.8459	0.013322	0.005107	0.009183	0.004769	-	NOSYM	1
51	-681.8366	0.014686	0.005250	0.008808	0.004770	-	NOSYM	1
52	-681.8366	0.014686	0.005250	0.008808	0.004770	-	NOSYM	1



B

Stp#	Energy (kcal/mol)	Gmax,adf (a.u.)	Grms,adf (a.u.)	Gmax,deloc. (a.u.)	Grms,deloc. (a.u.)	SymGeo	SymOrb	#negH
1	-745.1353	0.024066	0.008023	0.011428	0.005646	-	NOSYM	1
2	-745.8552	0.008880	0.003307	0.007256	0.002730	-	NOSYM	2
3	-746.2243	0.010676	0.003687	0.005765	0.002795	-	NOSYM	2
4	-746.9249	0.016928	0.005578	0.009335	0.004095	-	NOSYM	2
5	-747.2444	0.023025	0.008007	0.012505	0.005906	-	NOSYM	1
6	-746.3665	0.010340	0.003559	0.005417	0.002638	-	NOSYM	1
7	-746.2605	0.003828	0.000930	0.002093	0.000648	-	NOSYM	1
8	-746.2823	0.005166	0.001520	0.003190	0.001129	-	NOSYM	1
9	-746.2340	0.004106	0.001110	0.002523	0.000762	-	NOSYM	1
10	-746.2697	0.002947	0.000951	0.002121	0.000714	-	NOSYM	1
11	-746.2812	0.000768	0.000256	0.000341	0.000189	-	NOSYM	1
12	-746.2804	0.000700	0.000185	0.000318	0.000153	-	NOSYM	1
13	-746.2814	0.000089	0.000037	0.000194	0.000049	-	C(S)	1
14	-746.2814	0.000059	0.000017	0.000109	0.000026	-	C(S)	1
15	-746.2813	0.000026	0.000010	0.000022	0.000007	-	C(S)	1

Geometry CONVERGED !!!
Energy at optimized geometry : -746.2813 (kcal/mol)

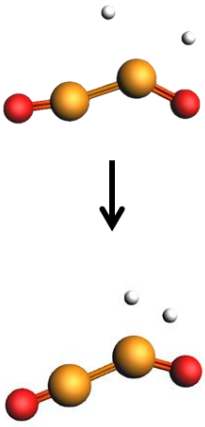


Figure 4.6 *Transition state calculation of the (A) 1st and (B) 2nd transition state geometry guess. Calculation indicates that the 1st geometry does not achieve geometry convergence compared to the 2nd geometry. Furthermore, the 2nd geometry showed only 1 negative Hessian value after convergence with a lesser geometry change from the initial geometry input.*

A transition state (TS) calculation is closely related to energy minimisation of a given structure. The main goal for a TS calculation is to find a stationary point on the energy surface based on monitoring the energy gradient that should disappear. The main

difference between a TS calculation and a geometry optimisation (minimisation of energy) is that a negative value for the Hessian matrix is present for the transition state.

Figure 4.6 shows the transition state calculation of the two geometries expected to be the transition state of the reaction $B_2O_2 + H_2$, which was acquired from the LT calculation. The representative geometry located at ca. -760 kcal/mol did not converge after 52 steps and showed that the geometry had a large deviation from its initial structure as shown in Figure 4.6A. The H-H distance had increased significantly from 115 pm to 234 pm. The hydrogen that was expected to bond with boron showed an increase in distance from 266 pm to 340 pm while the hydrogen that should bond to the oxygen showed a decrease in distance from 276 pm to 217 pm. This hydrogen atom also went closer to boron, moving to a distance of 130 pm. Thus, this geometry was not expected to be the true transition state of the reaction due to two reasons: the significant change of geometry after TS calculation, and the calculation of energy gradient showing no indication of disappearing.

On the other hand, the second representative geometry located at the higher energy, -710 kcal/mol, was shown to have converged with a lesser change of geometry from the initial state. The H-H distance was shown to have decreased with a changed value of 94 pm. The decrease in distance was also observed in the hydrogen that bonded to its corresponding atom, boron or oxygen, with decreased values of 54 pm and 18 pm, respectively. The converged calculation was also shown to have 1 negative Hessian value, indicating that it was on a saddle point of the energy surface, with a calculated energy value of -746.28 kcal/mol.

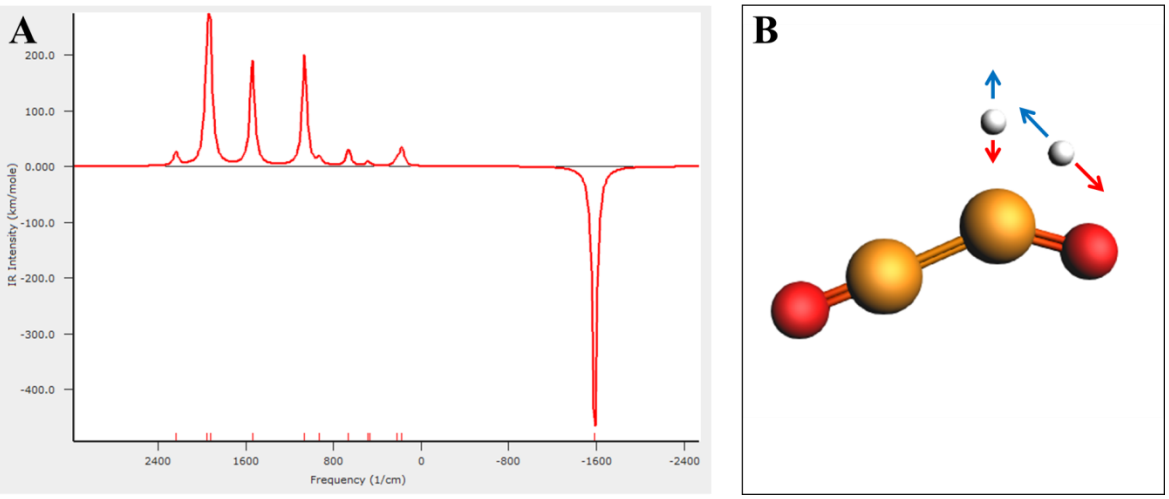


Figure 4.7 *Frequency calculation obtained from the converged TS calculation showing the (A) IR spectra and (B) vibration at -1,584 cm^{-1} portrayed by arrows indicating a true TS structure due to one and only one imaginary frequency.*

A TS is a first order saddle point on a potential energy surface. The vibrational spectrum of a TS is characterised by one and only one imaginary frequency, which means that in one direction in the nuclear configuration in space, the energy is at a maximum, and at a minimum in all other directions. In ADF, phonons are treated as collective oscillations of atoms around their equilibrium positions. Phonons are calculated within the standard harmonic theory implemented with a finite difference method [218]. To verify the stationary point of a TS, a vibrational frequency calculation was conducted at the same computational level with the reactant and product. The normal mode corresponding to the imaginary frequency in the TS usually reflects the change of geometry from the reactants going to the products. As shown in Figure 4.7, the frequency calculation was performed from the acquired TS geometry showing the vibrations of the geometry represented by IR spectra (Figure 4.7A), indicating only one imaginary frequency located at -1584 cm^{-1}. Figure 4.7B shows the corresponding vibration at -1584 cm^{-1}, where the two hydrogen atoms exhibited symmetric vibrations represented by the arrows. As a characteristic of the TS, the vibration corresponding to the blue arrows indicated the geometry of the reactant state while the red arrows designated the product state. Thus, the frequency calculation

confirmed that the geometry obtained from the LT and TS calculations was indeed the TS of the H_2 molecule binding with the B_2O_2 molecule.

Table 4.1 Vibrational frequencies and corresponding energies of various compounds in the H_2 + B_2O_2 reaction.

Species	Frequency	Energy, kcal/mol
B_2O_2 + H_2 (cmpx)	48.85, 172.03, 177.38, 195.46, 230.87, 322.40. 454.22, 458.51, 597.59, 1874.94, 2046.14, 4287	-784.97
TS1	*-1586.44*, 175.42, 221.69, 474.81, 500.90, 663.32, 928.72, 1076.19, 1549.84, 1926.33, 1957.37, 2230.91	-746.28
cis-OBB(H)OH	177.35, 264.60, 469.01, 637.53, 687.90, 881.72, 981.30, 1142.39, 1322.62, 1930.56, 2562.46, 3604.83	-798.79
TS2	*-889.69*, 161.55, 255.84, 460.12, 488.93, 696.46, 819.19, 1087.72, 1288.22, 1911.06, 2493.87, 3860.94	-790.58
trans-OBB(H)OH	159.51, 267.89, 487.19, 660.98, 684.97, 866.34, 983.81, 1152.95, 1299.60, 1923.33, 2596.44, 3609.46	-798.61
TS3	*-1641.37*, 161.78, 178.25, 402.74, 458.68, 659.17, 753.43, 972.44, 1493.43, 1885.71, 1945.17, 2598.16	-749.04
OBH + OBH (cmpx)	74.47, 75.19, 107.62, 134.50, 732.99, 734.76, 743.00, 745.46, 1774.02, 1782.14, 2858.14, 2858.37	-795.18

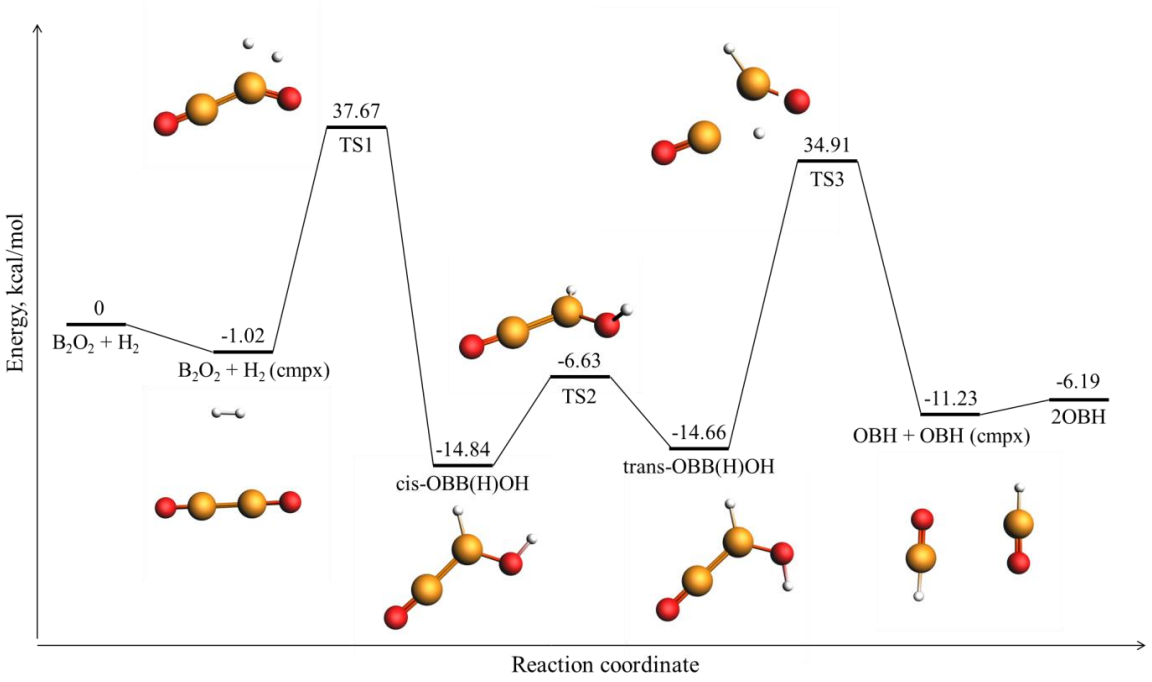


Figure 4.8 *Potential energy diagram of hydrogen breaking the B-B bond of the B_2O_2 boron precursor molecule.*

Table 4.1 presents the calculated vibrational frequencies of the H_2 + B_2O_2 reaction with corresponding energies, while Figure 4.8 shows the potential energy diagram along the reaction path. The mechanism investigated followed the attack of H_2 molecule on the BO fragment of B_2O_2 proceeding via transition state TS1 with an energy barrier of 38.69 kcal/mol. This reaction led to the formation of cis-OBB(H)OH configuration with an energy value that was -14.84 kcal/mol lower than that of the reactants. The cis-OBB(H)OH could then isomerise to a trans configuration by rotation of the dihedral angle B-B-O-H from a 180° to a 0° fragment corresponding to the TS2 with an energy barrier of 8.21 kcal/mol. The trans-OBB(H)OH was shown to have less stable energy, having an energy value that is 0.18 kcal/mol higher than that of cis-OBB(H)OH. The dissociation of two OBH molecules took place via the migration of the hydrogen from the oxygen to the boron, accompanied by a cleavage of the B-B bond. This process involved an energy barrier of 49.57 kcal/mol. The overall reaction was exothermic by -6.19 kcal/mol.

4.2.3 B_2O_2 + NH_3 potential energy surface

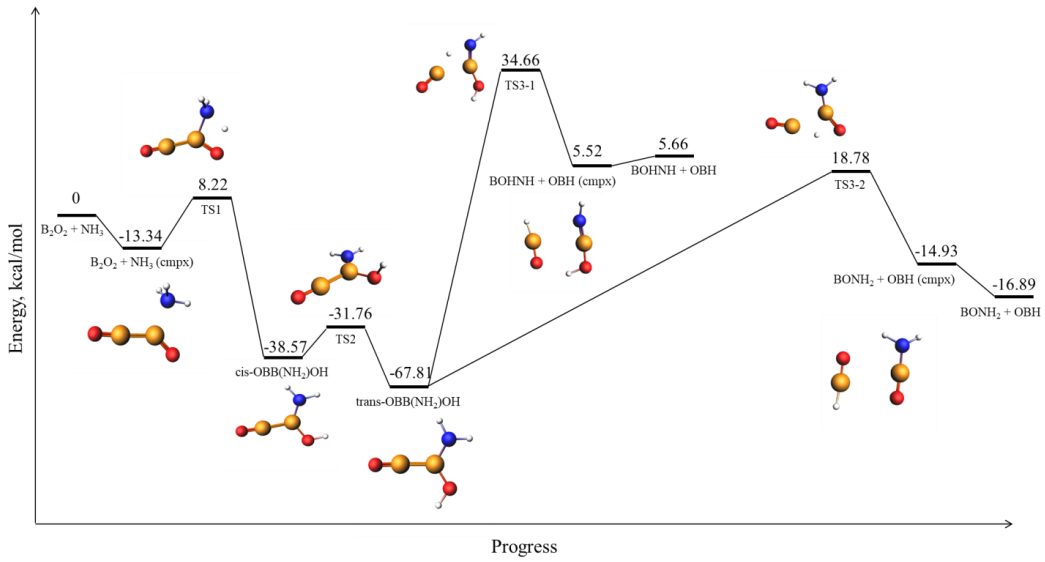


Figure 4.9 *Potential energy diagram of ammonia breaking the B-B bond of the B_2O_2 boron precursor molecule.*

The breaking of the B-B bond of the boron intermediate precursor was further investigated by using the ammonia and potential energy diagram shown in Figure 4.9. This diagram also provides insight into the formation of the B-N bonding, which is the initial state for the formation of the alternating B-N bonding towards the formation of the hexagonal BN network of the BN nanomaterial. The ammonia and B_2O_2 was shown to have a reactant complex, where the nitrogen of ammonia moved closer to the boron of the B_2O_2 with a distance of 176 pm and a bond angle change of the B-B-O from 180° to 136°. This B_2O_2 + NH_3 reactant complex was shown to have a more stable energy of -13.34 kcal/mol compared to the reactants alone. This reactant complex led to the formation of the B-N bond following a configuration of cis-OBB(NH_2)OH with the migration of one hydrogen from ammonia to the oxygen of B_2O_2 via TS1 having a barrier energy of 21.56 kcal/mol. The dihedral angle of B-B-O-H could than change from 180° to 0° via TS2 with an energy barrier of 6.81 kcal/mol leading to the formation of the trans-OBB(NH_2)OH. The rotation of the dihedral angle of B-B-O-H was observed to be an exothermic reaction, in contrast to the H_2 + B_2O_2 reaction mechanism, indicating that the amine group at cis-OBB(NH_2)OH had an effect on stability that could have been due to the higher electron density of the amine compared to the hydrogen atom alone. This stability was shown to have a significant difference in energy, with a value of -27.24 kcal/mol.

Two channels for breaking the B-B bond were then studied: one involved the migration of hydrogen from amine and another involved the migration of hydrogen from the hydroxyl group. The B-B bond dissociation via hydrogen from the amine group was shown to have an energy barrier of 102.47 kcal/mol leading to the formation of the product HOBNH + OBH complex through TS3-1. However, the B-B bond breaking via hydrogen from hydroxyl group was shown to have an energy barrier of 86.59 kcal/mol that produced

the $OBNH_2$ + OBH complex following the TS3-2. Although both mechanisms of B-B bond breaking were observed to be an endothermic reaction with respect to the trans-$OBB(NH_2)OH$ as reactant, an overall exothermic reaction was observed for B-B bond breaking via hydrogen from the hydroxyl group in terms of the molecular precursor B_2O_2 + NH_3 with an energy of -16.89 kcal/mol, while an overall endothermic reaction was calculated for B-B bond breaking via hydrogen from the amine group, resulting in an energy value of 5.6 kcal/mol. This indicates that the former pathway was likely to proceed, leading to the formation of a B-N bond and possibly the building blocks for further generation of the hexagonal B-N network of any BN nanomaterial.

In comparing the obtained energy barriers for molecular hydrogen and ammonia, it was observed that the H_2 molecule, with its lower barrier energy value of 49.57kcal/mol, was more likely to break the B-B bond of the B_2O_2 molecule than ammonia, with its barrier energy value of 86.59 kcal/mol. Kim *et al*. [219] claimed that it was crucial to add hydrogen as a reactant in the synthesis of BNNTs to achieve improved quality and yield. Without the presence of H_2, an abundant amount of amorphous boron was observed with a very low yield of BNNTs. This can be attributed to the recombination of the boron and nitrogen precursors being used. Although Kim *et al*. used a different nitrogen precursor, i.e. N_2, the calculations presented here demonstrate that the H_2 molecule can be a catalyst for the generation of B-N bonding.

Figure 4.10 shows the potential energy diagram of the OBH molecule generated from the H_2 + B_2O_2 reacted with NH_3 to produce the B-N bonding that can serve as the intermediate species for the synthesis of BN nanomaterials. According to McLean *et al*.'s [17] study on the synthesis of BNNT following the BOCVD method, this product is generated from the stoichiometric reaction $B_2O_{2(g)} + 2NH_{3(g)} \rightarrow 2BN_{(s)} + 2H_2O + H_{2(g)}$. It should be noted that in the experimental section of this work, no hydrogen gas was

introduced into the reaction system. However, at high temperature conditions, ammonia can decompose to produce hydrogen [220]. Thus, it is possible for the reaction of NH_3 + OBH to occur in the synthesis of BN nanomaterials.

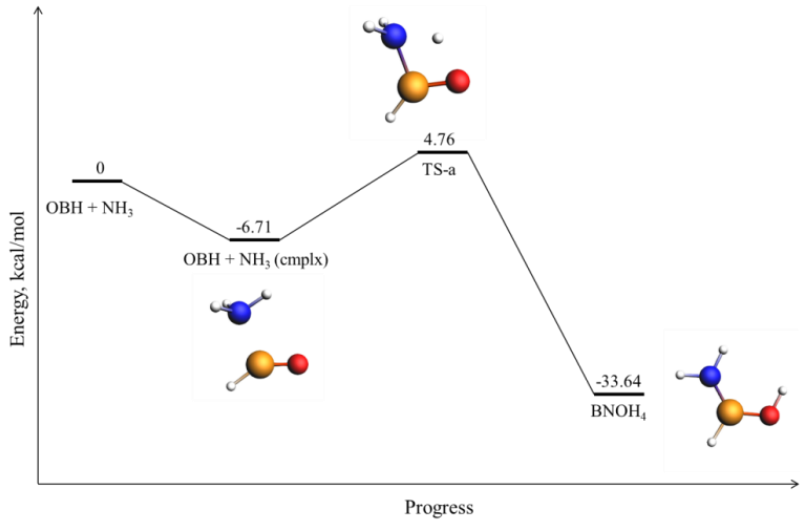


Figure 4.10 *Potential energy diagram of the reaction OBH + NH_3.*

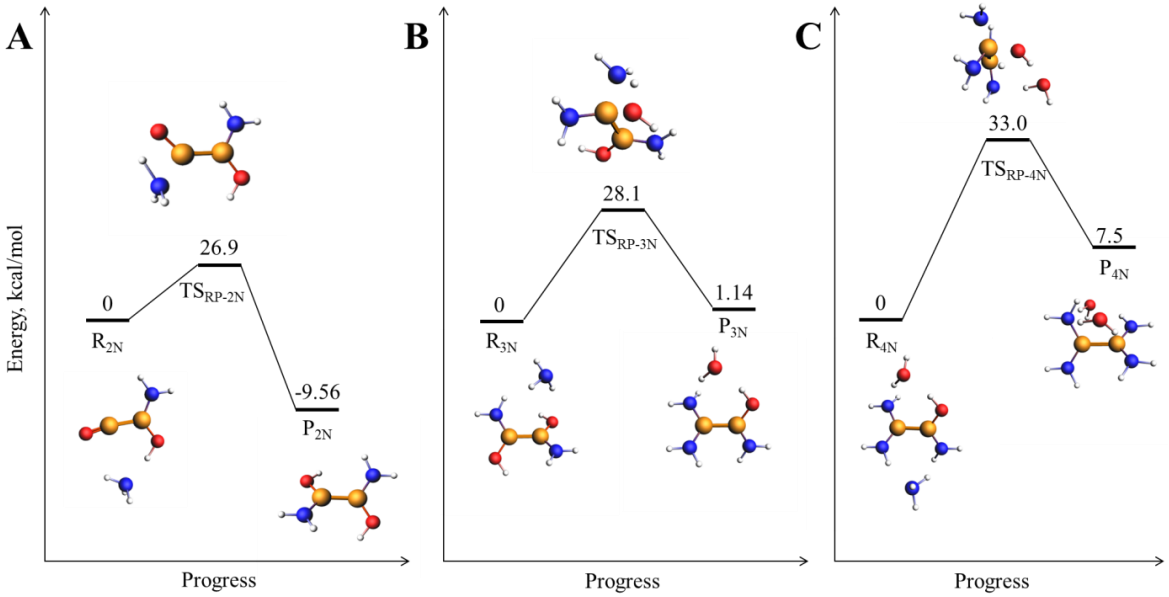


Figure 4.11 *Saturation of B-N bonding of B_2O_2 boron precursor molecule by ammonia showing the potential energy diagram of the (A) 2nd, (B) 3rd, and (C) 4th ammonia introduction. It can be seen that further ammonia reaction with boron oxide increased the energy barrier, which may be due to the water abstraction and weak interaction of incoming ammonia with the hydroxyl group.*

Saturation of B-N bonding by increasing the amount of ammonia in a B_2O_2 molecule is another approach that is investigated with the potential energy diagram shown in Figure 4.11. The second addition of ammonia was shown to attack the boron with less coordination, thus leading to the generation of a trans amine group with an energy barrier of 26.90 kcal/mol via $TS_{RP\text{-}2N}$. A slight increase in the energy barrier is attributed to the weak interaction of the incoming ammonia with the hydroxyl group showing a measured distance of 175 pm. The TS geometry showed that as ammonia got closer to forming the second B-N bond, the parental molecule B_2O_2 changed from a linear to a trans configuration, while the hydrogen atom from ammonia showed an increase in distance from 103 pm to 126 pm, indicating its migration to the oxygen of the trans-$OBB(NH_2)OH$ molecule. The process was shown to be an exothermic reaction with a dihedral bond angle at N-B-B-N of 147°.

The third addition of ammonia to produce the third B-N bond showed an abstraction of the water molecule as seen in Figure 4.11B. The abstraction of the water molecule occurred through the migration of the hydrogen atom from ammonia to the hydroxyl group with a barrier energy of 28.10 kcal/mol. As seen in the reactant complex, the hydrogen atoms of the ammonia tended to be pointing inwards to the trans-$HOB(NH_2)B(NH_2)OH$ molecule. A distance of 235 pm in between the hydrogen atom of the ammonia and the oxygen atom of the hydroxyl group was measured, suggesting that the oxygen preferred to interact with the hydrogen. A similar distance was also measured between the other hydrogen of the ammonia and the hydrogen from the amine group of the trans-$HOB(NH_2)B(NH_2)OH$ molecule, suggesting a weak interaction in the H-H bonding. These weak interactions are conjectured to be the reason behind the increased energy barrier.

The fourth addition of ammonia resulted in the abstraction of the hydroxyl group in the form of water, accommodating the B-N bond formation. The progression of the reaction was shown to be an endothermic reaction with a change of energy of 7.50 kcal/mol.

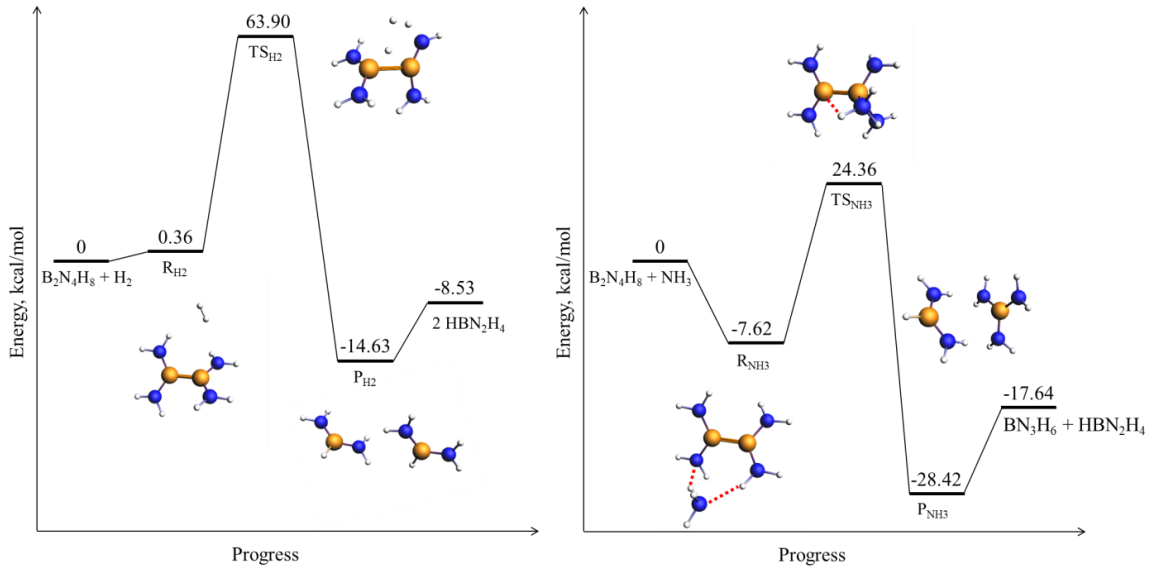


Figure 4.12 *Comparison of energy barrier of (A) hydrogen and (B) ammonia on breaking the B-B bond of the saturated B-N bond of B_2O_2 boron precursor molecule, suggesting that the ammonia molecule is more likely to break the B-B bond than the H_2 molecule.*

After the saturation of B-N bonding of B_2O_2 with ammonia, the breaking of the B-B bond was studied by comparing the hydrogen and ammonia molecule, as shown in Figure 4.12A and B, respectively. The reactant complex of the hydrogen molecule approaching the $B_2N_4H_6$ species where the hydrogen molecule was in close proximity to the B-B bonds, i.e. R_{H2}, showed that the minimum energy had slightly increased from the reactants of 0.36 kcal/mol. The resulting product presented two molecules of HBN_2H_4 where the hydrogen molecule had been dissociated and bonded to the boron atoms via TS_{H2} with an energy barrier of 63.90 kcal/mol and a local minima of the product complex, P_{H2}, of -14.63 kcal/mol. On the other hand, ammonia was shown to have a smaller energy barrier towards the breaking of the B-B bond. The product obtained from reacting

ammonia to the $B_2N_4H_6$ species resulted in BN_3H_6 + HBN_2H_4, which had a product complex P_{NH3} following the TS_{NH3} transition state with a smaller energy barrier of 24.36 kcal/mol.

The significant difference in barrier energies of the two reaction pathways was presumed to come from the hydrogens of the amine groups. For instance, the H_2 molecule already required energy to obtain the reactant complex, and at TS_{H2}, the dissociation of the H_2 molecule showed a possible recombination with the hydrogen from the amine group. This suggested that the H-H interaction of this system contributed to the high-energy barrier in breaking the B-B bond. As for the NH_3, the weak interaction of N-H seemed to serve as a guide for the incoming ammonia to bind to the boron that was indicated by the red dots on the reactant complex R_{NH3}. At TS_{NH3}, the nitrogen from ammonia was now on top of boron and its hydrogen was right on top of the opposite boron, suggesting that a direct dissociation would efficiently generate the products.

4.3 Results and discussion

4.3.1 Modelling the nucleation and growth of BNNTs

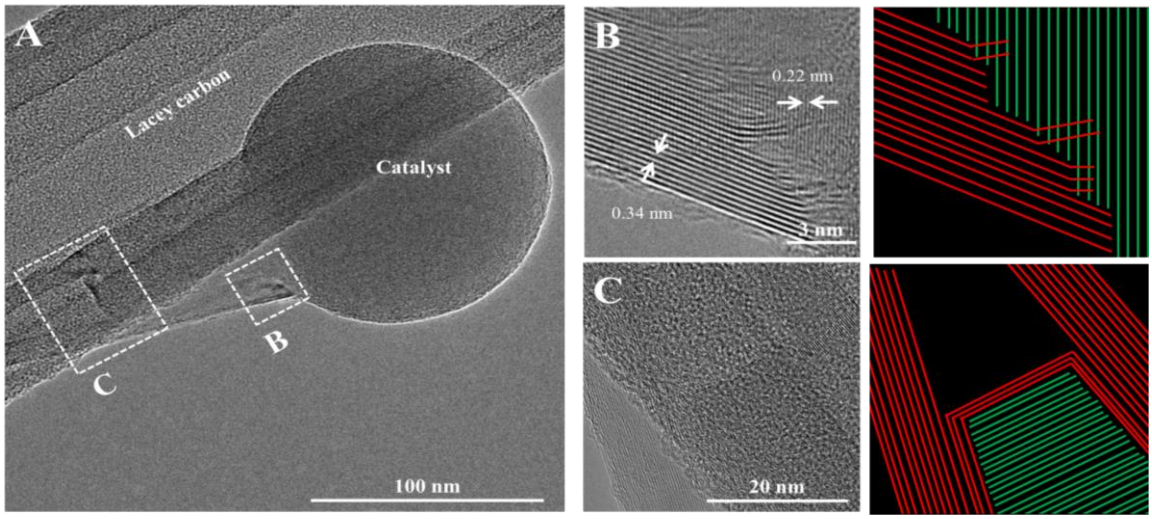


Figure 4.13 *TEM data to model the calculation for the growth of the BNNT. (A) TEM image of the tip of the BN nanotube supported by carbon lacey showing the catalyst and the BN wall of the BNNT. The white dashed square labelled B and C corresponds to the HRTEM image of (B) the interface between the BN wall and the catalyst showing their lattice spacing and (C) the end part of the catalyst with layers of BN, respectively. Right panels depict graphical representations of the HRTEM images.*

The TEM image shows the interface between the BN wall and the catalyst (Figure 4.13B) exhibiting a lattice spacing of 0.35 ± 6.6% nm and 0.22 ± 10.0% nm, respectively. The measured lattice spacing of the catalyst closely matches the MgO (200) facet that has been reported in the literature [221-223]. The graphical representation of the HRTEM image shows that the BN wall (red lines), consisting of BN sheets, was lying on the surface of the MgO (110) and (111) facets. Section 2.3.2 has demonstrated that the catalyst is mainly composed of magnesium and oxygen. Investigation of the end parts of the catalyst revealed layers of the BN wall, presented in Figure 4.13C. It can be inferred from the section of the interface that the BN sheets can also be on the (100) facet of the catalyst. As presented in section 2.3.4, the presence of an inner nanotube indicates that the boron and nitrogen precursors diffuse in the catalyst droplets and precipitate on the surface.

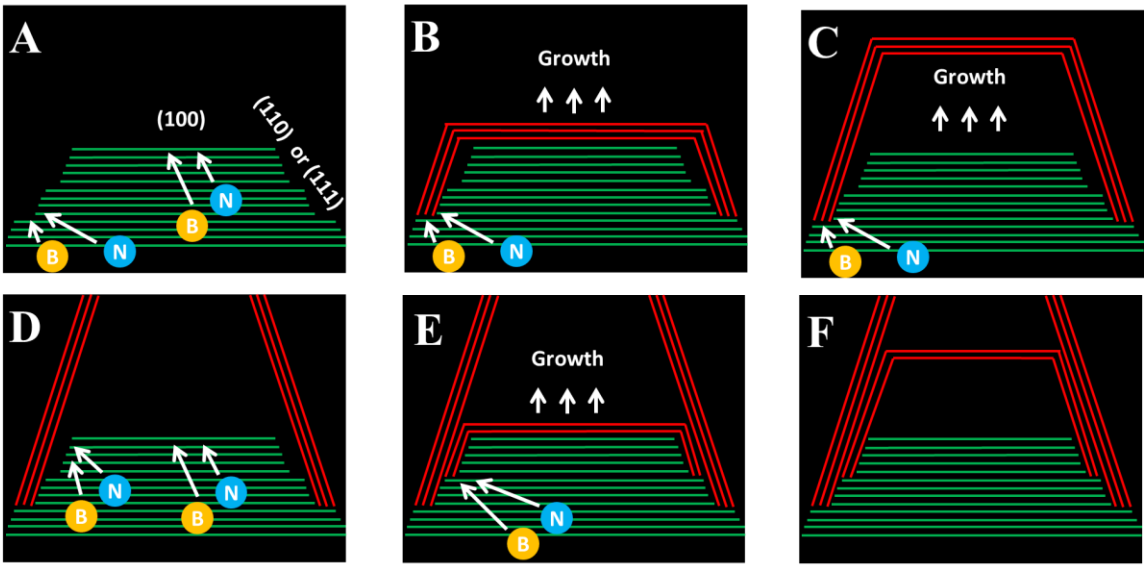


Figure 4.14 *Model representation for the nucleation and growth of a BNNT. (A) BN species form building blocks for the formation of BN sheets on the surface of the catalyst. (B) The precipitated BN sheets continue to grow, forming the nanotubular structure. (C) Continued growth of the generated BNNT. (D) Exposure of the surface of the catalyst promotes BN sheet precipitation. (E) Initial structure of the inner nanotube. (F) The inner nanotube continues to grow and proceeds to step D for further growth.*

Figure 4.14 presents a model for the processes of BNNT nucleation and growth based on this study's experimental results, which aids in the theoretical investigation of these processes. Firstly, the BN species generate BN sheets on the surface of the catalyst (Figure 4.14A). After the BN sheet fully covers the surface of the catalyst, the BN species are more likely to react on the edge part (Figure 4.14B), leading to the growth of a nanotubular structure (Figure 4.14C). The surface of the catalyst is then exposed again for the generation of other BN sheets (Figure 4.14D). The generated BN sheets then repeat the growth process to produce the inner nanotube (Figure 4.14E and F). The growth mechanism is terminated by cutting off the supply of the BN species. The catalyst was represented by different MgO facets of (100), (110), and (111). The ground state energies of these facets were calculated by performing geometry optimisation.

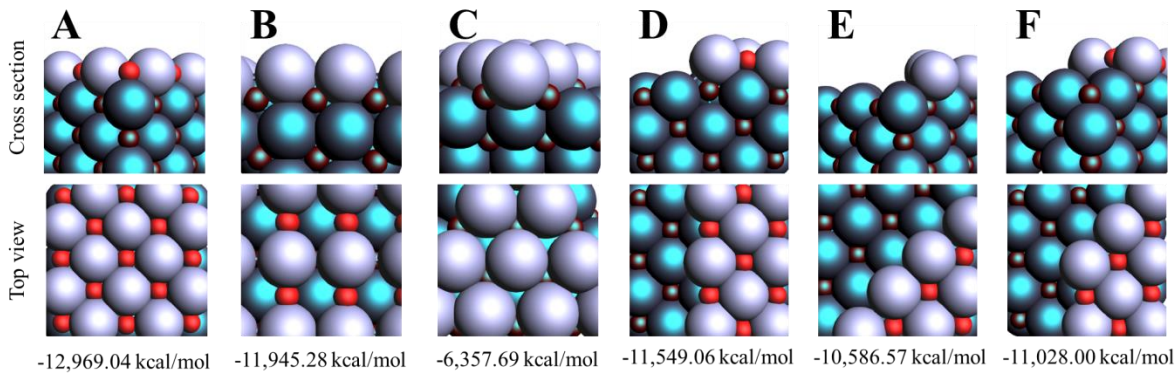


Figure 4.15 *Geometry optimisation with corresponding energies of different facets (A) (100), (B) (110), (C) (111) and step-edges (D) (100)-(110), (E) (100)-(111), (F) (100)-(110)-(111) of the MgO catalyst. The darker coloured atoms indicate the lower layers.*

With the aid of the HRTEM analysis, model systems were calculated to acquire energies at different facets and step-edges of the catalyst; these are presented in Figure 4.15. A slab of MgO containing 50 atoms of magnesium and 50 atoms of oxygen with a dimension of 5.956 x 8.038 x 8.315 Angstrom was optimised. This slab of MgO was chosen for this experiment based on the report of Chen *et al*. [224] showing that a cluster of (MgO)n with n greater than 20 exhibited similar properties to bulk MgO, such as bond distance between the atoms of magnesium and oxygen. The surface of the optimised geometry was then modified to represent the facets and step-edges of interest. The top three layers of the modified surface were relaxed during the calculations while the remaining layers were kept frozen to avoid structure deconstruction and to have a better representation of the surface [213, 225-227]. Darker-coloured atoms indicate lower layers of the facets and step-edges. As seen in Figure 4.15A to D, different surfaces of the MgO showed different energy values. These energies values are a prerequisite for obtaining the adsorption energy:

$$\Delta E_{(adsorption)} = E_{(BN\ precursor/MgO\ catalyst)} - (E_{(MgO\ catalyst)} + E_{(BN\ precursor)})$$

Where $E_{(BN\ precursor/MgO\ catalyst)}$ is the energy of the surface-adsorbate complex. In this case, the adsorbate is the boron and nitrogen precursor in atomic and molecular form. The $E_{(MgO\ catalyst)}$ is the energy calculated for different facets and step-edges, while the $E_{(BN\ precursor)}$ is the energy of the individual boron and nitrogen precursors. In this convention of adsorption energy, negative values indicate stable adsorption configuration [228].

The main objective of this section is to investigate the nature of the BN intermediate species adsorbing on different surfaces of MgO. It also aims to present a potential energy diagram for the formation of BN bonds from the intermediate species in atomic and molecular form. This is then correlated to the final structure, the hexagonal BN network.

4.3.2 BN precursors at atomic level

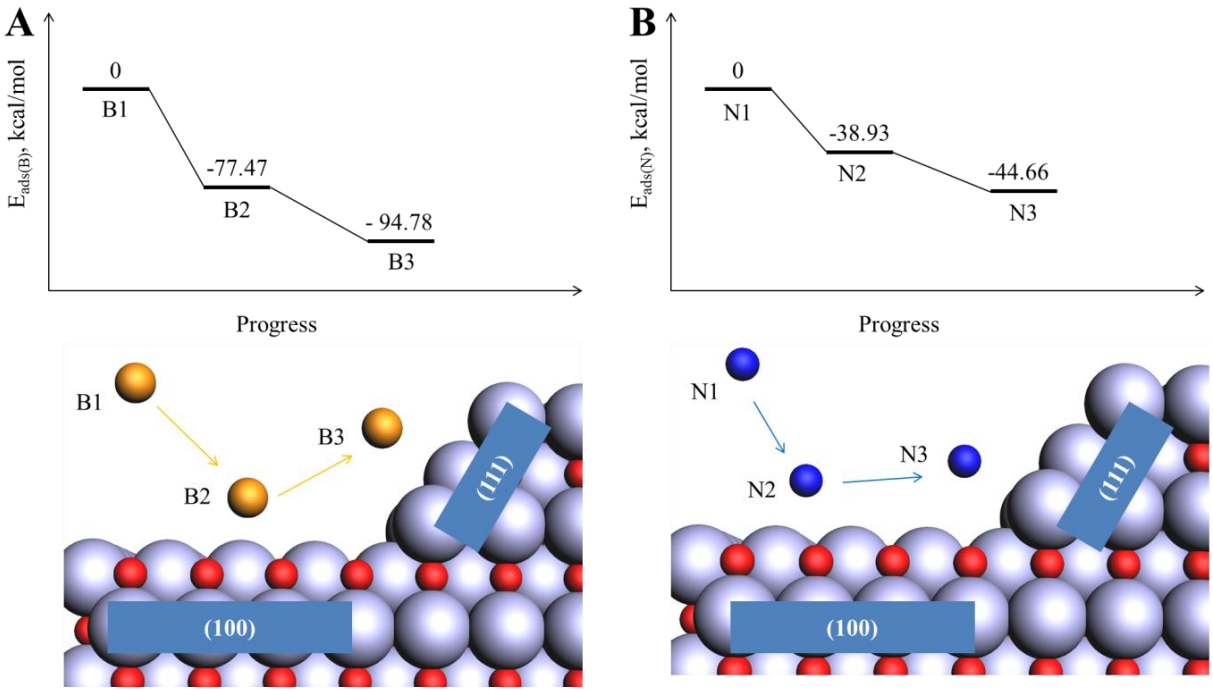


Figure 4.16 *Adsorption energy of (A) boron and (B) nitrogen in the catalyst of different facets.*

The first mechanism of BNNT nucleation and growth was investigated through atomic boron and nitrogen precursors. Decomposition tended to take place in the vicinity of low-coordinated metal surface atoms such as on the step-edge in between (100) and (111) or (100) and (110) facets [229-231]. The boron and nitrogen atoms resulting from the decomposition of boron oxide and ammonia adsorbed at various sites of the catalyst.

Based on the calculations shown in Figure 4.16, boron obtained the highest adsorption energy at the MgO (111) facet surface, indicating that there was an energetic driving force for the adsorption of boron atoms into the MgO (111) facet compared to the MgO (100) facet surface. In order for the boron atom to move towards the MgO (100) facet surface, it had to overcome an energy barrier of at least 17.31 kcal/mol. It should be noted that it was possible to achieve this pathway, since the experimental synthesis conditions involved a temperature of 1,200 °C, which correlated to a high energy input [232]. On the other hand, nitrogen atoms tended to be more stable on the MgO (100)-(111) step-edge. The difference in adsorption energy between boron and nitrogen atoms gives us an insight into the nucleation of the BN nanotube.

The high adsorption energy of the boron atom on the MgO (111) facet surface verified that the nucleation of BN sheet to form the BN nanotube occurred preferentially on this surface. This scenario also related to the synthesis conditions of the experiment, where the production of the catalyst and the boron oxide happened at the same time.

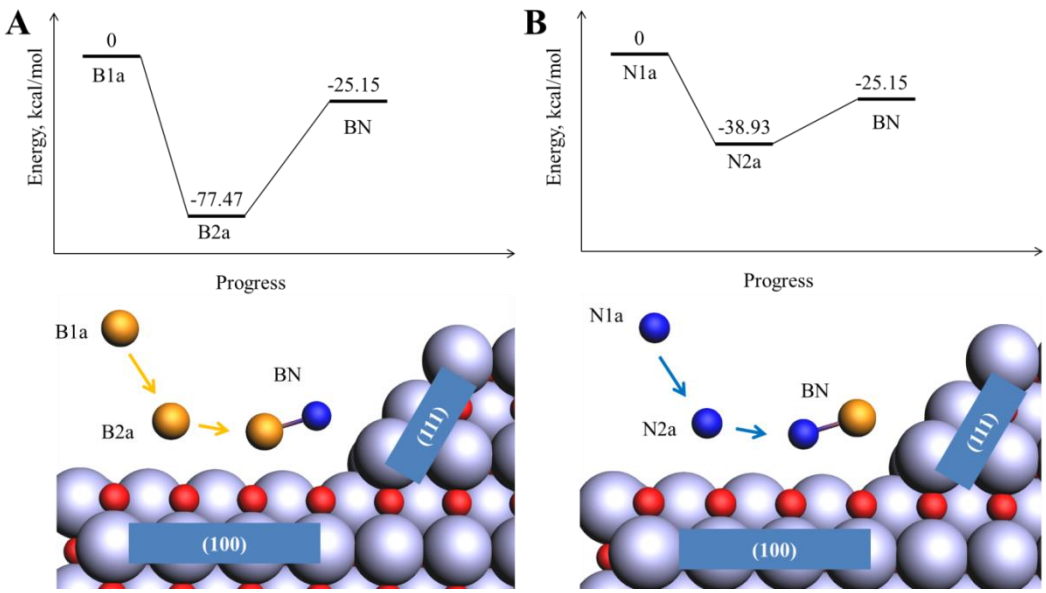


Figure 4.17 *Different formation pathways to generate B-N bonding where (A) boron moves towards nitrogen while (B) nitrogen moves towards boron to form BN with corresponding energy profiles.*

Further calculations comparing two different formation pathways of B-N bonding are shown in Figure 4.17. The first scenario involved a nitrogen atom situated at its most favourable adsorption site. As the boron atom diffused on the surface of the MgO and headed towards nitrogen to form the B-N bond, a huge energy barrier of at least 52.32 kcal/mol was observed. However, if boron served as the nucleation site located on the MgO (111) facet surface, a lower energy barrier of 7.78 kcal/mol was detected. This suggested that the nucleation of the hexagonal BN network that served as a component of the BNNT started with boron on the MgO (111) facet surface rather than nitrogen in the valley of the MgO (100)-(111) step-edge.

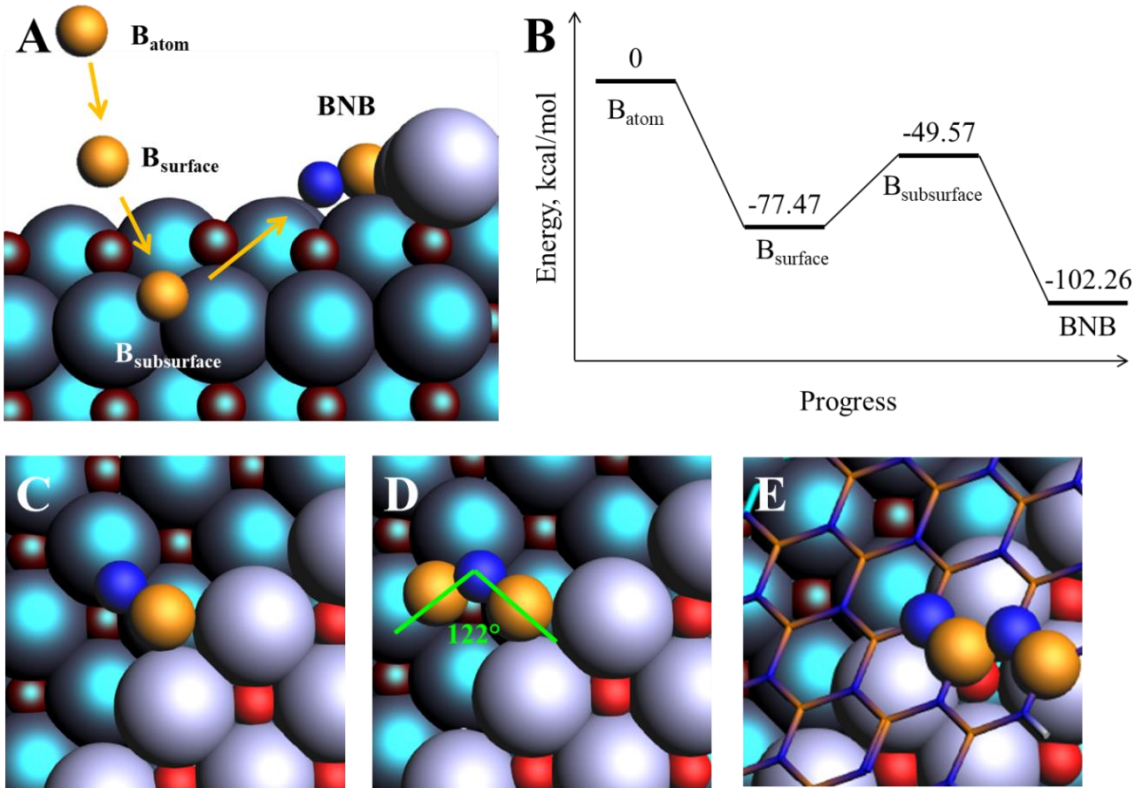


Figure 4.18 *(A) Mechanism and (B) potential energy diagram of boron atom toward the formation of the B-N bond on the adsorbed NB molecule on the MgO (100)-(111) step-edge. Atomic configuration of (C) NB molecule, (D) BNB molecule, and (E) BN sheet at the MgO (100)-(111) step-edge. The darker-coloured atoms indicate the lower layers.*

The third addition of boron atom to the generated BN molecule on the MgO (100)-(111) site-edge surface was investigated; results are shown in Figure 4.18. The diffusion of atomic precursors inside the catalyst is now accepted as being involved in the nucleation and growth of CNTs [233, 234]. Figure 4.18A shows the mechanism of the boron atom forming the B-N bond, where the boron atom was at vacuum (B_{atom}), and then adsorbed on the MgO (100) surface ($B_{surface}$), leading to two scenarios: (1) B-N bond formation through the B atom diffusing on the MgO (100) surface and (2) diffusion on the subsurface of MgO (100). Figure 4.18B shows the corresponding adsorption energies of the placements of boron atom. The process involving the adsorption of boron on the MgO (100) surface showed a change of energy to -77.47 kcal/mol. Direct B-N bond formation via diffusion on the surface led to a drop in energy to -102.26 kcal/mol. However, if the boron atom

diffused on the subsurface of MgO, an increase in energy was required with an energy barrier of at least 27.90 kcal/mol. Nevertheless, the overall change of energy to generate the B-N bond was shown to be an exothermic reaction, indicating that the reaction could proceed. It can be observed in Figure 4.18C that the orientation of the BN molecule was diagonal with respect to the MgO (100)-(111) site-edge surface, indicating preference of adsorption. The bonded boron atom shown in Figure 4.18D resulted in a B-N-B bond angle of 122°, which provided evidence of the formation of the hexagonal B-N structure where the B-N-B bond angle for the hexagonal BN structure was 120° [235-237]. Further addition of boron and nitrogen atoms then led to the growth of the BN sheet following a diagonal direction on the surface of the MgO (100)-(111) step-edge presented in Figure 4.18E.

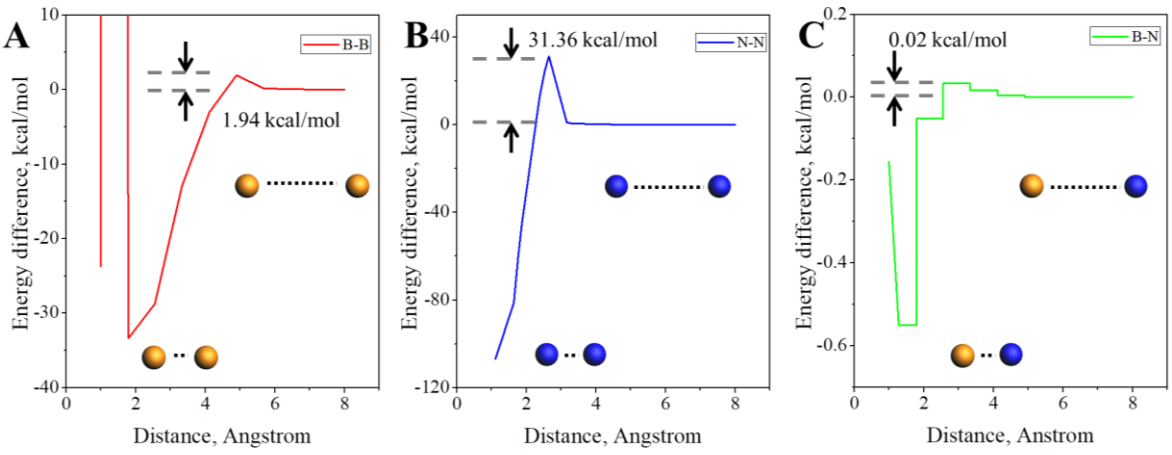


Figure 4.19 *Linear transit calculation of energy as a function of distance in a two-atomic (A) boron-boron, (B) nitrogen-nitrogen, and (C) boron-nitrogen system.*

To investigate the driving force behind the preferential B-N bonding, Figure 4.19 shows the linear transit calculation plotting the energy difference as a function of the distance between two atoms of boron, nitrogen, and boron-nitrogen from 8 to 1 Å, (Figure 4.19 A, B, and C, respectively). A lower energy barrier indicated that the reaction occurred

much faster, thus suggesting that in a system where atomic boron and nitrogen atoms were present, B-N bonding was preferred rather than B-B and N-N bond formation, since the former had the lower energy barrier of 0.02 kcal/mol. This finding also corroborates the results reported by Riikonen *et al*. [227], where B-N bond formation was favoured over B_2 and N_2 on investigating the stability of B-N bonding on a catalyst surface.

Although the calculations presented here involve the B-N bond formed with boron and nitrogen atoms, future work should include more detailed computations. This is because, when investigating the boron and nitrogen precursors at atomic level, more accurate energy values can be obtained when these atoms are modelled in radical form via a variation of their spin states. However, the radical form of BN species are more likely to be generated using very high-energy synthesis methods such as the arc-discharge method, laser ablation, and the plasma-induced method, which all result in the synthesis of single-walled BNNTs [219, 238, 239], which have higher energy formation presumably owing to their small diameters that have high curvature relating to high strain energy. In the synthesis of BN nanomaterials by the CVD method, the energy applied is not enough to promote generation of radical boron and nitrogen intermediate species [6, 13, 16]. Nevertheless, the results presented in this section add to our knowledge of the formation of B-N bonding and can serve as a reference point for further research. The second mechanism in the nucleation and growth of BNNTs considered in this study is the direct use of the molecular boron precursor B_2O_2 and the nitrogen precursor NH_3.

4.3.3 BN precursors at molecular level

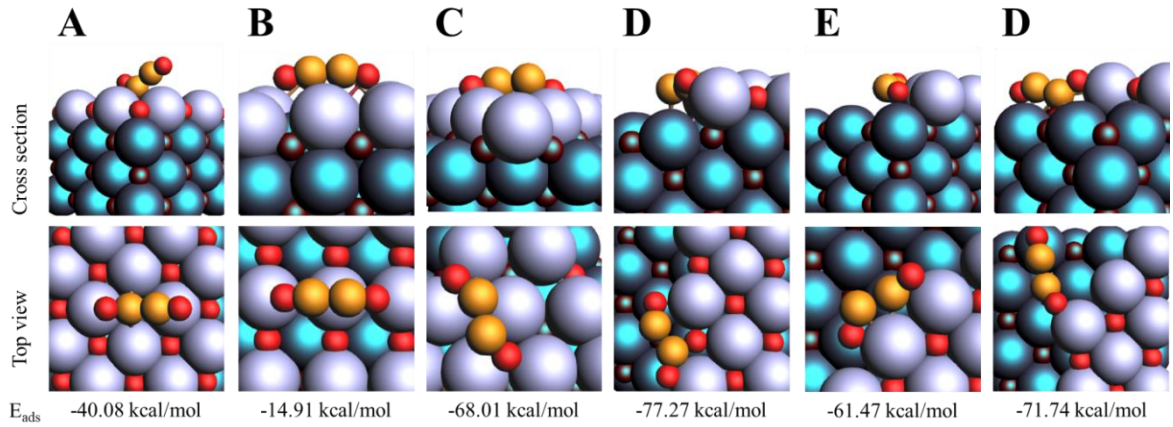


Figure 4.20 *Adsorption of boron oxide on different surfaces of magnesium oxide facets (A) (100), (B) (110), (C) (111), step-edges (D) (100)-(110), (E) (100)-(111), and (F) (100)-(110)-(111). Top panels show the cross-section view while bottom panels show top views. Colour coding: red is oxygen, yellow is boron, and grey is magnesium. The darker-coloured atoms indicate the lower layers.*

The molecular B_2O_2 boron intermediate species was placed on different surfaces of the MgO and were relaxed to obtain the local minimum energy presented in Figure 4.20 where top panels show the cross-section while bottom panels show the top view. Figure 4.20A shows the adsorption of B_2O_2 on top of the MgO (100) facet with a calculated adsorption energy of -40.08 kcal/mol. The linear configuration of B_2O_2 changed, where the measured angle of the O-B-B was 127.6 degrees with boron located on top of the oxygen. The B_2O_2 on top of the MgO (110) facet shown in Figure 4.20B gave the lowest adsorption energy with the least change of configuration and preferred to be on top of the magnesium atoms. Adsorption at MgO (111) facet (Figure 4.20C) showed the strongest adsorption among the facet surfaces of the MgO with a value of -68.01 kcal/mol, indicating that the atoms of the B_2O_2 were located at the bridges and hollow sites rather than on top of the Mg atoms. For the MgO (100)-(110) step-edge in Figure 4.20D, the B_2O_2 stayed on the step-edge with a strong adsorption of -77.27 kcal/mol, where the two atoms of boron from the B_2O_2 get closer to the oxygen atom between the (100) and (110)

facet of the MgO catalyst, changing its electronic configuration to a trans B_2O_2 isomer. This change in configuration was also seen on the MgO (100)-(111) step-edge presented in Figure 4.20E. The B_2O_2 at MgO (100)-(110)-(111) step-edge was adsorbed on the MgO (100) surface where one end of oxygen was adsorbed on the magnesium atom located in the corner of the top layer MgO (110)-(111).

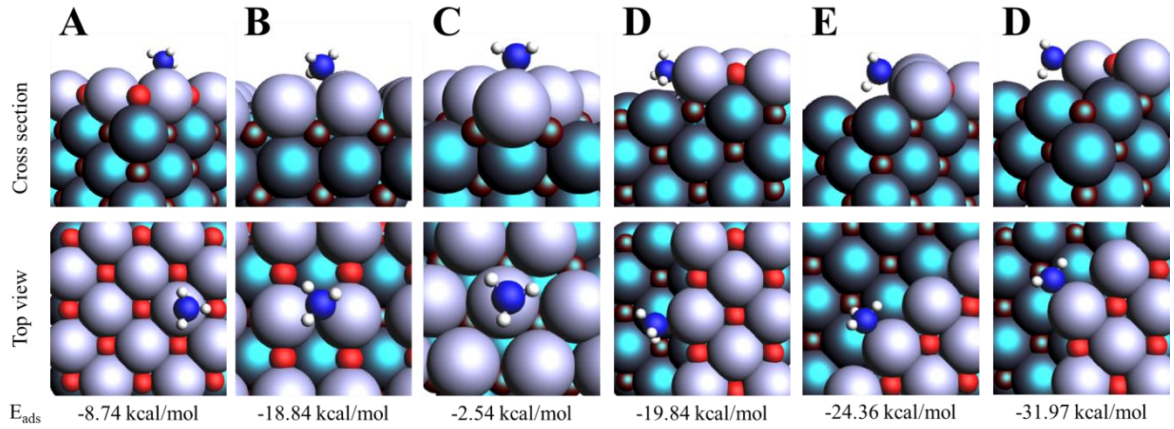


Figure 4.21 *Adsorption of ammonia on different surfaces of magnesium oxide facets A) (100), (B) (110), (C) (111), step-edges (D) (100)-(110), (E) (100)-(111), and (F) (100)-(110)-(111). Top panels show the cross-section while bottom panels show top views. Colour coding: white is hydrogen, red is oxygen, and grey is magnesium. The darker-coloured atoms indicate the lower layers.*

Figure 4.21 shows the local minima energy of ammonia being relaxed on the different surfaces of the MgO. Ammonia on the MgO (100) facet shown in Figure 4.21A preferred to be on top of the magnesium atom. At MgO (110) facet, the nitrogen of the ammonia tended to place itself at the bridge of the magnesium atoms while at MgO (111), ammonia was located on top of the magnesium atom (Figure 4.21B and C, respectively). Among the facets, ammonia adsorbed most strongly at MgO (110) and least at MgO (111), with calculated adsorption energies of -18.84 kcal/mol and -2.54 kcal/mol, respectively. In the case of ammonia on the MgO (100)-(110) step-edge depicted in Figure 4.21D, the oxygen atoms on the MgO (100) layer seemed to affect the orientation of ammonia,

suggesting that O-H interaction from the hydrogen atoms of ammonia led to the increase in adsorption energy of -19.84 kcal/mol. Less O-H interaction was observed in the MgO (100)-(111) and MgO (100)-(110)-(111); however, the magnesium to which nitrogen was adsorbed had a low coordination number, resulting in a stronger adsorption of ammonia, with calculated adsorption energies of -24.36 kcal/mol and -31.94 kcal/mol, respectively.

The adsorption configuration of ammonia where nitrogen preferred to be on top of the magnesium atom on different surfaces of MgO can be due to the electron densities of the two species. High electron density is expected at the lone pair site of ammonia that is attracted to the less depopulated electron density in the magnesium atom of the MgO surfaces. Overall, ammonia had smaller adsorption energy on the magnesium oxide surface, indicating that boron oxide can be the first point of nucleation for the formation of BN nanomaterials.

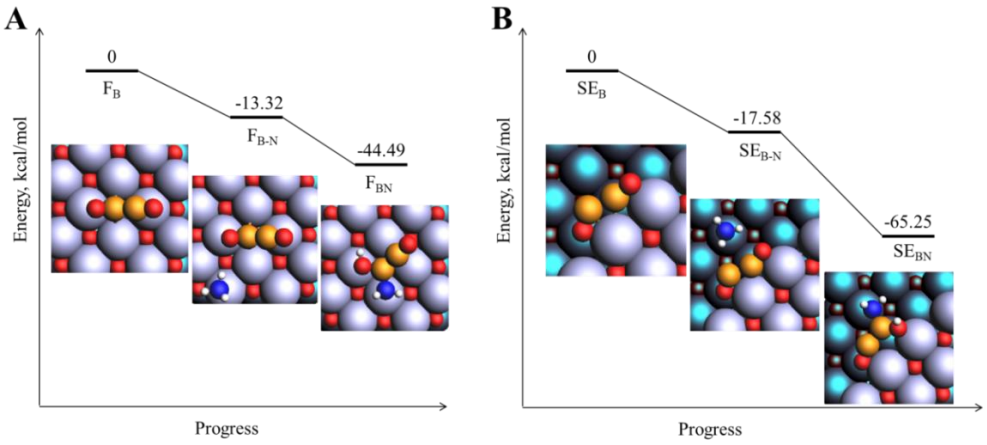


Figure 4.22 *Bond energy analysis of B-N bond formation on (A) facet (100) and (B) step-edge (100)-(111).*

Figure 4.22 shows the calculated results of the B-N bond formation on (A) the MgO (100) facet surface and (B) the MgO (100)-(111) step-edge surfaces where B_2O_2 had been adsorbed with the configuration of F_B and SE_B, respectively. As ammonia was adsorbed on the surface and moved closer to the B_2O_2, a decrease in energy was observed

in both systems, with the MgO (100)-(111) step-edge having a more stable energy of -4.26 kcal/mol. Once the ammonia bonded with the B_2O_2, a significant adsorption energy was realised, suggesting that the B-N bond formation on the MgO (100)-(111) step-edge surface was more stable than the facet surface.

To accommodate the B-N bond formation, the migration of hydrogen from ammonia took place in both scenarios. The B-N bond formation on the MgO (100)-(111) step-edge surface showed an increased distance of 69 pm between boron and the bridge site of Mg-Mg. Interestingly, the distance of the adsorbed nitrogen of ammonia on top of the magnesium atom showed a smaller change of 8 pm, indicating that the boron of the B_2O_2 had smaller adsorption on the magnesium atom compared to the adsorption of nitrogen in the ammonia on the magnesium atom. However, when the boron of the B_2O_2 was adsorbed on the oxygen atom on the surface of the MgO, as seen in Figure 4.22A, the boron atom tended to stay as it was, shifting instead the B-O monomer end on top of the Mg-Mg bridge site after the formation of the B-N bond.

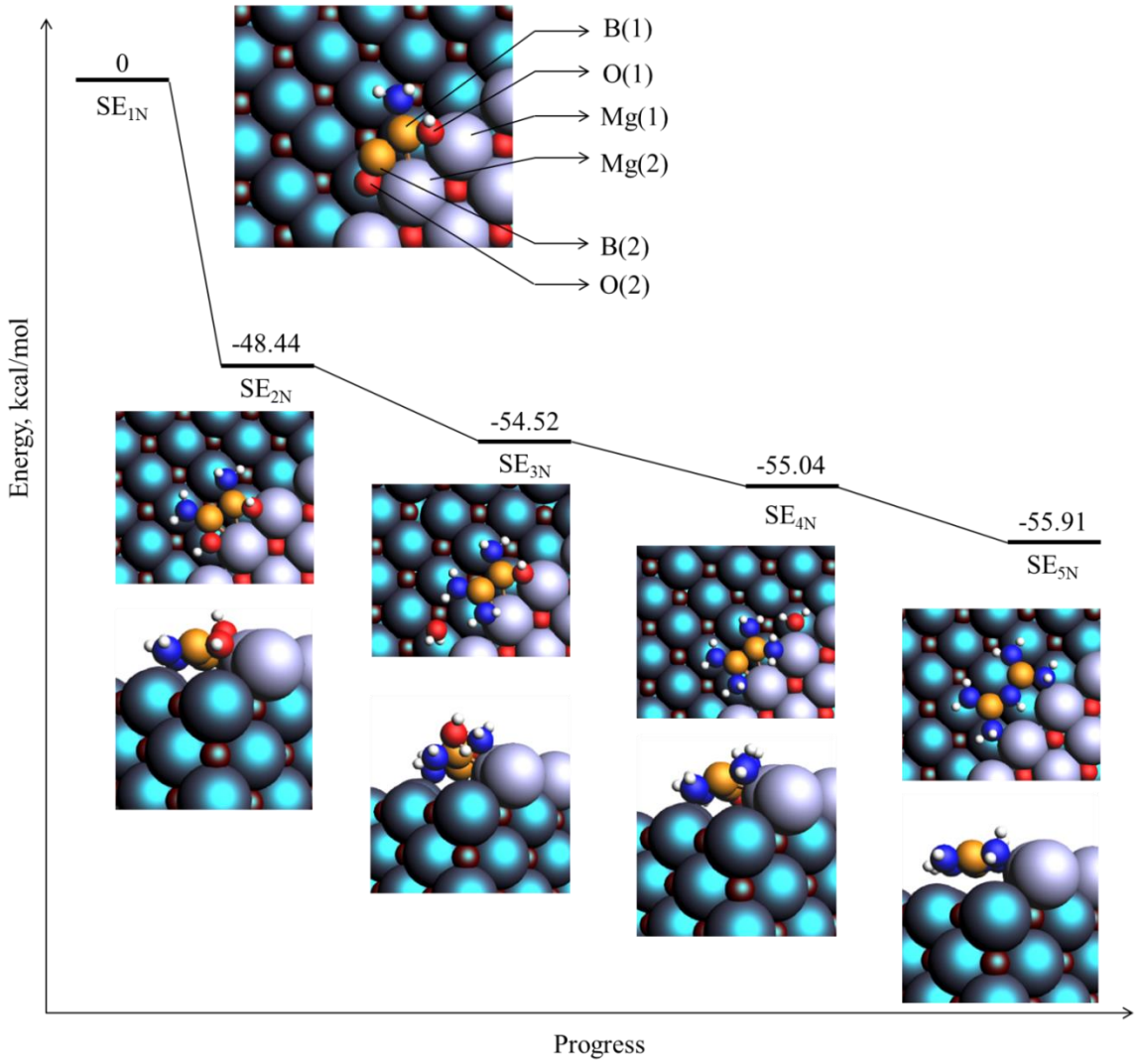


Figure 4.23 *Saturation of B-N bonding of B_2O_2 boron precursor molecule by periodic addition of ammonia to the site-edge (100)-(111) surface.*

Due to the more stable condition of the B-N bond formation on the site-edge surface, the nucleation of the hexagonal BN network was further investigated through the saturation of the B-N bonding by introducing more ammonia into the B_2O_2 on the MgO (100)-(111) step-edge surface, following similar phenomena presented earlier.

Figure 4.23 shows the bond energy analysis of the saturation of the B-N bonds. During a second B-N bond formation via SE_{2N}, ammonia was introduced into the terrace MgO (100) facet surface, where nitrogen bonded with B(2) and protonation of the O(2) took place, resulting in cis-$HOB(NH_2)B(NH_2)OH$. As previously observed, an increase in

distance from 245.5 pm to 275.3 pm between B(2) and Mg(2) occurred as the B-N bond was formed. The hydrogenated O(2) was then abstracted out of the system in the form of water as the incoming ammonia, initially adsorbed at the upper terrace of the MgO (100)-(111) step-edge, produced the third B-N bond at B(2) that led to the SE_{3N} configuration. Unlike the abstraction of the hydroxyl group via generation of a water molecule without the MgO, this process was shown to be exothermic, indicating that the reaction was spontaneous. The fourth ammonia molecule followed the same mechanism that formed the B-N bond at B(1) with a water molecule being generated via SE_{4N}. At saturated B-N bonds, introducing further ammonia resulted in the insertion of nitrogen in between the B-B bond along with the production of an H_2 molecule with the final structure shown in SE_{5N}. Instead of breaking the B-B bonds that generated two species that could serve as monomer for the formation of the hexagonal BN structure, the MgO (100)-(111) step-edge surface was shown to have held the structure in place. Both boron atoms were also observed to be detached from the magnesium atoms of the step-edge with a measured distance of 322.4 pm for both B(1)-Mg(1) and B(2)-Mg(2).

As seen from the cross-section view, the increase in the B-N bond of the adsorbed B_2O_2 molecule was associated with an increase in distance between the generated molecule and the terrace surface of the MgO catalyst. This observation indicated that there was a lift-off of the generated product complex from the surface of the MgO.

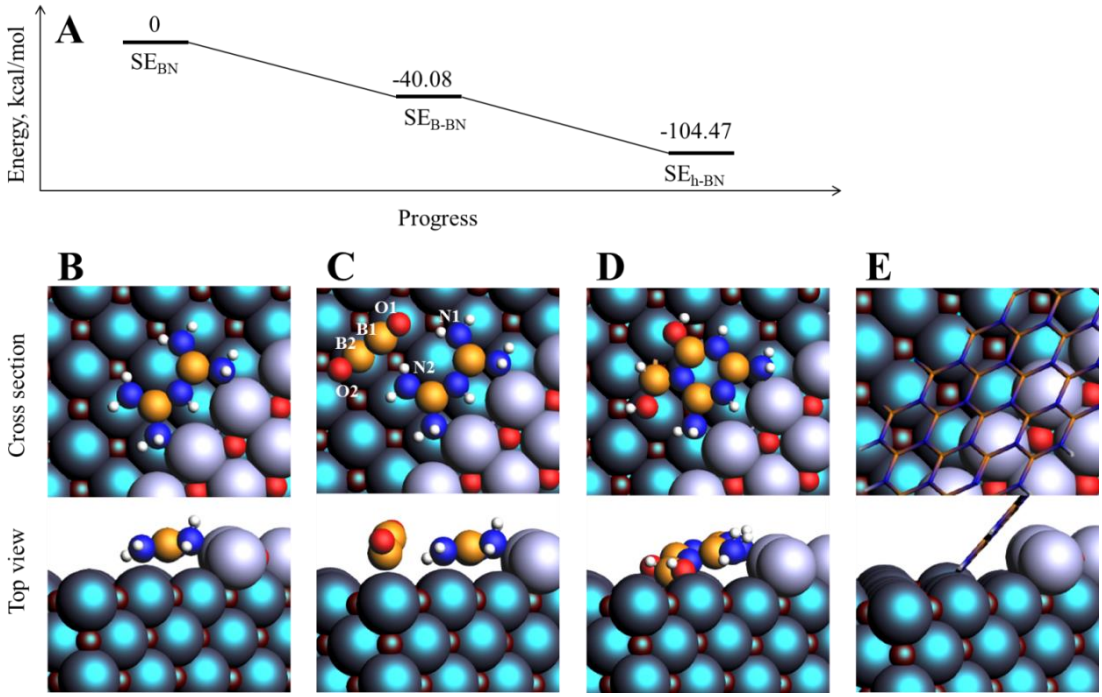


Figure 4.24 *Addition of B_2O_2 boron precursor molecule to the saturated B-N complex. The final structure shows the first formation of the hexagonal B-N network.*

After the saturation of B-N bonding and insertion of nitrogen in between the B-B bond forming the $B_2N_5H_9$, a B_2O_2 molecule was introduced to the system, and the reaction was studied as shown in Figure 4.24. A decrease of -40.08 kcal/mol energy was observed as the B_2O_2 molecule got closer to the $B_2N_5H_9$ molecule at $SE_{B\text{-}BN}$. Based on the geometric configuration shown in Figure 4.24C, both boron atoms of the incoming B_2O_2 molecule tended to approach the nitrogen N2. This led to the bonding of the B_2O_2 molecule to the $B_2N_5H_9$, resulting in the product molecule shown in Figure 4.24D, with a corresponding change in energy of -104.47 kcal/mol.

As previously seen, a hydrogen atom from N1 migrated to the O1 of the B_2O_2 molecule that formed the B-N bond between B1 and N1 atoms. The B1 atom was also bonded with the N2 atom, where the hydrogens from N2 had migrated to O2 and B2. The molecular structure of the product showed the hexagonal B-N network with a measured B-N bond of 145.45 ± 3.01 pm, which is in good agreement with the reports by Chejanovsky [240] and Wirtz [241]. This suggested that the repetition of the addition of boron and

nitrogen species led to the generation of the wall of the BN nanotube through the reaction sites of the hydroxyl group at the O1 and O2 atoms. The increased distance between the generated hexagonal BN network and the MgO (100)-(111) step-edge also indicated that the step-edge could initiate another nucleation for the synthesis of another hexagonal BN molecule that is presented in Figure 4.24D. The BN sheet that made up the wall of the BNNT was then expected to grow along the MgO (100)-(111) site-edge surface of the MgO, as presented in Figure 4.24E, which also showed a zigzag chirality.

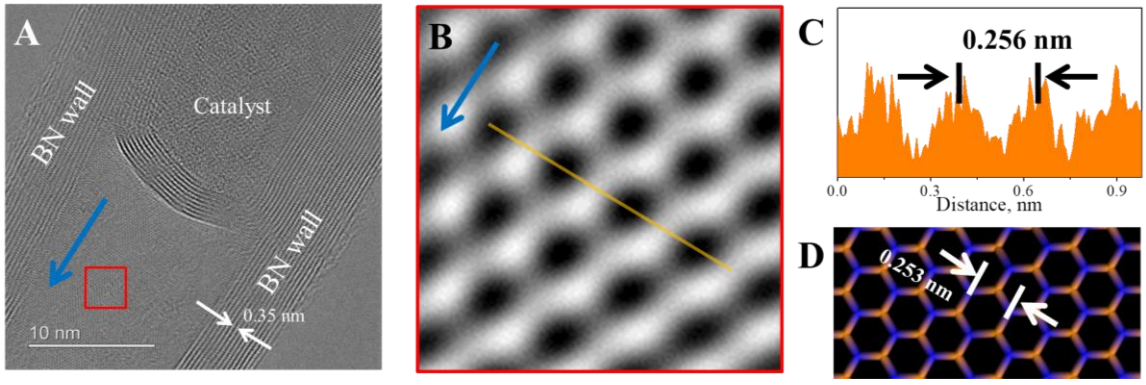


Figure 4.25 *(A) HRTEM of the interface between the BNNT and the catalyst. (B) Reverse FFT from panel A indicated by the red square showing the hexagonal network and chirality with respect to the long axis of the BNNT. (C) Measured distance of two BN bonds from panel B. (D) Calculated optimised geometry of a hexagonal BN structure. The blue arrows indicate the growth direction of the BNNT.*

The correlation between the theoretical results with the experimental results was studied through the chirality of the BNNTs presented in Figure 4.25. After taking HRTEM images on the interface between the catalyst particle and the BNNT presented in Figure 4.25A, it was observed that the tail part of the catalyst was coated with layers of BN nanosheets. On top of this coating was the wall of the BNNT with a measured interlayer spacing between the BN sheets of 0.35 ± 7.8% nm. As mentioned before, the growth of BNNTs follows the tip-growth mechanism; the blue arrows in Figure 4.25A and B indicate the growth direction. The hexagonal network of the BN nanosheet can be observed inside

the red square. A reverse FFT image process was applied to have a clearer view of the hexagonal pattern presented in Figure 4.25B. The greyscale line profile (orange line) of the image measured the distance of the neighbouring B-N bonds to be 0.256 nm, as shown in Figure 4.25C. This measured distance between B-N bonds are in good agreement with the calculations obtained by geometry optimisation of a hexagonal BN sheet measuring 0.253 nm shown in Figure 4.25D.

The theoretical calculations conducted in this thesis have provided a clearer understanding of the nucleation stage of the growth of BNNTs. As presented in the previous figure, the hexagonal BN pattern of the product molecule gives early insights into the chirality of the BNNT to be synthesised, which is in accordance with the results obtained from experiments.

It is important to note that there has been a gap in the literature relating to the nucleation and growth of BNNTs. Oku *et al*. [242] studied the atomic structure and stabilities of the zigzag and armchair chirality of BNNTs and inferred that the zigzag configuration of BNNTs was more stable after conducting calculations based on HRTEM and molecular mechanics. However, the group did not address the mechanism for the synthesis of BNNTs. Due to the very high energy input of the arc-discharge synthesis method they used, they were able to produce the less stable armchair configuration of BNNTs. Based on the calculations reported by Han *et al*. [243], high-energy synthesis methods such as the arc plasma method result in the formation of different BN structures such as BN nanocages, nanococoons, nanoflakes, and nanobamboos. Oku *et al*. later carried out a study correlating the experimental and theoretical studies of BNNT synthesis [129] by using the lower-energy CVD synthesis method.

Prior to this thesis, no direct evidence from experimental and theoretical results has so far been presented to address BNNT nucleation and growth. This work has been able to

show that the zigzag chirality of BNNTs are synthesised due to the adsorption chemistry of the B_2O_2 boron precursor molecule on the step-edge of the MgO that serves as the nucleation site for the growth of this nanomaterial.

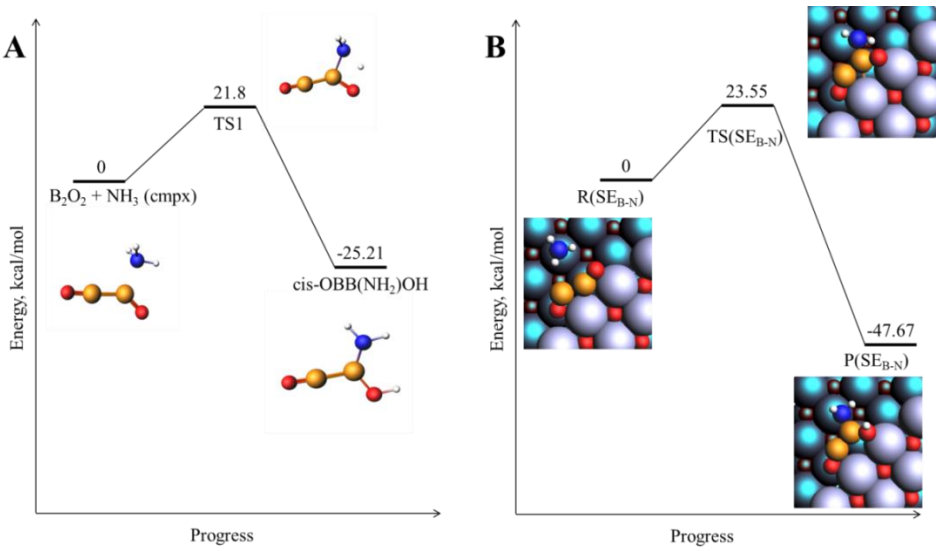


Figure 4.26 *Potential energy diagram comparing the energy barriers of the formation of B-N bonds from the boron and nitrogen precursor molecules in the (A) absence and (B) presence of magnesium oxide.*

Figure 4.26 shows the potential energy diagram comparing the energy barriers of the formation of B-N bonding in the absence and presence of MgO from boron and nitrogen precursor molecules (Figure 4.26A and B), respectively. In the absence of MgO, a B-N bond was generated, producing a cis-OBB(NH_2)OH molecule via transition state TS1. The energy barrier calculated at TS1 is 21.8 kcal/mol. While in the presence of MgO, specifically on the MgO (100)-(111) step-edge surface, the formation of B-N bond from ammonia and B_2O_2 molecule involved a barrier energy of 23.55 kcal/mol via TS(SE_{B-N}). Both reaction conditions showed a difference in barrier energy of 1.75 kcal/mol, suggesting that B-N bond would still take place whether in the absence or presence of MgO. Moreover, both were shown to be an exothermic process, indicating a typical shift of the reactants to the products. This demonstrates that MgO does not serve as a catalyst of the reaction that leads to the formation of the B-N bond, but rather as a 'container' for the

generation of the nanotubular structure of the BNNT. This has been experimentally shown in the previous chapter (section 3.3.1), where the absence of MgO generated BN nanosheets, while the presence of MgO synthesised BNNTs.

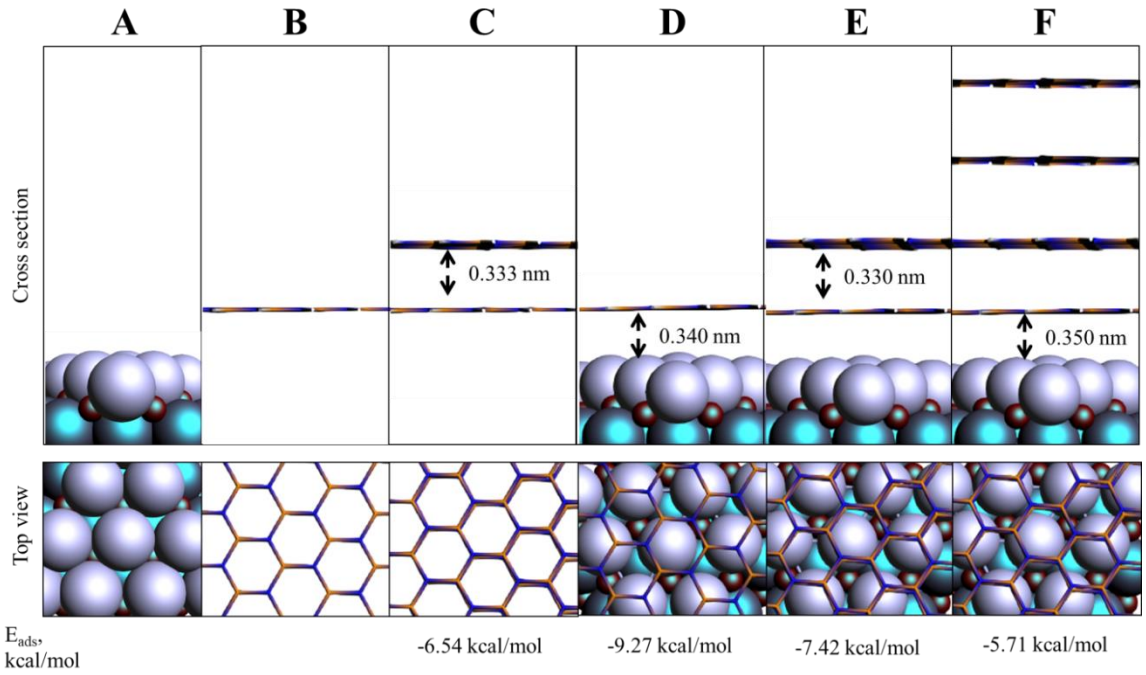


Figure 4.27 *Adsorption energy as a function of number of BN sheets on the surface of MgO (111) facet. (A) Pristine MgO (111) surface, (B) single BN sheet, (C) two BN sheets, (D) single BN sheet on (111) surface, (E) two BN sheets on (111) surface, and (F) four BN sheets on (111) surface. Top panels correspond to a cross-section view while bottom panels show top views.*

To investigate the multi-walled nature of the synthesised BNNTs, calculations of the adsorption energies in terms of varying the number of hexagonal BN on the MgO (111) surface were conducted; the results are shown in Figure 4.27. The top panels show the cross-section of the interface between the hexagonal BN and the MgO (111) surface while the bottom panels present the top view. Figure 4.27A and B depict the MgO (111) facet and the hexagonal BN. Figure 4.27D shows the obtained geometry at minimum energy, where the hexagonal BN was placed on top of the MgO (111) facet, with a calculated adsorption energy of -9.27 kcal/mol and an interface distance measured to be 0.340 nm. Figure 4.27C shows two layers of hexagonal BN with a measured interlayer spacing of

0.333 nm. A decrease in this distance was observed in the presence of the MgO (111) surface shown in Figure 4.27E. However, a decrease of 1.85 kcal/mol in the adsorption energy occurred upon the increase in the number of layers of the hexagonal BN from one to two. Further increase in the number of layers of the hexagonal BN was shown to decrease the adsorption energy to -5.71 kcal/mol, with four layers as shown in Figure 4.27F.

The decreasing trend of the adsorption of the BN sheets on the MgO (111) surface indicates that the multi-walled BNNT exhibited a lift-off from the MgO. The high adsorption energy of the single hexagonal BN layer can be the reason why no single-walled BNNTs were observed in the experimental results. Moreover, the measured average interlayer spacing of the hexagonal BN in the theoretical calculation was 0.330 ± 0.003 nm, which is in close agreement with the experimental results of this study, where a value of 0.335 ± 0.110 nm was obtained by HRTEM.

4.3.4 Activation energy of BNNT growth

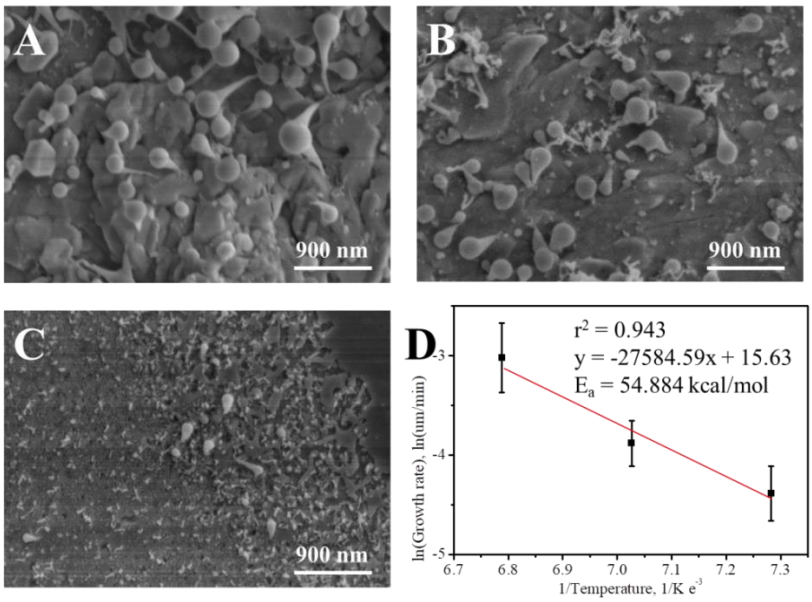


Figure 4.28 *SEM images of growth of BNNTs at constant time, 10 mins, at different temperatures (A) 1,200 °C, (B) 1,150 °C, and (C) 1,100 °C. (D) Determination of activation energy (E_a) from the Arrhenius plot of the growth rate of BNNTs.*

The activation energy of nanotube growth can be calculated by taking into consideration the Arrhenius equation:

$$k = Ae^{\frac{-Ea}{RT}}$$

Where k is the growth rate of nanotubes, Ea is the activation energy of nanotube growth, R is the universal gas constant, T is the absolute temperature, and A is a proportionality coefficient. Thus, taking the natural logarithm from both parts of the Arrhenius equation leads to the expression:

$$lnk = \frac{-Ea}{RT} + lnA$$

The equation shows that the natural logarithm of the growth rate has a linear relationship on the inverse growth temperature. The slope of this linear relationship is – Ea/R. Hence, the linear fitting of the relationship of ln k(1/T) directly yields the value of the activation energy of nanotube growth.

This approach has been used frequently in CNT synthesis. For example, Lee *et al*. [244] determined an activation energy of 30 kcal/mol for multi-walled CNTs synthesised by thermal CVD using C_2H_2 as carbon source and an Fe catalyst at 800-1100 °C. The first calculations of the activation energies of the growth of carbon filaments by the catalytic thermal decomposition of C_2H_2 on nickel [245], cobalt [246], iron [246, 247], vanadium [248], and molybdenum [248] were obtained in the range of 16.14 to 38.72 kcal/mol, from which it was inferred that bulk diffusion through the solid-state catalyst particle was the growth rate-limiting process.

Figure 4.28 shows the determination of the activation energy of BNNT growth. The embryonic stage of BNNTs grown at 10 mins was captured experimentally at different temperatures of 1,200°, 1,150°, and 1,100° C, shown in the SEM images in Figure 4.28A, B, and C, respectively. From several experimental runs, the average length of BNNTs grown at 1,100, 1,150, and 1,200 °C was measured to be 116.94 ± 30.45, 206.95 ± 46.67,

and 489.35 ± 35.61 nm, respectively, and an Arrhenius plot could be obtained as shown in Figure 4.27D. A good linear function fitting with an r^2 value of 0.943 was observed, providing an activation energy of 58.88 ± 5 kcal/mol. This energy was higher than the barrier energies calculated in this chapter. For instance, the energy required to form the B-N bond from B_2O_2 and ammonia molecule required 23.55 kcal/mol. The diffusion of boron and nitrogen atoms to generate the B-N bond was also less than the obtained activation energy; this is in accordance with the results presented by Riikonen *et al*. showing energy barriers in the range of 27.67 kcal/mol on the step-edge, 32.28 kcal/mol at facet of an iron surface [227], and 13.84 kcal/mol on the magnesium surface [249]. This indicates that the growth-rate-limiting process cannot solely be on account of the diffusion or B-N bond formation, but may also be due to the contributions of multiple chemical processes during the synthesis of BNNTs, as observed in studies done by the CNT synthesis community, which report activation energies in the range of 50.73 to 62.26 kcal/mol [250, 251].

4.4 Conclusion

In this chapter, DFT-based *ab initio* calculations were performed to correlate the experimental and theoretical perspectives on BNNT growth and nucleation. A potential energy diagram of reactions enabled the identification of energy barriers. The breaking of the B-B bond of the B_2O_2 boron precursor was investigated through hydrogen and ammonia molecules. At pristine B_2O_2, the hydrogen molecule was shown to have a smaller energy barrier than ammonia of 37.02 kcal/mol, while at saturated B-N bonding, ammonia broke the B-B bond at a lower energy barrier than a hydrogen molecule of 31.30 kcal/mol.

The chirality of the synthesised BNNTs was found to be due to the adsorption of the B_2O_2 molecule and atomic boron precursor on the MgO (100)-(111) step-edge surface. In the absence and presence of MgO, B-N bond formation still took place, because of the small difference in energy barriers (ca. 2 kcal/mol), a result that is in good agreement with this study's experimental results in the synthesis of BN nanosheets and nanotubes.

An investigation of energy change as a function of distance through linear transit calculations showed that the B-N system exhibited the lowest energy barrier, indicating that B-N bonding was preferred. It was demonstrated that the adsorption energy of the BN sheet decreased as the number of BN sheets on the surface of the MgO increased, suggesting the 'lift-off' of the BN wall.

Finally, the activation energy of BNNT growth was determined to be 58.88 kcal/mol, which can be attributed to the multiple chemical processes that occur during the synthesis BNNTs, since the calculated energy barriers in the diffusion of boron and nitrogen atoms on the surface of MgO and B-N bond formation showed lower energy values.

Chapter 5

Summary and future research

The objective of this thesis is to develop a fundamental understanding of the synthesis of BN nanomaterials, by providing clearer and more definitive answers to questions regarding their nucleation and growth that have challenged researchers in the nanomaterials community. This concluding chapter offers a summary of the major findings of this study and proposes new avenues of further research that can help us take full advantage of the extraordinary properties of BN nanomaterials and bring them much closer to real-world applications.

5.1 Summary of findings

5.1.1 The BOCVD method yields BNNTs of a high quality

The first step in this investigation was adapting the boron oxide chemical vapour deposition (BOCVD) method for BNNT synthesis. This method was identified as the most effective means of producing high-quality BNNTs, as determined by the composition, crystallinity, and reproducibility of the synthesised products. These factors were quantified using scanning electron microscopy (SEM), transmission electron microscopy (TEM),

energy-dispersive X-ray spectroscopy (EDX), Raman spectroscopy, and electron energy-loss spectroscopy (EELS).

5.1.2 The synthesis of BNNTs follows a tip-growth mechanism proved by studying the evolution of the catalyst droplets

The nucleation and growth of BNNTs was investigated through the evolution of the catalyst droplets in the synthesis. It was found that the gases generated during high-temperature exposure of the boron and magnesium oxide powder produced a thin-film deposition on the surface of the SiO_2 target substrate. Further characterisation though EDX and XPS depth profile confirmed that it was magnesium borate in the form of MgB_4O_7. The low melting point of the thin film of magnesium borate enabled its transformation into catalyst droplets through thermal dewetting. These droplets then served as nucleation sites for the generation of nanotubular BN materials.

The introduction of ammonia into the synthesis reaction induced the boron to diffuse from the magnesium borate droplet, which led to the conversion of the droplet into a magnesium oxide particle as indicated by the EDX analysis showing a decrease in boron content when the thin film transformed into the catalyst tip. In addition, the catalyst droplet was observed to have decreased in size from 290 (±58.97) nm during catalyst formation to 223.25 (±28.23) nm at 10 mins precipitation of the BNNTs. Although the conversion of magnesium borate into magnesium oxide occurred during the nucleation stage, the growth reaction was not deactivated by magnesium oxide; in fact, BNNT growth was still achieved after reactions of longer duration. A slight decrease in tip size to 11 nm was measured from the embryonic stage to the fully-grown BNNTs.

The use of iron oxide as the metal oxide added to amorphous boron hindered the formation of the catalyst droplets and resulted in the synthesis of BN nanosheets. Since the

boiling point of iron in the iron oxide in the powder precursor is 2,862 °C, much higher than the synthesis temperature of 1,200 °C, the iron transported to the surface of the target substrate was not enough to form a uniform thin film of metal borate (iron borate in this particular case), as confirmed through cross-section EDX analysis.

To demonstrate the feasibility of an iron-based catalyst medium, the use of iron-rich stainless steel as target substrate in the synthesis of BNNTs with bamboo morphology was also studied. A consistent tip-growth mechanism was observed in the iron-rich catalyst droplet; however, only periodic growth was achieved due to the segments of the bamboo structure.

5.1.3 The properties of BN nanomaterials can be controlled by synthesising different structures

The transformation of the thin film of magnesium borate into catalyst droplets enabled the use of different boron-containing precursors such as boron trioxide in the synthesis of BN nanomaterials. The thickness of the thin film of magnesium borate was controlled by varying the duration of the annealing of the powder precursor containing amorphous boron and magnesium oxide. Catalyst droplets of a smaller diameter were found to yield thinner BNNTs. Furthermore, carrying out the synthesis at different temperatures resulted in separated and clustered BNNTs.

This study was also able to demonstrate the successful synthesis of hybrid 1D nanostructures such as carbon-coated BNNTs and boron-doped CNTs: the former were generated through the addition of a carbon-containing gas precursor, while the latter was produced by supplying only boron- and carbon-containing gas precursors and not a nitrogen gas precursor.

This investigation has shown that that the properties of BN nanomaterials can be tailored by controlling their morphology. For instance, carbon coating was used to narrow the optical band gap of BNNTs from 5.8 eV to 4.9 eV. Different thermal conductivity values were observed by using different BN nanomaterials at 10 wt. % in isopropanol: 1D BNNTs measured 0.24 $Wm^{-1}K^{-1}$ while 2D BN nanosheets measured 0.18 $Wm^{-1}K^{-1}$. This variance is due to the difference in thermal transport path. Nanotubes exhibit a high aspect ratio owing to their 1D nanostructure, compared to the 2D nanostructure of BN nanosheets. These results demonstrate that BN nanomaterials in liquid solutions can be used as liquid coolants in systems that need thermal management, such as electronic devices, engines, and batteries.

5.1.4 Theoretical calculations support the experimental results and proved the synthesis of zigzag BNNT

The mechanisms of BNNT synthesis were further analysed using DFT-based *ab initio* theoretical calculations. The breaking of the B-B bond of B_2O_2 was studied by mapping the PES of the chemical reaction $B_2O_2 + H_2$ and $B_2O_2 + NH_3$, which led to the acquisition of energy barriers in the reactions. The direct B-B bond breaking of B_2O_2 via the hydrogen molecule was shown to have a smaller energy barrier than ammonia of 37.02 kcal/mol. However, when the B_2O_2 molecule was saturated with B-N bonding through periodic reaction to ammonia, ammonia broke the B-B bond with a smaller energy barrier than the hydrogen molecule of 31.30 kcal/mol.

The model for calculating the nucleation of BNNT on the catalyst droplet was guided by the HRTEM images acquired from the experiment, which showed the orientation of the BN wall with respect to the facets and step-edges of the magnesium oxide catalyst droplet. B-N bond formation reactions occurring on the MgO (100)-(111)

step-edge surface was shown to have more stable energy than those occurring on the MgO (111) facet surface. The introduction of the nitrogen and boron precursor generated the hexagonal B-N network of the BNNT, which exhibited a zigzag chirality on the MgO (100)-(111) step-edge surface. This zigzag chirality is in good agreement with the experimental observations acquired in the HRTEM analysis. The chirality of the synthesised BNNTs is due to the orientation of the adsorption of the B_2O_2 molecule and the atomic boron precursor on the MgO (100)-(111) step-edge surface.

On the basis of the small difference in energy barrier of ca. 2 kcal/mol derived from the theoretical calculations, it can also be concluded that that B-N bond formation can occur in the absence or presence of MgO, This theoretical result corroborates the experimental results indicating that synthesis without MgO produces BN nanotubes, while synthesis with MgO generates BN nanosheets.

An analysis of the bond formation of diatomic B-B, N-N, and B-N using linear transit calculation showed diatomic B-N to have the smallest energy barrier, thereby suggesting that B-N bonding is preferred. The lift-off of the BN wall from the surface of the catalyst droplet was found to be driven by the decrease in the adsorption energy of the BN sheet as the number of sheets on the surface of the MgO increased.

This study was able to capture experimentally the embryonic stage of BNNT growth. This enabled the correlation of the growth rate with the Arrhenius equation yielding an activation energy for BNNT growth of 58.88 kcal/mol. The activation energy is accounted for by the multiple chemical processes that occur during the synthesis of BNNTs, since the calculated energy barriers in the diffusion of boron and nitrogen atoms on the surface of MgO and B-N bond formation have lower energy values.

5.2 Future work

5.2.1 Aerosol-assisted CVD synthesis of BNNTs

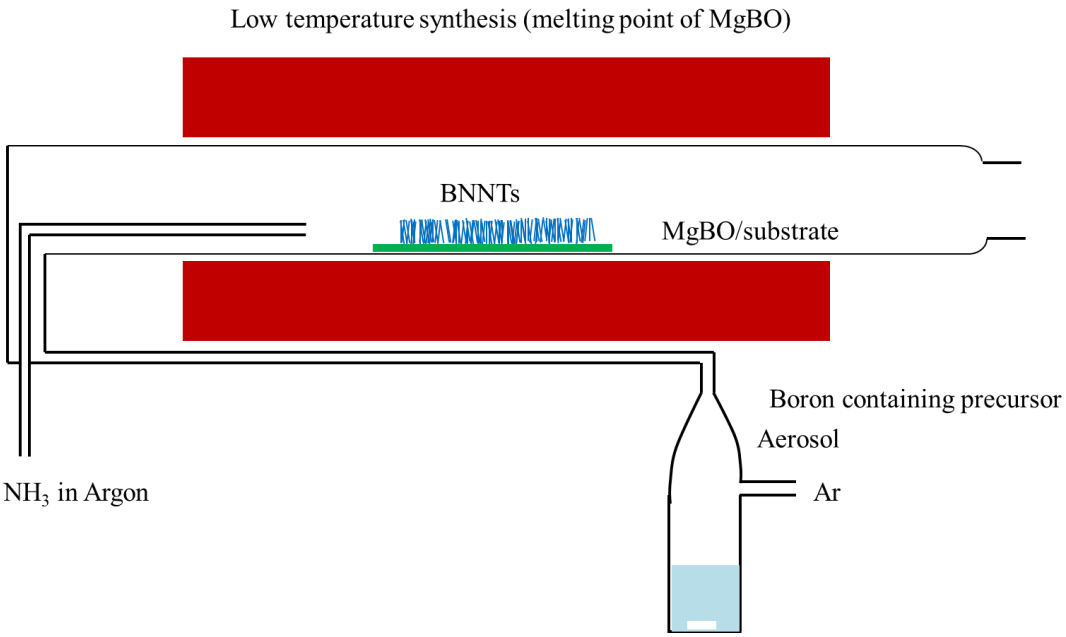


Figure 5.1 *Experimental setup for aerosol-assisted CVD synthesis of BNNTs.*

One approach to increasing the production of BNNTs involves the introduction of a high amount of the precursor during synthesis, particularly the boron-containing precursor. This can be achieved through the aerosol-assisted CVD (AACVD) method. Figure 5.1 is a schematic representation of how AACVD can be employed in the synthesis of BNNTs. The results of this study demonstrate that the boron precursor for BNNT synthesis is not limited to the *in situ* generation of B_2O_2, and that other boron-containing precursors such as boron trioxide can be used. This finding therefore motivates future investigations of other boron-containing precursors that can generate aerosol. Future research can also explore ways of optimising the upscaling method, such as determining the power input and frequency to be applied to the aerosol generator to be used with various boron-containing liquid precursors, and using the thin film of magnesium borate as a source for the production of the catalyst droplets that will generate nanotubular structures.

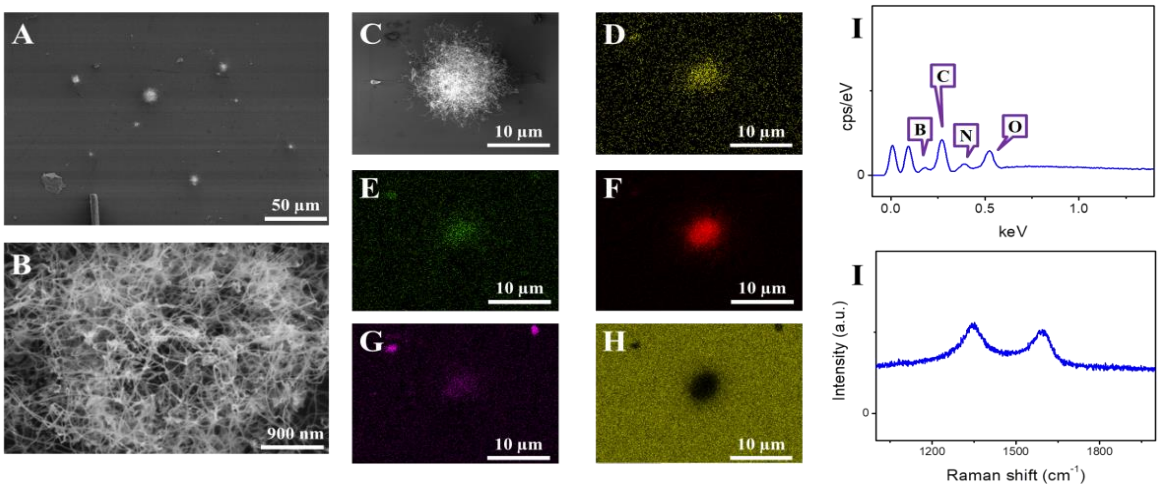


Figure 5.2 *Results utilising methyl borate in aerosol-assisted CVD synthesis. SEM images at (A) low and (B) high magnification. EDX analysis of the (C) region of interest showing detected elemental mapping of (D) boron, (E) nitrogen, (F) carbon, (G) oxygen, and (H) silicon. (I) Corresponding EDX spectrum and (J) Raman spectra of the synthesised material.*

The results of initial experiments utilising the AACVD method and methyl borate is shown in Figure 5.2. The SEM image at low magnification presented in Figure 5.2A shows less product coverage on the SiO_2 target substrate. At high magnification (Figure 5.2B), it can be observed that there were clustered morphologies composed of fibre-like structures. According to the EDX analysis, aside from the expected boron (Figure 5.2D) and nitrogen (Figure 5.2E), there was a presence of carbon (Figure 5.2F) and oxygen (Figure 5.2G) on the clustered structures. The EDX spectra in Figure 5.2H show similar peak intensities for boron and nitrogen, and relatively higher peak intensities for carbon and oxygen. The Raman spectra in Figure 5.2I indicate two strong peaks located at 1363.63 and 1601.39 cm^{-1}. The carbon detected in the synthesised product is due to the carbon present in the boron-containing precursor, trimethyl borate. As demonstrated in this work, the introduction of carbon-containing gas results in the carbon coating of the BNNTs. Here, it is not yet definite whether the carbon had been coated or if it was incorporated into the structure. Nevertheless, these initial results can still serve as a starting point for further work on upscaling BNNT production using the AACVD method.

5.2.2 BN nanomaterials used in composite science

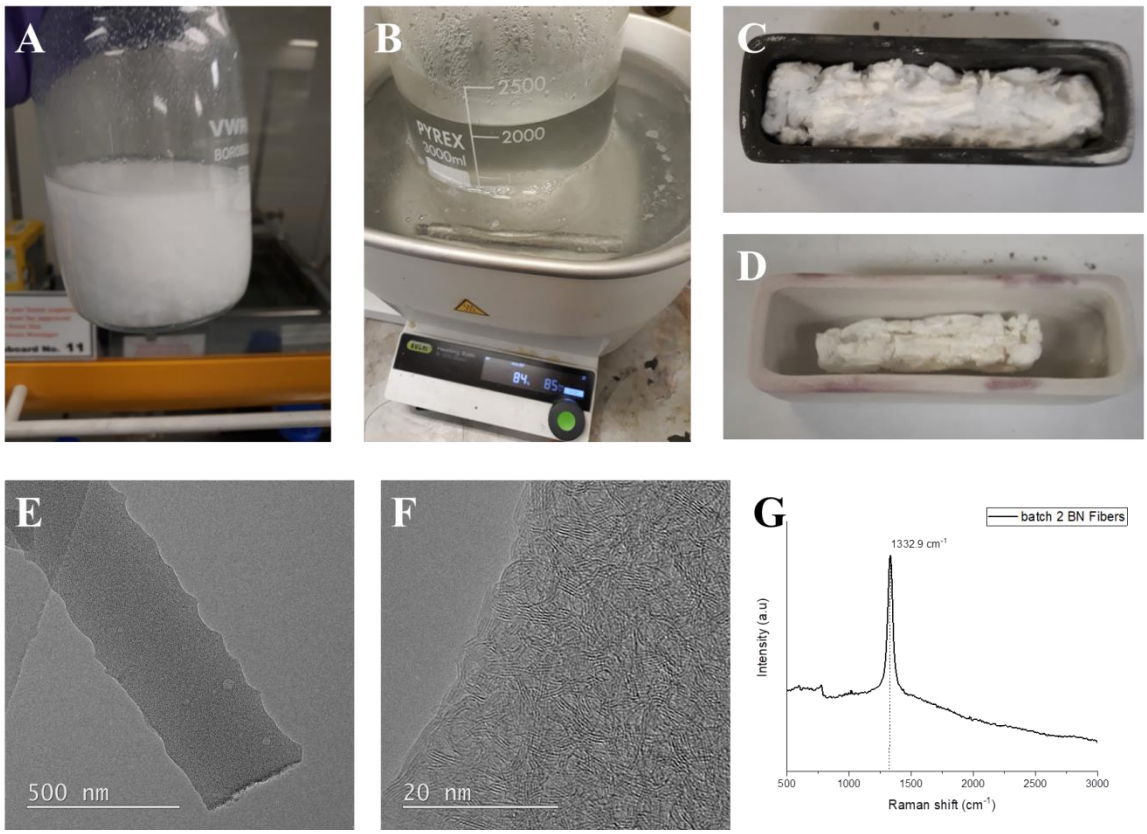


Figure 5.3 *Photograph images of (A) boric acid and melamine solution in water and (B) water bath process. A change of transparency of the solution is clearly seen. (C) The white felt-like product obtained after the freeze-drying step. (D) Photograph image after pyrolysis. TEM images at (E) low and (F) high magnification with (G) corresponding Raman spectra of the BN fibre produced by Ruth Jones.*

Composite science is another promising application for BN nanomaterials. However, gram-scale production should first be achieved in order to investigate the use of BN nanomaterials in composites. Here, a method adapted from Lin *et al*. [252] for synthesising BN fibres was demonstrated as an effective way to yield gram-scale quantities of BN nanomaterials. The synthesis involved dissolving H_3BO_3 and of $C_3N_6H_6$ in water (Figure 5.3A) and heating the solution at 85 °C for four hours (Figure 5.3B). The transparent hot solution was then frozen using liquid nitrogen. The frozen solution was placed inside a vacuum freeze dryer to dry for 2 to 3 days. The frozen sample turned into

the white, felt-like powder shown in Figure 5.3C. This powder was subjected to pyrolysis treatment by placing it inside a horizontal tube furnace at 1,300 ℃ for 4 hours. The heat treatment was conducted under inert atmosphere, argon, with a flow of 500 sccm. The synthesised material indeed had a fibre structure, without any indication of hollowness in the core section (Figure 5.3E). The HRTEM image shown in Figure 5.3F indicates the polycrystallinity of the BN sheets, and the Raman analysis shows the strong E_{2g} peak signalling the presence of a hexagonal BN network. The gram-scale quantity of the acquired product makes it possible to use it as a filler for composite fabrication. This highly promising synthesis method is currently being investigated and has resulted in a project within the University of Oxford's Nanomaterials by Design (NbD) research group [220].

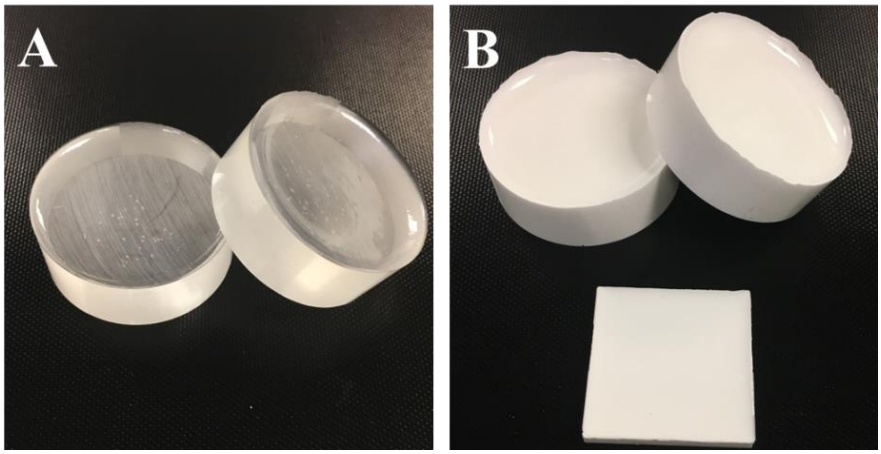


Figure 5.4 *Photograph images of composite fabrication with (A) blank epoxy, and (B) epoxy with 20 wt. % of commercially-made h-BN produced by Pierre Romain.*

Building on its existing knowledge of fabricating composite materials, the NbD group [220] is currently investigating the use of BN nanomaterials as fillers, particularly BN fibres, which for now is the only material that can be produced in large scale. Representatives of the fabricated composite are shown in Figure 5.4A and B, corresponding to a blank epoxy and to 20 wt. % filler of commercially produced h-BN, respectively. With dimensions of 1 cm height and 2 cm radius, these fabricated composites

can be subjected to mechanical, radio frequency, and thermal conductivity tests. Initial thermal conductivity measurements of these composites showed an improvement of 0.546 $Wm^{-1}K^{-1}$ from 0.230 $Wm^{-1}K^{-1}$ of the blank sample. Early studies of the use of BN fibres as filler showed an increase in thermal conductivity to 0.286 $Wm^{-1}K^{-1}$ at 10 wt. %. However, it should be noted that the fabrication method of these composites is not yet fully optimised. For example, the parameters for a good dispersion of BN fibres are yet to be determined.

Although still in its initial stages, this work has emerged as another research project in the NbD group [220], and constitutes a significant step towards the use of low-dimensional BN nanomaterials for thermal management applications, particularly as a component in fabricated composites used as thermal interface materials.

5.2.3 Calculation of properties for tailored applications

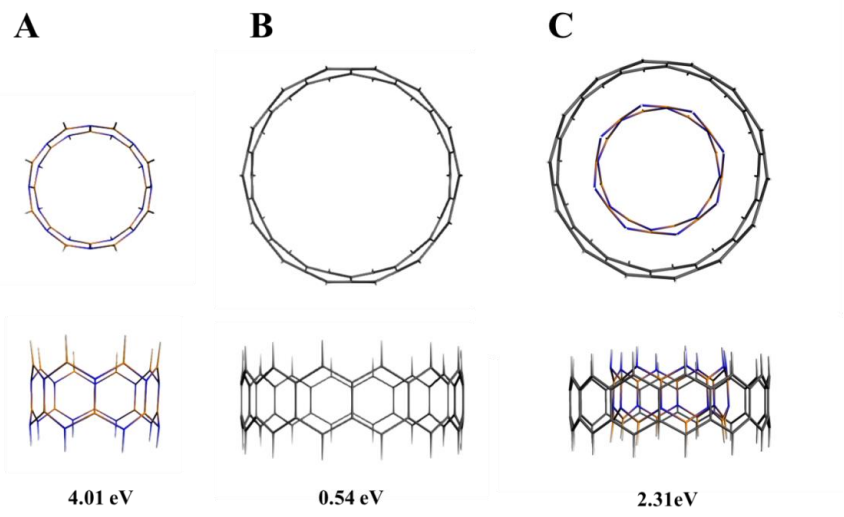


Figure 5.5 *Molecular structures for the calculation of band gap for (A) BNNT, (B) CNT, and (C) BNNT coated with CNT.*

One of the most significant contributions of this study is correlating experimental and theoretical work in order to shed light on various processes involved in the synthesis

of BN nanomaterials, as discussed in Chapter 4. Following on from this, there is a clear need to do further work corroborating empirical results with computational data to gain more knowledge of the various properties of BN nanomaterials; work such as comparing the band gap values of theoretical calculations to the synthesised hybrid nanostructures presented in Chapter 3.

Figure 5.5 shows the molecular representation for the calculation of the band gap of a BNNT coated with CNT. Although a nanoring does not represent a nanotube very well, initial calculations using nanorings serve as good starting point to provide insights regarding band gap properties. Results show that BN nanoring has a band gap of 4.01 eV (Figure 5.5A), the carbon nanoting has a band gap of 0.54 eV (Figure 5.5B), and the BN nanoring coated with carbon nanoring has a band gap of 2.31 eV (Figure 5.5C). These calculated band gap values deviate significantly from the band gap values measured in the experiments carried out in this study, such as the band gap value of 5.8 eV for BNNTs reported in section 3.3.5. This difference in theoretical and experimental band gap values can be attributed to factors used in the calculation such as the model molecule, the exchange-correlation potential, and the basis set. It is therefore necessary to undertake further work that will improve the existing model and increase the accuracy of the calculation demonstrated in section 4.2. Nevertheless, the initial calculations showed a decrease in optical band gap from BNNT to hybrid BNNT coated with CNT, which is in good agreement with the experimental results shown in section 3.3.5.

These future investigations will not only answer our remaining questions on the properties exhibited by nanomaterials, but will also ensure the continued collaboration between experimental and theoretical scientists working towards the development of nanomaterials for thermal management and other real-life applications.

Bibliography

1. Kroto, H.W., et al., *C-60 - Buckminsterfullerene.* Nature, 1985. **318**(6042): p. 162-163.
2. Geim, A.K. and I.V. Grigorieva, *Van der Waals heterostructures.* Nature, 2013. **499**(7459): p. 419-425.
3. Ponomarenko, L.A., et al., *Cloning of Dirac fermions in graphene superlattices.* Nature, 2013. **497**(7451): p. 594-597.
4. Iijima, S., *Helical Microtubules of Graphitic Carbon.* Nature, 1991. **354**(6348): p. 56-58.
5. Zhi, C.Y., et al., *Boron nitride nanotubes.* Materials Science & Engineering R-Reports, 2010. **70**(3-6): p. 92-111.
6. Lourie, O.R., et al., *CVD growth of boron nitride nanotubes.* Chemistry of Materials, 2000. **12**(7): p. 1808-+.
7. Koi, N., et al., *Structures and purification of boron nitride nanotubes synthesized from boron-based powders with iron particles.* Journal of Materials Science, 2008. **43**(8): p. 2955-2961.
8. Matveev, A.T., et al., *Boron nitride nanotube growth via boron oxide assisted chemical vapor transport-deposition process using LiNO3 as a promoter.* Nano Research, 2015. **8**(6): p. 2063-2072.
9. Ma, R., Y. Bando, and T. Sato, *CVD synthesis of boron nitride nanotubes without metal catalysts.* Chemical Physics Letters, 2001. **337**(1-3): p. 61-64.
10. Su, C.Y., et al., *Large-Scale Synthesis of Boron Nitride Nanotubes with Iron-Supported Catalysts.* Journal of Physical Chemistry C, 2009. **113**(33): p. 14732-14738.
11. Tang, C., et al., *A novel precursor for synthesis of pure boron nitride nanotubes.* Chemical Communications, 2002(12): p. 1290-1291.
12. Zhi, C.Y., et al., *Effective precursor for high yield synthesis of pure BN nanotubes.* Solid State Communications, 2005. **135**(1-2): p. 67-70.
13. Lee, C.H., et al., *Effective growth of boron nitride nanotubes by thermal chemical vapor deposition.* Nanotechnology, 2008. **19**(45).
14. Tang, C.C., Y. Bando, and T. Sato, *Catalytic growth of boron nitride nanotubes.* Chemical Physics Letters, 2002. **362**(3-4): p. 185-189.
15. Wagner, R.S. and W.C. Ellis, *Vapor-Liquid-Solid Mechanism of Single Crystal Growth (New Method Growth Catalysis from Impurity Whisker Epitaxial + Large Crystals Si E).* Applied Physics Letters, 1964. **4**(5): p. 89-&.
16. Pakdel, A., et al., *A comprehensive analysis of the CVD growth of boron nitride nanotubes.* Nanotechnology, 2012. **23**(21).
17. McLean, B., G.B. Webber, and A.J. Page, *Boron Nitride Nucleation Mechanism during Chemical Vapor Deposition.* Journal of Physical Chemistry C, 2018. **122**(42): p. 24341-24349.
18. Santra, B., et al., *Root-growth of boron nitride nanotubes: experiments and ab initio simulations.* Nanoscale, 2018. **10**(47): p. 22223-22230.
19. Songfeng, E., et al., *Boron nitride nanotubes grown on stainless steel from a mixture of diboron trioxide and boron.* Chemical Physics Letters, 2017. **687**: p. 307-311.
20. Souche, C., B. Jouffrey, and M. Nelhiebel, *Orientation sensitive EELS-analysis of boron nitride nanometric hollow spheres.* Micron, 1998. **29**(6): p. 419-424.

21. Watanabe, K., T. Taniguchi, and H. Kanda, *Direct-bandgap properties and evidence for ultraviolet lasing of hexagonal boron nitride single crystal.* Nature Materials, 2004. **3**(6): p. 404-409.
22. Li, L.H. and Y. Chen, *Atomically Thin Boron Nitride: Unique Properties and Applications.* Advanced Functional Materials, 2016. **26**(16): p. 2594-2608.
23. Novoselov, K.S., et al., *Electric field effect in atomically thin carbon films.* Science, 2004. **306**(5696): p. 666-669.
24. Bhimanapati, G.R., N.R. Glavin, and J.A. Robinson, *2D Boron Nitride: Synthesis and Applications.* 2d Materials, 2016. **95**: p. 101-147.
25. Song, L., et al., *Large Scale Growth and Characterization of Atomic Hexagonal Boron Nitride Layers.* Nano Letters, 2010. **10**(8): p. 3209-3215.
26. Lin, Y. and J.W. Connell, *Advances in 2D boron nitride nanostructures: nanosheets, nanoribbons, nanomeshes, and hybrids with graphene.* Nanoscale, 2012. **4**(22): p. 6908-6939.
27. Pease, R.S., *An X-Ray Study of Boron Nitride.* Acta Crystallographica, 1952. **5**(3): p. 356-&.
28. Chung, D.D.L., *Review graphite.* Journal of Materials Science, 2002. **37**(8): p. 1475-1489.
29. Pakdel, A., et al., *Boron Nitride Nanosheet Coatings with Controllable Water Repellency.* Acs Nano, 2011. **5**(8): p. 6507-6515.
30. Wang, J.S., C.H. Lee, and Y.K. Yap, *Recent advancements in boron nitride nanotubes.* Nanoscale, 2010. **2**(10): p. 2028-2034.
31. Tiano, A.L., et al., *Thermodynamic approach to boron nitride nanotube solubility and dispersion.* Nanoscale, 2016. **8**(7): p. 4348-4359.
32. Demczyk, B.G., et al., *Structure of boron nitride nanotubules.* Applied Physics Letters, 2001. **78**(18): p. 2772-2774.
33. Terrones, M., et al., *Pure and doped boron nitride nanotubes.* Materials Today, 2007. **10**(5): p. 30-38.
34. Oku, T., *Synthesis and atomic structures of boron nitride nanotubes.* Physica B-Condensed Matter, 2002. **323**(1-4): p. 357-359.
35. Ma, R.Z., et al., *Hydrogen uptake in boron nitride nanotubes at room temperature.* Journal of the American Chemical Society, 2002. **124**(26): p. 7672-7673.
36. Terrones, M., N. Grobert, and H. Terrones, *Synthetic routes to nanoscale BxCyNz architectures.* Carbon, 2002. **40**(10): p. 1665-1684.
37. Harrison, C., et al., *Polyethylene/boron nitride composites for space radiation shielding.* Journal of Applied Polymer Science, 2008. **109**(4): p. 2529-2538.
38. Thibeault, S.A., et al., *Nanomaterials for radiation shielding.* Mrs Bulletin, 2015. **40**(10): p. 836-841.
39. Langer, L., et al., *Electrical-Resistance of a Carbon Nanotube Bundle.* Journal of Materials Research, 1994. **9**(4): p. 927-932.
40. Tsang, S.C., et al., *A Simple Chemical Method of Opening and Filling Carbon Nanotubes.* Nature, 1994. **372**(6502): p. 159-162.
41. Rubio, A., J.L. Corkill, and M.L. Cohen, *Theory of Graphitic Boron-Nitride Nanotubes.* Physical Review B, 1994. **49**(7): p. 5081-5084.
42. Blase, X., et al., *Stability and Band-Gap Constancy of Boron-Nitride Nanotubes.* Europhysics Letters, 1994. **28**(5): p. 335-340.
43. Saito, Y., et al., *Carbon nanocapsules and single-layered nanotubes produced with platinum-group metals (Ru, Rh, Pd, Os, Ir, Pt) by arc discharge.* Journal of Applied Physics, 1996. **80**(5): p. 3062-3067.

44. Chopra, N.G., et al., *Boron-Nitride Nanotubes.* Science, 1995. **269**(5226): p. 966-967.
45. Loiseau, A., et al., *Boron nitride nanotubes with reduced numbers of layers synthesized by arc discharge.* Physical Review Letters, 1996. **76**(25): p. 4737-4740.
46. Loiseau, A., et al., *Boron nitride nanotubes.* Carbon, 1998. **36**(5-6): p. 743-752.
47. Cumings, J. and A. Zettl, *Mass-production of boron nitride double-wall nanotubes and nanococoons (vol 316, pg 211, 2000).* Chemical Physics Letters, 2000. **318**(4-5): p. 497-497.
48. Bartnitskaya, T.S., et al., *Synthesis, structure, and formation mechanism of boron nitride nanotubes.* Jetp Letters, 1999. **69**(2): p. 163-168.
49. Narita, I. and T. Oku, *Synthesis of boron nitride nanotubes by using YB6 powder.* Solid State Communications, 2002. **122**(9): p. 465-468.
50. Suenaga, K., et al., *Synthesis of nanoparticles and nanotubes with well-separated layers of boron nitride and carbon.* Science, 1997. **278**(5338): p. 653-655.
51. Golberg, D., et al., *Nanotubes in boron nitride laser heated at high pressure.* Applied Physics Letters, 1996. **69**(14): p. 2045-2047.
52. Laude, T., et al., *Long ropes of boron nitride nanotubes grown by a continuous laser heating.* Applied Physics Letters, 2000. **76**(22): p. 3239-3241.
53. Chen, Y., et al., *Large-quantity production of high-yield boron nitride nanotubes.* Journal of Materials Research, 2002. **17**(8): p. 1896-1899.
54. Lee, R.S., et al., *Catalyst-free synthesis of boron nitride single-wall nanotubes with a preferred zig-zag configuration.* Physical Review B, 2001. **64**(12).
55. Arenal, R., et al., *Root-growth mechanism for single-walled boron nitride nanotubes in laser vaporization technique.* Journal of the American Chemical Society, 2007. **129**(51): p. 16183-16189.
56. Han, W.Q., et al., *Synthesis of boron nitride nanotubes from carbon nanotubes by a substitution reaction.* Applied Physics Letters, 1998. **73**(21): p. 3085-3087.
57. Han, W.Q., et al., *Transformation of BxCyNz nanotubes to pure BN nanotubes.* Applied Physics Letters, 2002. **81**(6): p. 1110-1112.
58. Han, W.Q., H.G. Yu, and Z.X. Liu, *Convert graphene sheets to boron nitride and boron nitride-carbon sheets via a carbon-substitution reaction.* Applied Physics Letters, 2011. **98**(20).
59. Golberg, D., et al., *Preparation of aligned multi-walled BN and B/C/N nanotubular arrays and their characterization using HRTEM, EELS and energy-filtered TEM.* Physica B-Condensed Matter, 2002. **323**(1-4): p. 60-66.
60. Bi, J.Q., et al., *Large-scale synthesis of BN nanotubes using carbon nanotubes as template.* Materials Letters, 2009. **63**(15): p. 1299-1302.
61. Shelimov, K.B. and M. Moskovits, *Composite nanostructures based on template-crown boron nitride nanotubules.* Chemistry of Materials, 2000. **12**(1): p. 250-254.
62. Chen, Y., et al., *Synthesis of boron nitride nanotubes at low temperatures using reactive ball milling.* Chemical Physics Letters, 1999. **299**(3-4): p. 260-264.
63. Chen, Y., et al., *A solid-state process for formation of boron nitride nanotubes.* Applied Physics Letters, 1999. **74**(20): p. 2960-2962.
64. Yu, J., et al., *In situ formation of BN nanotubes during nitriding reactions.* Chemistry of Materials, 2005. **17**(20): p. 5172-5176.
65. Singhal, S.K., et al., *Growth and characterization of boron nitride nanotubes having novel morphologies using mechanothermal process.* Journal of Nanoparticle Research, 2010. **12**(6): p. 2201-2210.

66. Searcy, A.W. and C.E. Myers, *The Heat of Sublimation of Boron and the Gaseous Species of the Boron-Boric Oxide System.* Journal of Physical Chemistry, 1957. **61**(7): p. 957-960.
67. Kim, M.J., et al., *Double-Walled Boron Nitride Nanotubes Grown by Floating Catalyst Chemical Vapor Deposition.* Nano Letters, 2008. **8**(10): p. 3298-3302.
68. Golberg, D., et al., *Structural peculiarities of in situ deformation of a multi-walled BN nanotube inside a high-resolution analytical transmission electron microscope.* Acta Materialia, 2007. **55**(4): p. 1293-1298.
69. Akdim, B., et al., *Comparative theoretical study of single-wall carbon and boron-nitride nanotubes.* Physical Review B, 2003. **67**(24).
70. Coleman, J.N., U. Khan, and Y.K. Gun'ko, *Mechanical reinforcement of polymers using carbon nanotubes.* Advanced Materials, 2006. **18**(6): p. 689-706.
71. Hernandez, E., et al., *Elastic properties of C and BxCyNz composite nanotubes.* Physical Review Letters, 1998. **80**(20): p. 4502-4505.
72. Chang, C.W., et al., *Breakdown of Fourier's law in nanotube thermal conductors.* Physical Review Letters, 2008. **101**(7).
73. Golberg, D., et al., *Direct force measurements and kinking under elastic deformation of individual multiwalled boron nitride nanotubes.* Nano Letters, 2007. **7**(7): p. 2146-2151.
74. Suryavanshi, A.P., et al., *Elastic modulus and resonance behavior of boron nitride nanotubes.* Applied Physics Letters, 2004. **84**(14): p. 2527-2529.
75. Chopra, N.G. and A. Zettl, *Measurement of the elastic modulus of a multi-wall boron nitride nanotube.* Solid State Communications, 1998. **105**(5): p. 297-300.
76. Peng, Y.J., et al., *Ab initio studies of elastic properties and electronic structures of C and BN nanotubes.* Physica E-Low-Dimensional Systems & Nanostructures, 2006. **33**(1): p. 155-159.
77. Verma, V., V.K. Jindal, and K. Dharamvir, *Elastic moduli of a boron nitride nanotube.* Nanotechnology, 2007. **18**(43).
78. Dumitrica, T., et al., *Thermodynamics of yield in boron nitride nanotubes.* Physical Review B, 2003. **68**(8).
79. Bettinger, H.F., et al., *Mechanically induced defects and strength of BN nanotubes.* Physical Review B, 2002. **65**(4).
80. Berber, S., Y.K. Kwon, and D. Tomanek, *Unusually high thermal conductivity of carbon nanotubes.* Physical Review Letters, 2000. **84**(20): p. 4613-4616.
81. Xiao, Y., et al., *Specific heat of single-walled boron nitride nanotubes.* Applied Physics Letters, 2004. **84**(23): p. 4626-4628.
82. Stewart, D.A., I. Savic, and N. Mingo, *First-Principles Calculation of the Isotope Effect on Boron Nitride Nanotube Thermal Conductivity.* Nano Letters, 2009. **9**(1): p. 81-84.
83. Zettl, A., C.W. Chang, and G. Begtrup, *A new look at thermal properties of nanotubes.* Physica Status Solidi B-Basic Solid State Physics, 2007. **244**(11): p. 4181-4183.
84. Hone, J., et al., *Thermal conductivity of single-walled carbon nanotubes.* Physical Review B, 1999. **59**(4): p. R2514-R2516.
85. Kim, P., et al., *Thermal transport measurements of individual multiwalled nanotubes.* Physical Review Letters, 2001. **87**(21).
86. Chang, C.W., et al., *Isotope effect on the thermal conductivity of boron nitride nanotubes.* Physical Review Letters, 2006. **97**(8).
87. Ishigami, M., et al., *Observation of the giant stark effect in boron-nitride nanotubes.* Physical Review Letters, 2005. **94**(5).

88. Xiao, Y., et al., *Specific heat and quantized thermal conductance of single-walled boron nitride nanotubes.* Physical Review B, 2004. **69**(20).
89. Onn, D.G., et al., *Some Aspects of the Thermal-Conductivity of Isotopically Enriched Diamond Single-Crystals.* Physical Review Letters, 1992. **68**(18): p. 2806-2809.
90. Lan, H.P., et al., *Transverse dielectric properties of boron nitride nanotubes by ab initio electric field calculations.* Applied Physics Letters, 2009. **94**(18).
91. Dai, Y.T., et al., *Electric-field-induced deformation in boron nitride nanotubes.* Journal of Physics D-Applied Physics, 2009. **42**(8).
92. Radosavljevic, M., et al., *Electrical properties and transport in boron nitride nanotubes.* Applied Physics Letters, 2003. **82**(23): p. 4131-4133.
93. Zhi, C.Y., et al., *Perfectly dissolved boron nitride nanotubes due to polymer wrapping.* Journal of the American Chemical Society, 2005. **127**(46): p. 15996-15997.
94. Zhao, J.X. and B.Q. Dai, *DFT studies of electro-conductivity of carbon-doped boron nitride nanotube.* Materials Chemistry and Physics, 2004. **88**(2-3): p. 244-249.
95. Golberg, D., et al., *Synthesis, analysis, and electrical property measurements of compound nantubes in the B-C-N ceramic system.* Mrs Bulletin, 2004. **29**(1): p. 38-42.
96. Bai, X.D., et al., *Deformation-driven electrical transport of individual boron nitride nanotubes.* Nano Letters, 2007. **7**(3): p. 632-637.
97. Nakhmanson, S.M., et al., *Spontaneous polarization and piezoelectricity in boron nitride nanotubes.* Physical Review B, 2003. **67**(23).
98. Golberg, D., et al., *Synthesis and characterization of ropes made of BN multiwalled nanotubes.* Scripta Materialia, 2001. **44**(8-9): p. 1561-1565.
99. Chen, Y., et al., *Boron nitride nanotubes: Pronounced resistance to oxidation.* Applied Physics Letters, 2004. **84**(13): p. 2430-2432.
100. Song, W.-L., et al., *Polymer/Boron Nitride Nanocomposite Materials for Superior Thermal Transport Performance.* Angewandte Chemie International Edition, 2012. **51**(26): p. 6498-6501.
101. Amiri, A., M. Shanbedi, and M.J. AliAkbarzade, *The Specific Heat Capacity, Effective Thermal Conductivity, Density, and Viscosity of Coolants Containing Carboxylic Acid Functionalized Multi-Walled Carbon Nanotubes.* Journal of Dispersion Science and Technology, 2016. **37**(7): p. 949-955.
102. Zhu, D., et al., *Silver Nanowires Contained Nanofluids with Enhanced Optical Absorption and Thermal Transportation Properties.* ENERGY & ENVIRONMENTAL MATERIALS, 2019. **2**(1): p. 22-29.
103. Zhu, D., et al., *Intriguingly high thermal conductivity increment for CuO nanowires contained nanofluids with low viscosity.* Scientific Reports, 2018. **8**(1): p. 5282.
104. Das, S.K., et al., *Temperature Dependence of Thermal Conductivity Enhancement for Nanofluids.* Journal of Heat Transfer, 2003. **125**(4): p. 567-574.
105. Prakash, A., et al., *Investigation on Al2O3 Nanoparticles for Nanofluid Applications- A Review.* IOP Conference Series: Materials Science and Engineering, 2018. **377**: p. 012175.
106. Luyt, A.S., J.A. Molefi, and H. Krump, *Thermal, mechanical and electrical properties of copper powder filled low-density band linear low-density polyethylene composites.* Polymer Degradation and Stability, 2006. **91**(7): p. 1629-1636.

107. Prasher, R., *Thermal interface materials: Historical perspective, status, and future directions.* Proceedings of the Ieee, 2006. **94**(8): p. 1571-1586.
108. Leng, F., C.M. Tan, and M. Pecht, *Effect of Temperature on the Aging rate of Li Ion Battery Operating above Room Temperature.* Scientific Reports, 2015. **5**.
109. Spriggs, G.E., *13.5 Properties of diamond and cubic boron nitride: Datasheet from Landolt-Börnstein - Group VIII Advanced Materials and Technologies · Volume 2A2: "Powder Metallurgy Data. Refractory, Hard and Intermetallic Materials" in SpringerMaterials (https://doi.org/10.1007/10858641_7)*, P. Beiss, R. Ruthardt, and H. Warlimont, Editors., Springer-Verlag Berlin Heidelberg.
110. Harris, C.E., M.J. Shuart, and H.R. Gray, *Emerging materials for revolutionary aerospace vehicle structures and propulsion systems.* Sampe Journal, 2002. **38**(6): p. 33-43.
111. Abild-Pedersen, F., et al., *Mechanisms for catalytic carbon nanofiber growth studied by ab initio density functional theory calculations.* Physical Review B, 2006. **73**(11): p. 115419.
112. Lubej, M. and I. Plazl, *Theoretical descriptions of carbon nanotubes synthesis in a chemical vapor deposition reactor: A review.* Chemical and Biochemical Engineering Quarterly, 2012. **26**: p. 277-284.
113. Elliott, J.A., et al., *Atomistic modelling of CVD synthesis of carbon nanotubes and graphene.* Nanoscale, 2013. **5**(15): p. 6662-6676.
114. Banerjee, S., S. Naha, and I.K. Puri, *Molecular simulation of the carbon nanotube growth mode during catalytic synthesis.* Applied Physics Letters, 2008. **92**(23): p. 233121.
115. Charlier, J.C., et al., *Microscopic growth mechanisms for carbon and boron-nitride nanotubes.* Applied Physics A, 1999. **68**(3): p. 267-273.
116. Nørskov, J.K., et al., *Universality in Heterogeneous Catalysis.* Journal of Catalysis, 2002. **209**(2): p. 275-278.
117. Honkala, K., et al., *Ammonia synthesis from first-principles calculations.* Science, 2005. **307**(5709): p. 555-8.
118. Riikonen, S., et al., *Computational study of boron nitride nanotube synthesis: How catalyst morphology stabilizes the boron nitride bond.* Physical Review B, 2009. **80**(15): p. 155429.
119. Riikonen, S., et al., *Boron nitride formation on magnesium studied by ab initio calculations.* Physical Review B, 2010. **81**(12): p. 125442.
120. Golberg, D., et al., *Boron nitride nanotubes.* Advanced Materials, 2007. **19**(18): p. 2413-2432.
121. Meyer, R.R., et al., *Discrete Atom Imaging of One-Dimensional Crystals Formed Within Single-Walled Carbon Nanotubes.* Science, 2000. **289**(5483): p. 1324-1326.
122. Hutchison, J., et al., *The development and assessment of a high performance field-emission-gun analytical HREM for materials science applications.* 1999.
123. Kotakoski, J., et al., *Electron knock-on damage in hexagonal boron nitride monolayers.* Physical Review B, 2010. **82**(11): p. 113404.
124. Gilbert, S.M., et al., *Fabrication of Subnanometer-Precision Nanopores in Hexagonal Boron Nitride.* Scientific Reports, 2017. **7**(1): p. 15096.
125. Cretu, O., Y.-C. Lin, and K. Suenaga, *Inelastic electron irradiation damage in hexagonal boron nitride.* Micron, 2015. **72**: p. 21-27.
126. Park, H., G.H. Ryu, and Z. Lee, *Hole Defects on 2D Materials Formed by Electron Beam Irradiation: Toward Nanopore Devices.* Applied Microscopy, 2015. **45**: p. 107-114.

127. Li, J. and F. Banhart, *The Engineering of Hot Carbon Nanotubes with a Focused Electron Beam.* Nano Letters, 2004. **4**(6): p. 1143-1146.
128. Celik-Aktas, A., J.F. Stubbins, and J.-M. Zuo, *Electron beam machining of nanometer-sized tips from multiwalled boron nitride nanotubes.* Journal of Applied Physics, 2007. **102**(2): p. 024310.
129. Oku, T., et al., *Formation and atomic structures of boron nitride nanotubes with cup-stacked and Fe nanowire encapsulated structures.* Materials Transactions, 2007. **48**(4): p. 722-729.
130. Egerton, R.F., *Electron energy-loss spectroscopy in the electron microscope*. 2nd ed. 1996, New York: Plenum. xi, 485 p.
131. Verbeeck, J. and S. Van Aert, *Model based quantification of EELS spectra.* Ultramicroscopy, 2004. **101**(2): p. 207-224.
132. Verbeeck, J., S. Van Aert, and G. Bertoni, *Model-based quantification of EELS spectra: Including the fine structure.* Ultramicroscopy, 2006. **106**(11): p. 976-980.
133. Bertoni, G. and J. Verbeeck, *Accuracy and precision in model based EELS quantification.* Ultramicroscopy, 2008. **108**: p. 782-90.
134. Stenger, I., et al., *Low frequency Raman spectroscopy of few-atomic-layer thick hBN crystals.* 2d Materials, 2017. **4**(3).
135. Saitō, R., G. Dresselhaus, and M.S. Dresselhaus, *Physical properties of carbon nanotubes*. 1998, London: Imperial College Press. xii, 259 p.
136. Rao, A.M., et al., *Diameter-selective Raman scattering from vibrational modes in carbon nanotubes.* Science, 1997. **275**(5297): p. 187-191.
137. Arenal, R., et al., *Raman spectroscopy of single-wall boron nitride nanotubes.* Nano Letters, 2006. **6**(8): p. 1812-1816.
138. Wu, J., et al., *Raman spectroscopy and time-resolved photoluminescence of BN and BxCyNz nanotubes.* Nano Letters, 2004. **4**(4): p. 647-650.
139. Lu, J., et al., *Temperature-dependent Raman spectra of bamboo-like boron nitride nanotubes.* Applied Physics Express, 2014. **7**(2).
140. Lee, C.H., et al., *Patterned Growth of Boron Nitride Nanotubes by Catalytic Chemical Vapor Deposition.* Chemistry of Materials, 2010. **22**(5): p. 1782-1787.
141. Cramer, C.J., *Essentials of computational chemistry : theories and models*. 2002, Chichester: John Wiley. xvii, 542 p.
142. Jensen, F., *Introduction to computational chemistry*. 1999, Chichester: Wiley. xvi, 429 p.
143. Atkins, P.W. and R. Friedman, *Molecular quantum mechanics*. 4th ed. 2005, Oxford: Oxford University Press. xiv, 573 p.
144. Schrödinger, E., *An Undulatory Theory of the Mechanics of Atoms and Molecules.* Physical Review, 1926. **28**(6): p. 1049-1070.
145. Born, M. and R. Oppenheimer, *Zur Quantentheorie der Molekeln.* Annalen der Physik, 1927. **389**(20): p. 457-484.
146. Kozlowski, P.M. and L. Adamowicz, *Equivalent Quantum Approach to Nuclei and Electrons in Molecules.* Chemical Reviews, 1993. **93**(6): p. 2007-2022.
147. Pauli, W., *Über den Zusammenhang des Abschlusses der Elektronengruppen im Atom mit der Komplexstruktur der Spektren.* Zeitschrift für Physik, 1925. **31**(1): p. 765-783.
148. Parr, R.G. and W. Yang, *Density-functional theory of atoms and molecules*. International series of monographs on chemistry. 1989, New York ; Oxford; Oxford: Oxford University Press ; Clarendon Press. x, 333 p.

149. Hohenberg, P. and W. Kohn, *Inhomogeneous Electron Gas.* Physical Review B, 1964. **136**(3B): p. B864-+.
150. Kohn, W. and L.J. Sham, *Self-Consistent Equations Including Exchange and Correlation Effects.* Physical Review, 1965. **140**(4A): p. A1133-A1138.
151. Becke, A.D., *Density-Functional Exchange-Energy Approximation with Correct Asymptotic-Behavior.* Physical Review A, 1988. **38**(6): p. 3098-3100.
152. Perdew, J.P., *Density-Functional Approximation for the Correlation-Energy of the Inhomogeneous Electron-Gas.* Physical Review B, 1986. **33**(12): p. 8822-8824.
153. Li, J., et al., *Water-assisted chemical vapor deposition synthesis of boron nitride nanotubes and their photoluminescence property.* Nanotechnology, 2013. **24**(36).
154. McCaffrey, J.P., *Calibrating the TEM.* Microscopy Today, 2018. **5**(9): p. 16-17.
155. SARKAR, A., et al., *STUDIES ON NEON IRRADIATED AMORPHOUS CARBON USING X-RAY DIFFRACTION TECHNIQUE.* International Journal of Modern Physics B, 2008. **22**(07): p. 865-875.
156. Calderon, H.A., et al., *HRTEM low dose: the unfold of the morphed graphene, from amorphous carbon to morphed graphenes.* Advanced Structural and Chemical Imaging, 2016. **2**(1): p. 10.
157. Ma, R.Z., et al., *Growth, morphology, and structure of boron nitride nanotubes.* Chemistry of Materials, 2001. **13**(9): p. 2965-2971.
158. Stephan, O., et al., *Curvature-induced bonding changes in carbon nanotubes investigated by electron energy-loss spectrometry.* Physical Review B, 1996. **53**(20): p. 13824-13829.
159. Ong, C.W., et al., *X-ray photoemission spectroscopy of nonmetallic materials: Electronic structures of boron and BxOy.* Journal of Applied Physics, 2004. **95**(7): p. 3527-3534.
160. Moddeman, W.E., et al., *Surface Oxides of Boron and B12o2 as Determined by Xps.* Surface and Interface Analysis, 1989. **14**(5): p. 224-232.
161. Chen, S.H., et al., *Thermodynamic assessment of B2O3-MgO binary system.* Calphad-Computer Coupling of Phase Diagrams and Thermochemistry, 2015. **51**: p. 67-74.
162. Mutluer, T. and M. Timucin, *Phase-Equilibria in System Mgo-B2o3.* Journal of the American Ceramic Society, 1975. **58**(5-6): p. 196-197.
163. Ucyildiz, A. and I. Girgin, *Controlled synthesis, characterization and thermal properties of Mg2B2O5.* Central European Journal of Chemistry, 2010. **8**(4): p. 758-765.
164. Li, T.T., et al., *Highly Efficient Mass Production of Boron Nitride Nanosheets via a Borate Nitridation Method.* Journal of Physical Chemistry C, 2018. **122**(30): p. 17370-17377.
165. Mohlala, M.S., et al., *Carbon nanotube synthesis using ferrocene and ferrocenyl sulfide. The effect of sulfur.* Applied Organometallic Chemistry, 2007. **21**(4): p. 275-280.
166. Moisala, A., et al., *Single-walled carbon nanotube synthesis using ferrocene and iron pentacarbonyl in a laminar flow reactor.* Chemical Engineering Science, 2006. **61**(13): p. 4393-4402.
167. Mckee, G.S.B., C.P. Deck, and K.S. Vecchio, *Dimensional control of multi-walled carbon nanotubes in floating-catalyst CVD synthesis.* Carbon, 2009. **47**(8): p. 2085-2094.
168. Jacobson, N.S. and D.L. Myers, *High-Temperature Vaporization of B2O3(1) under Reducing Conditions.* Journal of Physical Chemistry B, 2011. **115**(45): p. 13253-13260.

169. Scheer, M.D., *The Gas Phase Constitution of Boric Oxide.* Journal of Physical Chemistry, 1957. **61**(9): p. 1184-1188.
170. Chase, M.W. and National Institute of Standards and Technology (U.S.), *NIST-JANAF thermochemical tables*. 4th ed. Journal of physical and chemical reference data Monograph. 1998, Washington, DC New York: American Chemical Society ; American Institute of Physics for the National Institute of Standards and Technology.
171. Williams, D.B. and C.B. Carter, *Transmission electron microscopy : a textbook for materials science*. 2nd. ed. 2009, New York ; London: Springer. lxii, 760 p., (I1-I15).
172. Muller, D.A., *Structure and bonding at the atomic scale by scanning transmission electron microscopy.* Nature Materials, 2009. **8**(4): p. 263-270.
173. Kociak, M., et al., *Experimental evidence of surface-plasmon coupling in anisotropic hollow nanoparticles.* Physical Review Letters, 2001. **87**(7).
174. Arenal, R., et al., *Optical gap measurements on individual boron nitride nanotubes by electron energy loss spectroscopy.* Microscopy and Microanalysis, 2008. **14**(3): p. 274-282.
175. Arenal, R., et al., *Electron energy loss spectroscopy measurement of the optical gaps on individual boron nitride single-walled and multiwalled nanotubes.* Physical Review Letters, 2005. **95**(12).
176. Benford, D.J., T.J. Powers, and S.H. Moseley, *Thermal conductivity of Kapton tape.* Cryogenics, 1999. **39**(1): p. 93-95.
177. Navick, X.F., et al., *Fabrication of ultra-low radioactivity detector holders for Edelweiss-II.* Nuclear Instruments & Methods in Physics Research Section a-Accelerators Spectrometers Detectors and Associated Equipment, 2004. **520**(1-3): p. 189-192.
178. Gustafsson, S.E., *Transient Plane Source Techniques for Thermal-Conductivity and Thermal-Diffusivity Measurements of Solid Materials.* Review of Scientific Instruments, 1991. **62**(3): p. 797-804.
179. Gustavsson, M., E. Karawacki, and S.E. Gustafsson, *Thermal-Conductivity, Thermal-Diffusivity, and Specific-Heat of Thin Samples from Transient Measurements with Hot Disk Sensors.* Review of Scientific Instruments, 1994. **65**(12): p. 3856-3859.
180. Lee, J.M., et al., *Fabrication of nano-structured polythiophene nanoparticles in aqueous dispersion.* Current Applied Physics, 2008. **8**(6): p. 659-663.
181. Xie, H., et al., *Nanofluids containing multiwalled carbon nanotubes and their enhanced thermal conductivities.* Journal of Applied Physics, 2003. **94**(8): p. 4967-4971.
182. Choi, C.S., S.J. Park, and H.J. Choi, *Carbon nanotube/polyaniline nanocomposites and their electrorheological characteristics under an applied electric field.* Current Applied Physics, 2007. **7**(4): p. 352-355.
183. Hong, K.S., T.-K. Hong, and H.-S. Yang, *Thermal conductivity of Fe nanofluids depending on the cluster size of nanoparticles.* Applied Physics Letters, 2006. **88**(3): p. 031901.
184. Fuentes, G.G., et al., *Electronic structure of multiwall boron nitride nanotubes.* Physical Review B, 2003. **67**(3).
185. McDougall, N.L., et al., *The Near Edge Structure of Hexagonal Boron Nitride.* Microscopy and Microanalysis, 2014. **20**(4): p. 1053-1059.

186. Duschanek, H. and P. Rogl, *Critical assessment and thermodynamic calculation of the binary system boron tungsten (B-W).* Journal of Phase Equilibria, 1995. **16**(2): p. 150-161.
187. Terrones, M., et al., *Metal particle catalysed production of nanoscale BN structures.* Chemical Physics Letters, 1996. **259**(5-6): p. 568-573.
188. Zhuang, C.C., et al., *Synthesis of boron nitride nanotube films with a nanoparticle catalyst.* Chinese Chemical Letters, 2016. **27**(6): p. 871-874.
189. Gai, P.L., et al., *Structural systematics in boron-doped single wall carbon nanotubes.* Journal of Materials Chemistry, 2004. **14**(4): p. 669-675.
190. Trentler, T.J., et al., *Solution-Liquid-Solid Growth of Crystalline Iii-V Semiconductors - an Analogy to Vapor-Liquid-Solid Growth.* Science, 1995. **270**(5243): p. 1791-1794.
191. Ahmad, P., et al., *Influence of growth duration on size and morphology of boron nitride nanotubes grown via chemical vapor deposition technique.* Journal of Physics and Chemistry of Solids, 2015. **85**: p. 226-232.
192. Kim, J., et al., *High Purity and Yield of Boron Nitride Nanotubes Using Amorphous Boron and a Nozzle-Type Reactor.* Materials, 2014. **7**(8): p. 5789-5801.
193. Chen, L.L., H.H. Ye, and Y. Gogotsi, *Synthesis of boron nitride coating on carbon nanotubes.* Journal of the American Ceramic Society, 2004. **87**(1): p. 147-151.
194. Nakanishi, R., et al., *Thin single-wall BN-nanotubes formed inside carbon nanotubes.* Scientific Reports, 2013. **3**.
195. Suenaga, K., et al., *Electron energy-loss spectroscopy of electron states in isolated carbon nanostructures.* Physical Review B, 2001. **63**(16).
196. Arenal, R., et al., *EELS measurements in single wall Boron nitride nanotubes.* Electronic Properties of Synthetic Nanostructures, 2004. **723**: p. 293-297.
197. Blase, X., et al., *Quasi-Particle Band-Structure of Bulk Hexagonal Boron-Nitride and Related Systems.* Physical Review B, 1995. **51**(11): p. 6868-6875.
198. Xiang, H.J., et al., *First-principles study of small-radius single-walled BN nanotubes.* Physical Review B, 2003. **68**(3).
199. Bangert, U., et al., *Doping of few-layered graphene and carbon nanotubes using ion implantation.* Physical Review B, 2010. **81**(24).
200. Ouyang, M., et al., *Energy Gaps in "Metallic" Single-Walled Carbon Nanotubes.* Science, 2001. **292**(5517): p. 702-705.
201. Verma, S.K., A.K. Tiwari, and D.S. Chauhan, *Experimental evaluation of flat plate solar collector using nanofluids.* Energy Conversion and Management, 2017. **134**: p. 103-115.
202. Hofmann, S., et al., *In situ observations of catalyst dynamics during surface-bound carbon nanotube nucleation.* Nano Letters, 2007. **7**(3): p. 602-608.
203. Yoshida, H., et al., *Atomic-scale in-situ observation of carbon nanotube growth from solid state iron carbide nanoparticles.* Nano Letters, 2008. **8**(7): p. 2082-2086.
204. Yatom, S., et al., *Detection of nanoparticles in carbon arc discharge with laser-induced incandescence.* Carbon, 2017. **117**: p. 154-162.
205. Gerakis, A., et al., *An all-optical, in situ diagnostic for large molecule and nanoparticle detection.* Synthesis and Photonics of Nanoscale Materials Xiv, 2017. **10093**.
206. Vekselman, V., et al., *Quantitative imaging of carbon dimer precursor for nanomaterial synthesis in the carbon arc.* Plasma Sources Science & Technology, 2018. **27**(2).

207. Baerends, E., et al., *SCM, Theoretical Chemistry.* ADF2012, 2013. **1**.
208. te Velde, G., et al., *Chemistry with ADF.* Journal of Computational Chemistry, 2001. **22**(9): p. 931-967.
209. Swart, M. and F.M. Bickelhaupt, *QUILD: QUantum-regions interconnected by local descriptions.* Journal of Computational Chemistry, 2008. **29**(5): p. 724-734.
210. Swart, M. and F.M. Bickelhaupt, *Optimization of strong and weak coordinates.* International Journal of Quantum Chemistry, 2006. **106**(12): p. 2536-2544.
211. Swart, M., *Accurate Spin-State Energies for Iron Complexes.* Journal of Chemical Theory and Computation, 2008. **4**(12): p. 2057-2066.
212. Swart, M., A.W. Ehlers, and K. Lammertsma, *Performance of the OPBE exchange-correlation functional.* Molecular Physics, 2004. **102**(23-24): p. 2467-2474.
213. Tyminska, N. and E. Zurek, *DFT-D Investigation of Active and Dormant Methylaluminoxane (MAO) Species Grafted onto a Magnesium Dichloride Cluster: A Model Study of Supported MAO.* Acs Catalysis, 2015. **5**(11): p. 6989-6998.
214. Swart, M., *A new family of hybrid density functionals.* Chemical Physics Letters, 2013. **580**: p. 166-171.
215. Ruscic, B.M., L.A. Curtiss, and J. Berkowitz, *Photoelectron-Spectrum and Structure of B2o2.* Journal of Chemical Physics, 1984. **80**(9): p. 3962-3968.
216. Politzer, P., P. Lane, and M.C. Concha, *Computational determination of the energetics of boron ignition/combustion reactions.* Journal of Physical Chemistry A, 1999. **103**(10): p. 1419-1425.
217. Wang, Z.X. and M.B. Huang, *Evidence for higher reactivity of B-2. Theoretical studies of insertions of B-2 and B into methane and water.* Journal of the American Chemical Society, 1998. **120**(27): p. 6758-6760.
218. Setyawan, W. and S. Curtarolo, *High-throughput electronic band structure calculations: Challenges and tools.* Computational Materials Science, 2010. **49**(2): p. 299-312.
219. Kim, K.S., et al., *Hydrogen-Catalyzed, Pilot-Scale Production of Small-Diameter Boron Nitride Nanotubes and Their Macroscopic Assemblies.* Acs Nano, 2014. **8**(6): p. 6211-6220.
220. Dirtu, D., et al., *Thermal decomposition of ammonia. N2H4 - an intermediate reaction product.* Central European Journal of Chemistry, 2006. **4**(4): p. 666-673.
221. He, M.S., et al., *Chiral-Selective Growth of Single-Walled Carbon Nanotubes on Lattice-Mismatched Epitaxial Cobalt Nanoparticles.* Scientific Reports, 2013. **3**.
222. Jain, N., et al., *Facile synthesis of defect-induced highly-luminescent pristine MgO nanostructures for promising solid-state lighting applications.* Rsc Advances, 2016. **6**(6): p. 4960-4968.
223. Goswami, R., et al., *TEM studies of microstructure, interfaces, and intermixing of FePt/MgO/FePt/Pt/Cr(Ru) films.* Journal of Nanoparticle Research, 2013. **15**(4).
224. Chen, M.Y., A.R. Felmy, and D.A. Dixon, *Structures and Stabilities of (MgO)(n) Nanoclusters.* Journal of Physical Chemistry A, 2014. **118**(17): p. 3136-3146.
225. Wang, H., et al., *Theoretical study of surface dependence of NH3 adsorption and decomposition on spinel-type MgAl2O4.* Rsc Advances, 2015. **5**(95): p. 77973-77985.
226. Helveg, S., et al., *Atomic-scale imaging of carbon nanofibre growth.* Nature, 2004. **427**(6973): p. 426-429.
227. Riikonen, S., et al., *Computational study of boron nitride nanotube synthesis: How catalyst morphology stabilizes the boron nitride bond.* Physical Review B, 2009. **80**(15).

228. Saidi, W.A., *Density Functional Theory Study of Nucleation and Growth of Pt Nanoparticles on MoS2(001) Surface.* Crystal Growth & Design, 2015. **15**(2): p. 642-652.
229. Bengaard, H.S., et al., *Steam reforming and graphite formation on Ni catalysts.* Journal of Catalysis, 2002. **209**(2): p. 365-384.
230. Vang, R.T., et al., *Controlling the catalytic bond-breaking selectivity of Ni surfaces by step blocking.* Nature Materials, 2005. **4**(2): p. 160-162.
231. Beebe, T.P., et al., *Kinetics of the Activated Dissociative Adsorption of Methane on the Low Index Planes of Nickel Single-Crystal Surfaces.* Journal of Chemical Physics, 1987. **87**(4): p. 2305-2315.
232. Ryu, H., et al., *Pitfalls in Computational Modeling of Chemical Reactions and How To Avoid Them.* Organometallics, 2018. **37**(19): p. 3228-3239.
233. Abild-Pedersen, F., et al., *Mechanisms for catalytic carbon nanofiber growth studied by ab initio density functional theory calculations.* Physical Review B, 2006. **73**(11).
234. Rao, R., et al., *Insights into carbon nanotube nucleation: Cap formation governed by catalyst interfacial step flow.* Scientific Reports, 2014. **4**.
235. Bu, H.X., et al., *The role of sp(2) and sp(3) hybridized bonds on the structural, mechanical, and electronic properties in a hard BN framework.* Rsc Advances, 2019. **9**(5): p. 2657-2665.
236. Pacile, D., et al., *The two-dimensional phase of boron nitride: Few-atomic-layer sheets and suspended membranes.* Applied Physics Letters, 2008. **92**(13).
237. Wu, Y.B., L.K. Wagner, and N.R. Aluru, *Hexagonal boron nitride and water interaction parameters.* Journal of Chemical Physics, 2016. **144**(16).
238. Yeh, Y.W., et al., *Stable synthesis of few-layered boron nitride nanotubes by anodic arc discharge.* Scientific Reports, 2017. **7**.
239. Yu, D.P., et al., *Synthesis of boron nitride nanotubes by means of excimer laser ablation at high temperature.* Applied Physics Letters, 1998. **72**(16): p. 1966-1968.
240. Chejanovsky, N., et al., *Quantum Light in Curved Low Dimensional Hexagonal Boron Nitride Systems.* Scientific Reports, 2017. **7**.
241. Wirtz, L., et al., *Ab initio calculations of the lattice dynamics of boron nitride nanotubes.* Physical Review B, 2003. **68**(4).
242. Oku, T. and I. Narita, *Atomic structures and stabilities of zigzag- and armchair-type boron nitride nanotubes studied by high-resolution electron microscopy and molecular mechanics calculation.* Diamond and Related Materials, 2004. **13**(4-8): p. 1254-1260.
243. Han, L.T. and P. Krstic, *A path for synthesis of boron-nitride nanostructures in volume of arc plasma.* Nanotechnology, 2017. **28**(7).
244. Lee, Y.T., et al., *Temperature-dependent growth of vertically aligned carbon nanotubes in the range 800-1100 degrees C.* Journal of Physical Chemistry B, 2002. **106**(31): p. 7614-7618.
245. Baker, R.T.K., et al., *Nucleation and Growth of Carbon Deposits from Nickel Catalyzed Decomposition of Acetylene.* Journal of Catalysis, 1972. **26**(1): p. 51-&.
246. Baker, R.T.K., et al., *Formation of Filamentous Carbon from Iron, Cobalt and Chromium Catalyzed Decomposition of Acetylene.* Journal of Catalysis, 1973. **30**(1): p. 86-95.
247. Baker, R.T.K., J.J. Chludzinski, and C.R.F. Lund, *Further-Studies of the Formation of Filamentous Carbon from the Interaction of Supported Iron Particles with Acetylene.* Carbon, 1987. **25**(2): p. 295-303.

248. Baker, R.T.K., et al., *The Formation of Filamentous Carbon from Decomposition of Acetylene over Vanadium and Molybdenum.* Carbon, 1983. **21**(5): p. 463-468.
249. Riikonen, S., et al., *Boron nitride formation on magnesium studied by ab initio calculations.* Physical Review B, 2010. **81**(12).
250. Puretzky, A.A., et al., *In situ measurements and modeling of carbon nanotube array growth kinetics during chemical vapor deposition.* Applied Physics a-Materials Science & Processing, 2005. **81**(2): p. 223-240.
251. Bronikowski, M.J., *Longer nanotubes at lower temperatures: The influence of effective activation energies on carbon nanotube growth by thermal chemical vapor deposition.* Journal of Physical Chemistry C, 2007. **111**(48): p. 17705-17712.
252. Lin, J., et al., *Ultrafine porous boron nitride nanofibers synthesized via a freeze-drying and pyrolysis process and their adsorption properties.* Rsc Advances, 2016. **6**(2): p. 1253-1259.
253. Bale, C.W., et al., *FactSage thermochemical software and databases, 2010-2016 (vol 54, pg 35, 2016).* Calphad-Computer Coupling of Phase Diagrams and Thermochemistry, 2016. **55**: p. 1-19.
254. German, R.M. and K.A. D'Angelo, *Enhanced sintering treatments for ferrous powders.* International Metals Reviews, 1984. **29**(1): p. 249-272.
255. Jakobsson, L.K., G. Tranell, and I.H. Jung, *Experimental Investigation and Thermodynamic Modeling of the B2O3-FeO-Fe2O3-Nd2O3 System for Recycling of NdFeB Magnet Scrap.* Metallurgical and Materials Transactions B-Process Metallurgy and Materials Processing Science, 2017. **48**(1): p. 60-72.
256. Kumari, K., S. Ram, and R.K. Kotnala, *Effect of temperature on magnetic and impedance properties of Fe3BO6 of nanotubular structure with a bonded B2O3 surface layer.* Journal of Applied Physics, 2018. **123**(9).

Appendix: Additional information

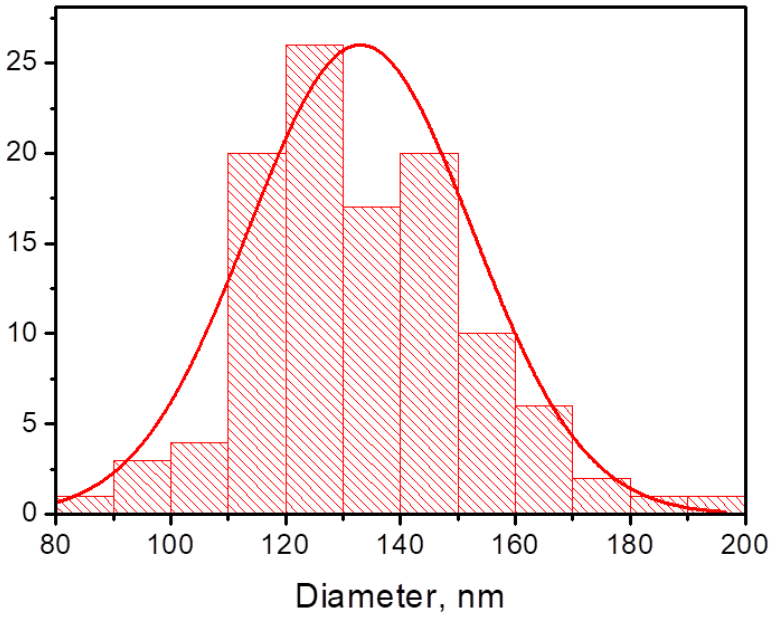


Figure A.1 Diameter distribution of the as-synthesised BNNTs.

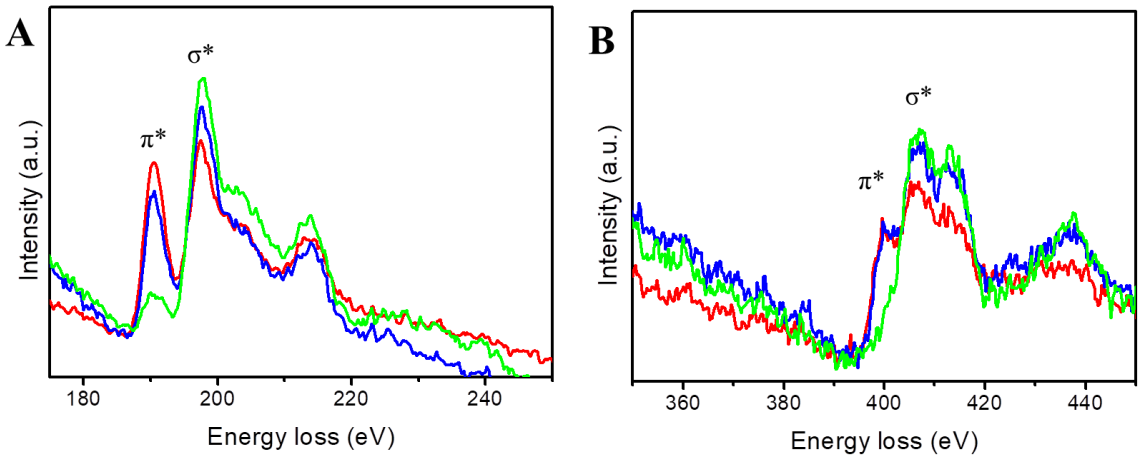


Figure A.2 EELS spectra from Figure 2 focussed on the K edge of (A) boron and (B) nitrogen clearly showing the weight change ratio of the π* and σ*.

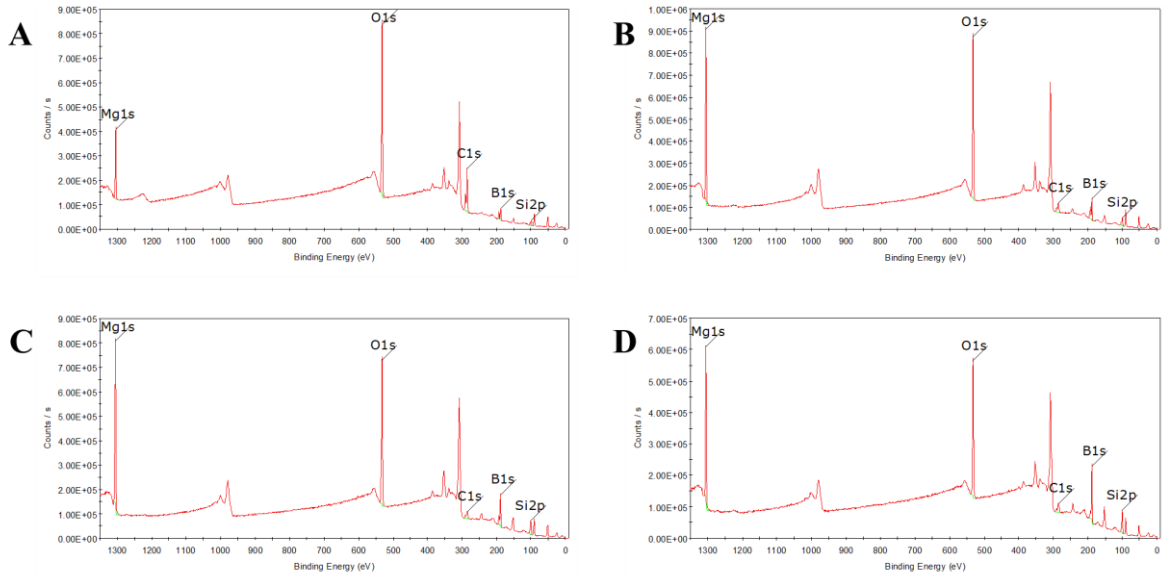


Figure A.3 Raw XPS ion beam etching data (A) Pristine thin film, (B) 10, (C) 30, and (D) 60 seconds of etching time.

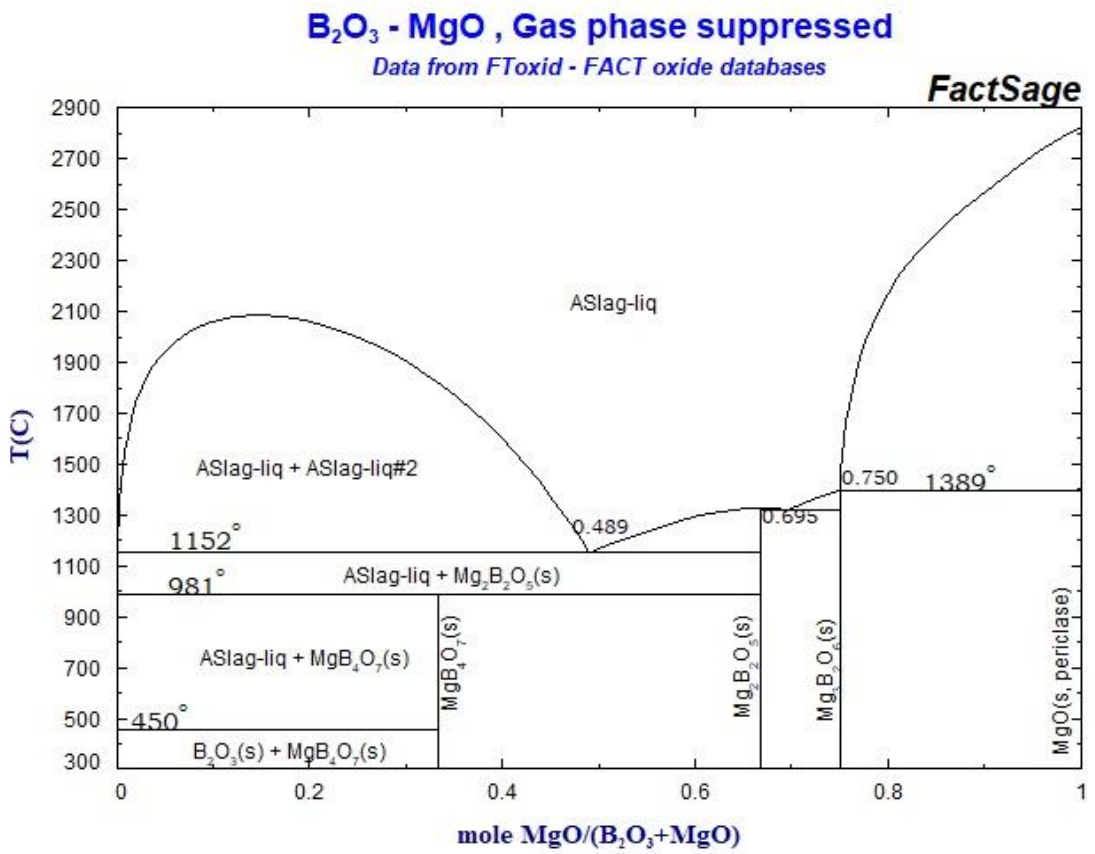


Figure A.4 Phase diagram of B_2O_3-MgO system[253].

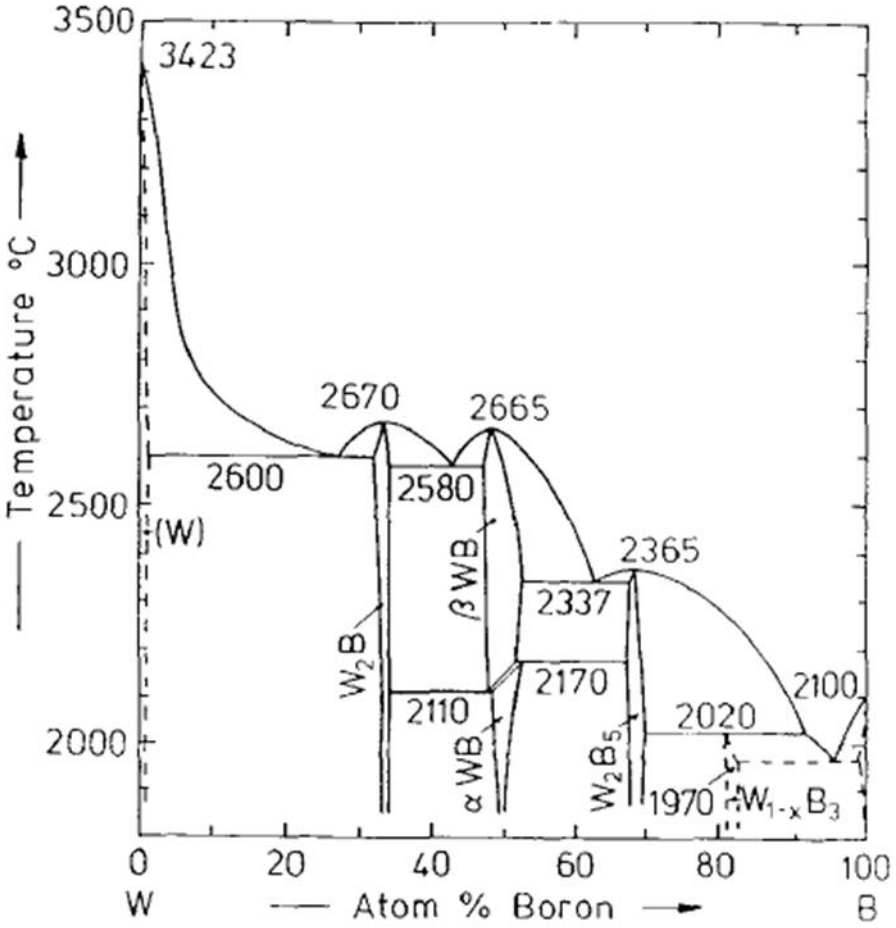


Figure A.5 Phase diagram of tungsten – boron[186].

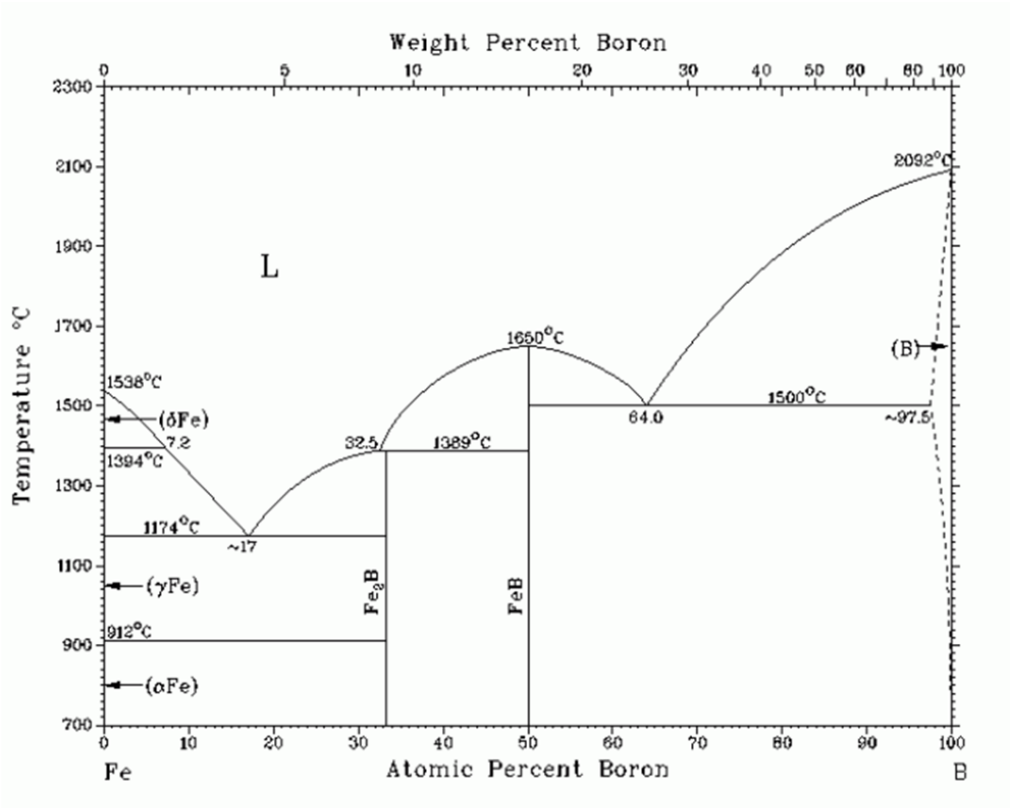


Figure A.6 Phase diagram of iron – boron[254].

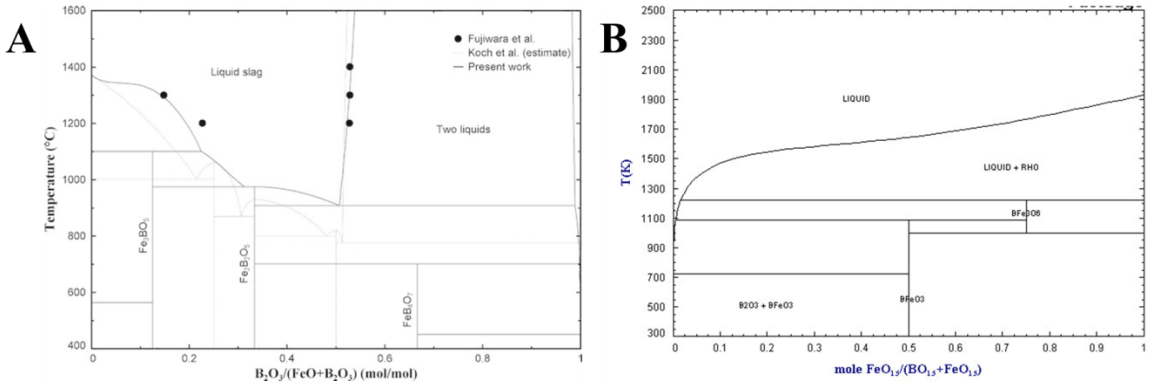


Figure A.7 Phase diagram of (A) FeO –B_2O_3 [255] and (B) Fe_2O_3 – B_2O_3 [256] system.

Coordinates of molecules

N_2

N	0.00000000	0.00000000	-0.55263759
N	0.00000000	0.00000000	0.55263759

B_2

B	0.00000000	0.00000000	-0.81703400
B	0.00000000	0.00000000	0.81703400

BN

B	0.00000000	0.00000000	-0.71964019
N	0.00000000	0.00000000	0.55709689

NH_3 (optimised)

N	-0.04108356	-0.03285226	0.29775513
H	-0.35033752	-0.92731390	-0.10065784
H	-0.65844329	0.68260338	-0.10365988
H	0.88991914	0.14456499	-0.09709014

H_2 (optimised)

H	0.00000000	0.00000000	-0.37637283
H	0.00000000	0.00000000	0.37637283

B_2O_2 (optimised)

O	0.00000000	0.00000000	-2.02978917
O	0.00000000	0.00000000	2.02978917
B	0.00000000	0.00000000	-0.81629314
B	0.00000000	0.00000000	0.81629314

H_2 + B_2O_2 complex (configuration 1, not optimised)

H	0.00000000	0.00000000	-0.37637283
H	0.00000000	0.00000000	0.37637283
O	1.47974007	-0.40423462	-2.00722127
O	1.47974007	-0.40423462	2.05235707
B	1.47974007	-0.40423462	-0.79372524
B	1.47974007	-0.40423462	0.83886104

H_2 + B_2O_2 complex (configuration 2, not optimised)

H	0.16443134	-0.15134254	-2.12309176
H	0.16443134	-0.15134254	-1.37034610
O	1.47974007	-0.40423462	-2.00722127
O	1.47974007	-0.40423462	2.05235707
B	1.47974007	-0.40423462	-0.79372524
B	1.47974007	-0.40423462	0.83886104

H_2 + B_2O_2 complex (configuration 3, not optimised)

H	1.17251741	-0.18145315	-3.50697691
H	1.89185358	-0.40073202	-3.54011724
O	1.47974007	-0.40423462	-2.00722127
O	1.47974007	-0.40423462	2.05235707
B	1.47974007	-0.40423462	-0.79372524
B	1.47974007	-0.40423462	0.83886104

H_2 + B_2O_2 complex (optimised)

H	-0.39462951	-2.65998772	0.00000000
H	0.35906472	-2.67060187	0.00000000
O	-2.03000334	0.25798114	0.00000000
O	2.03011498	0.24586049	0.00000000
B	-0.81619649	0.25649282	0.00000000
B	0.81632168	0.25144342	0.00000000

cis-OBB(H)OH (configuration 1, not optimised)

O	0.000000000000	0.000000000000	-2.029789170000
O	0.000000000000	0.000000000000	2.029789170000
B	0.000000000000	0.000000000000	-0.816293140000
B	0.000000000000	0.000000000000	0.816293140000
H	-0.168904295700	0.979057183200	-2.029787852000
H	-0.114422179600	0.983365427900	-0.816291826000

cis-OBB(H)OH (configuration 2, not optimised)

O	0.000000000000	0.000000000000	-2.029789170000
O	0.000000000000	0.000000000000	2.029789170000
B	0.000000000000	0.000000000000	-0.816293140000
B	0.000000000000	0.000000000000	0.816293140000
H	-0.146275539700	0.847889262300	-2.526547557000
H	-0.136381992500	1.172092126000	-0.816291574500

cis-OBB(H)OH (configuration 3, not optimised)

O	0.000000000000	0.000000000000	-2.029789170000
O	0.000000000000	0.000000000000	2.029789170000
B	0.000000000000	0.000000000000	-0.816293140000
B	0.000000000000	0.000000000000	0.816293140000
H	-0.000000448200	0.000002598002	-3.023308988000
H	-0.136381992500	1.172092126000	-0.816291574500

cis-OBB(H)OH (optimised)

O	-1.99448805	-0.17514961	-0.00041018
O	1.74352551	-0.40394316	0.00140298
B	-0.80918353	0.10780495	-0.00041394
B	0.80670643	0.58515073	0.00093565
H	1.12056395	1.74469898	0.00087637
H	2.66315922	-0.05452460	0.00004749

TS1 (1st high energy LT, Frame 23)

H	0.077683055280	-2.500663163390	-0.186613079064
H	1.223853372263	-2.377515592790	-0.133855149445
O	-2.041370850440	0.363743908377	0.018014587555
O	1.989197657792	0.272625579082	0.023384334896
B	-0.837530030377	0.213481581052	-0.012726901686
B	0.791215174174	0.060495963894	-0.018083064238

TS1 (2nd high energy LT, Frame 78)

H	0.534720981270	-1.990097659680	-0.204001058251
H	2.326234282181	-1.188880778027	-0.123961953864
O	-2.038714652159	0.476559464847	0.022121595866
O	1.922718467436	0.325794592102	0.033322966696
B	-0.852155709367	0.200294753296	-0.007589849700
B	0.755812443665	-0.323018496514	-0.042940287058

TS1 (1st high energy after TS run, Frame 23)

H	-0.10156724	3.53231363	0.02198405
H	1.14855875	1.55127514	-0.01112868
O	-1.97780140	-0.13876462	0.00548337
O	1.88394904	-0.48755203	0.00002065
B	-0.76823699	-0.00908090	-0.00452067
B	0.88147708	0.28036932	-0.01364397

TS1 (2nd high energy after TS run, Frame 78)

H	-1.068257000000	1.709168000000	0.000000000000
H	-1.866557000000	1.076802000000	0.000000000000
O	2.073911000000	-0.130040000000	0.000000000000
O	-1.918890000000	-0.316850000000	0.000000000000
B	0.868681000000	0.035556000000	0.000000000000
B	-0.783199000000	0.321623000000	0.000000000000

TS2 (cis-OBB(H)OH to trans-OBB(H)OH, converged)

O	-2.020828322000	-0.169324832400	-0.002315067474
O	1.770392231000	-0.396745129000	0.017348063370
B	-0.838278345200	0.118129734700	-0.011036192330
B	0.806363780800	0.562489475900	0.010857646370
H	1.109338873000	1.732300232000	-0.058609169990
H	2.235957061000	-0.825537007400	0.744878113300

trans-OBB(H)OH (optimised)

O	-1.98659524	-0.18437788	0.00000000
O	1.81323254	-0.34298788	0.00000000
B	-0.81330618	0.14623428	0.00000000
B	0.81721388	0.58735767	0.00000000
H	1.16304603	1.73412534	0.00000000
H	1.49797519	-1.27426979	0.00000000

TS3 (trans-OBB(H)OH to 2OBH, converged)

O	-2.363772155000	0.442812077100	-0.022366185850
O	1.454168382000	-0.578131969600	0.062040765390
B	-1.191447675000	0.124353070600	0.005473718509
B	0.780097590500	0.520755874200	0.071621239190
H	0.821256788700	1.720352445000	0.105313782600
H	0.103703850500	-0.674298290100	0.022891178590

2 OBH complex (optimised)

O	0.280228060000	-0.064182170000	-1.797085890000
O	-0.811021620000	0.209185880000	1.281145820000
B	-0.895420120000	0.224395370000	-1.709170000000
B	0.363801990000	-0.082109440000	1.190826520000
H	1.505372560000	-0.365204750000	1.141851000000
H	-2.037799040000	0.504462110000	-1.662678170000

OBH (optimised)

H	-2.061598041000	-0.131750175400	0.176182880100
B	-1.320443567000	-1.039959245000	0.258340466100
O	-0.557783224800	-1.980294791000	0.343606702600

NH_3 + B_2O_2 complex (optimised)

O	-2.35434421	0.10690688	0.02049957
O	1.44485504	1.03412959	-0.03115277
B	-1.13507205	0.15827051	0.00740285
B	0.54008966	0.16218033	-0.01355587
N	1.15438151	-1.48959510	-0.00965172
H	1.79546489	-1.56024448	-0.81430399
H	1.73352811	-1.58865720	0.83772323
H	0.48592760	-2.27617486	-0.04591829

R_{2N} (optimised)

O	-1.20063279	-0.75801237	0.60146912
O	1.82376506	1.26331996	-0.08874707
B	-0.97985607	0.53341917	0.20462197
B	0.62467488	1.04199599	0.00683160
N	-2.05184844	1.41861422	-0.03263328
H	-0.31997733	-1.24857720	0.72131423
H	-3.02373627	1.13146110	0.08423790
H	-1.93421591	2.38418518	-0.32551507
N	1.33401559	-1.80950941	0.82534829
H	1.79529310	-1.70548586	-0.08658944
H	1.87174472	-1.21756047	1.46997830
H	1.46061743	-2.78419192	1.12256707

$TS_{RP\text{-}2N}$ (optimised)

O	-2.153628649000	-0.345876846100	-0.297359553000
O	1.716030194000	0.684254436800	-0.082228082400
B	-0.839432603700	-0.198386290700	-0.749856996000
B	0.437466429000	0.467060363800	0.171623808500
N	-0.556335546200	-0.631061891000	-2.059064475000
H	-2.241778694000	-0.018693705890	0.611949257700
H	-1.247118601000	-1.035766069000	-2.685290997000
H	0.377449931200	-0.547150904400	-2.444358522000
N	0.376288220500	1.035344491000	1.686242189000
H	-0.148917593900	1.895745162000	1.871345422000
H	0.227223234200	0.375408566500	2.456053394000
H	1.529230390000	1.124597652000	1.179142073000

P_{2N} (optimised)

O	-2.153628649000	-0.345876846100	-0.297359553000
O	1.716030194000	0.684254436800	-0.082228082400
B	-0.839432603700	-0.198386290700	-0.749856996000
B	0.437466429000	0.467060363800	0.171623808500
N	-0.556335546200	-0.631061891000	-2.059064475000
H	-2.241778694000	-0.018693705890	0.611949257700
H	-1.247118601000	-1.035766069000	-2.685290997000
H	0.377449931200	-0.547150904400	-2.444358522000
N	0.376288220500	1.035344491000	1.686242189000
H	-0.148917593900	1.895745162000	1.871345422000
H	0.227223234200	0.375408566500	2.456053394000
H	1.529230390000	1.124597652000	1.179142073000

R_{3N} (optimised)

O	0.76018940	1.09844005	1.23851934
O	-2.32595005	-0.77381431	-0.26016473
B	-0.14511178	0.83339527	0.19945061
B	-0.96839305	-0.66208884	0.05381568
N	-0.31507891	1.87267094	-0.74153564
H	0.20007130	2.75307618	-0.69331689
H	-2.74278497	0.10865654	-0.31878861
H	-0.86281706	1.76352985	-1.59052505
N	-0.27552815	-1.87769902	0.26664109
H	0.75430722	0.36630057	1.88752010
H	-0.71744179	-2.79406845	0.18121591
H	0.73369652	-1.91057312	0.39225256
N	2.86032636	-0.46628220	-0.77616078
H	3.32089225	-1.26072750	-0.32008814
H	2.48195139	0.13770471	-0.03730585
H	2.05363192	-0.83744361	-1.28944856

$TS_{RP\text{-}3N}$ (optimised)

O	1.156534538000	0.839590055400	1.366627598000
O	-1.979596519000	-0.759869137100	-0.715415109500
B	0.337999708900	0.526313212400	-0.168983242500
B	-0.780881268800	-0.765519394900	0.001893862835
N	-0.190045415600	1.755936565000	-0.773603524600
H	0.457099849800	2.541288068000	-0.899017109300
H	-1.991809886000	0.035531645870	-1.289748160000
H	-1.040441343000	2.120294597000	-0.337797194900
N	-0.563817670400	-1.903207504000	0.824989258400
H	0.873266512400	0.179739517700	2.035492745000
H	-1.228778280000	-2.674788317000	0.890515228500
H	0.276838141400	-2.045301345000	1.376054888000
N	1.779294353000	0.125837466800	-0.717817015600
H	2.207666080000	0.757836260700	-1.404184135000
H	1.957802827000	0.372409619600	0.539557582400
H	1.885506002000	-0.840128870100	-1.038460727000

P_{3N} (optimised)

O	-0.44706012	-1.72779622	0.00843640
O	2.29617505	-1.24650075	0.36757531
B	-0.97624529	-0.44833768	-0.05429627
B	-0.00134283	0.96640874	-0.09315212
N	-2.39210736	-0.33778573	-0.07398431
H	-3.00725355	-1.15176636	-0.04622898
H	2.89731518	-1.71700659	-0.24731397
H	-2.87715327	0.54714115	-0.18888771
N	-0.26668305	2.05805397	0.76902048
H	0.53858419	-1.70694707	0.13951519
H	0.29713467	2.90694742	0.83011084
H	-0.98611469	2.00620117	1.48627167
N	1.17312211	1.01648104	-0.95105809
H	2.10929038	-0.36782654	-0.07609117
H	1.14232931	0.47730595	-1.81795130
H	1.68840301	1.89106861	-1.08751894

R_{4N} (optimised)

O	-0.16204763	1.71122635	-0.93968148
O	-2.86004505	1.10197948	-0.54883368
B	0.47899441	0.52407427	-0.63368551
B	-0.36313824	-0.91331954	-0.20888447
N	1.90891813	0.55972661	-0.64898883
H	2.41714705	1.36961388	-1.00971699
H	-3.43262210	1.29845202	-1.31964701
H	2.45900924	-0.29608591	-0.63389206
N	-0.04852215	-1.63102752	0.96153761
H	-1.14867884	1.63421798	-0.81901336
H	-0.55729597	-2.45775198	1.27809462
H	0.64214532	-1.27765576	1.64202383
N	-1.50146881	-1.32753627	-1.03032315
H	-2.56642752	0.14921077	-0.68297925
H	-1.45074135	-1.12356225	-2.03040169
H	-1.93356355	-2.24419626	-0.87695508
N	1.94407185	-0.01613702	2.53338485
H	1.46327106	0.65156986	3.14739315
H	2.86490379	-0.18937176	2.95193919
H	2.10214312	0.47051245	1.63792359

$TS_{RP\text{-}4N}$ (optimised)

O	0.48983431	-1.47647997	-0.70396996
O	-2.26546454	-1.32898796	-0.63893937
B	0.95729832	-0.09159208	0.00772230
B	-0.34655205	1.01680215	0.22863835
N	1.36614769	-0.98035478	1.33317926
H	0.83936704	-1.79094838	0.40937931
H	-2.69581818	-2.05191768	-0.13623562
H	0.86901656	-0.81566364	2.21311676
N	-0.38408904	2.16373828	-0.59387659
H	-0.51081935	-1.51952381	-0.77592688
H	-1.12953089	2.85843895	-0.63292620
H	0.31619586	2.26209615	-1.32916806
N	-1.48600545	0.74717658	1.10741945
H	-2.16612239	-0.57403662	0.02137920
H	-1.32562772	0.18668398	1.94493598
H	-2.17194066	1.48237319	1.30675152
N	2.09157213	0.45634860	-0.78635629
H	2.81286783	-0.21320526	-1.07397500
H	2.54446843	1.28519073	-0.39514839
H	2.37199779	-1.03298315	1.52906116

P_{4N} (optimised)

N	1.37737341	-1.53525303	0.90398940
N	-0.32343379	1.39289665	-0.85243918
B	0.15484012	-0.96715330	0.40006118
B	-0.03071215	0.73525322	0.39970589
N	-0.83422616	-1.78692423	-0.19195373
H	-0.77505039	-2.80206058	-0.26778976
H	-0.15034136	0.89915758	-1.72870523
H	-1.70480334	-1.39102475	-0.55800999
N	0.06950718	1.50925342	1.58453070
H	2.02476011	-0.98267017	1.46194377
H	-0.02362498	2.52416895	1.63131328
H	0.18055820	1.07843088	2.49843545
H	-0.31330393	2.40826888	-0.97362233
H	1.53498328	-2.53924701	1.00506381
O	-3.01353330	0.23580102	-0.97245730
H	-3.49206484	0.41535141	-0.13640522
H	-2.18213023	0.77637803	-0.89041787
O	2.71742726	-0.06750270	-1.44488408
H	2.34616766	-0.70829222	-0.78926602
H	2.20639137	0.74534395	-1.24821706

$B_2N_4H_8$ (optimised)

N	-1.47941961	1.22539823	0.53958498
N	1.57251269	-1.21859364	0.40823033
B	-0.82127159	0.03655576	0.10210786
B	0.88784189	-0.02186029	0.03841299
N	-1.58490974	-1.10517647	-0.28691961
H	-2.60359056	-1.14844746	-0.30479482
H	1.08039827	-1.99766361	0.83657786
H	-1.14554007	-1.91113145	-0.72280514
N	1.62447205	1.12504259	-0.38592527
H	-0.95946833	1.99813394	0.94588830
H	2.63881868	1.16535155	-0.48184451
H	1.15598662	1.93755686	-0.77721911
H	2.58590318	-1.33024345	0.42375051
H	-2.48918001	1.33184485	0.63322653

R_{H2} (optimised)

N	1.59607824	-0.93973060	0.40097287
N	-1.66775842	1.19442134	0.44241264
B	0.81895611	0.19044057	0.00334504
B	-0.88842152	0.08766031	-0.01136070
N	1.46606515	1.40043811	-0.38655351
H	2.47580806	1.53510453	-0.42863342
H	-1.23525580	1.99491173	0.89474525
H	0.94457666	2.17166415	-0.79366114
N	-1.52790399	-1.10390147	-0.46713613
H	1.15796896	-1.75504571	0.82101928
H	-2.53708100	-1.22899852	-0.54097590
H	-1.00245921	-1.83916819	-0.93176484
H	-2.68561511	1.20505843	0.50204655
H	2.61200587	-0.94422257	0.49126579
H	0.84055501	-2.70815892	-2.42565362
H	1.12258982	-2.26770024	-1.87932118

TS_{H2} (optimised)

N	1.77674085	-0.95659311	-0.54969935
N	-1.75226764	1.00369281	-0.52149559
B	1.01845825	0.07635108	-0.13574080
B	-0.98235266	-0.17756477	-0.32618697
N	1.11392530	1.32619016	0.51777931
H	2.00468409	1.68017830	0.85925142
H	-1.53731043	1.63452747	-1.29045649
H	0.30904521	1.90910637	0.73362197
N	-1.32223733	-1.23264980	0.55007725
H	1.05204927	-1.52239189	-1.48195311
H	-2.18944786	-1.30368249	1.07678119
H	-0.70636949	-2.03879673	0.63790790
H	-2.71202968	1.09858196	-0.19348863
H	2.76774405	-1.15609651	-0.47270260
H	0.25079775	-1.60478780	-2.05863710
H	-0.10528029	-0.45856558	-1.24151254

P_{H2} (optimised)

N	-1.63621923	0.51435640	0.38154914
N	1.37862537	-0.32332319	-0.00638458
B	-2.16751672	-0.78609139	0.21991445
B	2.26896283	0.64120107	-0.55026549
N	-3.55315221	-1.08272954	0.30450907
H	-4.27975141	-0.39293059	0.48521186
H	0.78955001	-0.90509649	-0.59698326
H	-3.91293945	-2.02486113	0.18717125
N	3.19399639	1.35654907	0.25041077
H	-0.63368815	0.68462908	0.29660287
H	3.31950080	1.21923893	1.25155413
H	3.81113965	2.06271882	-0.13926539
H	1.40370174	-0.64910456	0.95885333
H	-2.19190874	1.34917557	0.55511734
H	2.21457410	0.87937768	-1.72703997
H	-1.40686318	-1.69658250	0.00066928

R_{NH3} (optimised)

N	1.86465201	-1.09949414	1.29186713
N	-1.47426688	0.79015254	0.52072700
B	1.04395360	-0.28972794	0.44170248
B	-0.65726201	-0.38761381	0.62207797
N	1.62763635	0.57582885	-0.52315084
H	2.63261790	0.64505140	-0.68424160
H	-1.03689575	1.70758334	0.58372750
H	1.06518800	1.01627434	-1.26073703
N	-1.27530802	-1.64923091	0.86000585
H	1.47607026	-1.60517242	2.08305116
H	-2.27667364	-1.80173453	0.97940249
H	-0.74160209	-2.51350332	0.81788386
H	-2.46354672	0.81240292	0.77355825
H	2.88449575	-1.08328767	1.29271973
N	-0.60306069	1.27429851	-2.52182647
H	-1.07302037	2.03820457	-3.02084954
H	-0.63271042	0.45726183	-3.14248483
H	-1.18547168	1.04137249	-1.70303093

TS_{NH3} (optimised)

N	-2.01674112	-0.77975393	-0.03312975
N	1.37367134	-0.12414804	-1.38010324
B	-1.02599119	0.24314898	0.03711567
B	0.62233279	-0.25198854	0.07270501
N	-1.43343916	1.61709469	-0.00356467
H	-2.40396664	1.93073415	-0.02087843
H	0.84845078	0.37177002	-2.10753921
H	-0.78476167	2.38617660	0.13110021
N	0.84677006	-1.64036093	0.59663630
H	-1.73285972	-1.75588348	-0.07931017
H	1.82015767	-1.95602999	0.68384276
H	0.37112271	-1.84547119	1.47823197
H	1.71891271	-1.00975505	-1.76964584
H	-3.02260650	-0.63712334	-0.11437806
N	1.70476165	0.86766429	0.68366487
H	1.36292788	1.81333258	0.88579762
H	2.25764829	0.54630146	1.48631848
H	2.06728583	0.61871797	-0.55450749

P_{NH3} (optimised)

N	-1.92838764	0.90743329	0.05284766
N	1.65915732	-0.99363205	0.57097068
B	-2.37232356	-0.43722990	-0.04393197
B	1.60103375	0.25567363	-0.14528245
N	-1.49318310	-1.54085395	0.10912049
H	-0.48936646	-1.45802609	0.29233166
H	1.76126926	-1.00927126	1.58399580
H	-1.82442341	-2.49793682	0.04021847
N	1.82148043	0.28845504	-1.55806652
H	-2.56941533	1.68789462	-0.04969933
H	1.82970557	-0.57093306	-2.10298422
H	1.50520110	1.07954123	-2.11443215
H	2.08738671	-1.81118226	0.14085400
H	-0.96046334	1.18236398	0.24242819
N	1.22493261	1.45773350	0.55639199
H	1.29294405	1.50890137	1.57114856
H	-3.53918002	-0.64995465	-0.26448887
H	1.38615562	2.36734609	0.12779779

HBN_2H_4 (optimised)

N	-1.640238462000	0.513450027600	0.379363631800
H	-2.200072084000	1.342693543000	0.566689089700
B	-2.164146721000	-0.794477102200	0.218805372400
H	-0.645604662000	0.706560477500	0.314041664100
N	-3.550802631000	-1.077471073000	0.305486100400
H	-4.272648153000	-0.382553964200	0.485110850100
H	-1.402769420000	-1.699391619000	0.000464986132
H	-3.917671147000	-2.016743470000	0.187372394800

BN_3H_6 (optimised)

H	1.833543837000	-0.568051096900	-2.108302956000
N	1.674553144000	-0.991056705400	0.569974989600
H	1.534113903000	1.088078589000	-2.116944175000
B	1.584683655000	0.253035531500	-0.140014326700
H	2.029554848000	-1.836840675000	0.133579473700
H	1.295823853000	2.371758633000	0.112021582800
H	1.689289428000	-1.040267438000	1.584434870000
N	1.240919239000	1.460068609000	0.556522743900
N	1.820714391000	0.287705191400	-1.559100249000
H	1.233546850000	1.520733315000	1.570423651000

MgO (100) facet (optimised)

Mg	4.12319020	1.86590172	3.08796297
O	2.81790713	0.30277990	3.18334712
Mg	1.56127716	-1.27833378	3.17735316
O	0.25900314	-2.82153802	3.18318125
Mg	-1.01510121	-4.41301479	3.08964369
O	4.19570933	1.95543962	1.03060625
Mg	2.86210672	0.29216762	1.06085370
O	1.58061643	-1.29363738	1.04997323
Mg	0.27888574	-2.86344057	1.06114342
O	-1.08911420	-4.50070234	1.03030938
Mg	4.19791824	1.91574730	-0.97450657
O	2.88888496	0.27902636	-1.02392340
Mg	1.59667431	-1.30676727	-1.00218548
O	0.29701762	-2.88707019	-1.02369158
Mg	-1.04832126	-4.49512196	-0.97433396
O	4.20412441	1.89261835	-3.09071440
Mg	2.88211237	0.26263053	-3.11164515
O	1.61232187	-1.31956387	-3.17957939
Mg	0.31178032	-2.87823083	-3.11260255
O	-1.02440289	-4.49603513	-3.09154214
O	2.59104149	3.21481443	3.12754100
Mg	1.27292371	1.60563819	3.15716426
O	-0.02476906	0.02074691	3.19538941
Mg	-1.32182467	-1.56560801	3.15712012
O	-2.63933704	-3.17501029	3.12757303
Mg	2.62015168	3.21670952	1.06414944
O	1.29286062	1.59359486	1.02852902
Mg	-0.00643321	0.00675387	1.06641086
O	-1.30608964	-1.58217509	1.02826217
Mg	-2.63371414	-3.20395180	1.06339600
O	2.66545633	3.23637628	-1.03493872
Mg	1.30962043	1.58012384	-1.02362441
O	0.01025565	-0.00764155	-1.06390249
Mg	-1.28819111	-1.59490281	-1.02369579
O	-2.64545435	-3.25340722	-1.03544312
Mg	2.60366234	3.12725873	-3.04602881
O	1.32468946	1.56157182	-3.20129110
Mg	0.02733314	-0.02286872	-3.14770762
O	-1.26840618	-1.60709354	-3.20114999
Mg	-2.55068071	-3.17133234	-3.04634068
Mg	0.96794278	4.45192509	3.04630225
O	-0.30781007	2.86174798	3.14009765
Mg	-1.61070040	1.31790229	3.13451128
O	-2.86628397	-0.26298037	3.14006639
Mg	-4.17260850	-1.82823325	3.04547069
O	1.07578603	4.51143677	0.98704284
Mg	-0.29282405	2.87426646	1.01740221
O	-1.59502493	1.30514814	1.00649306
Mg	-2.87600751	-0.28174721	1.01731554
O	-4.20911123	-1.94538254	0.98676400
Mg	1.06699985	4.47894305	-1.01786726
O	-0.27734073	2.87074454	-1.06746126
Mg	-1.57907375	1.29148309	-1.04649057
O	-2.86897893	-0.29562770	-1.06739246
Mg	-4.17932840	-1.93303575	-1.01779029
O	1.07863265	4.45173222	-3.13449316
Mg	-0.25785968	2.83248989	-3.15510675
O	-1.55602456	1.27350499	-3.22261808
Mg	-2.82784470	-0.30746372	-3.15528732
O	-4.15002450	-1.93693712	-3.13337874
O	-0.58811637	5.67942848	2.98636853
Mg	-1.87096520	4.16848008	3.02395417
O	-3.21949023	2.63572217	3.08396934
Mg	-4.45617562	1.01144229	3.02460380
O	-5.68349257	-0.54599087	2.98611858
Mg	-0.57541789	5.70895924	1.02073900
O	-1.95771591	4.20804633	0.96397871
Mg	-3.21725411	2.63317452	1.01980576
O	-4.51279624	1.08860666	0.96422274
Mg	-5.71012802	-0.56224801	1.02052453
O	-0.56886392	5.78764350	-1.03285597
Mg	-1.91503383	4.18124025	-1.03997108
O	-3.23490597	2.64740237	-1.08026229
Mg	-4.47767542	1.05025297	-1.04017490
O	-5.78572092	-0.58600867	-1.03279800
Mg	-0.52842281	5.52999775	-2.95242187
O	-1.88736168	4.15479067	-3.15606159
Mg	-3.12228032	2.55628025	-3.09001208
O	-4.44610365	1.02926287	-3.15747733
Mg	-5.52501321	-0.57445080	-2.95203424
O	5.63621432	0.58556351	3.07185401
Mg	4.41030522	-0.97238677	3.11087700
O	3.17016669	-2.59576433	3.17125580
Mg	1.82496316	-4.12930891	3.11119255
O	0.54176757	-5.64053725	3.07300537
Mg	5.69635539	0.57362983	1.10690884
O	4.49881323	-1.07793354	1.05257406
Mg	3.20271434	-2.62191915	1.10781376
O	1.94409994	-4.19717278	1.05358480
Mg	0.56228067	-5.69669046	1.10772243
O	5.80372273	0.56975266	-0.94493761
Mg	4.49602454	-1.06682783	-0.95256582
O	3.25432907	-2.66426359	-0.99056149
Mg	1.93366155	-4.19734331	-0.95124678
O	0.58854789	-5.80243929	-0.94462735
Mg	5.57596138	0.53352442	-2.86862955
O	4.49967489	-1.07357884	-3.06914555
Mg	3.17549686	-2.59969435	-3.00347064
O	1.94064215	-4.19871374	-3.06854184
Mg	0.57941573	-5.57115613	-2.86757304

MgO (110) facet (optimised)

O	-1.70300740	1.80303605	-3.03111195
Mg	1.24382809	3.93191970	-3.11925458
O	0.35831192	-4.00163415	-1.58333847
Mg	0.20210510	-1.91003495	-1.61107939
O	2.69985729	4.19807722	-1.70459535
O	0.07839417	0.11390199	-1.67829173
Mg	-0.11491761	2.13350384	-1.62479648
O	0.28302900	-4.06847123	-4.40509007
O	-2.61874145	-4.22779117	-1.58943388
Mg	0.11113886	-1.94031941	-4.37650232
Mg	-2.79456997	-2.14026592	-1.61965672
O	-0.03109766	0.09152763	-4.37986548
O	-2.95966440	-0.12525820	-1.69052504
Mg	-0.22032560	2.12222081	-4.39253886
Mg	-3.10952291	1.89226636	-1.63386501
Mg	-1.78201084	3.83857478	-3.10789315
Mg	1.87317433	-4.14824369	-3.08749815
Mg	-1.15990036	-4.25275875	-3.06269406
O	1.83675539	-2.10786250	-3.04852417
O	-1.40166950	-2.22763678	-3.01713059
Mg	1.62302524	-0.10131598	-3.03427043
Mg	-1.53330902	-0.20882634	-3.01279113
O	1.52583650	1.91223992	-3.06192628
O	3.35316652	-4.08225340	-1.67649181
Mg	3.17267284	-2.01158562	-1.66632853
O	2.98714999	0.01463209	-1.64817507
Mg	2.75876855	2.05153715	-1.58892763
O	-0.28492406	4.22474116	-1.61481245
O	-0.36554412	4.25028128	-4.43901967
O	-3.26138184	3.98277086	-1.62249198
O	6.11068449	0.31963557	0.87371783
O	5.73027147	4.30825121	0.76050686
O	4.89820652	-1.66755098	2.62139210
Mg	3.16301897	-1.81524869	1.37995458
O	1.64190201	-1.95664036	-0.09151650
O	-3.32944168	3.96653619	1.40030164
Mg	-0.13276319	2.03604666	1.39974786
Mg	4.84802258	0.29535671	2.47736283
O	3.06873341	0.18254384	1.34075623
Mg	1.50841291	0.07467428	-0.13911677
Mg	-4.90632251	-0.26984089	2.43247078
O	-1.62407224	2.00788351	-0.12526890
O	4.69849033	2.26306040	2.54782709
Mg	2.93152737	2.17814973	1.36071382
O	1.34931366	2.14123790	-0.10987102
O	-6.13996334	-0.35072498	0.80479731
Mg	-5.08207749	3.60947815	2.35531678
Mg	5.88811883	2.31605125	0.84005748
Mg	1.73037112	-3.79580892	2.71980884
O	0.22677399	-4.09922421	1.41536737
Mg	-1.16236588	-4.08907833	-0.19039847
Mg	-4.71394191	3.79297849	-0.34144535
Mg	1.25303601	4.22072728	-0.21989077
O	1.66278890	-1.85285114	2.80439158
Mg	0.11278334	-1.97013129	1.41844971
O	-1.33699511	-2.04573018	-0.11264399
O	-4.97900028	1.68726922	2.55129006
Mg	-6.17741139	1.65803942	0.84425640
Mg	1.56657870	0.11741818	2.73392558
O	-0.00621201	0.03391768	1.37996729
Mg	-1.47925908	-0.01826121	-0.16657055
Mg	4.57767853	4.18334722	2.27452814
Mg	4.71034996	-3.85562975	-0.25901896
O	-6.25859088	3.65760191	0.85093677
Mg	-1.32361977	-3.95724038	2.69639893
O	-2.80784926	-4.24922589	1.40887382
Mg	-4.12434444	-4.26870735	-0.34044265
O	4.60068188	-1.82884907	-0.32662207
Mg	1.29827150	4.02479710	2.65467240
O	-1.47284879	-2.01948148	2.78903476
Mg	-2.94659446	-2.13535217	1.35766397
O	-4.31268848	-2.24052542	-0.39272433
O	-0.26185620	4.16730415	1.38665676
Mg	-1.76084969	4.06524839	-0.19455300
Mg	-1.60455448	-0.05744764	2.71181546
O	-3.09786588	-0.14479243	1.30757984
Mg	-4.47778361	-0.24105751	-0.39232329
Mg	4.48264476	0.18260774	-0.36500972
O	4.30583524	2.18923151	-0.38706816
O	-1.70821730	1.90910486	2.77326221
Mg	-3.20422956	1.84538421	1.35587070
O	-4.60059870	1.76455427	-0.38511266
O	6.20647002	-3.69687019	0.99902560
Mg	4.19308268	4.20579435	-0.45183356
O	2.79005288	4.30734085	1.35047837
Mg	-4.59100460	-4.13612825	2.34010622
O	-5.71825066	-4.33922937	0.81284282
Mg	6.13705333	-1.69453392	0.95005619
Mg	-1.78770778	3.84740553	2.67266780
O	1.44112193	2.08996003	2.78110758
O	-4.73636936	-2.21758307	2.54340205
Mg	-5.90573054	-2.34925025	0.81919000
Mg	4.97937099	-3.59714757	2.45859996
O	3.26133495	-3.94793324	1.43015942
Mg	1.76998846	-3.99681609	-0.16238738

MgO (111) facet (optimised)

O	2.59587935	-4.19948462	-1.01057382
O	2.35769686	4.30698603	-1.11706455
Mg	1.62365947	2.88982102	-2.28750803
O	0.88299769	1.45715027	-3.52181460
Mg	0.08867676	-0.05686514	-4.44700545
Mg	-1.62348699	-3.00405078	-0.05667257
Mg	0.72098630	4.35250449	-0.05135687
O	-0.10165786	2.89592803	-1.21515869
Mg	-0.84794591	1.42134672	-2.35969437
O	-1.63781874	-0.09339066	-3.55561833
Mg	-2.51052144	-4.53635307	2.08907074
O	-1.00153995	4.42038274	1.01525764
Mg	-1.78889589	2.90256707	-0.13186252
O	-2.52240240	1.40602826	-1.24682120
Mg	-3.27331140	-0.12355906	-2.35282177
Mg	2.70486347	-1.39807425	2.44855712
Mg	-2.76279488	4.43966078	1.97407872
O	-3.51984167	2.87036861	0.98216823
Mg	-4.21644500	1.31574031	-0.11682611
O	-4.89194557	-0.15439710	-1.21329884
O	1.74106129	-2.86024944	1.44525614
Mg	3.24745102	2.98917232	0.01816788
O	2.52772504	1.47594888	-1.14210934
Mg	1.74942426	0.01783973	-2.28866707
O	0.96496520	-1.49972021	-3.48417878
Mg	0.96423250	-4.30910534	0.05919753
O	1.57694409	2.98498492	1.37136289
Mg	0.79081791	1.46869820	0.08853819
O	0.02032397	-0.01497063	-1.08561925
Mg	-0.76554363	-1.52992813	-2.32157930
Mg	5.14261386	0.16962281	2.18820952
Mg	-0.19204790	3.12083952	2.33489400

O	-0.91887176	1.46111534	1.29896528
Mg	-1.67353616	-0.04750235	0.05646980
O	-2.43941549	-1.58022240	-1.20876058
O	4.28690057	-1.34701420	1.19233254
Mg	-2.65913757	-1.64147622	2.34178361
Mg	-2.74772892	1.54764664	2.30062107
O	-3.40572027	-0.07984769	1.30361923
Mg	-4.13536630	-1.55509717	-0.08050019
O	-3.35467835	-3.03941071	1.05754190
O	4.20296062	1.60968638	1.15631364
Mg	3.41194474	0.09359955	0.00924765
O	2.60753263	-1.36463763	-1.10738665
Mg	1.78378643	-2.85620913	-2.21549119
Mg	-0.01898114	-3.06804502	2.41311645
Mg	2.61854859	1.60163589	2.41146841
O	1.67143812	0.06166130	1.36954388
Mg	0.87257485	-1.42328531	0.12559255
O	0.06120871	-2.93080052	-1.14094902
O	-0.75265366	-4.44499014	1.12842801
Mg	3.41138707	-2.80537531	0.08877638
Mg	-0.05068364	0.03099491	2.56189107
O	-0.83642641	-1.47950384	1.33693122

MgO (100)-(110) step-edge (optimised)

Mg	3.88747521	1.41760111	-3.07646484
O	1.87579701	1.05703896	-3.14097758
Mg	-0.12458481	0.74992427	-3.15759568
O	-2.11651935	0.39163635	-3.13997048
Mg	-4.13687420	0.07892926	-3.07524518
O	3.90995557	2.02234668	-1.05361673
Mg	1.78465692	1.69167099	-1.11300945
O	-0.23095258	1.38334575	-1.10871261
Mg	-2.23732573	1.02167546	-1.11292205
O	-4.35600274	0.64484794	-1.05377395
Mg	3.73192511	2.67142238	0.81063515
O	1.68431842	2.36150430	0.85497870
Mg	-0.33809018	2.02190355	0.81729569
O	-2.36081465	1.68825506	0.85463799
Mg	-4.39845890	1.31717964	0.81008057
O	3.59292816	3.46399457	2.76410520
Mg	1.49516655	3.13773439	2.77109054
O	-0.47689574	2.85209492	2.80805654
Mg	-2.43527464	2.48390689	2.77071957
O	-4.52593016	2.11318264	2.76256439
O	4.26104364	-0.47120698	-2.53524786
Mg	2.21070867	-0.82773473	-2.55757053
O	0.19334372	-1.15618635	-2.58159875
Mg	-1.82141318	-1.49954394	-2.55628711
O	-3.87700092	-1.82841676	-2.53352203
Mg	4.16536058	0.09767496	-0.55424161
O	2.11260043	-0.18942612	-0.45843340
Mg	0.09371901	-0.56105505	-0.53002707
O	-1.93664366	-0.86398824	-0.45759210
Mg	-3.97182548	-1.25889368	-0.55283611
O	4.10814532	0.70277016	1.72452849
Mg	1.99033303	0.33955283	1.60628516
O	-0.01414657	0.08186677	1.63488430
Mg	-1.99411094	-0.32386025	1.60738018
O	-4.11601827	-0.66722774	1.72500112
Mg	3.66354980	1.63730151	3.38415092
O	1.79271040	1.29362547	3.59820185
Mg	-0.16312159	0.96775978	3.48582045
O	-2.11954877	0.64300824	3.59673922
Mg	-4.00207728	0.36232877	3.38423766
Mg	4.51140110	-2.39552936	-1.91145357
O	2.49803035	-2.71589851	-2.01696628
Mg	0.51636289	-3.09158677	-1.99718837
O	-1.48051748	-3.37856221	-2.01551666
Mg	-3.48803009	-3.72926644	-1.90843558
O	4.49983420	-1.74653018	0.04361795
Mg	2.40808154	-2.15682326	0.03870648
O	0.41252652	-2.46944412	0.04559328
Mg	-1.57636805	-2.82052927	0.04005187
O	-3.68752067	-3.11145588	0.04593496
Mg	4.30597899	-1.38190358	1.98866172
O	2.29838733	-1.59087544	2.09337955
Mg	0.33693448	-2.01257824	2.05874158
O	-1.65614377	-2.24920504	2.09445440
Mg	-3.62197881	-2.70315972	1.99069440
O	3.40795577	4.63449834	0.08224972
Mg	1.33104574	4.31324503	0.07716987
O	-0.67569871	4.04900564	0.08905511
Mg	-2.65983293	3.64917368	0.07605790
O	-4.72752817	3.28074557	0.08018035
O	4.78435517	-4.25435024	-1.33634408
Mg	2.83498074	-4.62883993	-1.37387045
O	0.84111530	-5.04150390	-1.43380711
Mg	-1.17902000	-5.29703665	-1.37303099
O	-3.14394594	-5.57604421	-1.33392700
Mg	4.71381031	-3.77052991	0.57850669
O	2.70734862	-4.17185042	0.60205474
Mg	0.75365159	-4.51478892	0.59141549
O	-1.20568830	-4.82344528	0.60295208
Mg	-3.23382555	-5.09521102	0.58071873
O	4.60016777	-3.23714090	2.49918892
Mg	2.64668134	-3.58114427	2.53718969
O	0.65890977	-3.94517280	2.63434464
Mg	-1.33995383	-4.24523009	2.53832830
O	-3.29913320	-4.55375701	2.50136755
Mg	3.14242942	5.14931194	1.91179111
O	1.20488671	5.06405118	2.03641494
Mg	-0.77968194	4.67027764	1.98177469
O	-2.78402577	4.40066528	2.03538117
Mg	-4.64391599	3.85351117	1.90923191
O	3.55504737	3.27296301	-3.64622625
Mg	1.58607019	2.97451356	-3.70493298
O	-0.44875382	2.69124130	-3.78840610
Mg	-2.46427026	2.29912435	-3.70516390
O	-4.42440068	1.94163094	-3.64657215
Mg	3.47364401	3.90286542	-1.80113763
O	1.43751381	3.69107048	-1.79687220
Mg	-0.55506504	3.32806990	-1.84650884
O	-2.55794697	3.02604835	-1.79774387
Mg	-4.55316229	2.56582708	-1.80245856

MgO (100)-(111) site-edge (optimised)

Mg	2.49737272	-4.59918561	3.04097906
Mg	0.00564159	-5.68331022	1.64571959
O	-1.42734081	-4.32565221	2.00503150
Mg	-2.74889034	-2.88065410	2.33735476
O	-4.16323191	-1.48660353	2.74126395
O	1.49776926	-4.33973091	1.26269722
Mg	0.01035082	-2.88195712	1.67855591
O	-1.37214086	-1.44089649	2.03185547
Mg	-2.71440561	0.00208564	2.39663373
O	-4.16078884	1.49305472	2.74139874
Mg	0.95546238	-4.35566209	-0.73310813
O	-0.49447699	-2.87676964	-0.38370313
Mg	-1.87707200	-1.43658259	-0.00673925
O	-3.29305572	0.00263523	0.34015820
Mg	-4.67537709	1.50956537	0.72222913
O	0.39125583	-4.34150293	-2.78452431
Mg	-1.03958145	-2.87089502	-2.41409368
O	-2.45018683	-1.44218201	-2.10672645
Mg	-3.79508637	0.00312931	-1.69665179
O	-5.22365792	1.49662697	-1.30362394
O	3.58793328	-2.92717800	2.75835867
Mg	2.30475836	-1.44860798	3.38688652
Mg	-5.38281633	0.00419273	2.90413442
O	-0.48976903	-5.79181810	-0.34193986
Mg	-1.93185781	-4.35455739	0.03745804
Mg	2.89374703	-2.89009091	0.83084107
O	1.45440816	-1.44884070	1.32312454
Mg	0.04705006	-0.00009573	1.76396022
O	-1.36977586	1.44293732	2.03197199
Mg	-2.74416135	2.88487634	2.33758516
O	2.34452423	-2.95105198	-1.16565519
Mg	0.90320112	-1.44544055	-0.73391808
O	-0.49252719	0.00042148	-0.38954211
Mg	-1.87472345	1.43961651	-0.00662057
O	-3.35691846	2.95661040	0.36558692
Mg	1.72978561	-2.87895091	-3.09708366
O	0.32322221	-1.44431928	-2.85507622
Mg	-1.04018281	0.00094336	-2.43081079
O	-2.44782039	1.44630169	-2.10662534
Mg	-3.78238158	2.88509166	-1.61560379
Mg	4.93752212	-1.43673371	2.27577059
O	3.57565482	-0.00302324	2.81645893
Mg	2.30721079	1.44457504	3.38694169
O	-3.36176299	-2.95125025	0.36534407
Mg	-4.67782756	-1.50209895	0.72210741
O	4.29191803	-1.51614376	0.34239933
Mg	2.86816209	-0.00237352	0.85140270
O	1.45678913	1.44639898	1.32322362
Mg	0.01506515	2.88179639	1.67876999
O	-1.42026053	4.32776827	2.00540188
Mg	3.71144767	-1.49678883	-1.55821313
O	2.28347765	-0.00178794	-1.15357921
Mg	0.90556580	1.44405675	-0.73384072
O	-0.48980044	2.87760832	-0.38347620
Mg	-1.92475240	4.35765833	0.03782928
O	3.11436070	-1.49302395	-3.57113966
Mg	1.69848376	-0.00123656	-3.17633879
O	0.32558927	1.44406673	-2.85495682
Mg	-1.03488390	2.87279660	-2.41386084
O	-2.46926073	4.34235680	-2.01342866
O	6.22694606	-0.00517161	1.82237154
Mg	4.93990239	1.42848030	2.27585308
O	3.59276898	2.92114804	2.75854453
Mg	2.50518179	4.59510702	3.04117212
O	-6.11271746	0.00487939	1.09681799
Mg	5.62740939	-0.00459786	-0.03591381
O	4.29441588	1.50912706	0.34251643
Mg	2.89848305	2.88532138	0.83104276
O	1.50486861	4.33718714	1.26303522
Mg	0.01493480	5.68313398	1.64617751
O	5.12205494	-0.00407764	-1.98763651
Mg	3.71390376	1.49091297	-1.55808385
O	2.34936547	2.94736949	-1.16543081
Mg	0.96258617	4.35420811	-0.73276246
O	-0.48033263	5.79263481	-0.34143901
Mg	4.35187121	-0.00335871	-3.75478711
O	3.11681529	1.48828316	-3.57100038
Mg	1.73451348	2.87643089	-3.09686306
O	0.39832700	4.34112488	-2.78415298
Mg	-0.98137989	5.58644741	-2.20612244
Mg	-0.99045323	-5.58463154	-2.20663233
O	-2.47633518	-4.33817997	-2.01381999
Mg	-3.78712138	-2.87886477	-1.61583344
O	-5.22611469	-1.48811898	-1.30373093
Mg	-6.36659488	0.00515055	-0.83106603

MgO (100)-(110)-(111) step-edge (optimised)

Mg	-1.70043097	-3.34660930	3.31308949
O	-1.17597719	-1.37529887	3.18310238
Mg	-0.70327481	0.58280812	3.04762962
O	-0.19205444	2.51466670	2.85490785
Mg	0.28315134	4.49280973	2.60270919
O	-2.33798014	-3.49491407	1.31522310
Mg	-1.82909907	-1.41146027	1.16246792
O	-1.34693943	0.55958493	0.93960608
Mg	-0.81519748	2.52128338	0.83005652
O	-0.29153831	4.54198355	0.60450570
Mg	-3.01927494	-3.45254827	-0.53326097
O	-2.51284653	-1.44719931	-0.82582350
Mg	-1.99291351	0.54493994	-1.00024352
O	-1.49149110	2.52105275	-1.33234843
Mg	-0.82555230	4.50689322	-1.31412090
O	-3.86046275	-3.47883411	-2.45726143
Mg	-3.36553858	-1.42866057	-2.71882765
O	-2.85821978	0.54862667	-3.03293896
Mg	-2.49616122	2.51740461	-3.17069381
Mg	-3.25034093	1.10477133	1.66843966
O	0.14241158	-3.92690460	2.78294314
Mg	0.67408699	-1.93146267	2.64441348
O	1.16491869	0.04285845	2.49959331
Mg	1.68064813	2.02744142	2.29370924
O	2.16597054	4.02255781	2.08778388
Mg	-0.45091832	-3.96435655	0.80721466
O	-0.00037102	-1.94468086	0.51031691
Mg	0.57013355	0.01851280	0.49321209
O	1.01425503	1.96976002	0.22046008
Mg	1.59842956	4.02262300	0.08675481
O	-1.09626307	-4.08868659	-1.42551800
Mg	-0.55886319	-1.99992130	-1.53619284
O	-0.14620933	0.03095482	-1.92989959
Mg	0.50891027	2.02819290	-1.77722446
O	0.99686543	3.99970155	-1.92824957
Mg	-2.07170323	-3.81453707	-3.09202427
O	-1.59716071	-2.02604234	-3.54742079
Mg	-1.11350666	-0.18251951	-3.64929791
O	-2.78052040	3.05528632	1.41455489
Mg	-2.15045581	5.00407686	1.25074332
Mg	2.03407449	-4.39699798	2.15426801

O	2.51424495	-2.41788347	2.08443972
Mg	3.06749299	-0.48587835	1.90615472
O	3.51296345	1.46335460	1.76322333
Mg	4.03295689	3.42152397	1.47889274
O	1.35151392	-4.49286210	0.21902306
Mg	1.93238654	-2.45250903	0.03362815
O	2.39547822	-0.49856124	-0.14813166
Mg	2.94010456	1.45238431	-0.29618564
O	3.41800167	3.48969936	-0.45909769
Mg	0.97050788	-4.44921418	-1.72825650
O	1.32251948	-2.47245963	-2.01845166
Mg	1.91478302	-0.54082555	-2.16820118
O	2.30432415	1.41620943	-2.36767690
Mg	2.90281592	3.38973754	-2.41763699
O	-4.92622058	-2.88464347	0.18220130
Mg	-4.41139146	-0.86524368	-0.04092331
O	-3.94909195	1.08520473	-0.27844475
Mg	-3.38996716	3.04045042	-0.46191360
O	-2.78828748	5.03645235	-0.72843390
O	3.85200117	-4.87207459	1.58201794
Mg	4.38799144	-2.96618427	1.44755335
O	4.96024485	-1.02474694	1.33571272
Mg	5.39379779	0.95445608	1.10860367
O	5.83817586	2.86858732	0.91475014
Mg	3.34648687	-4.92106153	-0.32550992
O	3.89701825	-2.96361265	-0.52693294
Mg	4.40490945	-1.05144296	-0.68940458
O	4.87374364	0.85890197	-0.85843344
Mg	5.31254618	2.86338300	-1.00110503
O	2.78261333	-4.92549066	-2.24006295
Mg	3.27920789	-3.01249659	-2.45375952
O	3.79605161	-1.07394778	-2.72164862
Mg	4.26382448	0.91556776	-2.79272087
O	4.72435883	2.83028318	-2.90502817
Mg	-5.48135410	-2.78357189	-1.64632371
O	-5.20252732	-0.87953316	-1.98954275
Mg	-4.68335256	1.06544211	-2.12530171
O	-4.27155449	3.03438262	-2.32923914
Mg	-3.76496719	4.94352008	-2.40924760
O	-3.51060217	-2.80366330	3.87575116
Mg	-3.05655938	-0.87165653	3.73705326
O	-2.61587606	1.12336919	3.61249272
Mg	-2.06985933	3.08411653	3.35766067
O	-1.56585043	4.98221169	3.12353836
Mg	-4.16797868	-2.83947150	2.04538546
O	-3.77467668	-0.84312462	1.82352383

B_2O_2 on MgO (100) facet (optimised)

Mg	-5.13133097	-2.22286681	3.04584091
O	-3.39617940	-3.07468827	3.26500771
Mg	-1.49295197	-3.74334503	3.22161180
O	0.37383269	-4.51445832	3.30482507
Mg	2.23820725	-5.03882390	3.12598871
O	-4.61118312	-0.35675854	3.21517060
Mg	-2.65908932	-1.11207518	3.25542994
O	-0.76967153	-1.85271844	3.34343653
Mg	1.13009683	-2.56052013	3.29755945
O	3.09166926	-3.29987142	3.29649597
Mg	-3.83970974	1.50793044	3.12210215
O	-1.94954163	0.78807576	3.29544680
Mg	-0.04080081	0.05784538	3.26694455
O	1.87139560	-0.67236256	3.33536521
Mg	3.76019287	-1.39638782	3.20566418
O	-3.17042737	3.41306811	3.15999697
Mg	-1.21112455	2.67515849	3.19973344
O	0.69155251	1.96844434	3.28703470
Mg	2.57847744	1.22719681	3.24180107
O	4.53302378	0.46944966	3.24102504
O	-5.34499447	-2.35201337	1.12608346
Mg	-3.39990589	-3.11832321	1.14993161
O	-1.52346501	-3.88673104	1.20809759
Mg	0.38237232	-4.56892886	1.19326225
O	2.34438468	-5.29245540	1.20802923
Mg	-4.62272465	-0.38661204	1.09839061
O	-2.66551256	-1.15742923	1.16514627
Mg	-0.76638059	-1.89771423	1.17095628
O	1.14782846	-2.61288379	1.20470782
Mg	3.11456796	-3.34844126	1.18467320
O	-3.93973238	1.51673243	1.10893956
Mg	-1.95429134	0.75778086	1.11765439
O	-0.02798654	0.02209131	1.18587249
Mg	1.88888839	-0.71129053	1.15996347
O	3.87915135	-1.47209013	1.19177709
Mg	-3.17901630	3.38904499	1.04248954
O	-1.20590101	2.65923123	1.10885988
Mg	0.70273847	1.94358462	1.11446233
O	2.60631862	1.19958358	1.14875941
Mg	4.56164218	0.43505441	1.12911898
Mg	-5.25523050	-2.35149583	-0.92127625
O	-3.39162210	-3.18959030	-0.84945769
Mg	-1.51215724	-3.90595924	-0.87894051
O	0.37139342	-4.62570045	-0.81003454
Mg	2.31982812	-5.24652990	-0.84249364
O	-4.63774636	-0.40465031	-0.90226729
Mg	-2.65370622	-1.16899081	-0.93370094
O	-0.74148644	-1.90953727	-0.90892443
Mg	1.16110944	-2.64715319	-0.87908240
O	3.15296796	-3.38298084	-0.81841287
Mg	-3.88010738	1.46257743	-1.00235957
O	-1.91943030	0.71359196	-0.94489890
Mg	-0.03902628	-0.00427098	-0.88271411
O	1.87147738	-0.73530547	-0.92136651
Mg	3.87605375	-1.50173877	-0.89436058
O	-3.19805914	3.36135901	-0.95745347
Mg	-1.21047116	2.60593426	-0.98947757
O	0.70845510	1.88210202	-0.96376427
Mg	2.61845161	1.16285643	-0.93526372
O	4.59350872	0.38282519	-0.87401849
O	-5.21642117	-2.36962249	-2.88275499
Mg	-3.38620754	-3.11202721	-2.90969463
O	-1.49650620	-3.93780829	-2.93656349
Mg	0.45149366	-4.58354906	-2.87054398
O	2.31236637	-5.24298562	-2.80457881
Mg	-4.55563442	-0.50620416	-2.95563260
O	-2.61257601	-1.21666689	-3.00701790
Mg	-0.78216249	-2.04664265	-2.99016476
O	1.14791726	-2.64866019	-2.98768166
Mg	3.06555215	-3.41674440	-2.89010547
O	-3.92757688	1.45052176	-3.05066895
Mg	-2.06352959	0.73220597	-3.36236421
O	0.06072197	-0.07839965	-3.38037050
Mg	2.01386429	-0.82112780	-3.03504252
O	3.89376073	-1.53863079	-2.93154055
Mg	-3.08937345	3.32886039	-3.01184350
O	-1.16877613	2.56072117	-3.06218422
Mg	0.74907267	1.95764118	-3.04699031
O	2.58898478	1.11848612	-3.04255534
Mg	4.53019534	0.41345550	-2.94755720
Mg	-2.31612799	5.14514742	2.93736014
O	-0.45190534	4.62819850	3.15120918
Mg	1.41238850	3.85594623	3.10916708
O	3.31824836	3.18700131	3.19159055
Mg	5.05505003	2.33013823	3.01743652
O	-2.40557877	5.33502566	1.01279398
Mg	-0.44554767	4.60843063	1.03591813
O	1.46625640	3.93074711	1.09290522
Mg	3.34061782	3.16668537	1.07858295
O	5.28522322	2.39631622	1.09461181
Mg	-2.35908840	5.22197230	-1.03345606
O	-0.41061605	4.60515764	-0.96406928
Mg	1.46670450	3.88353358	-0.99399277
O	3.35093762	3.16419176	-0.92512158
Mg	5.21585813	2.32570461	-0.95479053
O	-2.33783600	5.15864526	-2.99451172
Mg	-0.47956845	4.48970978	-3.02246976
O	1.47881332	3.84320146	-3.05167062
Mg	3.36155313	3.02673229	-2.98355995
O	5.18812009	2.27811068	-2.91624258
O	-1.34063760	0.42642845	-5.26642330
O	2.21562627	-0.95309718	-6.14612261
B	-0.19534559	-0.00283612	-4.81741245
B	1.14653372	-0.53054400	-5.72583168

B_2O_2 on MgO (110) facet (optimised)

O	-1.86142860	1.79420721	-3.11265762
Mg	1.08555950	3.91553592	-3.31008307
O	0.23469540	-4.00936434	-1.71118988
Mg	0.08241936	-1.91752668	-1.74249601
O	2.58950241	4.18405633	-1.94693835
O	-0.03887865	0.10640696	-1.81406723
Mg	-0.22564118	2.12667869	-1.76261533
O	0.06325256	-4.08779370	-4.52843430
O	-2.74134982	-4.22830614	-1.61501192
Mg	-0.10269743	-1.95913059	-4.50306555
Mg	-2.91333242	-2.14050609	-1.64811196
O	-0.24031526	0.07302646	-4.51023061
O	-3.07613380	-0.12541501	-1.72189514
Mg	-0.42522038	2.10409870	-4.52509520
Mg	-3.21936092	1.89268710	-1.66874987
Mg	-1.93834451	3.82959225	-3.19536802
Mg	1.69714023	-4.16593201	-3.26538876
Mg	-1.33356371	-4.26297254	-3.13694156
O	1.66673370	-2.12532400	-3.23387625
O	-1.56901054	-2.23709153	-3.09179216
Mg	1.45820612	-0.11822349	-3.22089553
Mg	-1.69580670	-0.21796811	-3.09156461
O	1.36473754	1.89543353	-3.25379448
O	3.22445160	-4.09765227	-1.90585303
Mg	3.04914576	-2.02652661	-1.89836517
O	2.86898208	0.00019580	-1.88252689
Mg	2.64740498	2.03787746	-1.82421156
O	-0.39042697	4.21834702	-1.75575190
O	-0.56707163	4.23229613	-4.57566337
O	-3.36596418	3.98358283	-1.66111384
Mg	1.44615675	0.06867662	-0.33928199
Mg	-4.83815116	-0.24597217	2.49015996
O	-1.67812160	2.02095437	-0.20976586
O	4.70445453	2.30346623	2.22903216
Mg	2.94777128	2.18276090	1.10953123
O	1.28691144	2.14918989	-0.30243538
O	-6.14516076	-0.33184176	0.90951810
Mg	-5.04751485	3.62643052	2.38258881
Mg	5.84686354	2.27918758	0.53555383
Mg	1.77375451	-3.79997420	2.47670828
O	0.21209424	-4.13758928	1.28658864
Mg	-1.23261256	-4.09120689	-0.27888170
Mg	-4.76681278	3.79739181	-0.31817311
Mg	1.20812224	4.22441139	-0.43245423
O	1.70182874	-1.87934125	2.60022354
Mg	0.09542124	-1.96507325	1.28424968
O	-1.39850963	-2.05221287	-0.19188496
O	-4.92766679	1.71495763	2.60166290
Mg	-6.18430929	1.66844295	0.93384438
Mg	1.59561757	0.12826727	2.45051400
O	-0.01476934	0.03879398	1.24070369
Mg	-1.54453609	-0.01774331	-0.20586582
Mg	4.62257494	4.20398515	1.92616285
Mg	4.66415239	-3.85840595	-0.57492462
O	-6.27379316	3.66883349	0.92452557
Mg	-1.29663772	-3.95074209	2.58792546
O	3.83775745	0.25177195	4.40545351
O	-0.21180319	0.03322175	4.63514290
B	2.62206797	0.16764335	4.69751702
B	1.02732883	0.07954063	4.83434638
O	-1.42101025	-2.04065564	2.69556011
Mg	-2.93959549	-2.10564390	1.36104917
O	-4.37258102	-2.22934966	-0.34728844
O	-0.26447221	4.21958529	1.24343953
Mg	-1.81518909	4.07337362	-0.29749816
Mg	-1.43246694	-0.03517970	2.84292539
O	-3.08075881	-0.13088141	1.32412848
Mg	-4.52134333	-0.23008627	-0.34188554
Mg	4.39577486	0.17063850	-0.59750991
O	4.23325923	2.17784484	-0.67848990
O	-1.65319206	1.96074988	2.67300658
Mg	-3.18590104	1.84255814	1.35217487
O	-4.64979052	1.77413023	-0.34811925
O	6.19790385	-3.70775977	0.63017602
Mg	4.15530084	4.18443734	-0.78128258
O	2.79626254	4.35085829	1.08137371
Mg	-4.57729324	-4.11235811	2.38241947
O	-5.75628957	-4.31594847	0.90053797
Mg	6.09125347	-1.68201105	0.64442147
Mg	-1.74577691	3.86870374	2.54365978
O	1.48210905	2.13397605	2.55822274
O	-4.69563844	-2.20030312	2.60182165
Mg	-5.92474256	-2.32315691	0.91663025
Mg	5.02072261	-3.62773229	2.12288449
O	3.25808611	-3.99439392	1.18148875
Mg	1.71326426	-4.00940138	-0.36187786
O	-2.83160629	-4.25978689	1.39803866
Mg	-4.19777261	-4.25395536	-0.30418167
O	4.52390455	-1.84236234	-0.61290367
Mg	1.35713326	4.04342748	2.39480222

O	6.04327297	0.30673230	0.61799965
O	5.72690964	4.29248475	0.37931425
O	4.90539372	-1.72103258	2.30579990
Mg	3.17097295	-1.82190435	1.14176871
O	1.57610681	-1.97307971	-0.27417732
O	-3.33588575	4.00191882	1.37092891
Mg	-0.14188830	2.04176162	1.25595987
Mg	4.79103851	0.28925358	2.38967979
O	3.04619825	0.17889895	1.08023068

B_2O_2 on MgO (111) facet (optimised)

Mg	2.79108614	1.45269594	2.70453721
O	1.31014847	0.66203181	3.84747722
Mg	-0.24171640	-0.16501158	4.67626017
Mg	1.30084116	-1.00442587	2.59416033
O	-0.26117089	-1.84137252	3.69334239
Mg	-0.26264518	-3.41041840	2.40471568
Mg	-0.07805763	1.60698675	2.61341617
O	-1.64283177	0.77549612	3.71237824
Mg	-1.64652675	-0.89055808	2.45879911
Mg	-2.94741644	1.67396942	2.44316464
O	-0.10088840	-3.37103421	-1.23659691
Mg	-1.64273829	-4.14455696	0.06480876
O	-3.08198776	-3.28992340	-1.07517711
O	1.66289981	4.19456070	-0.67765624
Mg	0.08878531	3.35641440	0.36618309
O	-1.40249321	2.54601396	1.43584179
B	0.80386882	1.49919307	-4.03076905
O	-2.02344373	1.51049165	-3.79141837
O	1.96353390	1.15896679	-3.43894517
B	-0.77533157	1.06253776	-3.96333402
O	-4.24829832	2.56702409	1.26640192
O	4.26233125	2.22466434	1.64643765
Mg	-2.96817988	0.25704566	-2.35970197
Mg	1.72833796	2.65543883	-1.97679785
O	0.09274484	1.69673522	-1.05181164
Mg	-3.04435566	-1.59243906	0.06983683
Mg	4.31381420	0.65931011	0.45691147
O	2.82383402	-0.22763196	1.53275075
Mg	-1.45219471	0.87873865	0.11344725
O	-3.00421466	0.00463782	1.27556322
Mg	-4.43007154	-2.32596280	-2.20317892
O	4.38045344	-0.98076574	-0.76975971
Mg	2.85195324	-1.84109336	0.34536055
O	1.30878013	-2.61539576	1.38678024
O	-4.39942949	-0.61798795	-1.17300623
Mg	-1.42285461	2.79073492	-2.16660728
Mg	4.35397723	-2.67442056	-1.81452696
O	2.85598733	-3.53928019	-0.80564001
Mg	1.24369451	-4.26529035	0.19893216
O	-0.27672667	-4.97147826	1.20077513
O	-2.83497787	1.83797784	-1.11405855
Mg	2.98954592	3.18367586	0.50332499
O	1.42304282	2.42849621	1.55865308
Mg	-2.80412869	3.41258325	0.24125420
Mg	0.09633010	-0.02863227	-2.16901576
Mg	-4.31539799	1.00538732	0.06965219
O	3.02799934	1.60141818	-0.87027089
Mg	1.45565287	0.76282497	0.25389611
O	-0.08016070	-0.06251135	1.30784281
O	-1.48294599	-0.78643045	-1.21083924
Mg	0.26357144	5.15082076	-1.72744780
Mg	3.11320390	-0.01516650	-2.06494584
O	1.48397903	-0.91595643	-1.10587303
Mg	-0.09987828	-1.71416940	0.09729517
O	-1.67094051	-2.49715737	1.25525964
O	-1.30382430	4.30913568	-0.83209321
Mg	-1.63472935	-2.59342039	-2.30961733
Mg	1.57861805	-2.76381100	-2.15897381

B_2O_2 on MgO (100)-(110) site-edge (optimised)

Mg	-0.35577909	-3.81318590	3.49831190
O	-0.52547511	-1.77769010	3.41411526
Mg	-0.74878253	0.22757666	3.28117768
O	-0.93426082	2.23034228	3.11932436
Mg	-1.16800767	4.25239652	2.91535674
O	-0.97445898	-4.12585066	1.53025567
Mg	-1.18596950	-2.00247325	1.41943349
O	-1.41339093	0.00892261	1.24209577
Mg	-1.59352734	2.03998400	1.11035978
O	-1.79755783	4.16782989	0.90955158
Mg	-1.65777003	-4.26632466	-0.30741443
O	-1.85233482	-2.23269888	-0.58380053
Mg	-2.05306072	-0.18661764	-0.68044647
O	-2.28469934	1.84408205	-0.84506932
Mg	-2.47985583	3.91643327	-0.92665988
O	-2.44661542	-4.53852023	-2.25569716
Mg	-2.64486298	-2.43876266	-2.46581404
O	-2.83761293	-0.44604938	-2.69609400
Mg	-3.06535072	1.58617746	-2.75016962
O	-3.29153631	3.72462827	-2.85620574
O	1.55827303	-3.73537019	2.90274319
Mg	1.37683708	-1.66236452	2.78778465
O	1.16250167	0.37073799	2.66338148
Mg	0.96574739	2.40291320	2.49801523
O	0.73823208	4.46102003	2.33667927
Mg	0.95648100	-3.95147710	0.93840254
O	0.70711641	-1.88003472	0.72166851
Mg	0.54377721	0.17389261	0.63313276
O	0.29382071	2.19818078	0.42441457
Mg	0.14329221	4.27354048	0.36886408
O	0.30355974	-4.22615097	-1.16287344
Mg	0.14536094	-2.07579915	-1.23677129
O	-0.13558675	-0.06492115	-1.51368045
Mg	-0.26096531	1.99488828	-1.61251436
O	-0.48865962	4.12702431	-1.85116795
Mg	-0.62092420	-4.63856048	-2.83686300
O	-0.76853503	-2.30902751	-3.39321518
Mg	-0.92059094	-0.11763059	-3.37963068
O	-1.24771977	1.78965804	-3.56707625
Mg	-1.46957309	3.67573632	-3.47952586
Mg	3.47116471	-3.52001399	2.22133154
O	3.25911164	-1.48906640	2.19716015
Mg	3.10645170	0.51719673	2.03125876
O	2.86001851	2.51479567	1.91873472
Mg	2.67554793	4.53548159	1.67742092
O	2.81526310	-3.80540439	0.28528140
Mg	2.67448434	-1.69323297	0.15674561
O	2.44422659	0.30245374	-0.00322187
Mg	2.27344673	2.31979959	-0.12066314
O	2.00614474	4.43825324	-0.25485611
Mg	2.39282152	-3.88717734	-1.67924049
O	2.02523416	-1.90484270	-1.93171138
Mg	1.94859765	0.13951983	-2.05454587
O	1.67191957	2.12923642	-2.12595461
Mg	1.60818851	4.14128637	-2.17528303
O	-3.62969897	-4.40377903	0.41536666
Mg	-3.84144981	-2.33334269	0.24365038
O	-4.08909877	-0.34988844	0.05923519
Mg	-4.24049445	1.66115507	-0.04655976
O	-4.45600209	3.73575022	-0.17863654
O	5.32885947	-3.34053513	1.61317565
Mg	5.18457717	-1.36170047	1.51744857
O	5.06150924	0.66706001	1.43394847
Mg	4.78695033	2.67636913	1.23928335
O	4.54412841	4.63889443	1.07560959
Mg	4.81848366	-3.53170918	-0.28558197
O	4.66949645	-1.49719379	-0.44613204
Mg	4.49732465	0.47635976	-0.57958803
O	4.29481787	2.44420081	-0.71694911
Mg	4.03586752	4.47009997	-0.82634243
O	4.25995459	-3.68683911	-2.18688145
Mg	4.08412870	-1.72644334	-2.36247816
O	3.91032311	0.27193356	-2.58900146
Mg	3.66896130	2.28988743	-2.64061671
O	3.46893627	4.26564022	-2.72841465
Mg	-4.19433736	-4.44846705	-1.41668497
O	-4.57083436	-2.56740482	-1.72656843
Mg	-4.69317805	-0.55107337	-1.83469670
O	-4.98455445	1.43986509	-2.01434274
Mg	-4.98802118	3.39243134	-1.99168966
O	-2.23446568	-3.91935023	4.11162287
Mg	-2.44932628	-1.94731901	4.01704953
O	-2.70715726	0.07538735	3.94029947
Mg	-2.86164632	2.10390778	3.71452886
O	-3.03882086	4.07342311	3.51906097
Mg	-2.89077036	-4.14364510	2.29031135
O	-3.19952777	-2.13444325	2.10635562
Mg	-3.36394454	-0.12836466	2.00906277
O	-3.60831254	1.85953134	1.82064068
Mg	-3.69738291	3.89882491	1.69176934
O	0.58644029	-4.12184431	-4.26809206
O	1.13324731	-0.14670926	-4.37327873
B	0.33122612	-2.83058060	-4.12797007
B	1.14832019	-1.38819000	-4.44955738

B_2O_2 on MgO (100)-(111) site-edge (optimised)

Mg	-2.78929351	4.66459235	2.76930430
Mg	-0.11936259	5.65473560	1.61295267
O	1.29902995	4.28371669	2.04814358
Mg	2.59299301	2.82268627	2.44815213
O	3.98987779	1.42090668	2.89243770
O	-1.57927676	4.28324851	1.15668937
Mg	-0.13124748	2.85057898	1.71581830
O	1.24335088	1.36684100	2.02868003
Mg	2.56741109	-0.06622366	2.46480984
O	3.99867775	-1.55954428	2.84999759
Mg	-0.92803938	4.32738396	-0.80447691
O	0.49145085	2.84656588	-0.39863950
Mg	1.85810959	1.41478441	0.02955905
O	3.25258411	-0.03672413	0.42691398
Mg	4.62496126	-1.53996818	0.86425587
O	-0.26791637	4.33730443	-2.83100809
Mg	1.14589894	2.87280139	-2.39895055
O	2.53867793	1.43937302	-2.04027053
Mg	3.87045501	-0.00067303	-1.57861248
O	5.27848519	-1.49707294	-1.13140887
O	-3.73732992	2.87095810	2.49001301
Mg	-2.40854426	1.45412502	2.99897223
Mg	5.20710611	-0.06679260	3.10690486
O	0.48084062	5.76512556	-0.33503144
Mg	1.89698176	4.32252560	0.11664878
Mg	-2.95825523	2.86583935	0.59247432
O	-1.54034777	1.39616579	1.13772665
Mg	-0.13938354	-0.06076420	1.58638446
O	1.24785819	-1.50970740	1.98657720
Mg	2.61781115	-2.94592539	2.35571298
O	-2.30771179	2.92924151	-1.34296037
Mg	-0.87462701	1.43038225	-0.85383544
O	0.49553868	-0.03615350	-0.45252423
Mg	1.87842763	-1.47098097	-0.02110311
O	3.33298551	-2.99007693	0.41353591
Mg	-1.58631258	2.88355115	-3.23556313
O	-0.19347197	1.44336986	-2.93273265
Mg	1.15888700	0.00228621	-2.46339969
O	2.54983143	-1.44617076	-2.08447346
Mg	3.86884295	-2.88275531	-1.54255410
Mg	-5.03055299	1.36534379	1.97450907
O	-3.65536323	-0.07414091	2.60049926
Mg	-2.45123222	-1.59579968	3.07190569
O	3.30881972	2.91424097	0.50264772
Mg	4.61169925	1.46928755	0.90979772
O	-4.30804244	1.44983159	0.06586983
Mg	-2.90625036	-0.05710149	0.60290873
O	-1.52370145	-1.53175976	1.15907303
Mg	-0.07553861	-2.95898086	1.51039023
O	1.32077696	-4.39736151	1.92416737
Mg	-3.63877283	1.46614394	-1.81386061
O	-2.22624232	-0.03395903	-1.35170493
Mg	-0.86512443	-1.48106403	-0.90534491
O	0.51339363	-2.91072102	-0.49224475
Mg	1.94026591	-4.39637825	-0.01456062
O	-2.94701574	1.48818832	-3.78778877
Mg	-1.54302740	0.00289847	-3.34887379
O	-0.18214439	-1.44517034	-2.97591183
Mg	1.16785182	-2.87245348	-2.49052602
O	2.58372646	-4.34209777	-2.03187399
O	-6.27623122	-0.07702462	1.46094684
Mg	-5.01928010	-1.51218474	1.94290887
O	-3.69899948	-3.03385362	2.45303879
Mg	-2.73427753	-4.82739945	2.66173946
O	6.03015359	-0.04188111	1.33643837
Mg	-5.61424071	-0.05154558	-0.38501089
O	-4.29147153	-1.56363052	0.04005917
Mg	-2.92703255	-2.96140077	0.54350152
O	-1.54956379	-4.40043590	1.03229274
Mg	-0.08479992	-5.75923246	1.46691530
O	-5.02198208	-0.03250794	-2.31465712
Mg	-3.63029293	-1.52151512	-1.84867461
O	-2.28275114	-2.98130187	-1.41205381
Mg	-0.90950786	-4.39467309	-0.93970168
O	0.51916111	-5.82773636	-0.49102897
Mg	-4.17215864	-0.00190960	-4.05212715
O	-2.93694112	-1.49063407	-3.82655209
Mg	-1.56988136	-2.87884432	-3.31377619

O	-0.24277946	-4.34258788	-2.95150728
Mg	1.11542499	-5.58900985	-2.32342550
Mg	1.08058062	5.58147241	-2.17090611
O	2.55528454	4.33225120	-1.90733625
Mg	3.84514889	2.87581604	-1.45568874
O	5.26798283	1.48421929	-1.08717409
Mg	6.39234367	-0.00888075	-0.57423110
O	-0.81407545	2.48935489	3.83721304
O	-1.05018468	-1.40455004	4.53957071
B	-0.26107667	1.39776953	4.31335073
B	-0.78668900	-0.22106554	4.06891113

B_2O_2 on MgO (100)-(110)-(111) site-edge (optimised)

Mg	2.96844984	2.83444878	3.15178998
O	1.82793406	1.13820037	3.17063743
Mg	0.75315068	-0.57053849	3.15719170
O	-0.37196732	-2.24093277	3.12222348
Mg	-1.45587771	-3.97994601	3.01362331
O	3.49400154	2.68389152	1.12669329
Mg	2.33805511	0.86804695	1.12722399
O	1.22789317	-0.84938074	1.06485032
Mg	0.11153250	-2.55220684	1.07903254
O	-1.06100697	-4.29160959	1.00654068
Mg	4.01270721	2.33861783	-0.74616850
O	2.86217625	0.59952658	-0.87228950
Mg	1.72685143	-1.13387774	-0.91241497
O	0.59285383	-2.84923307	-1.05681986
Mg	-0.63869651	-4.55715270	-0.95547029
O	4.65768873	2.01090119	-2.71414867
Mg	3.47172071	0.20795671	-2.82062794
O	2.30598975	-1.49514419	-2.98002747
Mg	1.40422756	-3.30443991	-2.96405933
B	-1.98353535	-1.11343917	-3.87782450
O	1.37029942	3.95910989	2.67396721
Mg	0.23334962	2.22885865	2.66055448
O	-0.88817805	0.51746758	2.65813721
Mg	-2.00414076	-1.20227009	2.65194360
O	-3.13101786	-2.93657144	2.56022859
Mg	1.83403235	3.72423145	0.67231628
O	0.73027135	1.95240011	0.54139567
Mg	-0.40903318	0.25587704	0.58897604
O	-1.53219137	-1.43919050	0.50450499
Mg	-2.69044674	-3.21571062	0.54360124
O	2.33588360	3.54764264	-1.55866422
Mg	1.17419739	1.72085076	-1.51852599
O	0.06973020	-0.05768151	-1.62789553
Mg	-1.09172736	-1.79610547	-1.42901641
O	-2.25862555	-3.43184985	-1.46867612
Mg	3.03616818	2.88062485	-3.26021958
O	1.94930371	1.34202179	-3.52645993
Mg	0.82415250	-0.22490518	-3.56767446
B	-3.02096645	-2.38025706	-4.37327418
O	-3.85225428	-3.26851352	-4.18734369
Mg	-0.30415466	4.98122294	2.10668683
O	-1.40359960	3.25454570	2.16171446
Mg	-2.53692342	1.60685570	2.16759702
O	-3.61616096	-0.10168185	2.18728156
Mg	-4.74652953	-1.82440049	2.02331776
O	0.24561871	4.77841482	0.14600448
Mg	-0.95306602	3.01717461	0.10201546
O	-2.05173845	1.26851175	0.00807596
Mg	-3.21378225	-0.36853241	0.20947997
O	-4.28481131	-2.15072408	0.02427007
Mg	0.49185254	4.53947885	-1.80653480
O	-0.48993702	2.77838739	-1.96169233
Mg	-1.60536647	1.15187220	-2.01830725
O	-2.48598782	-0.65968960	-2.62967735
Mg	-4.03442312	-2.56869766	-1.98123150
O	5.66665099	1.20638435	-0.10294999
Mg	4.51418413	-0.54151931	-0.16783092
O	3.43555523	-2.23469537	-0.25033671
Mg	2.30968943	-3.95176433	-0.27374070
O	1.08647970	-5.63252073	-0.35363832
O	-1.91769738	5.98470036	1.58669352
Mg	-3.03319397	4.35357992	1.58227698
O	-4.19697071	2.68387687	1.61158008
Mg	-5.26305883	0.96609872	1.55715017
O	-6.28562447	-0.71789588	1.46871201
Mg	-1.52747791	5.79604790	-0.33890967
O	-2.68987107	4.09932043	-0.40839731
Mg	-3.75495159	2.43831650	-0.42723305
O	-4.79757152	0.75974260	-0.46127492
Mg	-5.88778695	-0.96773936	-0.45393466
O	-1.11211664	5.54271910	-2.27115833
Mg	-2.19137848	3.88408286	-2.35525195
O	-3.30911394	2.15479703	-2.48177752
Mg	-4.44552557	0.49155543	-2.43642635
O	-5.39750196	-1.19679070	-2.35692676
Mg	6.00675589	0.84756400	-1.95887628
O	5.09558787	-0.86354186	-2.16886166
Mg	3.97818421	-2.54084190	-2.14648534
O	2.99099370	-4.27827917	-2.17619112
Mg	1.80788797	-5.91371165	-2.16466890
O	4.53991268	1.76119649	3.66201021
Mg	3.48173403	0.07475206	3.67013112
O	2.41421825	-1.66775907	3.69585934
Mg	1.26338547	-3.36246829	3.58521164
O	0.15982351	-5.00256381	3.49599037
Mg	5.06028291	1.49455002	1.80259944
O	4.03276528	-0.26857698	1.73158801
Mg	2.90522301	-1.94837525	1.72152224
O	1.82600982	-3.64723444	1.62835150
Mg	0.60566179	-5.30702099	1.60296966
O	-0.82551078	-0.77365221	-4.42072082

NH_3 on MgO (100) facet (optimised)

Mg	-1.98741190	5.19949753	3.05560956
O	-2.94099463	3.51679009	3.24453596
Mg	-3.71883609	1.65447359	3.15689993
O	-4.60033957	-0.16357720	3.20702392
Mg	-5.22914979	-1.98953525	2.98347016
O	-0.15427674	4.57151071	3.21684477
Mg	-1.02388279	2.66287612	3.21666515
O	-1.87352003	0.82080324	3.26428549
Mg	-2.69207438	-1.03404172	3.17922480
O	-3.54722742	-2.95001158	3.14130014
Mg	1.66192242	3.69016791	3.10410109
O	0.83274792	1.84491858	3.23793115
Mg	-0.00855032	-0.01949990	3.16146568
O	-0.85050175	-1.88511024	3.20008833
Mg	-1.68421741	-3.72513237	3.02851421
O	3.52626419	2.91264342	3.12655667
Mg	2.67246601	0.99512661	3.12427450
O	1.85616484	-0.86114499	3.17287447
Mg	1.00470252	-2.70024210	3.08695137
O	0.13285207	-4.60840240	3.05040264
O	-2.10497705	5.46427648	1.14020498
Mg	-2.98881173	3.56492074	1.12823022
O	-3.86638680	1.74145454	1.14963789
Mg	-4.65244782	-0.12200051	1.09133304
O	-5.49240064	-2.04177279	1.06444619
Mg	-0.18462750	4.62517981	1.10111887
O	-1.06800444	2.72345499	1.13053435
Mg	-1.91282162	0.86078138	1.08832320
O	-2.75099787	-1.00600580	1.09277176
Mg	-3.59310431	-2.92531098	1.02414081
O	1.67906227	3.83920794	1.09515698
Mg	0.79918378	1.88652072	1.06094937
O	-0.04408122	0.01741286	1.08117836
Mg	-0.88786226	-1.85059785	1.02306114
O	-1.77032323	-3.80278456	1.01752085
Mg	3.50124464	2.96155184	1.00962627
O	2.66068574	1.04171952	1.03740116
Mg	1.82480002	-0.82537957	0.98832036
O	0.97749402	-2.68768430	0.99974376
Mg	0.09373841	-4.58653407	0.93335307
Mg	-2.10636546	5.41468343	-0.91325281
O	-3.05272711	3.60677572	-0.87519305
Mg	-3.86068655	1.76065130	-0.94911510
O	-4.71095317	-0.06850974	-0.91225585
Mg	-5.44070822	-1.97336222	-0.98833473
O	-0.20000772	4.68551030	-0.90288903
Mg	-1.09827386	2.75028961	-0.95224912
O	-1.95046729	0.89826049	-0.96065969
Mg	-2.77598615	-0.96514316	-0.98998910
O	-3.63316646	-2.92047797	-0.98042079
Mg	1.62744567	3.83560847	-1.00385283
O	0.76420342	1.92658622	-0.98880187
Mg	-0.07299759	0.05226387	-1.06169662
O	-0.92556873	-1.81676538	-1.02692739
Mg	-1.78663441	-3.72571090	-1.08075052
O	3.47638166	3.03192540	-0.99172474
Mg	2.61229247	1.06625688	-1.05269917
O	1.79319947	-0.79089197	-1.06505036
Mg	0.94218509	-2.63290291	-1.09056190
O	0.03984286	-4.58083557	-1.06889509
O	-2.12425439	5.41035575	-2.87901514
Mg	-2.97244408	3.61915792	-2.93455031
O	-3.87957029	1.78957848	-3.01320204
Mg	-4.65109138	-0.10190275	-2.97175949
O	-5.43455554	-1.92396055	-2.95361645
Mg	-0.30341672	4.62715791	-2.96002725
O	-1.12535196	2.76496054	-3.07683480
Mg	-1.98583971	0.93581452	-3.08543695
O	-2.78861388	-0.91963846	-3.11435522
Mg	-3.64305107	-2.76984421	-3.03571530
O	1.58390858	3.85730036	-3.06943428
Mg	0.72952080	1.95799904	-3.11152737
O	-0.13251066	0.09997689	-3.16822208
Mg	-0.95612870	-1.77546053	-3.14905265
O	-1.81523983	-3.67334746	-3.14625883
Mg	3.41778100	2.95072031	-3.04655110
O	2.56292570	1.11349602	-3.15805230
Mg	1.73243539	-0.74057042	-3.31002124
O	0.89053284	-2.59259085	-3.19698808
Mg	0.07668588	-4.44894987	-3.12092455
Mg	5.20222532	1.95942066	2.87925453
O	4.58025328	0.12613093	3.05947535
Mg	3.69558934	-1.68915554	2.97390139
O	2.91996937	-3.55460802	3.02301993
Mg	1.95870878	-5.23006008	2.80753277
O	5.40159201	2.07918261	0.95699261
Mg	4.55957380	0.15837097	0.94329538
O	3.77553303	-1.70574892	0.96104965
Mg	2.89636412	-3.52652211	0.90598788
O	2.01284878	-5.42779732	0.88147758
Mg	5.28060752	2.08497843	-1.09163559
O	4.55187625	0.17750945	-1.05844760
Mg	3.69401647	-1.64809673	-1.14436221
O	2.89264503	-3.50015816	-1.09590514
Mg	1.94433166	-5.30650436	-1.16641536
O	5.21211090	2.10161786	-3.05871768
Mg	4.42286532	0.28128280	-3.09804729
O	3.68972150	-1.62516500	-3.20510509
Mg	2.74614713	-3.43889442	-3.13619811
O	1.90125773	-5.23360387	-3.13335716
N	2.04339768	-0.86587046	-5.51524631
H	2.98617062	-1.27530619	-5.41997611
H	1.46529726	-1.52843353	-6.04392710
H	2.12673597	-0.00159642	-6.06148773

NH_3 on MgO (110) facet (optimised)

O	-1.70447464	-1.79708137	3.08727463
Mg	1.24346351	-3.92417357	3.18158046
O	0.35399281	4.00471121	1.62399198
Mg	0.19887739	1.91311360	1.65739816
O	2.69981475	-4.19341252	1.76783613
O	0.07621733	-0.11069770	1.73009586
Mg	-0.11603024	-2.13053849	1.68206572
O	0.27831006	4.07917844	4.44554183
O	-2.62317930	4.22932439	1.62909193
Mg	0.10753774	1.95086702	4.42271690
Mg	-2.79791888	2.14179718	1.66496644
O	-0.03363552	-0.08103760	4.43158479
O	-2.96196758	0.12690333	1.74129054
Mg	-0.22180199	-2.11178768	4.44975371
Mg	-3.11076256	-1.89084602	1.69009555
Mg	-1.78242238	-3.83244498	3.16957841
Mg	1.86858376	4.15620223	3.12794130
Mg	-1.16454199	4.25906058	3.10246534
O	1.83323802	2.11570385	3.09450893
O	-1.40524505	2.23369587	3.06237577
Mg	1.62056018	0.10901431	3.08568206
Mg	-1.53582713	0.21481241	3.06350698
O	1.52442198	-1.90450962	3.11879858
O	3.34879273	4.08715222	1.71730881
Mg	3.16938439	2.01637020	1.71275094
O	2.98492465	-0.00998628	1.70008144
Mg	2.75761724	-2.04716421	1.64634169
O	-0.28494060	-4.22188399	1.67774435
O	-0.36591245	-4.23978973	4.50200023
O	-3.26152561	-3.98145297	1.68438551
O	-1.46313150	2.03246116	-2.74122386
Mg	-2.93812699	2.14148380	-1.31007086

O	-4.30947689	2.23907995	0.42806852
O	-0.25678683	-4.17753931	-1.30758566
Mg	-1.75011586	-4.06585066	0.25111258
Mg	-1.57713501	0.08156159	-2.61851604
O	-3.08475096	0.14469928	-1.26048749
Mg	-4.46935147	0.23787349	0.42973114
Mg	4.47007705	-0.17912821	0.40786913
O	4.29874574	-2.18405556	0.43794780
O	-1.66940967	-1.90270014	-2.75650274
Mg	-3.18079803	-1.84656927	-1.31700190
O	-4.59081265	-1.76480324	0.42512196
O	6.21497913	3.69384167	-0.94338333
Mg	4.18850628	-4.20341479	0.50932930
O	2.80990651	-4.33200220	-1.26692765
Mg	-4.58043803	4.13612449	-2.30518671
O	-5.71463821	4.33541262	-0.78384488
Mg	6.13552587	1.69085699	-0.89760139
Mg	-1.75311893	-3.85549779	-2.62625497
O	1.45709355	-2.14749378	-2.69551291
O	-4.71835301	2.21634795	-2.51136729
Mg	-5.89679880	2.34412569	-0.79149480
Mg	4.98857902	3.59493098	-2.40012563
O	3.27420535	3.96466802	-1.37857424
Mg	1.77474504	3.99932310	0.21482197
N	0.22186022	-0.47838218	-4.58528312
H	-0.29986508	0.25307074	-5.08794627
H	0.84919766	-0.92169782	-5.27074232
H	-0.41743179	-1.24647890	-4.27453153
O	6.10509815	-0.31788496	-0.82294783
O	5.74212716	-4.30189518	-0.68890491
O	4.90324076	1.66904555	-2.57686912
Mg	3.15514739	1.80901376	-1.34847343
O	1.64432154	1.96237962	0.14286383
O	-3.30330019	-3.95732154	-1.35657796
Mg	-0.10251887	-2.04266671	-1.33680100
Mg	4.83474661	-0.29723951	-2.42490387
O	3.05462023	-0.18246175	-1.31517554
Mg	1.51530774	-0.07404275	0.17206672
Mg	-4.88219700	0.26759332	-2.39856541
O	-1.61989729	-2.00660204	0.16976530
O	4.70587792	-2.26984057	-2.49597045
Mg	2.93060745	-2.17610342	-1.31394169
O	1.35115731	-2.14106963	0.17443739
O	-6.12546808	0.34534214	-0.78064973
Mg	-5.04811667	-3.61346153	-2.32334857
Mg	5.88774177	-2.31126626	-0.78103380
Mg	1.73777920	3.81571353	-2.65170676
O	0.23004933	4.11747503	-1.35964926
Mg	-1.16120422	4.09314591	0.23665576
Mg	-4.69764349	-3.79130253	0.38158792
Mg	1.25897066	-4.22009974	0.29101706
O	1.66930134	1.88672586	-2.74272312
Mg	0.13247450	1.97670429	-1.36646339
O	-1.33575387	2.04927209	0.15812204
O	-4.94611531	-1.68941533	-2.52154795
Mg	-6.15653293	-1.66370938	-0.81838086
Mg	1.49284172	-0.11334771	-2.77951209
O	-0.00194181	-0.03277571	-1.31511736
Mg	-1.46515664	0.01788899	0.22547110
Mg	4.58923803	-4.18659946	-2.20215454
Mg	4.71146008	3.85558747	0.30833345
O	-6.23350624	-3.66245978	-0.82668065
Mg	-1.31382838	3.96740268	-2.64226229
O	-2.80389659	4.25547468	-1.36377415
Mg	-4.12556308	4.26812538	0.37826709
O	4.59592555	1.83106619	0.37231281
Mg	1.30981238	-4.06817069	-2.56681006

NH_3 on MgO (111) facet (optimised)

Mg	1.63836267	2.89106242	-2.34107078
O	0.86426080	1.48058900	-3.58040643
Mg	0.03877891	-0.01342032	-4.51083071
Mg	-0.85410775	1.45765808	-2.39945126
O	-1.67813199	-0.03455336	-3.60063073
Mg	-3.30053351	-0.05356016	-2.38001495
Mg	1.72408435	0.01775937	-2.37053592
O	0.90543577	-1.47735685	-3.57139181
Mg	-0.81240955	-1.49470108	-2.38990805
Mg	1.71920791	-2.85705267	-2.32467605
O	0.00741915	-0.00132250	-1.13244975
O	-0.84204388	-1.47588836	1.30987941
Mg	5.26242153	0.08497566	2.00271834
Mg	-0.10833362	3.14625399	2.30949484
O	-0.87841552	1.46068131	1.31860706
Mg	-1.67973691	-0.02490667	0.02025465
N	-0.30031283	0.11257379	4.51339250
H	-1.28985492	0.30051556	4.78170767
H	-0.01640229	-0.79454056	4.94205938
H	0.28246118	0.86588374	4.93400609
Mg	-2.69459943	-1.66558941	2.29224722
Mg	-2.73944566	1.59329449	2.28583355
O	-3.38913379	-0.04446315	1.28050038
Mg	-4.15904202	-1.50167799	-0.12311164
O	-3.38779008	-3.01429882	0.97992656
O	4.25596268	1.54470984	1.03350062
Mg	3.42250858	0.04654815	-0.09256678
O	2.57648622	-1.38521220	-1.21389288
O	4.28569864	-1.41453743	1.06471802
O	-2.46770163	-1.52870356	-1.25301858
O	2.52871210	-4.22417918	-1.15397957
O	2.40808951	4.28807226	-1.17986662
Mg	-0.00505524	-3.11782289	2.34587549
Mg	2.72316547	1.56670180	2.33360578
O	1.69847037	0.03182528	1.30275303
Mg	-1.66209275	-2.98609703	-0.12560442
Mg	0.78963023	4.34819370	-0.08821435
O	-0.07397474	2.90599043	-1.24322640
Mg	0.86586240	-1.44601319	0.03555667
O	0.00729994	-2.91495406	-1.22835197
Mg	-2.58102645	-4.57951739	1.96583892
O	-0.92635757	4.43127491	0.99547430
Mg	-1.74791979	2.93533310	-0.14712056
O	-2.50997595	1.45226218	-1.25928420
O	-0.79559294	-4.43977122	1.03905067
Mg	2.73739988	-1.48157397	2.35698261
Mg	-2.70624215	4.51846741	1.93066918
O	-3.46912025	2.92145154	0.96996853
Mg	-4.19966863	1.37657988	-0.12576331
O	-4.90554958	-0.07270224	-1.22878276
O	1.72650640	-2.89971324	1.30709436
Mg	3.30273619	2.94738991	-0.07119206
O	2.53280038	1.45220280	-1.22103956
Mg	3.37953690	-2.85265825	-0.04529640
Mg	0.01292287	-0.00757850	2.39575999
Mg	0.91180812	-4.32175811	-0.05605300
O	1.64222705	2.95537814	1.30660993
Mg	0.82488654	1.46825273	0.03213439

NH_3 on MgO (100)-(110) site-edge (optimised)

H	0.17625453	-1.82024451	4.74815523
H	1.49866112	-1.02836855	4.10833366
H	0.91824607	-0.61199736	5.59779604
N	0.62126007	-0.89503604	4.65461726
Mg	3.89515621	1.40264842	-3.04362996
O	1.88554737	1.03498504	-3.11142091
Mg	-0.11596632	0.72846464	-3.13207910
O	-2.10739507	0.37100723	-3.12136940
Mg	-4.12846306	0.06359905	-3.06108519
O	3.90814978	2.05233857	-1.04510571
Mg	1.78204738	1.71448780	-1.10080149
O	-0.23265126	1.40226524	-1.09931111
Mg	-2.24088096	1.04074249	-1.10655045
O	-4.36148523	0.66748286	-1.05785724
Mg	3.72654006	2.75285573	0.79428486
O	1.68097212	2.41951069	0.84763972
Mg	-0.34767938	2.06040754	0.83261677
O	-2.37695825	1.73518338	0.84443881
Mg	-4.41828175	1.37526232	0.79243618
O	3.61062882	3.57367476	2.72327264
Mg	1.47879911	3.20613775	2.76221260
O	-0.48443601	2.88848996	2.81073055
Mg	-2.44265944	2.53898092	2.76279428
O	-4.56528591	2.18973794	2.72956225
O	4.27052002	-0.47840260	-2.45385699
Mg	2.21974620	-0.83486534	-2.48525868
O	0.20203119	-1.16700920	-2.51794447
Mg	-1.81656399	-1.50732442	-2.49832235
O	-3.87173340	-1.83754141	-2.48432116
Mg	4.16533073	0.13873141	-0.48520006
O	2.11105282	-0.15616343	-0.40178389
Mg	0.08515659	-0.52093708	-0.47904091
O	-1.94597143	-0.83493795	-0.42141985
Mg	-3.98426976	-1.22678749	-0.51191700
O	4.11760717	0.77963193	1.73875939
Mg	1.97954971	0.44334189	1.64223291
O	-0.02680352	0.14434129	1.64051113
Mg	-2.02145946	-0.24152297	1.64270146
O	-4.15487480	-0.60348696	1.72828395
Mg	3.69063345	1.76715291	3.37186867
O	1.83355718	1.41120266	3.59005802
Mg	-0.16583880	0.93000567	3.56476627
O	-2.17599563	0.71798845	3.58964134
Mg	-4.05394084	0.45023850	3.37666000
Mg	4.51444140	-2.38989075	-1.78622528
O	2.50373515	-2.71463467	-1.90183249
Mg	0.52059495	-3.08757875	-1.89465001
O	-1.47518660	-3.37933704	-1.91954756
Mg	-3.48571417	-3.72643218	-1.82088671
O	4.48261073	-1.70467024	0.15359165
Mg	2.39941216	-2.10411526	0.13467318
O	0.40486277	-2.42643451	0.13130343
Mg	-1.59501594	-2.77389375	0.11649088
O	-3.70132083	-3.07546043	0.11530924
Mg	4.28686186	-1.28316539	2.08052510
O	2.27243760	-1.48056063	2.21600786
Mg	0.28901125	-1.90176901	2.09453662
O	-1.69310225	-2.16355853	2.15074134
Mg	-3.65749766	-2.61839054	2.04643685
O	3.38561350	4.69413146	0.03270698
Mg	1.31416789	4.35259183	0.04262985
O	-0.68340732	4.07823211	0.06179319
Mg	-2.66268263	3.68239385	0.04267845
O	-4.73016997	3.32658200	0.03375116
O	4.77979493	-4.23765323	-1.15906551
Mg	2.83236699	-4.61008846	-1.21003219
O	0.84363016	-5.02533424	-1.27788424
Mg	-1.17623351	-5.28103183	-1.23145430
O	-3.13904398	-5.56247758	-1.20121670
Mg	4.69372103	-3.70895394	0.74118264
O	2.68418957	-4.10243740	0.76217378
Mg	0.73488311	-4.44799957	0.73097058
O	-1.21693122	-4.76483110	0.73830007
Mg	-3.24846155	-5.04133234	0.70086211
O	4.56257962	-3.12534226	2.65075593
Mg	2.60801420	-3.46341997	2.67582740
O	0.61702649	-3.80061194	2.78821129
Mg	-1.37821749	-4.13072413	2.65072416
O	-3.33262857	-4.45636979	2.60990471
Mg	3.11954258	5.23224490	1.85772887
O	1.18576429	5.12192797	1.99972331
Mg	-0.79109650	4.70514943	1.95674751
O	-2.79174085	4.45115419	1.99938508
Mg	-4.65196543	3.91658563	1.86090012
O	3.55773226	3.24446557	-3.66068439
Mg	1.59063028	2.94169939	-3.71730513
O	-0.43825898	2.65657402	-3.80241602
Mg	-2.45070565	2.26954195	-3.72151436
O	-4.41021573	1.91682472	-3.66934060
Mg	3.46280736	3.92022853	-1.83261068
O	1.43204080	3.69857287	-1.82448892
Mg	-0.55557502	3.32998005	-1.86756903
O	-2.55480070	3.03253178	-1.82688232
Mg	-4.54842304	2.57759308	-1.83706612

NH_3 on MgO (100)-(111) site-edge (optimised)

Mg	2.61416259	-4.60333702	3.13167773
Mg	0.04798717	-5.58360388	1.84801553
O	-1.37997846	-4.20766047	2.18671626
Mg	-2.72535163	-2.75572671	2.48967081
O	-4.10934970	-1.35326744	2.86485452
O	1.52920543	-4.23756152	1.41128357
Mg	0.02816494	-2.79925776	1.74373830
O	-1.29714185	-1.32388937	2.20833270
Mg	-2.70394008	0.13361625	2.47684703
O	-4.12564669	1.62175607	2.77709740
Mg	0.97543866	-4.32037278	-0.58122835
O	-0.47133585	-2.81865688	-0.24915122
Mg	-1.87654277	-1.37864693	0.08663239
O	-3.25551297	0.06017130	0.41832395
Mg	-4.67715299	1.57273091	0.76766471
O	0.40504237	-4.35381925	-2.60952051
Mg	-1.03807518	-2.87655611	-2.28397791
O	-2.43572344	-1.44428664	-2.00007190
Mg	-3.80640888	0.00826837	-1.61963834

O	-5.20879580	1.50017815	-1.26136607
O	3.61949341	-2.82767216	2.87139471
Mg	2.35391380	-1.37932457	3.35128139
Mg	-5.38109513	0.13848447	3.02627790
O	-0.46585620	-5.73606483	-0.12847932
Mg	-1.91946347	-4.30009105	0.21686143
Mg	2.92351440	-2.82028465	0.93222444
O	1.46607518	-1.34725707	1.46866004
Mg	0.04069811	0.14646903	1.71309207
O	-1.34757776	1.55676709	2.04559082
Mg	-2.73479153	3.00650359	2.32684766
O	2.35910090	-2.91083535	-1.03648413
Mg	0.91514714	-1.40194730	-0.66858489
O	-0.47366109	0.04428326	-0.32767669
Mg	-1.88090795	1.50697305	0.01094221
O	-3.34648160	3.01708113	0.35316400
Mg	1.74052600	-2.89823368	-2.97752279
O	0.33302435	-1.46114969	-2.75905290
Mg	-1.04575198	-0.00603827	-2.37925827
O	-2.44116044	1.43935631	-2.07897476
Mg	-3.79519879	2.88527705	-1.62111553
Mg	4.95144164	-1.30411989	2.36868699
O	3.52611976	0.14555973	2.92269976
Mg	2.30968034	1.72931385	3.39530104
O	-3.31830171	-2.87525823	0.52524582
Mg	-4.67161586	-1.42094095	0.85268472
O	4.29226414	-1.42831645	0.44685101
Mg	2.87491978	0.10573982	0.90109249
O	1.47605034	1.54958370	1.32269135
Mg	0.02903382	3.00079385	1.67599796
O	-1.40743626	4.44456460	1.94257819
Mg	3.72289563	-1.46353543	-1.47070060
O	2.28931625	0.02863082	-1.09588439
Mg	0.91244706	1.49884966	-0.73712331
O	-0.48179243	2.92408165	-0.40671381
Mg	-1.92461809	4.41014288	-0.01804218
O	3.12371844	-1.52317592	-3.47713695
Mg	1.70431045	-0.02294508	-3.13130645
O	0.32969360	1.42396774	-2.83662574
Mg	-1.04399822	2.86177545	-2.43340340
O	-2.47560044	4.33461991	-2.06993735
O	6.20882216	0.12329693	1.89200494
Mg	4.93416965	1.57734217	2.29348584
O	3.63624546	3.10325906	2.68787568
Mg	2.54043951	4.80670212	2.92960227
O	-6.07513794	0.08019703	1.18538513
Mg	5.63075697	0.07299030	0.01892780
O	4.29432407	1.57735443	0.35455743
Mg	2.91129794	2.99481306	0.78184237
O	1.51209646	4.43706944	1.18162604
Mg	0.02159477	5.79976580	1.53984226
O	5.12807757	0.00956599	-1.93229998
Mg	3.71825173	1.51610585	-1.55411889
O	2.35735952	2.98285509	-1.20535813
Mg	0.95545587	4.39650710	-0.80173439
O	-0.48681580	5.84030178	-0.45087972
Mg	4.36526040	-0.03881151	-3.71117867
O	3.11925378	1.45238610	-3.55943571
Mg	1.73160143	2.85725227	-3.13067011
O	0.38974090	4.32199840	-2.85214213
Mg	-0.99574446	5.57482185	-2.30178606
Mg	-0.97961385	-5.58598657	-1.99986995
O	-2.46030178	-4.33367872	-1.82241127
Mg	-3.78563100	-2.86272604	-1.46184503
O	-5.20374207	-1.47419993	-1.17457423
Mg	-6.39639048	0.02532617	-0.74848005
N	0.56716450	-1.32070881	4.59791888
H	0.45577917	-1.93652757	5.42261197
H	0.56268083	-0.32168523	4.91419138
H	-0.29357155	-1.40832383	4.01036288

NH_3 on MgO (100)-(110)-(111) site-edge (optimised)

Mg	2.51844421	-4.59763838	3.03706028
Mg	0.02196071	-5.68203471	1.65104696
O	-1.40900559	-4.32404447	2.01585933
Mg	-2.73032622	-2.87851935	2.35369040
O	-4.13846085	-1.48468451	2.76363508
O	1.51351535	-4.33861695	1.26050415
Mg	0.02679934	-2.88168197	1.68329078
O	-1.35062090	-1.43824066	2.04484743
Mg	-2.69625936	0.00457675	2.41223691
O	-4.13634103	1.49594039	2.76220986
Mg	0.96205517	-4.35470771	-0.73193699
O	-0.48542863	-2.87534582	-0.37598809
Mg	-1.86785115	-1.43521095	0.00563204
O	-3.28019789	0.00382225	0.35794090
Mg	-4.66400338	1.51071153	0.74545266
O	0.38957390	-4.34148807	-2.78040515
Mg	-1.04021656	-2.87018401	-2.40463857
O	-2.44819508	-1.44218045	-2.09196706
Mg	-3.79356794	0.00341419	-1.67677579
O	-5.21744879	1.49680294	-1.27893055
O	3.61393195	-2.92683440	2.74577857
Mg	2.33090219	-1.45496230	3.37807332
Mg	-5.36436007	0.00676179	2.93372256
O	-0.48157871	-5.79060212	-0.33465841
Mg	-1.92232957	-4.35299719	0.05087061
Mg	2.90737155	-2.88935317	0.82306371
O	1.46862063	-1.44432774	1.32729851
Mg	0.06180339	0.00252369	1.76503698
O	-1.34908760	1.44442046	2.04313276
Mg	-2.72571898	2.88768808	2.35110428
O	2.34904822	-2.94943036	-1.16953525
Mg	0.90948867	-1.44419047	-0.73334215
O	-0.48370976	0.00142078	-0.38377571
Mg	-1.86569793	1.44090069	0.00428020
O	-3.34450485	2.95767440	0.38177517
Mg	1.72659915	-2.87859525	-3.09929356
O	0.32135610	-1.44434197	-2.85150510
Mg	-1.04120779	0.00108607	-2.42278541
O	-2.44615638	1.44634787	-2.09338280
Mg	-3.78069780	2.88460677	-1.59734371
Mg	4.95706257	-1.43430176	2.25993703
O	3.58822133	-0.00003379	2.81312330
Mg	2.33309082	1.45966278	3.37805852
O	-3.34871292	-2.94983230	0.38454391
Mg	-4.66628445	-1.50032514	0.74684217
O	4.30171820	-1.51323883	0.33050634
Mg	2.88114344	0.00012860	0.84342159
O	1.47136420	1.44592668	1.32394734
Mg	0.03144602	2.88609215	1.68084007
O	-1.40257886	4.33060598	2.01147855
Mg	3.71467949	-1.49562620	-1.56907017
O	2.28792545	-0.00094449	-1.15819618
Mg	0.91163126	1.44525935	-0.73489167
O	-0.48137240	2.87836099	-0.37891702
Mg	-1.91579734	4.35880931	0.04685969
O	3.10917672	-1.49319036	-3.57876573
Mg	1.69490974	-0.00128425	-3.17967184
O	0.32341361	1.44377021	-2.85305885
Mg	-1.03608474	2.87239869	-2.40739689
O	-2.46825218	4.34206742	-2.00212692
O	6.24098315	-0.00182532	1.80271881
Mg	4.95891582	1.43347364	2.25854684
O	3.61938746	2.92859537	2.74105790
Mg	2.52666893	4.60186631	3.03098909
O	-6.09607689	0.00629735	1.12564770
Mg	5.63647174	-0.00230740	-0.05504262
O	4.30409906	1.51022517	0.32866038
Mg	2.91162673	2.88934026	0.81991100
O	1.51955293	4.34005366	1.25586006
Mg	0.03073039	5.68704513	1.64576620
O	5.12309020	-0.00329494	-2.00414830
Mg	3.71678549	1.49191924	-1.57065752
O	2.35341459	2.94777504	-1.17301597
Mg	0.96835191	4.35568360	-0.73619437
O	-0.47330249	5.79370847	-0.34041896
Mg	4.34646260	-0.00344546	-3.76938284
O	3.11124629	1.48790668	-3.58042016
Mg	1.73064663	2.87618271	-3.10224409
O	0.39564569	4.34092344	-2.78492800
Mg	-0.98219380	5.58556775	-2.20186309
Mg	-0.99021266	-5.58309202	-2.19657500
O	-2.47441595	-4.33774981	-1.99790862
Mg	-3.78502497	-2.87766905	-1.59470638
O	-5.21965899	-1.48776590	-1.27750028
Mg	-6.36394717	0.00569193	-0.80085711
N	0.42051507	-0.24416328	5.30822864
H	-0.07038914	-1.05201719	5.75666217
H	1.35545042	-0.19034341	5.75645422
H	-0.06868686	0.63853461	5.57703096

F_{B-N} (optimised)

Mg	-2.22172993	5.22418602	-3.01691901
O	-0.35627858	4.70903768	-3.21699372
Mg	1.50545031	3.93586977	-3.16330766
O	3.41178824	3.27014579	-3.23369716
Mg	5.14686006	2.41273669	-3.05040543
O	-3.07395846	3.49358266	-3.25750551
Mg	-1.11624374	2.75394610	-3.28318704
O	0.78691874	2.04946073	-3.35795471
Mg	2.67275522	1.30863572	-3.30113580
O	4.62799855	0.55312067	-3.28797068
Mg	-3.74451220	1.58453427	-3.23481477
O	-1.85365409	0.86659193	-3.39445241
Mg	0.05361481	0.13604822	-3.35375610
O	1.96741881	-0.59025049	-3.41025067
Mg	3.85460018	-1.31456031	-3.26846275
O	-4.51576397	-0.28110354	-3.34042601
Mg	-2.56439501	-1.03792957	-3.36508550
O	-0.67355012	-1.77466979	-3.44310629
Mg	1.22507623	-2.48088603	-3.38580823
O	3.18819783	-3.21723825	-3.37474230
O	-2.32655620	5.40538982	-1.09142908
Mg	-0.36868375	4.67621254	-1.10126395
O	1.54230119	3.99973598	-1.14473120
Mg	3.41644870	3.23773012	-1.12070144
O	5.36182744	2.47010004	-1.12525797
Mg	-3.09939200	3.45795225	-1.14071084
O	-1.12725465	2.72899431	-1.19213989
Mg	0.77933873	2.01272977	-1.18562100
O	2.68384117	1.27186036	-1.20712310
Mg	4.63918252	0.50735558	-1.17647216
O	-3.86034591	1.58863711	-1.22509433
Mg	-1.87757360	0.82480697	-1.21765095
O	0.05110408	0.09283890	-1.27474335
Mg	1.96718946	-0.64088482	-1.23593291
O	3.95857650	-1.39832888	-1.25393423
Mg	-4.54594401	-0.31995646	-1.22649294
O	-2.58689543	-1.08993930	-1.27736509
Mg	-0.68944674	-1.83209172	-1.27085272
O	1.22909763	-2.54105141	-1.29546789
Mg	3.19538575	-3.27650749	-1.26179325
Mg	-2.29829015	5.27933457	0.95457934
O	-0.35111614	4.65933423	0.90195696
Mg	1.52508058	3.93889108	0.94271122
O	3.41039403	3.22530947	0.88417275
Mg	5.27605732	2.38853907	0.92244672
O	-3.13383535	3.42211509	0.86042272
Mg	-1.14953084	2.66296607	0.90761936
O	0.76766835	1.93983339	0.89797285
Mg	2.67880805	1.22367298	0.87619798
O	4.65545261	0.44665756	0.82659368
Mg	-3.81864288	1.52472903	0.88085747
O	-1.85708773	0.77625048	0.84386618
Mg	0.01998142	0.05410787	0.78625469
O	1.93245766	-0.67166529	0.84700411
Mg	3.93684575	-1.43846831	0.83279475
O	-4.57511690	-0.33654092	0.76316267
Mg	-2.59712196	-1.12135476	0.82183686
O	-0.67683136	-1.84766511	0.80110679
Mg	1.22296988	-2.58767734	0.78716552
O	3.21981160	-3.31781998	0.74123905
O	-2.29368195	5.20450003	2.91680647
Mg	-0.43680507	4.53340160	2.95856728
O	1.51987420	3.88770093	3.00231734
Mg	3.40531491	3.07600556	2.94074883
O	5.23361865	2.33064043	2.88411787
Mg	-3.04829095	3.37592152	2.91488782
O	-1.12671227	2.60069701	2.99686859
Mg	0.79293684	1.99858626	2.98666416
O	2.63473523	1.16785792	2.98710962
Mg	4.57747129	0.46499517	2.89683005
O	-3.88887641	1.50818048	2.93339957
Mg	-2.02793874	0.77122954	3.24106291
O	0.10107060	-0.02515256	3.31994384
Mg	2.05528290	-0.76766295	2.95918653
O	3.94006407	-1.48202571	2.87304991
Mg	-4.51694859	-0.44079955	2.79688720
O	-2.56747398	-1.14723737	2.86336904
Mg	-0.74478640	-2.00556219	2.86676614
O	1.19737683	-2.58974575	2.89522929
Mg	3.11253209	-3.36017119	2.81239774
Mg	-5.03515377	-2.15079853	-3.17659845

O	-3.30001082	-3.00025740	-3.38682427
Mg	-1.40008190	-3.66722847	-3.32920673
O	0.46971588	-4.43543987	-3.40538653
Mg	2.33350676	-4.95762135	-3.21631492
O	-5.26600943	-2.28570410	-1.26065877
Mg	-3.32488326	-3.05493930	-1.25899915
O	-1.44584490	-3.81894953	-1.31718844
Mg	0.46139744	-4.49920470	-1.29402560
O	2.43044545	-5.22028109	-1.30067780
Mg	-5.18864921	-2.29435332	0.79688127
O	-3.33629496	-3.13282294	0.74689649
Mg	-1.45992261	-3.85209118	0.77957087
O	0.44259588	-4.56394648	0.70114486
Mg	2.38691615	-5.18242083	0.75039147
O	-5.20753602	-2.27824130	2.74945927
Mg	-3.35000755	-3.06390648	2.90117147
O	-1.42105554	-3.89374256	2.81214509
Mg	0.50346664	-4.52936810	2.76248117
O	2.36685614	-5.18665385	2.71372177
O	-1.40239725	0.30244471	5.16450583
O	2.14299428	-1.01576178	6.15141928
B	-0.21555169	-0.04231655	4.73946983
B	1.09686433	-0.59271428	5.67787198
N	-3.43180850	-2.80680746	5.11510763
H	-3.14708364	-3.44365190	5.86734262
H	-2.90131576	-1.92786786	5.22964808
H	-4.42776346	-2.57603075	5.24359120

F_{BN} (optimised)

Mg	4.22360419	2.02060423	2.63526639
O	2.96940640	0.40419155	2.73987326
Mg	1.85140950	-1.27325172	2.79684778
O	0.56064724	-2.83325897	2.90114290
Mg	-0.67366095	-4.48762380	2.85266990
O	4.15005978	2.13074411	0.56293654
Mg	2.89659455	0.41358261	0.65623959
O	1.65619413	-1.21628664	0.72900529
Mg	0.43386374	-2.85072159	0.78951125
O	-0.85764754	-4.53792367	0.80818221
Mg	4.03585279	2.10467378	-1.43708463
O	2.78603853	0.41389589	-1.41857915
Mg	1.56625750	-1.22317098	-1.34066055
O	0.33175929	-2.84954685	-1.29511450
Mg	-0.94063937	-4.51433936	-1.19250606
O	3.91026634	2.09675630	-3.54827468
Mg	2.65647831	0.41581844	-3.50606262
O	1.44893843	-1.21494972	-3.51042941
Mg	0.21942464	-2.82345311	-3.38510785
O	-1.04434390	-4.49503503	-3.30471778
O	2.64300326	3.32602115	2.75597468
Mg	1.42326930	1.70334871	2.84169799
O	0.22357085	0.00235212	3.21766558
Mg	-1.16250344	-1.70293892	3.07825646
O	-2.36750818	-3.34210143	2.99266570
Mg	2.54058755	3.33504805	0.70035362
O	1.25715471	1.62939648	0.75607293
Mg	0.02015908	0.00815244	0.80233833
O	-1.18150491	-1.62134682	0.89397384
Mg	-2.46153742	-3.31275862	0.95257198
O	2.44421340	3.35486699	-1.38887750
Mg	1.16185185	1.65199688	-1.31341138
O	-0.07307223	0.01048391	-1.28933725
Mg	-1.30478297	-1.62936501	-1.18528855
O	-2.58194867	-3.33313541	-1.13904715
Mg	2.26816007	3.26498826	-3.39758833
O	1.04621763	1.64861636	-3.48546151
Mg	-0.18173312	0.01570519	-3.37392935
O	-1.41047499	-1.61908456	-3.36384564
Mg	-2.61743780	-3.23384526	-3.15468089
Mg	0.95080552	4.49168550	2.78916751
O	-0.24052939	2.84098403	2.93468511
Mg	-1.57212486	1.29639342	3.16406944
O	-2.69859260	-0.39687757	3.03569201
Mg	-3.94934689	-2.01621020	3.03058965
O	0.93696429	4.55605135	0.73162746
Mg	-0.37234895	2.85938005	0.84519844
O	-1.58553945	1.23316518	0.91565170
Mg	-2.81138018	-0.39060359	0.97286992
O	-4.08468360	-2.11615896	0.97729803
Mg	0.80313488	4.53611810	-1.26543501
O	-0.47185945	2.87193760	-1.24401700
Mg	-1.71009784	1.24730886	-1.15791926
O	-2.92602675	-0.39252324	-1.12011531
Mg	-4.17030177	-2.07933649	-1.01855850
O	0.68946810	4.52401407	-3.37777958
Mg	-0.57943981	2.85396585	-3.33315856
O	-1.81366921	1.24515931	-3.33842495
Mg	-3.01348525	-0.38487989	-3.21139182
O	-4.26372754	-2.06798068	-3.13304786
O	-0.65649439	5.64830197	2.83447360
Mg	-1.87791083	4.08998171	2.93099386
O	-3.19884106	2.52626160	3.05169010
Mg	-4.34548161	0.81522438	3.05170163
O	-5.50727162	-0.79196308	3.06999774
Mg	-0.76078266	5.68669392	0.87206738
O	-2.07890857	4.12789145	0.88596775
Mg	-3.27556829	2.50296565	1.00932164
O	-4.51109318	0.90768494	1.00322034
Mg	-5.63576094	-0.79384604	1.11034140
O	-0.87979140	5.77770273	-1.17271865
Mg	-2.15727620	4.11792356	-1.11292133
O	-3.40842766	2.52795292	-1.08742406
Mg	-4.58864297	0.88459909	-0.99307482
O	-5.82752113	-0.80365743	-0.93207891
Mg	-0.94530826	5.53749142	-3.09226405
O	-2.25620888	4.10857972	-3.22617982
Mg	-3.41931684	2.46102037	-3.10388645
O	-4.67992198	0.88209154	-3.10801263
Mg	-5.68138069	-0.76636978	-2.86097113
O	5.77471122	0.80165462	2.49320923
Mg	4.62179861	-0.80086051	2.61420187
O	3.46399370	-2.49894541	2.69807643
Mg	2.16357782	-4.08889668	2.71162253
O	0.93391057	-5.64061077	2.73193480
Mg	5.70865596	0.80879797	0.53454219
O	4.57606939	-0.89234882	0.53650477
Mg	3.36559686	-2.49727873	0.64472947
O	2.15507794	-4.11290752	0.65439149
Mg	0.83919893	-5.67284537	0.76905845
O	5.68968627	0.82507222	-1.52025612
Mg	4.45341914	-0.86172451	-1.46358876
O	3.26958806	-2.50591420	-1.44107749
Mg	2.01884567	-4.09551527	-1.34421246
O	0.74559373	-5.75526341	-1.27759580
Mg	5.34831447	0.79449379	-3.42637787
O	4.32570589	-0.85306021	-3.57494985
Mg	3.07022095	-2.43060214	-3.44835895
O	1.90124856	-4.07719895	-3.45430321
Mg	0.61141606	-5.50733363	-3.19437706
O	-0.52260467	-1.40682762	5.09834077
O	2.73701493	0.20246563	6.10689045
B	0.11342769	-0.09484622	4.74477100
B	1.66998253	0.06962670	5.51939258
N	-0.89585740	0.98398288	5.20367399
H	0.13963134	-2.12965917	5.01445931
H	-1.48886575	0.61859067	5.95713421
H	-0.47000956	1.85455868	5.53805046

$SE_{B\text{-}N}$ (optimised)

Mg	-2.75932650	4.64235823	2.78877945
Mg	-0.10842471	5.65318202	1.60803154
O	1.31305968	4.28432749	2.04350579
Mg	2.61514581	2.81407200	2.43007347
O	4.03517126	1.43427143	2.87332980
O	-1.57817272	4.28121116	1.15426576
Mg	-0.12646331	2.85338881	1.73573154
O	1.24507945	1.36875082	2.04509332
Mg	2.55609915	-0.07718315	2.63251235
O	4.08227544	-1.59425600	2.80769012
Mg	-0.92462347	4.32115293	-0.80117383
O	0.49363876	2.84120821	-0.39510384
Mg	1.87552270	1.40957949	0.04203361
O	3.27167909	-0.03313920	0.40525875
Mg	4.64412621	-1.52737646	0.83060719
O	-0.27439216	4.33293612	-2.83038759
Mg	1.14370285	2.86941283	-2.39814503
O	2.53555755	1.44197413	-2.05431370
Mg	3.87120674	0.00564156	-1.59677965
O	5.28875194	-1.48921114	-1.17477402
O	-3.78836722	2.89342530	2.46627872
Mg	-2.49034570	1.48943498	3.02040297
Mg	5.24314692	-0.06698749	3.05003055
O	0.48062629	5.76274235	-0.33944445
Mg	1.89938913	4.31772069	0.10953493
Mg	-2.96437792	2.86986633	0.59030780
O	-1.53745517	1.38634120	1.17848144
Mg	-0.08313692	-0.05826347	1.55573137
O	1.27387675	-1.51675482	1.97071481
Mg	2.67082425	-2.93597909	2.32092590
O	-2.30612217	2.92100761	-1.33779766
Mg	-0.87046482	1.43122337	-0.84491985
O	0.50314014	-0.03471720	-0.45202373
Mg	1.90497565	-1.46244906	-0.01712312
O	3.35356133	-2.98852375	0.38089755
Mg	-1.58704966	2.87750871	-3.23355874
O	-0.19689045	1.43942033	-2.92993218
Mg	1.16326389	0.00374710	-2.46779640
O	2.55044013	-1.44453218	-2.10089453
Mg	3.87734150	-2.87585450	-1.57084785
Mg	-5.07112674	1.37267467	1.94019504
O	-3.70249340	-0.06430615	2.57514371
Mg	-2.46972367	-1.54969557	3.09062109
O	3.31335444	2.91427542	0.48606094
Mg	4.61574485	1.46350424	0.88695028
O	-4.31321686	1.44826446	0.05463967
Mg	-2.90715798	-0.04912035	0.61389323
O	-1.50433397	-1.50502878	1.21392785
Mg	-0.04706397	-2.95008325	1.52531267
O	1.35697821	-4.39279559	1.92524949
Mg	-3.63628803	1.45883478	-1.81634693
O	-2.22045578	-0.03665770	-1.33789132
Mg	-0.85217540	-1.47887208	-0.90180799
O	0.52229318	-2.90619700	-0.48728758
Mg	1.95772245	-4.38852989	-0.02335259
O	-2.94674732	1.47790262	-3.78552131
Mg	-1.54063182	-0.00204051	-3.34219460
O	-0.18221742	-1.44740349	-2.96953740
Mg	1.17113487	-2.87100936	-2.48883914
O	2.58511235	-4.34230891	-2.04595112
O	-6.30477596	-0.08345707	1.42955382
Mg	-5.03473681	-1.50682851	1.93327288
O	-3.68772194	-3.01377609	2.47759147
Mg	-2.69974696	-4.79354787	2.70183721
O	6.06130733	-0.02644087	1.28437457
Mg	-5.61494315	-0.06271280	-0.40136189
O	-4.28331252	-1.56842633	0.04596169
Mg	-2.90747919	-2.94849361	0.57004667
O	-1.52900950	-4.38749747	1.05604834
Mg	-0.05494765	-5.74280348	1.47837200
O	-5.01677230	-0.04688193	-2.31834511
Mg	-3.62158272	-1.52757967	-1.83920580
O	-2.26898028	-2.97561500	-1.38809542
Mg	-0.89697607	-4.38853836	-0.92283697
O	0.53009061	-5.82334320	-0.48203867
Mg	-4.16758305	-0.01620129	-4.05349137
O	-2.93211398	-1.50194738	-3.81608341
Mg	-1.56614187	-2.88374136	-3.30094259
O	-0.24604625	-4.34616555	-2.94056336
Mg	1.11615812	-5.58847793	-2.32002366
Mg	1.07506327	5.57941207	-2.17635521
O	2.55017342	4.33390875	-1.91724939
Mg	3.84371705	2.87791724	-1.47413753
O	5.27015824	1.49620845	-1.12537691
Mg	6.39843981	0.00570400	-0.62406243
O	-0.91370337	2.68599047	3.79387278
O	-0.94682722	-1.26062139	4.46922202
B	-0.46916484	1.62453235	4.42063984
B	-1.06306206	0.01772109	4.27553309
N	1.99645294	-0.34227714	4.73417260
H	1.38172836	0.45058384	5.02464857
H	1.37738752	-1.16325701	4.80898662
H	2.73697987	-0.44930323	5.43661729

SE_{BN} (optimised)

Mg	-2.85661732	4.77847902	2.68086433
Mg	-0.12201663	5.64501259	1.62111122
O	1.29153857	4.27186377	2.07140243
Mg	2.59792638	2.79627630	2.45040446
O	3.96838485	1.38050808	2.93555787
O	-1.58352429	4.28561074	1.14844269
Mg	-0.12828262	2.83670915	1.71692193
O	1.25081785	1.37193806	2.04186693
Mg	2.45661859	-0.12263154	2.73601571
O	4.01268334	-1.61769908	2.84267139

Mg	-0.91651330	4.32363900	-0.80145111
O	0.49650743	2.84048588	-0.38632797
Mg	1.86443009	1.38614964	0.06372194
O	3.26751922	-0.04868589	0.39134668
Mg	4.60819137	-1.53421290	0.84276663
O	-0.25799455	4.33744471	-2.82118996
Mg	1.15414987	2.86744429	-2.38342279
O	2.54241198	1.44364792	-2.04507797
Mg	3.87351872	0.00326449	-1.59093488
O	5.28915147	-1.49382345	-1.16393118
O	-3.82327757	2.96324813	2.42283592
Mg	-2.51591502	1.58926004	2.96150290
Mg	5.18575341	-0.10850409	3.09037026
O	0.49099923	5.76049547	-0.31992945
Mg	1.90047235	4.30903265	0.13622663
Mg	-2.97313951	2.89377139	0.55859580
O	-1.55241872	1.41087968	1.16401638
Mg	-0.11282747	-0.07847487	1.68119612
O	1.28681196	-1.57469814	1.90242343
Mg	2.66715070	-2.98371511	2.27386934
O	-2.30585705	2.92958981	-1.34793140
Mg	-0.86456026	1.42498119	-0.83451411
O	0.49704455	-0.03615921	-0.44991602
Mg	1.89168007	-1.46329204	-0.03163898
O	3.36240917	-3.01909167	0.35973099
Mg	-1.57899559	2.88084200	-3.23127640
O	-0.19442290	1.44531271	-2.92839704
Mg	1.16200550	0.00731005	-2.46043184
O	2.55116881	-1.44659068	-2.11354451
Mg	3.87769075	-2.87806699	-1.58429265
Mg	-5.06778551	1.41214812	1.94067289
O	-3.62112975	-0.00844461	2.63170747
Mg	-2.36771205	-1.48936143	3.11204060
O	3.31441068	2.90667961	0.52316368
Mg	4.57989309	1.42861029	0.92830707
O	-4.31235007	1.45087066	0.05834761
Mg	-2.88714185	-0.04013545	0.61475262
O	-1.50494041	-1.51871754	1.17780409
Mg	-0.04700681	-2.97170597	1.47792062
O	1.35372695	-4.43234524	1.88762552
Mg	-3.63564667	1.45911895	-1.81380847
O	-2.22427221	-0.03130983	-1.33998369
Mg	-0.85133454	-1.47304160	-0.89590449
O	0.51718715	-2.92412499	-0.52035004
Mg	1.95249630	-4.40442955	-0.06346846
O	-2.95279688	1.48215774	-3.78210970
Mg	-1.54314595	0.00434084	-3.34066528
O	-0.18761821	-1.44079513	-2.97749675
Mg	1.16528693	-2.86619490	-2.51088360
O	2.57765201	-4.34556123	-2.07811292
O	-6.26033619	-0.07689580	1.48600274
Mg	-4.96844889	-1.47525145	1.99687575
O	-3.62523669	-2.96167964	2.52586038
Mg	-2.62870333	-4.72012823	2.76642118
O	6.02528677	-0.05440154	1.33349756
Mg	-5.60354996	-0.07033983	-0.36773585
O	-4.27200136	-1.55729032	0.07980522
Mg	-2.90081632	-2.94454753	0.58458846
O	-1.53835848	-4.40859735	1.03966766
Mg	-0.06070933	-5.75852534	1.43839795
O	-5.02299172	-0.05110953	-2.29805063
Mg	-3.62275485	-1.52438820	-1.82448568
O	-2.28144558	-2.97690354	-1.39216638
Mg	-0.91166656	-4.39236061	-0.95140248
O	0.51311936	-5.83702190	-0.52269112
Mg	-4.17673358	-0.01313841	-4.03772612
O	-2.94274727	-1.49495007	-3.81221407
Mg	-1.57679474	-2.87224499	-3.30631374
O	-0.26096270	-4.34129342	-2.96994857
Mg	1.10151366	-5.58363014	-2.35860438
Mg	1.09339661	5.57540408	-2.15236707
O	2.56385795	4.33116867	-1.88572048
Mg	3.84939829	2.86948162	-1.43512394
O	5.27333754	1.49115481	-1.08372167
Mg	6.38387791	-0.00541878	-0.57632535
O	-1.35579762	-1.18197559	4.82685429
O	-0.96129492	2.46402972	3.88989940
B	-0.24886783	-0.26234544	4.30081189
B	-0.46389741	1.33333087	4.28532393
N	1.19529446	-0.73843880	4.51950444
H	-1.28417242	-1.49012715	5.75938578
H	1.25248529	-1.75306686	4.35754339
H	1.52472793	-0.57303070	5.47908747

SE_{2N} (optimised)

Mg	-3.38219522	4.48599150	2.22897520
Mg	-0.91391976	5.64660416	0.95904095
O	0.66649856	4.54834603	1.46792070
Mg	2.13789128	3.29246628	2.05612058
O	3.76691892	2.16375609	2.53319328
O	-2.17259870	4.09004117	0.61694607
Mg	-0.46074824	2.89113546	1.12061140
O	1.08493997	1.68142170	1.60532047
Mg	2.48668780	0.46406233	2.49645687
O	4.26398393	-0.77922220	2.68411683
Mg	-1.56942446	4.02942334	-1.34378114
O	0.07159038	2.81349457	-0.86358521
Mg	1.66407803	1.60682510	-0.31334411
O	3.25886059	0.42985896	0.10900836
Mg	4.79807701	-0.79334010	0.66155937
O	-0.96045634	3.94629136	-3.36075461
Mg	0.67577508	2.73469760	-2.85389420
O	2.26553277	1.57032065	-2.42820415
Mg	3.80362687	0.38253323	-1.88481473
O	5.43193194	-0.84428594	-1.36445806
O	-4.02871016	2.56063204	2.20997176
Mg	-2.47270932	1.41287217	2.86377371
Mg	5.19869020	0.89712861	2.75755405
O	-0.36315180	5.69360296	-1.01286356
Mg	1.27664801	4.51230724	-0.47447646
Mg	-3.30651300	2.42790897	0.29419392
O	-1.68664984	1.27943162	0.92663745
Mg	-0.06598672	0.05839343	1.55781894
O	1.54600917	-1.20898382	1.83866513
Mg	3.12184813	-2.36248786	2.29226653
O	-2.73607510	2.39692084	-1.67189705
Mg	-1.07167071	1.15992030	-1.10745964
O	0.49734549	-0.03570540	-0.65215333
Mg	2.08309529	-1.19383142	-0.12120512
O	3.77624852	-2.48005319	0.35644702
Mg	-2.06616671	2.26567846	-3.57083391
O	-0.47315939	1.08688502	-3.21123835
Mg	1.09508865	-0.09408933	-2.65710328
O	2.69284063	-1.28875034	-2.23077713
Mg	4.22089130	-2.45234811	-1.60854473
Mg	-5.07335018	0.83429884	1.91794409
O	-3.46808155	-0.28418090	2.60796667
Mg	-1.97740107	-1.44632594	3.24022033
O	2.86117031	3.37422213	-0.00126567
Mg	4.31988595	2.13743827	0.50302893
O	-4.45596775	0.80509749	-0.02492653
Mg	-2.80968309	-0.41283168	0.59811249
O	-1.21844484	-1.61356038	1.20177749
Mg	0.42632192	-2.81287990	1.58896592
O	2.04034869	-4.01609591	2.07750296
Mg	-3.85351519	0.71875111	-1.92200933
O	-2.22686082	-0.50169418	-1.38949322
Mg	-0.64283322	-1.68157754	-0.86896635
O	0.93185072	-2.88327819	-0.42353494
Mg	2.57869916	-4.08731941	0.11335864
O	-3.24164424	0.64189484	-3.92074661
Mg	-1.61507710	-0.57254115	-3.41219148
O	-0.05078339	-1.76409280	-2.98282223
Mg	1.51038080	-2.92357043	-2.43233716
O	3.13547730	-4.13778086	-1.92077979
O	-6.09903534	-0.82628161	1.64586749
Mg	-4.59356636	-1.96831519	2.21766363
O	-3.02233609	-3.16479595	2.83428978
Mg	-1.76841902	-4.70254507	3.19667869
O	5.98885784	0.92193583	0.97914635
Mg	-5.52818264	-0.91724443	-0.23186642
O	-3.98438451	-2.16049048	0.27297249
Mg	-2.40514011	-3.26573330	0.84940850
O	-0.84289181	-4.49159384	1.35993374
Mg	0.82988177	-5.56143882	1.81112566
O	-5.02177921	-1.00957610	-2.19369397
Mg	-3.40787185	-2.22230938	-1.65219698
O	-1.85475746	-3.41769807	-1.15792380
Mg	-0.28367094	-4.57370150	-0.65180595
O	1.35016587	-5.75436711	-0.15336731
Mg	-4.24158968	-1.02865271	-3.96415644
O	-2.80215922	-2.29210331	-3.66899825
Mg	-1.23016479	-3.40184732	-3.09948097
O	0.29685921	-4.62945740	-2.69191325
Mg	1.84483803	-5.59382312	-2.02687157
Mg	0.21846700	5.41200510	-2.83809014
O	1.86453344	4.43591753	-2.52301174
Mg	3.36186848	3.22312279	-1.96764478
O	4.97438668	2.10700420	-1.54957571
Mg	6.29311542	0.84213713	-0.93770477
O	-1.32902883	-0.40599979	4.85454981
O	-1.38482451	2.83383030	3.89911578
B	-0.22493736	0.42534546	4.08426615
B	-0.17000695	2.11341184	4.20107553
N	1.23668461	-0.08195882	4.33258944
H	-1.23648588	-0.44671293	5.83509355
H	1.30555245	-1.09876999	4.19140693
H	1.56173166	0.09466527	5.29710719
N	1.02773329	2.96367338	4.27510276
H	0.88850198	3.94816701	4.52860050
H	1.82194804	2.56665244	4.78449772
H	-1.36026133	3.83298812	3.77877144

SE_{3N} (optimised)

Mg	-3.29709482	4.43753867	2.23506878
Mg	-0.85416599	5.64279916	0.92181662
O	0.74965308	4.55514498	1.39303314
Mg	2.24068081	3.31886906	1.88032789
O	3.80435215	2.18640070	2.46913551
O	-2.11008382	4.06763959	0.61991958
Mg	-0.40072320	2.88649321	1.14040421
O	1.13322860	1.68669228	1.60815987
Mg	2.50888890	0.47270823	2.49850965
O	4.28649448	-0.76343005	2.65329073
Mg	-1.53391510	4.00105259	-1.35672696
O	0.10446234	2.79017724	-0.88119258
Mg	1.68577340	1.57391980	-0.34477657
O	3.28852080	0.41512647	0.05880176
Mg	4.81978132	-0.80564663	0.62633138
O	-0.94999256	3.91146428	-3.38686688
Mg	0.68817380	2.69949366	-2.88784427
O	2.28288796	1.53721531	-2.47629959
Mg	3.82276131	0.34568724	-1.93337468
O	5.45344089	-0.87968401	-1.40229021
O	-4.00499079	2.54454406	2.18558860
Mg	-2.47819720	1.36858281	2.88382807
Mg	5.22988464	0.91030272	2.70307466
O	-0.33920071	5.67301925	-1.06500284
Mg	1.30531427	4.49432555	-0.55484902
Mg	-3.26627640	2.40396550	0.29332710
O	-1.64922457	1.26640220	0.94808589
Mg	-0.05064334	0.05065669	1.61174099
O	1.56968144	-1.20892120	1.82126618
Mg	3.14615810	-2.36155896	2.27322686
O	-2.70795504	2.37646527	-1.67207287
Mg	-1.04364200	1.13868729	-1.10823472
O	0.52216222	-0.05372564	-0.67265940
Mg	2.10246773	-1.20803984	-0.13868905
O	3.79687149	-2.49287793	0.34049465
Mg	-2.05315008	2.23751392	-3.58080652
O	-0.45978938	1.05901140	-3.22757717
Mg	1.11014749	-0.12526498	-2.68202691
O	2.71007892	-1.31958875	-2.25782022
Mg	4.23692755	-2.48328837	-1.62793964
Mg	-5.05656041	0.80809026	1.90147295
O	-3.46977938	-0.32705988	2.60763649
Mg	-1.98567608	-1.52816908	3.20432979
O	2.90642610	3.35343921	-0.08559025
Mg	4.36651880	2.11055439	0.42021252
O	-4.42368240	0.78418882	-0.03029031
Mg	-2.78503346	-0.43407777	0.59486192
O	-1.20153769	-1.63527219	1.19557887
Mg	0.44998242	-2.82243958	1.57603322
O	2.05959846	-4.01773863	2.07229427
Mg	-3.83023896	0.69864905	-1.92779927
O	-2.20438555	-0.51838744	-1.39393261
Mg	-0.62117497	-1.69937756	-0.87551214
O	0.95358226	-2.89846754	-0.43495316
Mg	2.59767160	-4.10489023	0.10801988
O	-3.22732470	0.62267246	-3.92729355
Mg	-1.59914890	-0.59697349	-3.42066839
O	-0.03564686	-1.79041464	-2.99641754
Mg	1.52686854	-2.95186180	-2.44441767
O	3.15377612	-4.16458639	-1.92838976

O	-6.09235309	-0.84574178	1.62038374
Mg	-4.59547924	-2.00596164	2.18898110
O	-3.03471795	-3.22772048	2.78922589
Mg	-1.79174708	-4.78986511	3.14453281
O	6.01757658	0.91062594	0.91957438
Mg	-5.50849586	-0.93382365	-0.25068358
O	-3.96894171	-2.17813141	0.25287758
Mg	-2.39101488	-3.29251884	0.82609212
O	-0.81854638	-4.50009877	1.34635761
Mg	0.84766280	-5.57637532	1.81478066
O	-5.00395195	-1.02248649	-2.20618807
Mg	-3.38917824	-2.24038611	-1.66486567
O	-1.83541712	-3.43650329	-1.17052639
Mg	-0.26164322	-4.59300597	-0.65695850
O	1.37289401	-5.76957088	-0.15363144
Mg	-4.22648920	-1.04677723	-3.97548545
O	-2.78728703	-2.31118089	-3.67822765
Mg	-1.21306266	-3.42651521	-3.10812464
O	0.31506609	-4.65483972	-2.69727720
Mg	1.86328824	-5.62057644	-2.02811715
Mg	0.22723916	5.38127106	-2.89565649
O	1.87831659	4.40362331	-2.58829932
Mg	3.38527250	3.18348703	-2.04956380
O	5.00355201	2.06924410	-1.62412030
Mg	6.32224073	0.80471091	-1.00049058
O	-1.15642266	-0.87261793	4.87334546
O	-1.12951068	5.38019626	4.76691417
B	-0.26388202	0.23409208	4.17251872
B	-0.52757980	1.83954931	4.57489539
N	1.27385227	-0.09025129	4.30431683
H	-0.98060872	-1.03431028	5.82691692
H	1.41815294	-1.09981751	4.16484920
H	1.60846005	0.11382517	5.25992078
N	0.47543152	2.85074396	4.43130916
H	0.31551099	3.84821915	4.59306090
H	1.45370690	2.56789700	4.40318568
H	-1.48062851	5.48557396	3.82577728
N	-1.93447987	2.34260734	4.74003209
H	-2.04372023	3.35181337	4.92523117
H	-1.59491382	6.10130995	5.24805145
H	-2.47873462	1.80580500	5.42815174

SE_{4N} (optimised)

Mg	-3.41626931	4.42691277	2.27698372
Mg	-0.93816999	5.62372219	1.01225226
O	0.64003362	4.51948755	1.51586790
Mg	2.07342824	3.24848123	2.14818489
O	3.72864045	2.11304761	2.60286041
O	-2.17594315	4.04589249	0.67829341
Mg	-0.46815251	2.85874528	1.15187867
O	1.06496032	1.63162900	1.62437548
Mg	2.46639069	0.43282712	2.49492901
O	4.21768964	-0.84021691	2.73400091
Mg	-1.57097689	4.01883247	-1.29601377
O	0.06659192	2.79538467	-0.82533610
Mg	1.65549688	1.58601793	-0.27661250
O	3.24110906	0.39593645	0.16986888
Mg	4.77614325	-0.83252424	0.71418502
O	-0.94788664	3.95103377	-3.31567265
Mg	0.68587063	2.73689935	-2.80729659
O	2.27275501	1.56278373	-2.37514725
Mg	3.80280731	0.36949997	-1.82369877
O	5.42534187	-0.86638922	-1.30110011
O	-4.04569754	2.49045925	2.23393720
Mg	-2.46732720	1.35832239	2.87598559
Mg	5.15570831	0.83909864	2.83315435
O	-0.37286990	5.67759431	-0.95417448
Mg	1.27102612	4.49556967	-0.40869165
Mg	-3.31861512	2.39740251	0.32335540
O	-1.69626262	1.23799788	0.95331104
Mg	-0.09592140	0.02772674	1.59369990
O	1.51308041	-1.25288695	1.87769534
Mg	3.09028005	-2.43100393	2.29669854
O	-2.73468442	2.39023424	-1.64131804
Mg	-1.07366397	1.14529432	-1.08500508
O	0.48775788	-0.05999636	-0.62778406
Mg	2.05835589	-1.22307832	-0.08757761
O	3.75041585	-2.51825967	0.38349073
Mg	-2.05167647	2.28064732	-3.54190501
O	-0.46025988	1.09345618	-3.18481270
Mg	1.10107643	-0.09467679	-2.62908535
O	2.69331809	-1.29631806	-2.19546232
Mg	4.21190487	-2.46816767	-1.57575150
Mg	-5.06898198	0.76588821	1.93648488
O	-3.46039281	-0.37975097	2.64389196
Mg	-2.02575373	-1.69164704	3.25450142
O	2.84748412	3.34749918	0.06691141
Mg	4.29770746	2.11192817	0.58274598
O	-4.45367991	0.77259721	-0.01314818
Mg	-2.81843460	-0.45224654	0.61104921
O	-1.24897739	-1.65740477	1.22044372
Mg	0.37472572	-2.86376682	1.63464407
O	2.00226397	-4.08931128	2.06757371
Mg	-3.84750241	0.71839018	-1.91475433
O	-2.22644329	-0.51015159	-1.38800404
Mg	-0.65120857	-1.69752820	-0.86375768
O	0.91104965	-2.90723609	-0.41163234
Mg	2.54287376	-4.12214794	0.11179097
O	-3.22393052	0.66737440	-3.91547891
Mg	-1.60281465	-0.55638344	-3.41023043
O	-0.04215123	-1.75719154	-2.98338401
Mg	1.50833872	-2.92253198	-2.42406536
O	3.12692540	-4.14803605	-1.91621036
O	-6.11149107	-0.87396922	1.61973739
Mg	-4.62920738	-2.04941105	2.15932100
O	-3.13944658	-3.33976272	2.71540572
Mg	-2.01934126	-5.01848209	2.95181840
O	5.96283039	0.87738653	1.06340811
Mg	-5.53616858	-0.92554172	-0.26257038
O	-4.00117281	-2.17713289	0.22101133
Mg	-2.43430782	-3.29817646	0.77767000
O	-0.90293837	-4.56063277	1.27818968
Mg	0.76736233	-5.62369778	1.75866000
O	-5.02262735	-0.99343148	-2.22580904
Mg	-3.41243711	-2.21360076	-1.69404259
O	-1.86467193	-3.41993831	-1.20494568
Mg	-0.30226781	-4.58864805	-0.69352191
O	1.32253156	-5.78768068	-0.19558783
Mg	-4.22935414	-0.99425976	-3.99138923
O	-2.79297784	-2.26583486	-3.70263365
Mg	-1.22429459	-3.38395461	-3.13459067
O	0.29685835	-4.62252050	-2.72416360
Mg	1.83592083	-5.59790474	-2.05798580
Mg	0.22710375	5.41260833	-2.77467783
O	1.87266851	4.43151861	-2.45503176
Mg	3.36535765	3.21439726	-1.89142775
O	4.97229273	2.08674386	-1.46492279
Mg	6.28392203	0.81739067	-0.85112547
O	-0.22701077	-2.93379281	3.78163040
H	-1.58652964	3.75679573	4.17617034
B	-0.28540007	0.34599956	4.26306952
B	-0.31223283	1.98225319	4.38840895
N	1.18819076	-0.17017801	4.37471616
H	0.38409614	-2.43354043	4.38073611
H	1.37707014	-1.08793896	3.95505311
H	1.57565920	-0.16658051	5.33080681
N	0.90456169	2.85266044	4.23931582
H	0.77954019	3.79698763	4.62286718
H	1.72264391	2.41877007	4.68505226
H	-2.20184966	2.63817601	5.22564290
N	-1.62957863	2.73963488	4.37429576
N	-1.38629513	-0.61482314	4.98649750
H	-0.97644194	-1.05649761	5.82745124
H	-2.15586012	-0.04444533	5.37213101
H	-0.17303907	-3.93206640	4.02440217

SE_{5N} (optimised)

Mg	-3.09861204	4.85278211	2.21539420
Mg	-0.37426742	5.70700228	1.21841231
O	0.97229045	4.35933565	1.82228814
Mg	2.26420130	2.91431557	2.33155917
O	3.57136693	1.54770754	2.96432907
O	-1.80694800	4.35765868	0.68068805
Mg	-0.33890124	2.92573824	1.22819234
O	0.91157368	1.48183806	1.85021745
Mg	2.26344609	0.05697308	2.39516081
O	3.57061887	-1.40678701	3.03008210
Mg	-1.00107689	4.34683968	-1.24766073
O	0.37589960	2.86525255	-0.67346168
Mg	1.74121671	1.44754225	-0.11272974
O	3.04846730	0.01554961	0.46919916
Mg	4.41818852	-1.47087699	1.09532280
O	-0.20328011	4.28462088	-3.17395044
Mg	1.19858964	2.83177393	-2.62767678
O	2.53910561	1.40535806	-2.09567186
Mg	3.86245973	-0.02689028	-1.47982642
O	5.18586963	-1.50448811	-0.86006332
O	-4.08840927	3.05524504	1.92056806
Mg	-2.84787675	1.70635311	2.60778294
Mg	4.84200679	0.07916707	3.39056749
O	0.37360983	5.77901646	-0.66498481
Mg	1.77865306	4.36925038	-0.09326408
Mg	-3.14085530	2.94198425	0.07920383
O	-1.76258320	1.47870708	0.90869267
Mg	-0.34343118	0.03333445	1.31717849
O	0.91189379	-1.39016739	1.91381581
Mg	2.26632656	-2.80082181	2.45520240
O	-2.34058623	2.91148388	-1.78014214
Mg	-0.93974184	1.43091473	-1.21429501
O	0.37019632	-0.00858188	-0.62039744
Mg	1.74174419	-1.44013602	-0.05057765
O	3.11590977	-2.93153292	0.58594693
Mg	-1.49385387	2.81134566	-3.64751916
O	-0.12422036	1.38193603	-3.18734116
Mg	1.20803514	-0.05154759	-2.59380497
O	2.54000176	-1.48518946	-2.03297451
Mg	3.83087487	-2.90455517	-1.33104940
Mg	-5.31819712	1.49502240	1.37787480
O	-3.90874760	0.05558590	2.26294873
Mg	-2.84598659	-1.57609020	2.68149263
O	3.11483301	2.96524192	0.45765439
Mg	4.41755263	1.52892132	1.03032240
O	-4.42662255	1.48925399	-0.44183658
Mg	-3.07556973	0.00963378	0.22395826
O	-1.76157378	-1.42742018	0.97203851
Mg	-0.33798856	-2.86040867	1.35325833
O	0.97455767	-4.26637345	2.00930786
Mg	-3.64588178	1.43655634	-2.31425133
O	-2.26797773	-0.03153287	-1.66444045
Mg	-0.93947613	-1.47298853	-1.15138666
O	0.37703642	-2.88191421	-0.54877033
Mg	1.77978316	-4.35830618	0.09598213
O	-2.81655104	1.39846026	-4.20936281
Mg	-1.45505711	-0.07536997	-3.67232094
O	-0.12300318	-1.50952221	-3.12490706
Mg	1.20019576	-2.93366003	-2.50255975
O	2.55379566	-4.37798765	-1.85357658
O	-6.49037984	0.02269378	0.85853046
Mg	-5.31631328	-1.42333251	1.44329164
O	-4.08492653	-2.95624467	2.05473933
Mg	-3.09581643	-4.73869254	2.42899668
O	5.73055246	0.04012694	1.61019277
Mg	-5.71276755	-0.01720736	-0.96287121
O	-4.42587870	-1.49891768	-0.37588613
Mg	-3.13943910	-2.92605268	0.20917281
O	-1.80539255	-4.31451885	0.87029330
Mg	-0.37171626	-5.63840842	1.46594630
O	-4.98906005	-0.05770176	-2.82787155
Mg	-3.64508728	-1.52777742	-2.24917176
O	-2.33920877	-2.97683347	-1.65149091
Mg	-0.99998866	-4.38778320	-1.05779646
O	0.37509090	-5.79203572	-0.41348255
Mg	-4.06143059	-0.09459641	-4.56424595
O	-2.81566031	-1.57088406	-4.14474705
Mg	-1.49171616	-2.95746451	-3.52209585
O	-0.20133220	-4.40854918	-2.98525577
Mg	1.11815573	-5.65391951	-2.22729517
Mg	1.11546550	5.56190956	-2.47081770
O	2.55166646	4.30347831	-2.04241590
Mg	3.82911418	2.85423408	-1.45657313
O	5.18513647	1.47690899	-0.92483868
Mg	6.31461299	-0.00045199	-0.26990296
H	1.88017482	-1.22410782	4.97279113
H	-1.66497578	0.10123063	4.17240266
B	-0.25497682	-1.27067964	4.57492318
B	-0.25441129	1.48988334	4.51112819
N	1.00210509	-1.75213147	4.98198723
N	-0.65582569	0.10621471	4.39712905
H	1.14246099	-2.74569613	5.16902578
H	1.88081028	1.45761895	4.90884653
N	1.00424839	1.98830494	4.89251846
H	1.14579834	2.98779144	5.04326134
N	-1.39546263	2.43482225	4.17909508
H	-1.08634636	3.40053976	3.93396462

H	-2.00993136	2.57917685	4.99986546
N	-1.39683981	-2.22927581	4.28520501
H	-2.00872671	-2.33790512	5.11334832
H	-1.08723626	-3.20445585	4.08186310

$SE_{h\text{-}BN}$ (optimised)

Mg	-3.20235845	4.87742359	2.15074208
Mg	-0.57407263	5.80138329	0.98303081
O	0.75011669	4.47925273	1.61173801
Mg	1.98255313	3.10804582	2.25784534
O	3.18971805	1.52976548	3.20639690
O	-1.98098188	4.39899281	0.53796035
Mg	-0.52660371	2.99662431	1.11587792
O	0.70847522	1.55256908	1.79420110
Mg	1.89959828	0.10196379	2.43732448
O	3.42091460	-1.69591957	3.04985975
Mg	-1.15543189	4.32796717	-1.39760760
O	0.22988758	2.85096112	-0.75794253
Mg	1.57254384	1.44261491	-0.11434067
O	2.84532497	-0.00097811	0.61262738
Mg	4.23118511	-1.50704198	1.16570706
O	-0.31868796	4.18770231	-3.30555916
Mg	1.07576357	2.75884370	-2.68222371
O	2.41485931	1.34776549	-2.05172857
Mg	3.74401840	-0.07259914	-1.40648276
O	5.02083364	-1.52960752	-0.69568705
O	-4.11694167	3.04575438	1.95569020
Mg	-2.81406447	1.73467103	2.63997278
Mg	4.50559607	0.07250377	3.64808815
O	0.20051649	5.78639264	-0.88296557
Mg	1.60197160	4.38879300	-0.22300371
Mg	-3.27344195	2.93816867	0.03805951
O	-1.89267802	1.48930230	0.84796099
Mg	-0.52456176	0.04067018	1.26468108
O	0.70362041	-1.41100195	1.95782773
Mg	1.97721067	-2.91569865	2.42255025
O	-2.48187331	2.86978084	-1.85078109
Mg	-1.08389081	1.40361219	-1.26262369
O	0.22441457	-0.03876923	-0.62308570
Mg	1.57094652	-1.46960757	-0.02765372
O	2.90006760	-2.96333457	0.63594003
Mg	-1.62587189	2.72404974	-3.72522051
O	-0.25067157	1.30400296	-3.21882960
Mg	1.07894271	-0.10939398	-2.58672307
O	2.40607411	-1.52520180	-1.97089819
Mg	3.67782078	-2.95343236	-1.25820038
Mg	-5.35732757	1.49866899	1.46191926
O	-3.91831038	0.06826803	2.35090419
Mg	-2.90812974	-1.61677315	2.72012638
O	2.95141297	2.96774643	0.49616692
Mg	4.20917736	1.50701172	1.07707949
O	-4.55392786	1.48298575	-0.42116869
Mg	-3.20988427	0.00491444	0.23260671
O	-1.90940310	-1.44231766	0.96679787
Mg	-0.54939386	-2.89957228	1.33619178
O	0.71923572	-4.33009505	2.01498383
Mg	-3.79133874	1.39917126	-2.32725515
O	-2.41458735	-0.06558811	-1.66697037
Mg	-1.09541087	-1.50924163	-1.16280592
O	0.20720444	-2.91445120	-0.53162279
Mg	1.57560859	-4.41605810	0.09511937
O	-2.96342185	1.32012727	-4.23463608
Mg	-1.60321308	-0.14353746	-3.68809228
O	-0.26480519	-1.56481644	-3.11418354
Mg	1.05270088	-2.98557303	-2.48141009
O	2.38869423	-4.42262308	-1.81092041
O	-6.56068418	0.04634408	0.96359451
Mg	-5.41045230	-1.41473643	1.52107457
O	-4.20535106	-2.95165731	2.10755090
Mg	-3.29705880	-4.78536100	2.42497735
O	5.40001579	0.06346763	1.86522837
Mg	-5.84910673	-0.01135823	-0.89922284
O	-4.57111929	-1.50061296	-0.33041770
Mg	-3.30658056	-2.94028662	0.22547538
O	-2.00240289	-4.34393511	0.86714856
Mg	-0.60930801	-5.71190305	1.44647310
O	-5.14463454	-0.08609583	-2.79247319
Mg	-3.80646736	-1.55579966	-2.22578116
O	-2.50638846	-3.00573532	-1.63734402
Mg	-1.18155570	-4.43201190	-1.06349402
O	0.17779233	-5.83698391	-0.41187184
Mg	-4.23206371	-0.15844679	-4.55199577
O	-2.97976194	-1.62854154	-4.12646505
Mg	-1.65234510	-3.00901216	-3.51363028
O	-0.36140698	-4.44873174	-2.96936122
Mg	0.95341337	-5.71813218	-2.22662216
Mg	0.99456177	5.49483842	-2.64958762
O	2.42750548	4.24018705	-2.10473858
Mg	3.70099842	2.81166146	-1.43172036
O	5.01981704	1.42557940	-0.79149141
Mg	6.20296395	-0.02120177	-0.06302121
H	3.34089116	-1.61535185	4.07861339
H	-1.99123383	-0.00969777	4.57716886
B	-0.47198992	-1.48842361	4.72801172
B	-0.13085173	1.01488742	4.52089002
N	0.89139218	-1.62773365	5.10547982
N	-0.97971223	-0.14917208	4.64386706
H	1.27535777	-2.54890726	5.32770968
H	2.18253435	3.92406776	4.84682458
N	1.28836286	0.82421852	4.67025738
H	3.18132382	1.93529596	5.46615274
N	-0.95839670	2.23041697	4.15164089
H	-0.36797914	3.04126493	3.90487751
H	-1.48755957	2.55620913	4.97839241
N	-1.45340524	-2.54665596	4.29087675
H	-2.11122397	-2.83252650	5.03640964
H	-1.01877854	-3.44601229	3.99777361
O	3.18637215	-0.67284159	5.24920460
O	1.80507896	3.24288944	4.25825226
B	1.85015132	-0.48033627	5.11791158
B	2.43726305	1.89230130	4.50433303